



High Performance, Earth Abundant and Non-Toxic Thin Film Solar Cells by Atomic Layer Deposition and Chemical Vapor Deposition

Citation

Chua, Danny. 2019. High Performance, Earth Abundant and Non-Toxic Thin Film Solar Cells by Atomic Layer Deposition and Chemical Vapor Deposition. Doctoral dissertation, Harvard University, Graduate School of Arts & Sciences.

Permanent link

<http://nrs.harvard.edu/urn-3:HUL.InstRepos:42029577>

Terms of Use

This article was downloaded from Harvard University's DASH repository, and is made available under the terms and conditions applicable to Other Posted Material, as set forth at <http://nrs.harvard.edu/urn-3:HUL.InstRepos:dash.current.terms-of-use#LAA>

Share Your Story

The Harvard community has made this article openly available.
Please share how this access benefits you. [Submit a story](#).

[Accessibility](#)

**High Performance,
Earth Abundant and Non-Toxic
Thin Film Solar Cells
by Atomic Layer Deposition
and Chemical Vapor Deposition**

A dissertation presented

by

Danny Chua

To

The School of Engineering and Applied Sciences

in partial fulfillment of the requirements

for the degree of

Doctor of Philosophy

in the subject of

Applied Physics

Harvard University

Cambridge, Massachusetts

April 2019

© 2019 by Danny Chua

All rights reserved.

Abstract

Cuprous oxide (Cu_2O) and tin sulfide (SnS) are two of the most promising absorber layers for thin film solar cells. Both photovoltaic absorber materials are non-toxic, Earth-abundant and low-cost semiconductor materials that demonstrate excellent surface morphology, crystal structure, phase and elemental purity, and opto-electronic properties for use in high performance solar cells.

Cuprous oxide (Cu_2O) thin films were grown by chemical vapor deposition (CVD) using precursors (*N, N'*-di-*sec*-butylacetamidinato)copper(I) and degassed water at low substrate temperatures of 125 to 225 °C. Despite being a widely studied material, vapor deposition of Cu_2O faces numerous challenges in avoiding material agglomeration, in obtaining high phase purity, and in limiting the process temperature to below 200 °C for temperature sensitive applications. We present pinhole-free single-phase oxide films that exhibit Hall mobilities up to $17 \text{ cm}^2 \text{ V}^{-1} \text{ s}^{-1}$ and wide band gaps exceeding 2.6 eV that are free from contaminants such as nitrogen, carbon, and cupric oxide (CuO). With good control of growth parameters (source temperature, substrate temperature, flow rate of carrier gas, etc), the film morphologies could be tuned to achieve both smooth, pinhole-free coatings as well as highly crystalline thin films with rough surfaces that are highly advantageous for applications to solar cells.

Thin film solar cells were fabricated using cuprous oxide (Cu_2O) absorber layers grown by chemical vapor deposition (CVD) and gallium oxide (Ga_2O_3) buffer layers grown by atomic layer deposition (ALD) on the cuprous oxide CVD films. The *in-situ* formation of heterojunction in the same deposition system without exposure to oxygen-rich ambient was found to be effective in mitigating the creation of detrimental cupric oxide (CuO) at the interface, resulting in

a pristine photovoltaic junction capable of delivering an enhanced open-circuit voltage of 1.78 V. Numerical device simulations of a novel two-layer absorber architecture (CVD-Cu₂O on ECD-Cu₂O) showed promising possibilities (theoretical 13.2 % efficiency) for a solar cell combining *in-situ* junction formation with electrochemical deposition of the absorber layer.

Thin film solar cells fabricated using non-toxic, Earth-abundant tin sulfide (SnS) absorber layers have performance limiting mid-gap defects that necessitates effective defect mitigation strategies. High temperature annealing treatments that enable performance enhancements are investigated using photoluminescence techniques to probe their effectiveness under annealing ambient of various sulfur contents. Decoupling of charge recombination on the surface from the bulk, and in grain interior from grain boundaries were leveraged to elucidate the impact of annealing conditions on photovoltaic device performances, leading to an enhanced open-circuit voltage of 0.38 V and an optimized photo-conversion efficiency of 4.99%.

Tin germanium oxide, (Sn,Ge)O₂, films were prepared using atomic layer deposition and tailored to SnS absorber layer by incorporating various amounts of germanium into tin oxide to adjust band alignments at the interfaces of SnS/(Sn,Ge)O₂ photovoltaic devices. Carrier concentrations of (Sn,Ge)O₂ were suppressed from 10²⁰ to 10¹⁸ cm⁻³ with germanium incorporation, with nitrogen doping of further reducing carrier concentrations by another order of magnitude. Excellent tunability of both band energy levels and carrier concentrations of (Sn,Ge)O₂ allowed optimizing SnS-based solar cells. SnS/(Sn,Ge)O₂:N devices were demonstrated, with an open-circuit voltage as high as 400 mV, due to effective mitigation of interfacial recombination of photogenerated carriers at the SnS/(Sn,Ge)O₂:N absorber-buffer heterojunction interface.

Acknowledgements

First and foremost, I would like to extend my most sincere gratitude to my doctoral adviser, Professor Roy G. Gordon, for giving me the opportunity to join the group, and for his guidance and support through my research endeavors to make this work possible. Professor Gordon is an esteemed scientist, a resourceful mentor, and an unparalleled role model. His vision, wisdom, and dedication have never ceased to amaze and inspire me. I am truly appreciative of his invaluable guidance, support, and encouragement throughout my graduate career. His unswerving pursuit of truth and knowledge will always prompt me to rise above obstacles and strive for excellence.

I would like to express my appreciation to Professor Eric Mazur and Professor Frans Spaepen for serving on my dissertation defense committee. In addition, I would like to thank our collaborators, Professor Tonio Buonassisi at MIT, for his insightful advice, and Dr. Richard Haight at IBM, for his technical expertise.

I am indebted to all the professors and mentors who have given me invaluable guidance throughout my academic career. In particular, I would like to extend my sincere appreciation to my undergraduate adviser at National University of Singapore, Professor Ho Ghim Wei, for her mentorship, support and encouragement over the years. Professor Ho introduced me to the world of photovoltaics and provided me with unlimited freedom in my research endeavors, inspiring in me a child-like curiosity about the natural world especially at an atomic level. I would also like to express my appreciation to undergraduate dean Professor Wang Chien Ming for believing in my unconventional approaches to problem solving and providing incredible opportunities during my undergraduate years.

I would like to acknowledge my collaborators in the Gordon group: Dr. Prasert Sinsersuksakul, Dr. Sang Bok Kim, Dr. Kecheng Li, Dr. Ashwin Jayaraman, Dr. Rachel Heasley, Dr. Helen H. Park, Prof. Jaeyeong Heo, Prof. Sang Woon Lee, and Prof. Luke Davis. My thanks also go to our collaborators in the Buonassisi group at MIT: Prof. Yun Seog Lee, Dr. Sincheng Siah, Dr. Riley Brandt, Dr. Alex Polizzotti, Dr. Vera Steinmann, Dr. Katy Hartman, Dr. Rupak Chakraborty, Dr. Niall Mangan and Prof. Rafael Jaramillo. It has been a great privilege to be part of this collaboration. I would like to extend my appreciation to my collaborators in the CZTS team at IBM Thomas J. Watson Research Center including Dr. Richard Haight and Dr. Oki Gunawan. Furthermore, I would like to thank the staff at Harvard's CNS for their assistance.

I would like to recognize my other colleagues in the Gordon group: Dr. Leizhi Sun, Dr. Xizhu Zhao, Dr. Chuanxi Yang, Dr. Yeung Au, Dr. Xinwei Wang, Dr. Jing Yang, Dr. Xiabing Lou, Dr. Lu Sun, Dr. Jun Feng, Dr. Lauren Hartle, Christina Chang and many more. I would like to thank our group administrators, Teri Howard and Patricia McGarry, for their tireless efforts on my behalf. I feel very fortunate to be a member of the Gordon family. Moreover, I am thankful to all my friends for making my graduate life special and memorable. I am honored to have enjoyed the care, support, and friendship of so many brilliant and inspiring people.

Last but not least, I would like to extend my deepest appreciation to my loving parents, close relatives and grandparents. I would like to thank my uncle Chua Chin Soon for introducing me to the world of semiconductors and computers, and for giving me my first computer when I was 5, the first of many more to come. My dissertation is dedicated to my parents, Chua Cheng Qing and Cheng Soon Kiew. Without their unconditional love and support, I could never have come this far. Throughout my life, my parents have overcome many obstacles and made tremendous

sacrifices so that I could receive the best education possible. Thank you again for providing me the necessary wisdom, relentless strength and boundless freedom that I need to succeed.

Danny Chua

Cambridge, Massachusetts

April 30, 2019

Table of Contents

Abstract.....	iii
Acknowledgements	v
Table of Contents	viii
List of Figures.....	xiv
List of Tables	xxv
1 Introduction.....	1
1.1 Motivation	1
1.2 Solar Cells	2
1.2.1 Absorber Layers.....	6
1.2.2 Buffer Layers	6
1.2.3 Principles of Solar Cells.....	8
1.3 Deposition Techniques.....	16
1.3.1 Chemical Vapor Deposition.....	16
1.3.2 Atomic Layer Deposition and Pulsed Vapor Deposition.....	16
1.4 Dissertation Overview.....	17
1.5 References	19
2 Chemical Vapor Deposition of Cuprous Oxide Thin Films	20
2.1 Chapter Abstract.....	20

2.2	Introduction	21
2.3	Experiments.....	22
2.4	Results and Discussion.....	25
2.4.1	Growth Rates	25
2.4.2	Elemental Composition.....	26
2.4.3	Phase Purity	29
2.4.4	CVD Growth Regimes.....	29
2.4.5	Electrical Properties	35
2.4.6	Structural Properties.....	38
2.4.7	Optical Properties.....	40
2.4.8	Photoluminescence	41
2.5	Conclusion.....	45
2.6	References	46
3	Improved Cu₂O-Based Solar Cells Using Atomic Layer Deposition to Control the Cu Oxidation State at the p-n Junction	48
3.1	Chapter Abstract.....	48
3.2	Introduction	49
3.3	Experiments.....	50
3.4	Results and Discussion.....	52
3.4.1	Using ALD to Control of the Oxidation State of Copper at the Interface	52

3.4.2	Impact of Cu Oxidation States on the Cu ₂ O-based Solar Cells	63
3.5	Conclusions	67
3.6	Reference.....	68
4	Gallium Oxide Buffer Layer for Cuprous Oxide Solar Cells	71
4.1	Chapter Abstract.....	71
4.2	Introduction	72
4.3	Experiments.....	74
4.4	Results and Discussion.....	81
4.5	Conclusions	92
4.6	Reference.....	93
5	Enhancement of the Open Circuit Voltages in Cu₂O/Ga₂O₃ Heterojunction Solar Cells through the Mitigation of Interfacial Recombination	97
5.1	Chapter Abstract.....	97
5.2	Introduction	98
5.3	Methods.....	100
5.4	Results and Discussion.....	102
5.4.1	Interfacial Cu Oxidation States at the Cu ₂ O/Ga ₂ O ₃ Bilyaers.....	102
5.4.2	Cu ₂ O/Ga ₂ O ₃ Heterojunction Solar Cell Devices	103
5.4.3	Numerical Simulations of Solar Cell Devices using SCAPS-1D.....	108
5.5	Conclusion.....	115

5.6	References	117
6	Probing Defect Mitigating Enhancements of High Temperature Annealing Treatments on Tin Sulfide Thin Films Solar Cells	119
6.1	Chapter Abstract.....	119
6.2	Introduction	120
6.3	Experimental	122
6.4	Results and Discussion.....	125
6.4.1	Film Morphology and Structure.....	125
6.4.2	Electrical Characterization.....	128
6.4.3	Spectral Resolved Photoluminescence Measurements	130
6.4.4	Time Resolved Photoluminescence Measurements.....	132
6.4.5	Photovoltaic Device Characterization.....	135
6.5	Conclusions	138
6.6	Reference.....	139
7	Atomic Layer Deposition of Tin Germanium Oxide as a Tunable Electron Transport Layer Optimized for SnS-based Solar Cells.....	141
7.1	Chapter Abstract.....	141
7.2	Introduction	142
7.3	Experimental	144
7.4	Results and Discussion.....	147

7.4.1	Growth	147
7.4.2	Elemental Composition.....	147
7.4.3	Structural Properties.....	151
7.4.4	Electron Carrier Suppression from Germanium Incorporation	151
7.4.5	Band Gap and Band Alignment	155
7.5	SnS/(Sn,Ge)O ₂ Heterojunction Solar Cell Devices.....	158
7.6	Conclusions	159
7.7	References	162
8	Oxygen Doped Tin Sulfide Buffer Layer for SnS-Based Heterojunction Solar Cells	164
8.1	Chapter Abstract.....	164
8.2	Introduction	165
8.3	Experimental	166
8.4	Results and Discussion.....	168
8.4.1	ALD Growth Behavior	168
8.4.2	Film Composition	171
8.4.3	Film Morphology and Structure.....	175
8.4.4	Electrical Properties	178
8.4.5	Optical Properties.....	180
8.4.6	Band Alignment	182
8.5	Conclusions	183

8.6	Reference.....	184
Appendix A. Deposition Systems.....		185
A1.	Hybrid ALD-CVD Reactor: Cu ₂ O, Ga ₂ O ₃ , ZnO:Al	185
A2.	ALD Reactor: SnS, ZnOS:N	186
A3.	ALD Reactor: SnS, In ₂ O ₃	187
A4.	ALD Reactor: (Sn, Ge)O ₂	188
A5.	Thermal Oxidation System: Cu ₂ O.....	189
Appendix B. Thermal Oxidation of Cu Sheets to Cu₂O.....		190
Appendix C. High Temperature Annealing Treatments of Doped Ga₂O₃ Thin Films ...		195
Appendix D. Photovoltaic Device Simulations		197

List of Figures

Figure 1.1. Progress in the best research cell efficiencies up to 2019. [4]..... 4

Figure 1.2. Comparison of the efficiencies of (a) the performance and cost leaders at the cell and module levels, and (b) of the current contenders to mono-Si in chronological order. [5]..... 5

Figure 2.1. Formula for the copper (I) precursor (*N,N-di-sec-butylacetamidinato*)copper(I) used in the CVD of Cu₂O thin films. 22

Figure 2.2. (a) Temperature dependent growth rate plot at different process pressures. (b) Arrhenius plots and linear fits at different process pressure and at a constant substrate temperature of 200°C. 25

Figure 2.3. XPS spectrums of (a) the Cu-2p depth profiling scan indicating the presence of CuO (Cu²⁺) on the surface of Cu₂O which is removed by sputtering for 120 seconds, (b) the O-1s depth profiling scan showing presence of copper hydroxides in the film deposited at the lowest temperature of 125 °C, (c) the amount of C contamination in the film with various substrate temperatures, and (d) the amount of N incorporated into the film at various substrate temperatures..... 27

Figure 2.4. XPS spectrum of CVD Cu₂O films deposited at 200°C after 120 seconds of Ar+ sputtering, showing (a) Cu2p scan. (b) O1s scan..... 28

Figure 2.5. Cross-sectional SEM images showing Cu₂O thin films grown under CVD conditions that preserve a continuous film at various film thickness of (a) 80 nm, and (b) 320 nm. 31

Figure 2.6. Evolution of CVD Cu₂O film shown in a series of SEM micrographs. At low film thickness, islands nucleate and grow on top of a continuous compact film. As the film thickens, the clusters coalesce to form a continuous firm with larger grain sizes. 32

Figure 2.7. (a) Raman spectrum of CVD Cu₂O films of varying film thickness deposited at 200°C. The Raman peak at 519 cm⁻¹ is observed to shrink as the film thickness increases. (b) A shift in the Raman peak at around 217 cm⁻¹ due to the film experiencing tensile stress before the islands coalesce and compressive stress as the film grows thicker. 33

Figure 2.8. Raman spectrums of CVD Cu₂O films deposited at various temperatures ranging from 125°C to 200°C..... 34

Figure 2.9. Resistivity, carrier concentration and Hall mobility of Cu₂O CVD thin films (a) of thickness of about 50-nm for various deposition temperatures, and (b) for various film thickness deposited at 200°C. 35

Figure 2.10. XRD spectra of Cu₂O thin films (a) for various film thickness deposited in the high-growth regime at 200°C, and (b) a close-up view showing the left shift in the (200) peak..... 38

Figure 2.11. Tauc plot of $(\alpha h\nu)^2$ vs. photon energy for Cu₂O CVD films at film thicknesses of 60 nm, 120 nm, 240 nm and 360 nm. 41

Figure 2.12. (a) Inter-band photoluminescence emission profile of Cu₂O thin film at various temperature, and (b) the variation in band gap values of Cu₂O at different temperatures compared to a fitted model based on the Varshni relation..... 43

Figure 2.13. PL spectrum showing (a) the various PL components that make up the PL emission spectra obtained at room temperature, and (b) the temperature dependence of various defect-related PL bands..... 44

Figure 3.1. XPS spectra of Cu-2p core levels for an as-grown Cu₂O film surface and sputtered surfaces by Ar-ion at 1 keV in situ. The peaks from Cu¹⁺ and Cu²⁺ states are shown in red and blue asterisks respectively. The native CuO surface layer, which is removed by sputtering, is estimated to be 1 nm thin. 59

Figure 3.2. Normalized XPS spectra of Cu-2*p* of Cu₂O surfaces before and after heat treatments. As grown Cu₂O samples were kept in the ALD chamber under vacuum without ALD treatment. The same duration with the ALD treatment was used..... 59

Figure 3.3. The Zn precursor in the a-ZTO ALD process is experimentally observed to reduce the oxidation state of the Cu₂O absorber’s native CuO surface layer to Cu₂O. **(a)** Normalized XPS spectra of Cu-2*p* of Cu₂O surface after a pulse of DEZ and Sn(II) molecules on electrochemically-deposited Cu₂O films having nanometer-scale-thick CuO surface layers. **(b)** XPS spectra of Zn-2*p* core levels after a pulse of only DEZ molecules on the Cu₂O film at 90 °C, showing same Zn-2*p* core level with ZnO film grown by ALD using DEZ and H₂O₂. **(c)** The Cu-*LMM* kinetic energies from Cu₂O and metallic Cu after the growth of a-ZTO layer by ALD at 90 °C. (20-nm-thick Cu film was prepared by e-beam evaporation at room temperature for the comparison). **(d)** XPS spectra of Cu-2*p* core levels with 10-nm-thick a-ZTO films deposited on Cu₂O at reaction temperatures between 90 and 170 °C, showing no signal from elemental Cu for all temperatures, which indicates no Cu diffusion occurred..... 60

Figure 3.4. H₂O₂ exposure can re-oxidize the Cu₂O surface layer to CuO. Shown are normalized XPS spectra of Cu-2*p* for three different Cu₂O films. Only H₂O₂ pulses were injected on Cu₂O samples at reaction temperatures of 90 and 170 °C..... 61

Figure 3.5. ALD reaction temperature can control the oxidation state of the Cu₂O surface layer. **(a)** Normalized XPS spectra of Cu-2*p* from the Cu₂O samples after the growth of a-ZTO films at reaction temperatures between 90 and 170 °C. **(b)** The deconvoluted XPS spectra of Cu-2*p* of Cu₂O surface with a-ZTO film grown at 170 °C, showing a peak shoulder at ~933.7 eV corresponding to the Cu²⁺ state..... 61

Figure 3.6. Characteristics of solar cell devices with varying Cu oxidation state at the Cu₂O/a-ZTO interface controlled by ALD temperature. (a) A cross-sectional SEM image of Cu₂O-based solar cells with the device structure (ZnO:Al / a-ZTO / Cu₂O / Au). (b) J-V characteristics of the devices under 1-sun (AM 1.5G) illuminated conditions. (c) A summary of VOC and PCE of the devices as a function of the a-ZTO ALD temperature. (d). C-f characteristics of solar cell devices at room temperature with 0 mV and 10 mV for DC and AC bias, with a-ZTO films at reaction temperatures between 50 and 120 °C. 62

Figure 3.7. NREL certified *J-V* characteristics of the best device, with an a-ZTO buffer layer grown at 70 °C, under 1-sun (ASTM G173 global) illumination. 65

Figure 3.8. *J-V* characteristics of the devices under 1-sun (AM 1.5G) illuminated conditions with and without the additional heat treatment of Cu₂O film at 150 °C for 2 hours under vacuum, before the deposition of a-ZTO buffer layer at 70 °C and ZnO:Al layer at 120 °C. 66

Figure 3.9. Normalized QE spectrum of the device with a-ZTO buffer layer grown at 70 °C. A filtered QE system at NREL was used. 66

Figure 4.1. (a) The molecular structure of the ALD Ga precursor, bis(μ-dimethylamino)tetrakis(dimethylamino)digallium. (b) The surface morphology of a Ga₂O₃ film deposited on Si wafer measured by AFM. (c) The optical transmission (*T*) and reflection (*R*) spectra of a 0.2-μm-thick Ga₂O₃ film on a UV-grade quartz substrate. (d) Bandgap estimation of the ALD Ga₂O₃ film by a linear extrapolation. 75

Figure 4.2. (a) The electronic band alignment of the Ga₂O₃ / Cu₂O heterojunction derived from XPS and optical bandgap measurements, showing a type-II heterojunction with a ΔE_{CB} of -0.18 ± 0.2 eV. (b) The XPS spectra of the Cu-2*p* core level for an as-grown Cu₂O sample and a Ga₂O₃

(2 nm) / Cu₂O stack sample, which shows a reduction of the Cu²⁺-related peaks (asterisks) by the Ga₂O₃ overlayer. 76

Figure 4.3. (a) A photograph of the fabricated Cu₂O-based thin-film solar cell device, showing a 3 × 6 array of fully-isolated 3 mm × 5 mm size cells. (b) A cross-sectional SEM image of the device, showing the device structure of ZnO:Al (80 nm) / Ga₂O₃ (10 nm) / Cu₂O (~2.5 μm) / Au (200 nm) on a SiO₂ (0.3 μm) / Si substrate. The red dashed line indicates the ALD Ga₂O₃ buffer layer..... 77

Figure 4.4. The *J-V* curve and photovoltaic characteristics under AM1.5 global normal spectral irradiance (ASTM G173, IEC 60904-3 edition 2 at 25 °C), measured at NREL. 78

Figure 4.5. (a) J-V characteristics of the device under a dark condition in a semi-log scale and a linear scale (inset). The slope of the semi-log scale plot shows an ideality factor of ~2.05 near a bias condition of 1 V. (b) Temperature-dependence of the VOC and JSC of the device under a ~0.9-sun illumination condition. The dotted line indicates a linear extrapolation of the VOC to a temperature of 0 K. 79

Figure 4.6. (a) The spectra of bias-dependent EQE of the device and calculated absorption depth (α^{-1}) of Cu₂O. (b) The change of EQE under various bias conditions relative to a zero bias condition. (c) Calculated optical absorption spectra of each layer in the device by the FDTD optical simulation, indicating a *J*_{SC} entitlement of 11.5 mA·cm⁻². The simulation shows a negligible optical loss by the Ga₂O₃ layer. The achieved *J*_{SC} (7.37 mA·cm⁻²) suggests this device is not optically limited, but instead limited by poor carrier collection. 80

Figure 4.7. The RBS spectrum of a 200-nm-thick Ga₂O₃ film deposited on a glassy carbon substrate. The atomic ratio of Ga:O is measured to be 1:1.6. 88

Figure 4.8. XRD spectra ($\theta - 2\theta$ scan) of a blank quartz substrate and 200-nm-thick Ga₂O₃ film deposited on a quartz substrate. 88

Figure 4.9. XPS spectra of Ga₂O₃ thin-film for (a) Ga-2*p* core level (b) valence band. The positions of the Ga-2*p*_{3/2} peak and the valence band edge are measured to be 1117.60 eV and 3.14 ± 0.15 eV, respectively. 89

Figure 4.10. XPS spectra of Ga-2*p* and Cu-2*p* core levels of the Ga₂O₃ (1 nm) / Cu₂O stack sample. The energy level difference between the peaks of Ga-2*p*_{3/2} and Cu-2*p*_{3/2} is measured to be 185.26 eV. 90

Figure 4.11. An EQE spectrum of the device, under a zero voltage bias and a light bias of 0.4 mA into the 0.15-cm²-size cell area. A white light-emitting-diode is used to enhance bias light intensity and a bias current. 90

Figure 4.12. An implied photovoltaic $J_{\text{imp}}-V_{\text{imp}}$ curve determined from $J_{\text{SC}}-V_{\text{OC}}$ measurements using a steady-state illumination, exhibiting a pseudo-PCE of 7.2% and a pseudo-FF of 84%. A solar simulator with a set of neutral density filters were used to produce various illumination intensities (n -sun). The V_{OC} at n -sun and J_{SC} at n -sun under the various illumination conditions were measured. The J_{imp} and V_{imp} were obtained by the relations of $J_{\text{imp}} = J_{\text{SC}} \text{ at } 1\text{-sun} - J_{\text{SC}} \text{ at } n\text{-sun}$ and $V_{\text{imp}} = V_{\text{OC}} \text{ at } n\text{-sun}$ 91

Figure 5.1. XPS depth profile measurement of the Cu-2*p* core levels sputtered in-situ by Ar⁺ ions showing the presence of CuO is limited to only the surface of the CVD grown film. 105

Figure 5.2. (a) Normalized XPS spectra of Cu-2*p* of a Cu₂O/Ga₂O₃ heterojunction exposed to room temperature air, showing a peak shoulder at ≈ 933.3 eV attributed to the Cu²⁺ phase. (b) Comparison of normalized XPS spectra of Cu-2*p* from the Cu₂O samples with various amounts

of CuO at the Cu₂O/Ga₂O₃ heterojunction after exposure to varying amounts of air to the Cu₂O surface before the deposition of the Ga₂O₃ overlayers. 106

Figure 5.3. (a) J-V characteristics of the devices with varying oxidative air exposure treatments at the Cu₂O/Ga₂O₃ interface under 1-sun (AM 1.5G) illumination conditions. (b) A cross-sectional SEM image of Cu₂O-based solar cells with the device structure

(Au/Cu₂O/Ga₂O₃/ZnO:Al). Scale bar represents 200 nm. 107

Figure 5.4. Comparison of current-voltage characteristics of Cu₂O/Ga₂O₃ devices (a) with different degrees of air exposure at the interface, proxied using varying amounts of interfacial defect densities, and (b) with varying amounts of bulk defect density in the Cu₂O absorber layer.

..... 111

Figure 5.5. Simulated cell efficiencies for Cu₂O/Ga₂O₃ devices (a) with varying carrier concentrations of both the Cu₂O absorber layer and the undoped Ga₂O₃ hole transport buffer layer, and (b) with varying carrier concentration of the Cu₂O absorber layer and varying

conduction band offset of Cu₂O absorber with Ga₂O₃ buffer layer. 112

Figure 5.6. (a) Device stack comprising of a 2-layer absorber consisting of a thick layer electrochemically deposited with an ultra-thin layer deposited using chemical vapor deposition, including silver front metallization, aluminum-doped zinc oxide window layer, gallium oxide

buffer layer, gold back contact coated on thermally oxidized silicon substrates. (b) Comparison of current-voltage measurement (dashed line) simulations (solid line) using different absorber

layers in the Cu₂O/Ga₂O₃ device stack. 113

Figure 5.7. Simulated J-V characteristics of an optimized Cu₂O-based device using the 2-layer absorber approach. 115

Figure 6.1. Plane-view and cross-section view SEM images of SnS ALD thin films for (a) unannealed and annealed in (b) H₂S atmosphere (10 Torr, 400°C, 1 hour), (c) N₂ atmosphere (10 Torr, 400°C, 1 hour), and (d) high vacuum (0.1 Torr, 400°C, 1 hour) 126

Figure 6.2. XRD spectrum of as-deposited SnS ALD thin films and of SnS ALD thin films annealed under 3 different ambient..... 127

Figure 6.3. Hall measurement results of (black) resistivity, (red)mobility and (blue) hole density of SnS ALD thin films subjected to various anneal ambients during the post-deposition anneal treatment. 128

Figure 6.4. Cross-sectional PL intensity depth profile maps comparing the intensity enhancements in the grain interiors and grain boundaries of SnS films annealed in (a) 0.1 Torr of N₂ ambient and (b) 10 Torr of H₂S ambient, and topological intensity maps when annealed in (c) 0.1 Torr of N₂ ambient and (d) 10 Torr of H₂S ambient. All scale bars represent 1 μm. Bar plots comparing the differences in photoluminescence intensities after annealing in a sulfur-rich and a sulfur-poor ambient (e) between the grain boundaries and grain interiors at the surface of the film, and (f) between the grain boundaries and grain interiors at the top and at the bottom of the grain from PL depth-profile measurements. 134

Figure 6.5. JV characteristics of Mo/SnS/SnO₂/Zn(O,S)/ZnO/ITO/Ag devices with various post-deposition anneal treatments applied to the SnS absorber, measured under AM 1.5 under dark (dashed) and AM 1.5 illumination (solid)..... 137

Figure 7.1. (a) The high resolution XPS spectra of the Ge-3d core level of SnO₂ ALD films and the increase in the XPS peak intensity with increasing amount of Ge incorporation in the film, and (b) plot displaying the variations in elemental compositions O/(Sn+Ge+O), Sn/(Sn+Ge+O), and Ge/(Sn+Ge) vs. the GeO₂/SnO₂ ALD cycle ratio. 148

Figure 7.2. XPS measurements after 30 seconds of in-situ Ar⁺ sputtering of the film surface of the (a) Sn-3d core level, (b) O-1s core level, (c) C-1s core level, and (d) N-2p core level of a typical ALD (Sn,Ge)O₂ film. 150

Figure 7.3. Plot of resistivities (black), electron carrier concentration (blue), and hall carrier mobility (red) with varying Ge content incorporated into SnO₂ films. 153

Figure 7.4. The O 1s region of XPS spectra of SnO₂ thin films with Ge contents of (a) 0 at.%, (b) 1 at.%, and (c) 14 at.% from films ALD deposited with SnO₂/GeO₂ ALD cycle ratios of 1:0, 9:1, and 1:1 respectively. 154

Figure 7.5. Effect of various amounts of germanium incorporation in SnO₂ films on (a) optical bandgaps as determined from absorption data, and (b) offsets of both the valance bands and conduction bands at the heterojunction formed with SnS. 155

Figure 7.6. (a) Current density-voltage characteristics of Mo/SnS/(Sn,Ge)O₂/ZnO/ITO devices at various (Sn,Ge)O₂ compositions under dark (dotted line) and AM 1.5 illumination (solid line), and (b) a cross-sectional SEM image of the solar cell device with structure Mo back contact/SnS annealed in 4% H₂S absorber/(Sn,Ge)O₂ buffer/ZnO/In₂O₃:Sn window/Ag front contact. Scale bar represents 100 nm. 161

Figure 8.1. Mass change monitored using QCM during (a) 2 ALD super-cycles each containing a sub-cycle of SnS followed by a sub-cycle of SnO at 120 °C, and (b) 1 ALD cycle of SnO and 2 ALD cycles of SnS at 120 °C..... 168

Figure 8.2. Mass change monitored using QCM during (a) 4 cycles of ALD SnS at 120 °C using Sn(Actamd) and H₂S, and (b) 6 cycles of SnO ALD at 120 °C using Sn(Actamd) and water. .. 169

Figure 8.3. Depth profile measurements of Sn(S,O) 19:1 ALD film, showing the survey spectra. Inset: (a) High resolution spectra of the C 1s core level, and (b) high resolution spectra of the N 1s core level. 173

Figure 8.4. High resolution XPS spectra showing (a) the Sn 3d core levels of SnS ALD films with various O concentrations, and (b) the deconvolution of the Sn 3d core levels of Sn(S,O) 19:1 ALD film. The dotted lines are the split-orbital components of the deconvoluted spectra, the solid lines are the experimental data. 174

Figure 8.5. XRD spectrum of undoped and oxygen doped SnS films with ALD subcycle ratios 39:1, 19:1, 9:1. (b) is the expansion of (a) to clearly show the (111) and (040) peaks. 175

Figure 8.6. Plane-view SEM micrographs of (a) SnS films, and Sn(S,O) films with SnS/SnO ALD sub-cycle ratios of (b) 39:1, (c) 19:1, and (d) 1:1. All ALD films were deposited on thermal oxide for 800 ALD cycles at 120°C. The scale bar is 100 nm. 176

Figure 8.7. Plot of (a) Hall mobility, (b) hole carrier concentration, and (c) resistivity of Sn(S,O) thin films with various O/(O+S) ratios. 179

Figure 8.8. UV-VIS-NIR measurements of Sn(S,O) thin films with different SnS/SnO ALD subcycle ratios, displaying the (a) transmittance, and (b) reflectance traces. (c) The extracted optical band gap values from the Tauc plot. 180

Figure 8.9. Energy level offsets at the SnS/Sn(S,O) heterojunction interface for valence bands (red) and conduction bands (black). 182

Figure 8.10. Schematic of the deposition system for CVD Cu₂O, ALD Ga₂O₃, ALD ZnO:Al. 185

Figure 8.11. Schematics of the ALD deposition system for SnS and ZnOS:N, and the H₂S annealing of SnS. 186

Figure 8.12. Schematics of the ALD deposition system for SnS and In₂O₃. 187

Figure 8.13. Schematics of the ALD deposition system for (Sn,Ge)O₂. 188

Figure 8.14. Schematics of the thermal oxidation system for oxidizing Cu sheets to Cu₂O 189

Figure 8.15. (a) Copper sheets suspended on a quartz rack using platinum wires and positioned in the middle of the annealing furnace. (b) Temperature profile of the 3-stage oxidation process for oxidizing Cu sheets to Cu₂O. 191

Figure 8.16. (a) Optical micrograph of the thermally oxidized Cu₂O surface showing the merging of small grains into larger grains of up to 1.2 mm in dimension. (b) 35mm camera image of the thermally oxidized Cu₂O sheet. 193

Figure 8.17. (a) Spectrally-resolved photoluminescence image focused on a Cu₂O grain. (b) Confocal microscope image of the same Cu₂O grain. 194

List of Tables

Table 1. Experimental conditions of CVD of Cu ₂ O.....	24
Table 2. Summary of the values of binding energies for Cu ₂ O CVD films.....	29
Table 3. Comparison of solar cell parameters of devices with different oxidative exposures to the Cu ₂ O/Ga ₂ O ₃ heterojunction interface	105
Table 4. Elemental composition of ALD (Sn,Ge)O ₂ films measured by high resolution XPS. $x = [Ge]/([Sn]+[Ge])$	147
Table 5. Average mass gain (Δm_1) and mass loss (Δm_2) for (a) the SnS ALD cycle, (b) the SnO ALD cycle, (c) the SnS cycle after the initial SnO cycle, and (d) the first and second SnS cycle after the initial SnO cycle.	171
Table 6. Elemental composition of ALD Sn _x (S,O) films measured by high resolution XPS. $x = [O]/([O]+[S])$	171
Table 7. Summary of post-anneal sheet resistances of Ga ₂ O ₃ , Sn-doped Ga ₂ O ₃ and Ge-doped Ga ₂ O ₃ under various annealing conditions.	195

1 Introduction

1.1 Motivation

When solar cells were first introduced, the exorbitant costs have severely limited their use cases to exotic applications such as in space missions and on satellites as a light-weight and reliable form of energy generation. The Earth's surface enjoys over 150 million terawatt-hours of solar irradiation and capturing just a fraction of it in the Sahara using today's photovoltaic capabilities is sufficient to meet the global energy demands many times over for the foreseeable future.

Unrelenting research and development in photovoltaics over the decades coupled with rising concerns over climate change and energy security have become powerful drivers to further fuel economic and technological breakthroughs in terrestrial photovoltaics (**Figure 1.1**), contributing to the astounding compounded annual growth rate (CAGR) of 24% from 2010 to 2017 for the global photovoltaics market. However, photovoltaics is still unable to match other classes of power-generations based on the levelized cost of energy (LCOE), contributing merely about 1% to electricity generation mix in the US [1]. This is indicative of an urgent need to revolutionize costs and efficiencies of photovoltaics technologies in order to meet grid parity and to be truly cost competitive. Crystalline silicon (c-Si) is the dominant photovoltaic technology today and also the current efficiency leader (**Figure 1.2a**). Despite not being the cost leader of the photovoltaics market, the popularity of c-Si deployment on space-limited rooftops stems from the high power generation densities and wide availability. The most critical factor for the production cost of solar cells lie in the 200-300 μm thick Si wafer which is responsible for over half of the costs of fabrication at the module level.

The window of opportunity opens for the nascent class of thin film photovoltaics, which hold the promise of low-cost photovoltaics by leveraging micrometers thick layer of photoactive semiconductors, featuring the cost leader cadmium telluride (CdTe) followed by copper gallium indium selenide (CIGS), amorphous silicon (a-Si) and new entrants like the ones based on perovskite. However, CdTe technology is hindered by the scarcity of tellurium and the toxicity of cadmium, while CIGS suffer from scalability issues. New material systems for thin film technology that can overcome the shortcomings of the current players in the thin-film class of photovoltaics need to be explored and be swiftly moving down both the cost curve and the experience curve.

Tremendous progress in solar cell efficiencies can be observed with the thin film class of photovoltaics in **Figure 1.2b**. As technological development continues aggressively, the desire for cost-effective, scalable, high performance solar cells using non-toxic earth abundant materials is soaring as the world accelerates towards widespread penetration of solar photovoltaics and clinch on to the vast rewards that await.

1.2 Solar Cells

A solar cell is an opto-electronic device that converts light energy to electrical energy by using the photovoltaic effect. The photovoltaic energy conversion process comprises of three steps: charge generation through photon absorption, charge separation across the asymmetric junction and charge transport to the device terminals. The performance of a solar cell is typically described using the parameters J_{SC} , V_{OC} , FF and η (described further in 1.2.3.3 and 1.2.3.4) measured under a standard testing condition using an AM 1.5 spectrum with an incident power density of 100 mW cm^{-2} and at a temperature of 25°C .

Thin film solar cells offer a generous cost reduction compared to the traditional c-Si which requires electronic grade silicon feedstock for its fabrication. Thin-film photovoltaics are based on using a 100x thinner absorber layer in the order of micrometers to completely absorb the incident sunlight, allowing for remarkable savings in material costs. This achievement is made possible by leveraging semiconductors with enhanced absorptions in the solar spectrum compared to c-Si. In addition, the drastically thinner device enables the use of semiconductor materials with much shorter minority carrier diffusion lengths, liberating us from the requirement of using ultra high purity materials and providing improved tolerance for defects and impurities in the manufacturing process.

Thin film photovoltaics utilize a common device stack with the following structure: back metal contacts/p-type absorber layer/n-type buffer layer/n⁺-type window layer/anti-reflection coating/top metal contacts. Each of these layers play a unique and essential role in obtaining a high-performance solar cell. The absorber layer is designed to have an optimal optical band gap, a high optical absorption coefficient, a high quantum yield and a sufficiently long minority carrier diffusion length. The n-type buffer layer forms the p-n junction with the p-type absorber layer, which requires an optimal conduction band offset with the absorber layer to reduce the interfacial recombination at the heterojunction, and also requires an optical band gap larger than that of the absorber layer to avoid optical losses before the incident photons undergo photogeneration in the absorber layer. Further details regarding the other layers in the stack can be found in [2, 3].

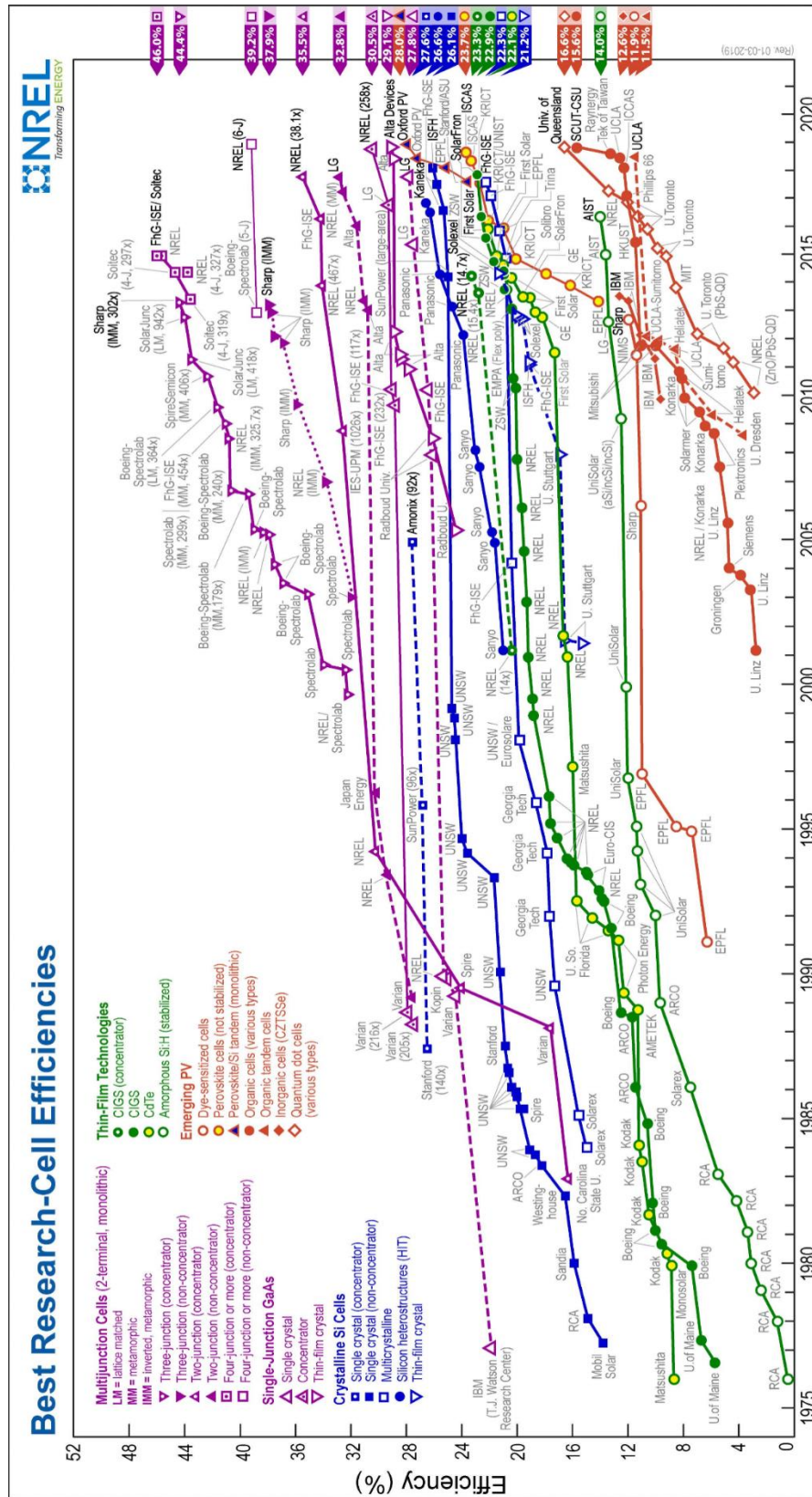


Figure 1.1. Progress in the best research cell efficiencies up to 2019. [4]

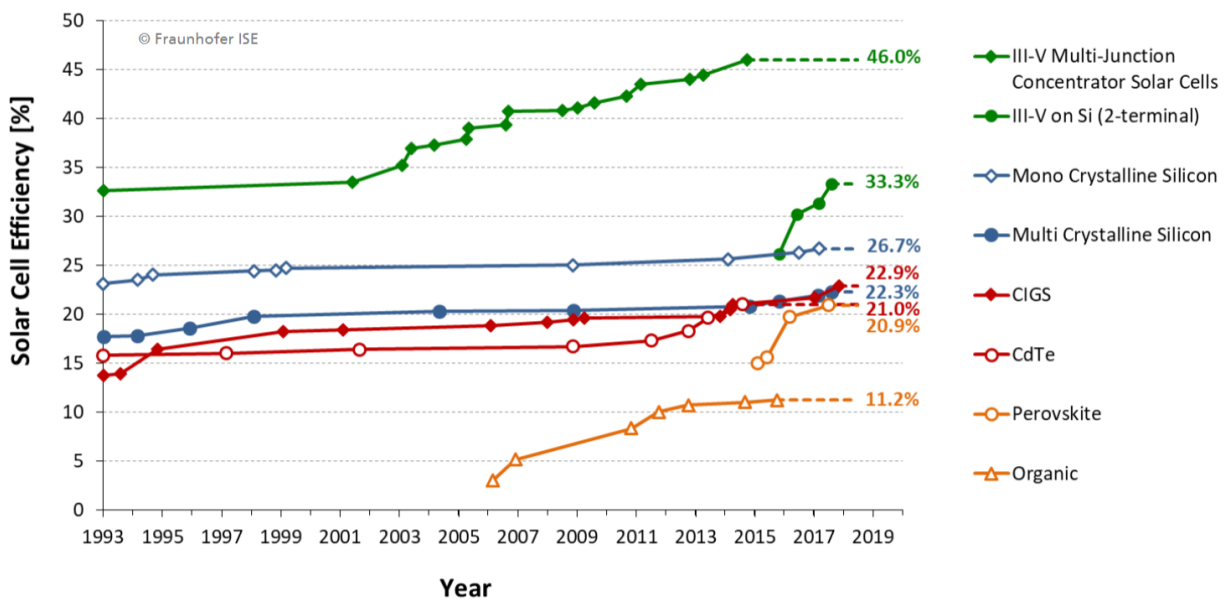
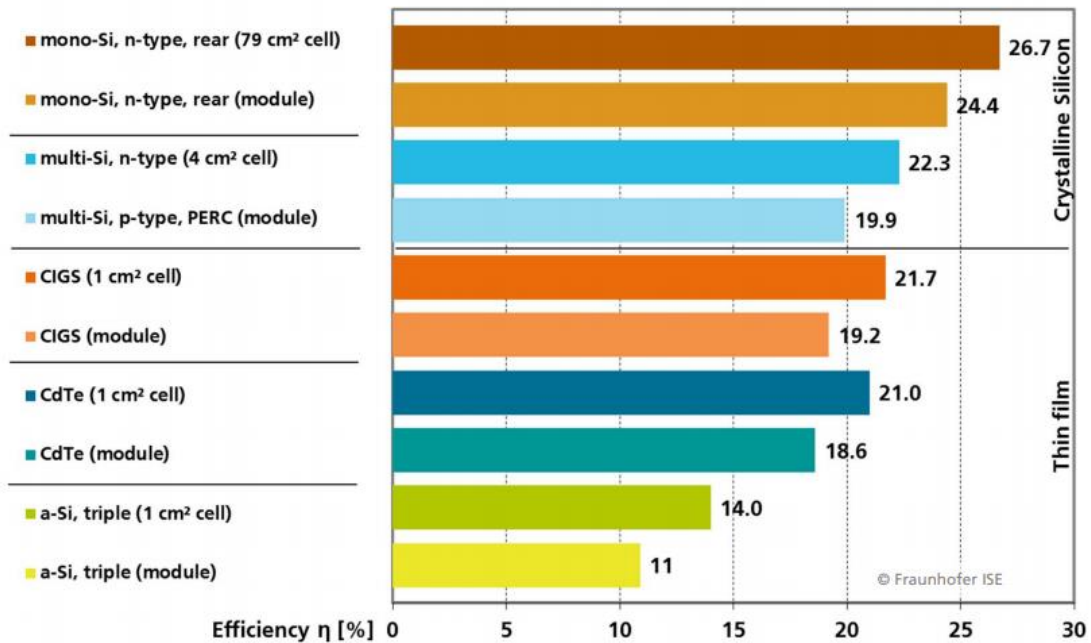


Figure 1.2. Comparison of the efficiencies of (a) the performance and cost leaders at the cell and module levels, and (b) of the current contenders to mono-Si in chronological order. [5]

1.2.1 Absorber Layers

The absorber layer is a p-type semiconductor material with excellent photogeneration capabilities and superior charge collection efficiencies. The absorber material is required to possess a suitable optical band gap to maximize absorption of the incident radiation spectrum in addition to exhibiting excellent optical absorption coefficient to minimize the amount of material necessary for absorbing most of the incident photons. To facilitate charge collection of the photogenerated carriers, the absorber layer must demonstrate long carrier diffusion lengths at least comparable to the layer thickness in addition to having low parasitic resistances such as series resistance (R_s) and shunt resistance (R_{sh}).

The materials used in the absorber layers of state-of-the-art thin film solar cells contains toxic and/or rare elements that are typically costly as well, such as indium and gallium in Cu(In,Ga)(S,Se)_2 and cadmium in CdTe. This makes it crucial to investigate earth-abundant, non-toxic, low cost absorber materials with SnS and Cu_2O being prime candidates for incorporation in next-generation solar cells.

1.2.2 Buffer Layers

The buffer layer is typically a n-type semiconductor material that forms the p-n junction with the p-type absorber layer. Interfacial recombination at this junction is a major loss mechanism that the buffer layer aims to minimize by matching the conduction band alignments between the absorber and the window layer. This is achieved through the manipulation of the conduction band offset at the absorber-buffer interface and by improving band bending across the p-n junction, usually effectively serving as both a hole blocking layer (HBL) and an electron transport layer (ETL).

When considering photovoltaic devices in the substrate configuration, the buffer layer must have an optical band gap larger than that of the absorber layer such that incident radiation does not get absorbed by the buffer layer before being absorbed by the absorber material. The buffer layer must also be thin enough to avoid contributing to resistive losses and optical losses. If the conduction band offset at the absorber-buffer interface is too high, a type-I spike structure is formed and photocurrent collection will be inhibited. On the other hand, if the conduction band offset is negative, a type-II cliff structure is created where the recombination current at the interface will be amplified and voltage losses will occur from the reduction in the built-in voltage. Simulation studies on thin film solar cells have found that a type-I spike structure with a positive conduction band offset of +0.4 eV to be optimal [6].

Our strategy in engineering the band offsets comes from the ability to tune the band levels of the conduction and valance bands of non-binary materials by varying the ratio of the cations or anions. Depletion region widths and the degree of band banding can be controlled by careful control of the carrier density of the buffer material via an extrinsic dopant. This work discusses on the use of compounds $\text{Ga}_2\text{O}_3:\text{Al}$, $(\text{Sn,Ge})\text{O}_2$ and $\text{Zn}(\text{O,S}):\text{N}$ with tunable electrical, electronic and optical attributes for the creation of the optimal n-type partner material to the p-type absorber.

1.2.3 Principles of Solar Cells

1.2.3.1 Generation and Charge Transport

The generation mechanism in photovoltaic devices is dominated by photo-generation, the production of light-generated electron-hole pairs through the absorption of incident photons with photon energies greater than the optical bandgap of the semiconductor absorber material. The absorption coefficient α determines how the penetration depth before photons of a particular wavelength is absorbed, where the intensity below the surface is described by the Beer-Lambert law

$$I(x) = I(0)e^{-\alpha x}$$

where x is the depth below the surface.

If an incident photon has an energy larger than the material band gap, the photogenerated carriers will eventually lose the excess energy through thermalization. If an incident photon has energy lower than the band gap, it interacts weakly with the photovoltaic material without being absorbed.

The rate of photogeneration below the surface is given by

$$g(E, x) = b(E, x)\alpha(E, x)$$

where $b(E, x)$ is the photon flux at depth x . Therefore, the total photogeneration rate is the integral over all photon energies larger than the optical band gap of the photovoltaic material

$$G(x) = \int g(E, x)dE$$

Photogenerated carriers are separated by two fundamental processes known as diffusion and drift. Diffusion arises from a gradient in carrier concentration which causes a uniform

distribution of electrons and holes throughout the material over time without application of an external force on the system. This process results in a diffusion current given by the following equation for 1D flow

$$J_{diff,n} = qD_n \frac{dn(x)}{dx}$$

$$J_{diff,p} = -qD_p \frac{dp(x)}{dx}$$

for electrons and holes, respectively, where q is the elementary charge, D_n and D_p are the diffusion coefficients for electrons and holes, n and p are the carrier concentrations for electrons and holes. The total diffusion current density J_{diff} is subsequently given by

$$J_{diff} = J_{diff,n}(x) + J_{diff,p}(x)$$

On the other hand, drift results due to the presence of an electric field created in the depletion region, resulting in a drift current density $J_{drift,x}$ given by the 1D equation

$$J_{drift,x} = q(n\mu_n + p\mu_p)E_x$$

where q is the elementary charge, n and p are the carrier concentrations for electrons and holes, J_x is the drift current density in the x-direction, E_x is the electric field applied in the x-direction.

The total current density passing through a junction is the sum of the diffusion current density and the drift current density given by

$$J_n = q\mu_n nE + qD_n \frac{dn(x)}{dx}$$

$$J_p = q\mu_p pE + qD_p \frac{dp(x)}{dx}$$

which can generally be represented by the diode equation

$$J = J_0(e^{\frac{qV}{k_B T}} - 1)$$

where J_0 is the dark saturation current density or the reverse saturation current density. J_0 depends on the recombination in the solar cell, where large J_0 values correlate with larger recombination currents. At equilibrium, the diffusion current equals to the drift current, so the net current density is zero.

1.2.3.2 Recombination

The three fundamental forms of recombination in a semiconductor are radiative recombination, Auger recombination and Shockley-Reed-Hall recombination.

Radiative (band-to-band) recombination is the dominant recombination mechanism in direct bandgap materials where a photon is released due to an electron in the conduction band recombining with a hole in the valence band. Since this interband transition has an energy similar to the bandgap of the semiconductor it occurs in, it is poorly absorbed and is able to escape re-absorption by the emitting semiconductor. Radiative recombination is the dominant recombination pathway that limits the carrier lifetimes in thin film solar cells, including GaAs and SnS. The recombination rate for radiative recombination U_{rad} is given by

$$U_{rad} = B_{rad}(np - n_i^2)$$

which can be simplified to

$$U_{rad} = \frac{n - n_0}{\tau_{n,rad}}$$

$$U_{rad} = \frac{p - p_0}{\tau_{p,rad}}$$

where the minority carrier lifetimes for radiative recombination are given for electrons and holes, respectively, by

$$\tau_{n,rad} = \frac{1}{B_{rad}N_a}$$

$$\tau_{p,rad} = \frac{1}{B_{rad}N_d}$$

Auger recombination involves three carriers. When an electron recombines with a hole to emit energy equal to the band gap, instead of emitting it as heat or photons, this energy is transferred to the third carrier which is an electron in the conduction band. The excited carrier eventually thermalizes back down to the conduction band edge, releasing energy as heat. Auger recombination is more dominant in high carrier concentrations due to heavy doping or high level injection under concentration radiation. Under these conditions, auger recombination becomes the limiting factor for the carrier lifetimes. The recombination rate for Auger recombination for hole-hole collisions in a p-type material and electron-electron collisions in a n-type material are given by

$$U_{auger} = \frac{np^2 - n_0p_0^2}{\tau_{auger,n}N_a^2}$$

$$U_{auger} = \frac{np^2 - n_0p_0^2}{\tau_{auger,n}N_d^2}$$

where the minority carrier lifetime for Auger recombination for electrons and holes are given by

$$\tau_{auger,n} = \frac{1}{A_n N_a^2}$$

$$\tau_{auger,n} = \frac{1}{A_p N_d^2}$$

Shockley-Reed-Hall (SRH) recombination is a two-step recombination process that is assisted by defect trap states in the band gap. A free carrier is first trapped by an energy state introduced by defects or impurities that are unintentionally introduced or intentionally doped into the material. Recombination occurs if this trapped carrier meets another carrier of the opposite charge that is excited into the same energy state before the trapped carrier is able to escape via thermal emission. Energy levels near the middle of the band gap act as effective recombination centers due to the increased difficulty of escaping the energy level after a carrier is trapped by the mid-gap defect state. Consequently, recombination is less likely when the defect level is near either of the band edges where the trapped carriers have much higher probabilities of being re-emitted back to the band edges. The recombination rate for SRH recombination is given by

$$U_{SRH} = \frac{np - n_i^2}{\tau_{SRH,n}(p + p_t) + \tau_{SRH,p}(n + n_t)}$$

where n_p (p_t) is the electron (hole) carrier concentration when its Fermi level is equal to the trap level, and the minority carrier lifetime for SRH recombination for electrons and holes are given by

$$\tau_{SRH,n} = \frac{1}{v_n \sigma_n N_t}$$

$$\tau_{SRH,p} = \frac{1}{v_p \sigma_p N_t}$$

where v_n (v_p) is the mean thermal velocity of the electron (hole), σ_n (σ_p) is the capture cross-section of the trap for electrons (holes), N_t is the density of trap states.

The bulk minority carrier lifetime τ_{eff} is affected by all three fundamental forms of recombination, given by

$$\frac{1}{\tau_{bulk}} = \frac{1}{\tau_{rad}} + \frac{1}{\tau_{SRH}} + \frac{1}{\tau_{auger}}$$

Surface recombination is promoted by defects and impurities at the semiconductor surfaces and at the interfaces between two semiconductor materials. Surface recombination velocity S_{eff} (also commonly abbreviated as SRV) is a parameter commonly used to describe the degree of recombination at a surface, with the surface lifetime given by the approximation

$$\tau_{surf} = \frac{W}{2S} + \frac{1}{D} \left(\frac{W}{\pi} \right)^2$$

where W is the sample thickness, S is the surface recombination velocity, and D is the carrier diffusivity.

The effective carrier lifetime is influenced by recombination both in the bulk and at the surface, given by

$$\frac{1}{\tau_{eff}} = \frac{1}{\tau_{bulk}} + \frac{1}{\tau_{surf}}$$

A long effective minority carrier lifetime τ_{eff} means that these photogenerated carriers can persist in the material for an extended amount of time before experiencing recombination, and is indicative of high performance in solar cells.

1.2.3.3 Short-Circuit Current and Open-Circuit Voltage

The short-circuit current density J_{SC} is defined as the photocurrent density under a short-circuit condition at zero bias. The short-circuit current is the largest current that can be collected from the solar cell. Under ideal conditions with no resistive losses in the device, the short-circuit current is equal to the photo-generated current. An approximation of the short-circuit current density, assuming uniform generation and perfect surface passivation, is given by

$$J_{SC} = qG(L_n + L_p)$$

where q is the elementary charge, G is the generation rate, and L_n and L_p are the diffusion lengths for electrons and holes, respectively. The above equation suggests the significant dependences of the short-circuit current density on the photogeneration properties of the photovoltaic material and on its bulk defect densities.

The open-circuit voltage V_{OC} is defined as the maximum voltage attainable by the solar cell under an open-circuit condition at zero current density. From the non-diode equation, we can derive the expression for the open-circuit voltage as

$$V_{OC} = \frac{nk_B T}{q} \ln \left(\frac{J_{SC}}{J_0} + 1 \right)$$

where n is the diode ideality factor, k_B is the Boltzmann's constant, T is the absolute temperature, q is the elementary charge, J_0 is the saturation current density. Note that increasing the quality of

the diode will not only increase the ideality factor n , but also improve the dark saturation current density J_0 , typically resulting in a lower V_{OC} .

1.2.3.4 Fill Factor and Photo Conversion Efficiency

The power density of a solar cell P is given by

$$P = JV$$

The maximum power point P_{max} is the desired operating point in the J-V curve where the power density reaches a maximum at a voltage V_{max} with a corresponding current density J_{max} .

The fill factor, also frequently known in the abbreviated form FF , is defined as the ratio of the maximum power density to the product of J_{SC} and V_{OC}

$$FF = \frac{J_{max}V_{max}}{J_{sc}V_{oc}}$$

The fill factor is a parameter that visually describes the “squareness” of the J-V curve, is a value ranging from 0 to 1, with a FF of 1 representing a perfect square-shaped J-V curve and higher fill factor values representative of higher performing devices.

The power conversion efficiency η of a solar cell, also commonly referred to as PCE , is the universally accepted parameter used in the evaluation of solar cell performances, defined by the ratio of the maximum power density P_{max} to the incident light power density P_{in}

$$\eta = \frac{P_{max}}{P_{in}} = \frac{J_{max}V_{max}}{P_{in}} = \frac{V_{oc}J_{sc}FF}{P_{in}}$$

1.3 Deposition Techniques

1.3.1 Chemical Vapor Deposition

Chemical vapor deposition (CVD) is a widely used thin film deposition technique where a non-volatile solid is deposited on the surface of a substrate from the gas phase reactions of volatile chemical vapors on or near the heated substrate, typically in a vacuum environment. The reaction by-products and unreacted precursor vapors are continuously being removed from the reaction zone. This manufacturing process can fabricate thin films with excellent control over the thickness of the coating by controlling the process duration. CVD precursors are easily purified through distillation, allowing for the production of high purity materials without the need for higher vacuum levels as compared to physical vapor deposition (PVD). CVD also produces highly conformal films over challenging structures with high aspect ratios without direct line of sight, which is a huge benefit of choosing CVD over PVD methods when coating such challenging surfaces.

1.3.2 Atomic Layer Deposition and Pulsed Vapor Deposition

Atomic layer deposition (ALD) divides the continuous CVD process into an iterative sequence of discrete self-limiting cycles where the injected chemical vapors react with the surface instead of with each other in the vapor phase. Since each ALD cycle involves self-terminating reactions, the resulting independence from gas transport makes it capable of producing highly uniform, perfectly conformal, pinhole-free films of controllable thickness down to the sub-monolayer level with remarkable accuracy by varying the number of deposition cycles. ALD films are fabricated stepwise layer-by-layer where each precursor vapor is exposed sequentially to the substrate at an elevated temperature and every precursor step is separated by

purge steps using nitrogen gas to remove the excess reactants and the byproducts of the reaction. The reaction zone is also purged and evacuated at the end of an ALD cycle.

Pulsed chemical vapor deposition (pulsed-CVD) is a slightly modified variant of ALD that increases the rate of film deposition of an ALD process. By eliminating the nitrogen purge step between precursor doses while still preserving the nitrogen purge step between ALD cycles, significant reduction in cycle time can be achieved. Consequently, without proper gas flow control, film uniformity may be degraded when gas phase reactions occur. The pulsed-CVD technique is highly applicable in situations where the deposition of thick layers of material demand preparation methods that leverages the advantages of ALD without compromising deposition throughput and perfect film uniformity is not critical, such as for the fabrication of the SnS absorber layer that is in the order of micrometers in thickness.

1.4 Dissertation Overview

This dissertation presents the development of high-performance solar cells using non-toxic, earth-abundant materials, with the central theme of controlling both bulk and interfacial defects that are limiting performances in thin film photovoltaics systems based on the SnS and Cu₂O absorber layers.

Accelerating the photovoltaic performances of Cu₂O-based thin film solar cells is the focus of Chapters 2-5. Chapter 2 presents on the CVD process for preparing high quality Cu₂O thin films at low temperatures and a detailed investigation on the CVD process and material characteristics of CVD-Cu₂O. Chapter 3 focuses on the impact of the oxidation state of Cu at the heterojunction interface of Cu₂O-based solar cells. Chapter 4 investigates the use of ALD Ga₂O₃

as a novel n-type buffer material for Cu_2O solar cells to achieve a record performance with a high open-circuit voltage of 1.2 V. Chapter 5 leverages all the insights gained in the past chapters to further mitigate interfacial recombination at the heterojunction by taking advantages of compatible CVD and ALD processes we have developed, paving the path towards the 10% efficiency target by surpassing the previous open-circuit voltage record with a new and astounding 1.7 V.

Improving SnS-based solar cells is the focus of Chapters 6-8. Chapter 6 discusses the route to improving the film quality of SnS through thermal annealing and presents the improvements in device efficiencies. Chapter 7 introduces $(\text{Sn,Ge})\text{O}_2$ as a novel n-type buffer layer capable of achieving a record high open-circuit voltage of 0.4V and studies the material properties of this novel material. Chapter 8 features Sn(O,S) as an alternative n-type partner layer to SnS and highlights the desirable properties of this semiconductor.

1.5 References

1. Administration, U.S.E.I. *What is U.S. electricity generation by energy source?* 2018; Available from: <https://www.eia.gov/tools/faqs/faq.php?id=427&t=3>.
2. Poortmans, J., Arkhipov, V., *Thin Film Solar Cells: Fabrication, Characterization and Applications*. 2006: Wiley.
3. Scheer, R., Schock, H.-W., *Chalcogenide Photovoltaics: Physics, Technologies, and Thin Film Devices*. 2011: Wiley-VCH.
4. NREL, *Best Research-Cell Efficiencies*. 2018.
5. Green, M.A., et al., *Solar cell efficiency tables (version 52)*. Progress in Photovoltaics: Research and Applications, 2018. **26**(7): p. 427-436.
6. Niemegeers, A., M. Burgelman, and A. De Vos, *On the CdS/CuInSe₂ conduction band discontinuity*. Applied Physics Letters, 1995. **67**(6): p. 843-845.

2 Chemical Vapor Deposition of Cuprous Oxide Thin Films

2.1 Chapter Abstract

Cuprous oxide (Cu_2O) thin films were deposited by chemical vapor deposition (CVD) using precursors (N,N-di-sec-butylacetamidinato)copper(I) and water at low substrate temperatures of 125 to 225°C. The deposited films were single phase oxides that exhibited high hole mobilities, wide band gaps and are free from nitrogen, carbon and cupric oxide contaminations. With good control of growth parameters, the film morphologies can be tuned to achieve both smooth, pinhole-free coatings as well as highly crystalline thin films with rough surfaces that are highly advantageous for energy applications.

2.2 Introduction

Cuprous oxide (Cu_2O) is an exceptional p-type semiconductor oxide that demonstrates many highly desirable characteristics while being non-toxic and cost-effective due to copper being widely abundant in nature. Cu_2O exhibits excellent electrical properties, including high hole mobilities of up to $90 \text{ cm}^2 \text{ V}^{-1} \text{ s}^{-1}$ [1] and long minority carrier diffusion lengths. Cu_2O has a direct energy gap range from 2.1 to 2.6 eV [1-3] and demonstrates high absorption coefficient in the visible range. In addition, Cu_2O crystallizes in a cubic structure with lattice parameter $a = 4.27 \text{ \AA}$.

Cu_2O has been prepared using a wide variety of techniques such as electrochemical deposition (ECD) [4], sol-gel process [5], RF magnetron sputtering [6], molecular beam epitaxy (MBE) [7], thermal oxidation [8] and chemical oxidation [9], consequently demonstrating a variety of different properties dependent on the preparation method. Due to its electronic and optical properties, this material has been demonstrated to have widespread technological applications encompassing solar cells [4], gas sensors [10] and photodiodes [11]. Among the various fabrication techniques, CVD is a highly attractive method due to its scalability, high conformality and excellent control over growth parameters capable of depositing high purity materials over a wide variety of substrates. The CVD of Cu_2O film is typically carried out using copper precursors such as copper iodide CuI [12], copper hexafluoroacetylacetonate $\text{Cu}(\text{hfac})_2$ [13] and copper acetylacetonate $\text{Cu}(\text{acac})_2$ [14] where the high temperatures required has been reported to pose challenges in avoiding agglomeration due the high mobility of copper [13, 15-17] and in obtaining carbon-free single phase Cu_2O [18].

In this work, we report on the thermal CVD of high purity Cu_2O thin films at low process temperatures of 125°C to 225°C using *(N,N-di-sec-butylacetamidinato)copper(I)* ($[\text{Cu}(\text{sBu-Me-$

and)]₂ as the metal precursor and discuss its growth characteristics, chemical, structural and opto-electronic properties.

2.3 Experiments

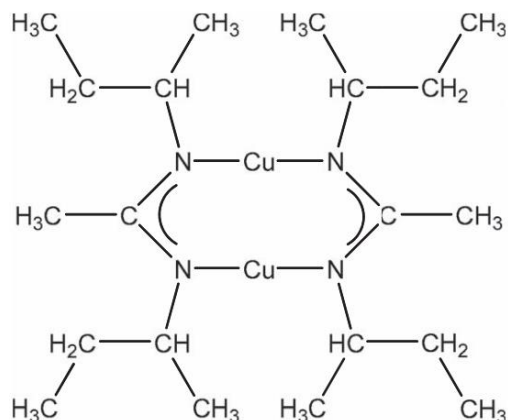


Figure 2.1. Formula for the copper (I) precursor (*N,N*-di-sec-butylacetamidinato)copper(I) used in the CVD of Cu₂O thin films.

(*N,N*-di-sec-butylacetamidinato)copper(I) dimer (Dow Chemical Company) is an amidinate precursor used in this work for depositing copper(I) oxide, with the chemical formula as shown in **Figure 2.1** whose preparation has been previously reported [19]. Deionized water is used as the oxygen source for the vapor deposition. To prepare cuprous oxide by using CVD, the copper(I) precursor was sublimed from a bubbler maintained at a temperature of 98°C into a 100 sccm flow of purified nitrogen gas. Water is evaporated from a bubbler maintained at a temperature of 25°C into a 5 sccm flow of purified nitrogen gas. Both reactants are mixed together with a 40 sccm flow of purified nitrogen before injection into the process chamber of a custom built hot-walled tubular reactor. The process chamber is maintained at temperatures varying from 125°C to 250°C using a Linberg Blue Minimite furnace and the process pressure is held at 1 Torr to 10 Torr using an MKS exhaust throttle valve (253B) coupled to the MKS

Baratron absolute capacitance manometer (626C12TBE) and regulated using an MKS 600 series pressure controller. Thermally oxidized silicon wafers, glassy carbon planchets, and quartz were utilized as substrates for the deposition of Cu_2O . The substrates were treated by UV/ozone cleaner (Samco model UV-1, wavelengths = 185 nm and 254 nm) for 5 minutes at room temperature before being introduced into the process chamber. These substrates are supported by a 316L stainless steel substrate holder with an embedded K-type thermocouple probe for temperature monitoring. **Table 1** summarizes the fabrication conditions of the CVD Cu_2O films.

The elemental composition of the Cu_2O thin films are quantified using X-ray Photoelectron Spectroscopy (XPS, K-alpha XPS, Thermo Scientific) to determine the ratios of Cu to O, as well as to measure the amount of copper in the various oxidation states (0, +1, +2) and the amount of carbon and nitrogen contamination underneath the film's surface. The film thickness is measured using X-ray Reflectivity (XRR, Bruker D8 Discover), spectroscopic ellipsometry (SE, J.A. Woollam) and scanning electron microscopy (SEM, Ultra 55 FESEM, Zeiss). The film morphology and the surface morphology are evaluated by SEM. Steady-state spectral photoluminescence (PL) and Raman spectroscopy measurements were performed using a 532 nm laser operating at 2 mW through a 50X confocal microscope objective with an 1800 blaze grating and a Synapse CCD detector (LabRam Evolution Multiline Raman/PL spectrophotometer, Horiba). Hall mobilities, carrier concentrations and resistivities are measured using a hall effect measurement system. Four 100 nm-thick Au electrodes (1 mm in diameter, with a 5 nm-thick Ti adhesion layer) were deposited at each corner of a 1 cm \times 1 cm sample using e-beam evaporation (Denton).

Table 1. Experimental conditions of CVD of Cu₂O

CVD Parameters		Cuprous Oxide
Cu	Precursor	(N,N-di-sec-butylacetamidinato)copper(I)
	Temperature of Precursor Bubbler	98 °C
	Flow Rate of N ₂ Carrier Gas	100 sccm
O	Source	Deionized Water
	Temperature of Precursor Bubbler	25 °C
	Flow Rate of N ₂ Carrier Gas	5 sccm
	Flow Rate of N₂ Carrier Gas	40 sccm
	Process Pressure	1 – 10 Torr
	Substrate Temperature	125 – 250 °C

2.4 Results and Discussion

2.4.1 Growth Rates

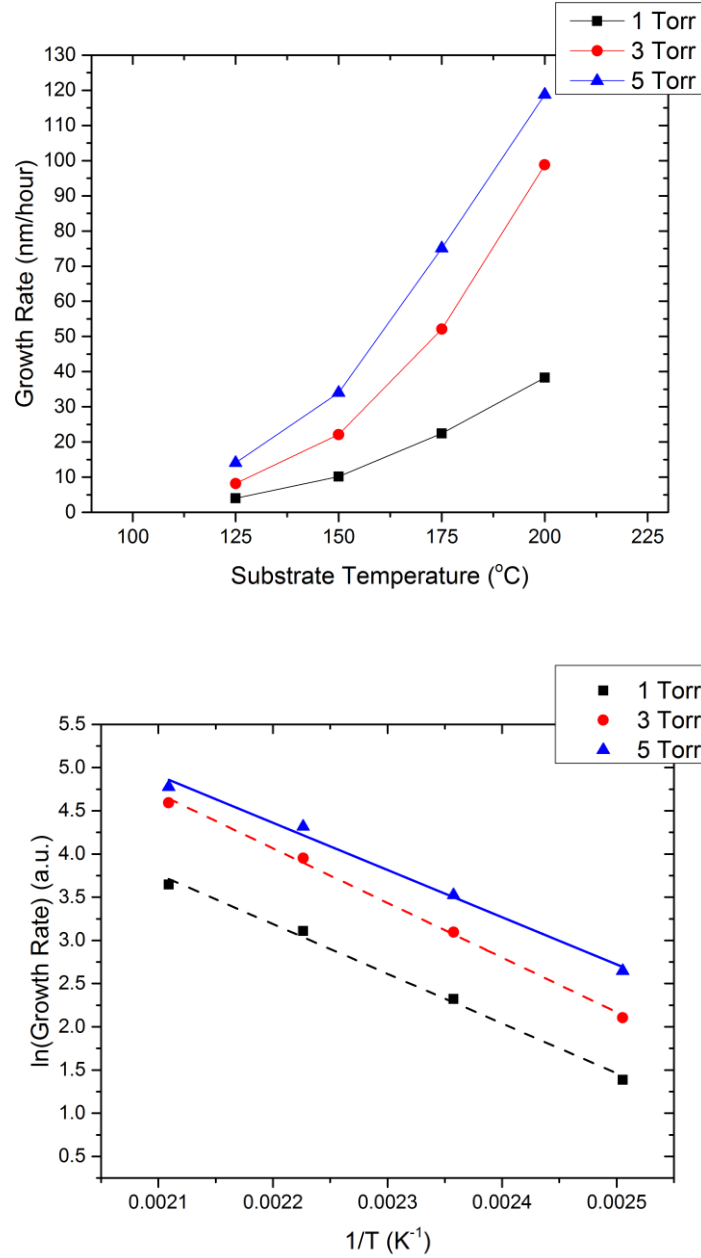


Figure 2.2. (a) Temperature dependent growth rate plot at different process pressures. (b) Arrhenius plots and linear fits at different process pressure and at a constant substrate temperature of 200°C.

Cu₂O thin film was deposited at various temperatures of 100 °C, 125 °C, 150 °C, 175 °C, 200 °C and 225 °C. The growth rate is observed to increase with increasing temperature. Cu₂O was also deposited at various pressures of 1 Torr, 3 Torr and 5 Torr at a constant substrate temperature of 200 °C. The growth rate was found to be pressure dependent as well, and rises as the chamber pressure increases. The amount of Cu₂O deposited was determined by XRR and visualized in **Figure 2.2a**. These results show that the CVD process for fabricating Cu₂O is highly controllable by setting the appropriate substrate temperature and process pressure.

By plotting the natural logarithm of growth rate versus the reciprocal of substrate temperature (from 125 °C to 200 °C), the resulting traces follow a straight line and the activation energies of the Cu₂O deposition process with different process pressures can be calculated based on the Arrhenius' equation. The Cu₂O activation energy is estimated to be 48.6 ± 3.5 kJ/mol on substrates of thermally oxidized silicon.

2.4.2 Elemental Composition

Our CVD processes are able to achieve high purity Cu₂O that is free of CuO, metallic Cu, nitrogen and carbon. XPS spectrums were collected from the bulk of the film after exposing the Cu₂O thin films to 120 seconds of 1000 eV Ar⁺ in-situ sputtering to remove surface contamination immediately before the measurements were made.

Cuprous oxide can be identified in the Cu2p scan as a higher energy shoulder at 934.4 eV and 954.2 eV. CuO contamination also shows up in the O1s scan as a higher energy shoulder at 530.7 eV. Due to oxidation in the oxygen-rich ambient atmosphere, a layer of CuO is always formed on the surface of the Cu₂O CVD films, which is detectable by XPS measurements when left in

the air for a sufficiently long duration. This CuO layer on the surface is easily removed via Ar⁺ sputtering in the XPS analysis chamber. In the Cu2p scan in **Figure 2.3**, the higher energy shoulder peaks of the two main peaks and the satellite peaks in the 940-945 eV region are no longer detectable after 60 seconds of Ar⁺ sputtering. As a result, all XPS spectrums gathered in this study are measured only after 120 seconds of Ar⁺ sputtering.

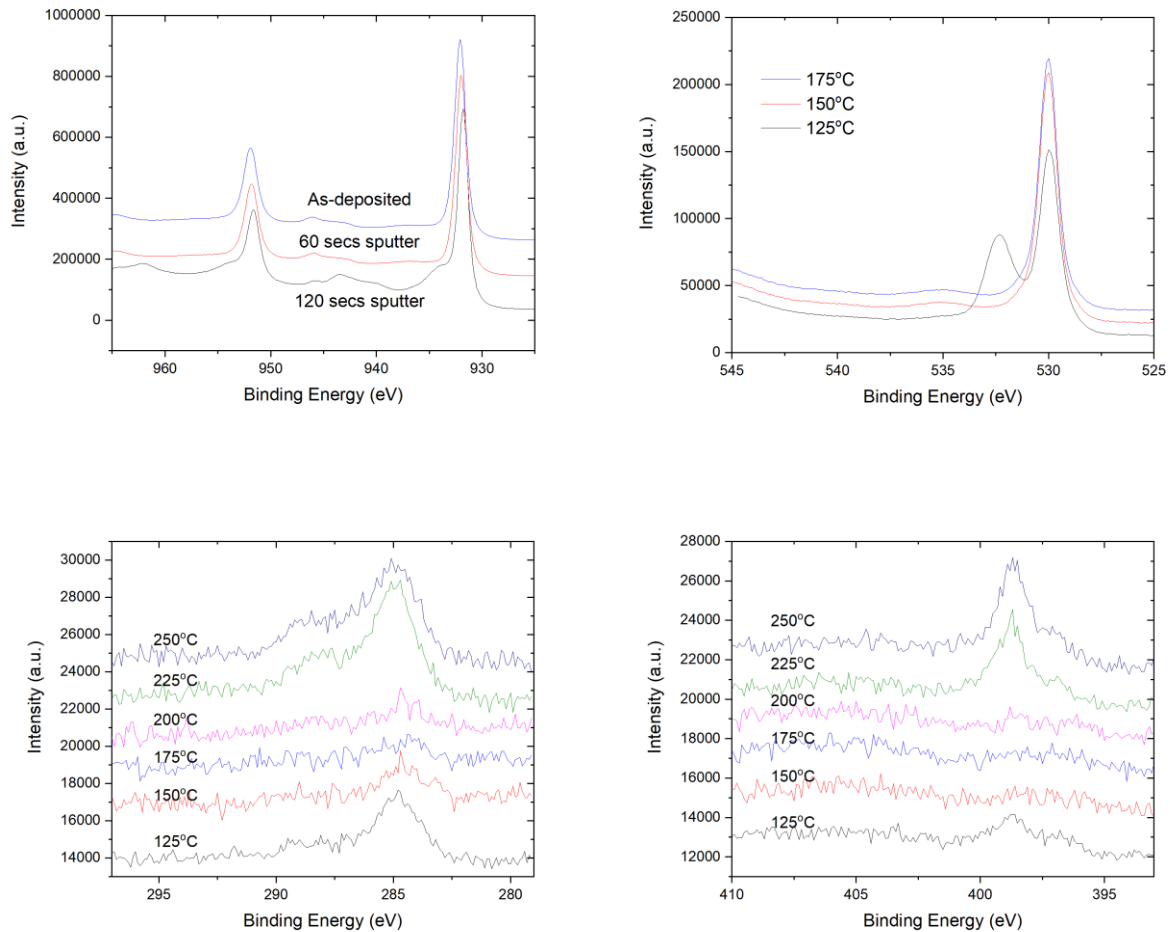


Figure 2.3. XPS spectrums of (a) the Cu-2p depth profiling scan indicating the presence of CuO (Cu²⁺) on the surface of Cu₂O which is removed by sputtering for 120 seconds, (b) the O-1s depth profiling scan showing presence of copper hydroxides in the film deposited at the lowest temperature of 125 °C, (c) the amount of C contamination in the film with various substrate temperatures, and (d) the amount of N incorporated into the film at various substrate temperatures.

Samples grown at temperatures up to 230 °C show less than 1 at. % of C content in the bulk of the film. Significant amounts of carbon (> 10 at. %) and nitrogen (>2 at.%) are only observed at substrate temperatures of at least 225 °C. Carbon is also present at process temperature of 125 °C and lower, indicating incomplete ligand exchange which results in the incorporation of these ligands in the film. XPS analysis also shows the presence of Cu(OH) at substrate temperatures of 125 °C and lower due to incomplete dehydration reactions of Cu(OH) at lower temperatures. Discussions from here on will be using substrates maintained within the CVD temperature window from 125°C and 200°C.

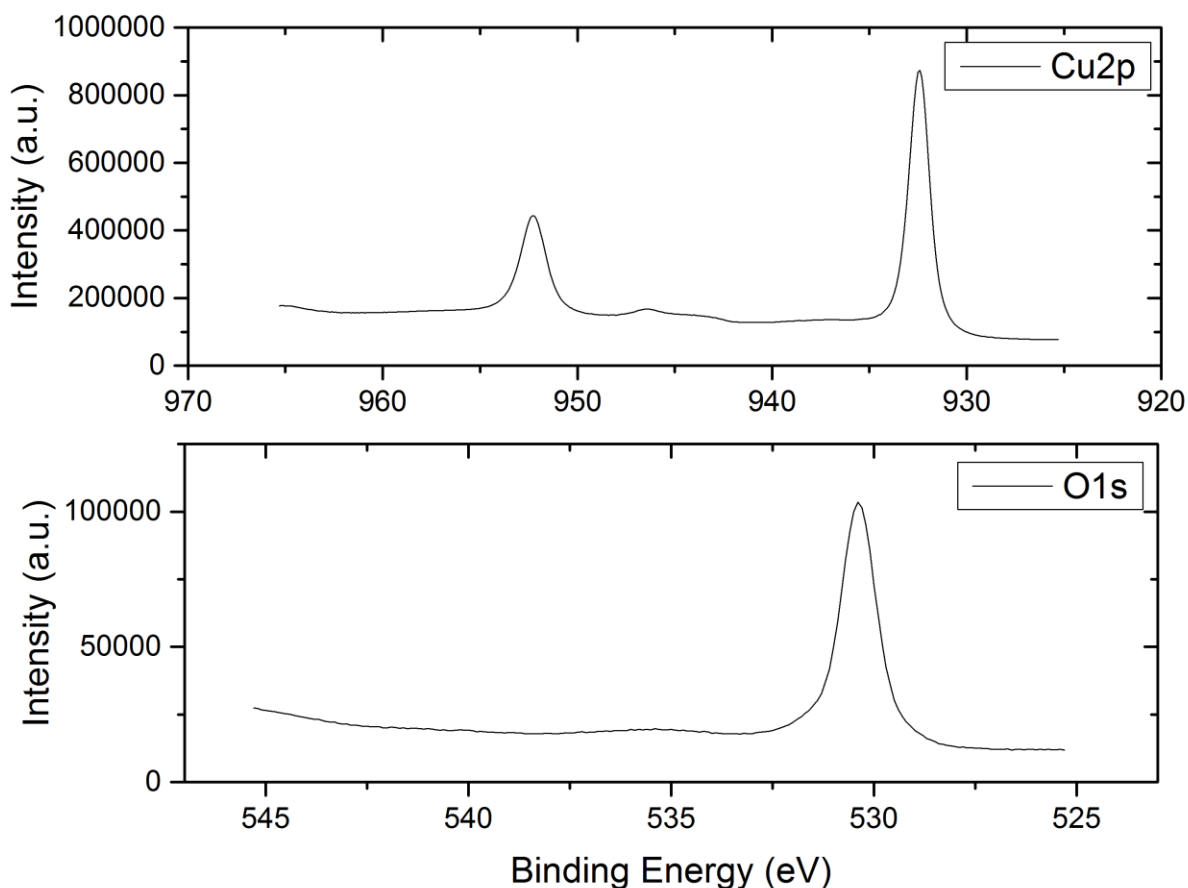


Figure 2.4. XPS spectrum of CVD Cu₂O films deposited at 200°C after 120 seconds of Ar⁺ sputtering, showing (a) Cu2p scan. (b) O1s scan.

Table 2. Summary of the values of binding energies for Cu₂O CVD films.

Binding Energy (eV)			
	Cu2p 3/2	Cu2p 5/2	O1s
Cu ₂ O	932.0	951.9	27.8
CuO	933.8	954.2	27.8

2.4.3 Phase Purity

In an effort to confirm the high phase purity of the Cu₂O, Raman spectrums were taken of the CVD grown Cu₂O films deposited between 150 and 200 °C. **Figure 2.7a** presents the characteristic Raman shift peak of CVD Cu₂O at 217 cm⁻¹ which is a strong narrow peak due to the second order scattering from the 110 cm⁻¹ Γ_{12}^- phonon (not observable in the figure) [20]. Bands corresponding to minor Cu₂O phases were also detected at 519 and 630 cm⁻¹ assigned to the Γ_{25}^+ and Γ_{15}^- modes, respectively [20-23]. No known peaks corresponding to the CuO phase at 298, 347, 591 cm⁻¹ are observed [23]. This confirms that the CVD grown Cu₂O films are of extremely high phase purity and free of deleterious CuO contaminations. **Figure 2.8** shows that when the growth temperature is increased from 125 to 200 °C, the Raman bands at 217 and 630 cm⁻¹ are observed to become more intense.

2.4.4 CVD Growth Regimes

2.4.4.1 High Growth Rate Regime.

At growth temperatures of 200 °C and higher, the CVD process undergoes a high growth rate regime that progresses through multiple phases. This evolution is shown in the series of SEM micrographs found in **Figure 2.5**. Cu₂O deposition starts off with the nucleation of small clusters

of Cu₂O on top of a compact fully formed layer. It is suggested that an ultra-thin continuous layer of film is first established, followed by the agglomeration of the Cu₂O material [17]. As the growth proceeds, more islands are formed and the sizes of these islands grow larger. Eventually the islands coalesce together to form a continuous layer of Cu₂O film. The suppression of agglomeration at film thicknesses larger than a critical thickness also contributes to promoting preferential growth of films with continuous surface morphologies [16]. The post-coalescence grain sizes are now much larger as a result of the merging of islands into larger grains. These grains are an order of magnitude larger compared to the smaller grains observed in the initial compact layer at the start of the CVD process. Bigger grain sizes are typically desirable in semiconductor applications such as in photovoltaics as larger grains usually translate to better electrical properties.

In order to monitor the two growth regimes, Raman spectrums were taken for Cu₂O films of four different thicknesses with deposition durations of 2, 4, 6 and 12 hours grown at a process temperature of 200°C, corresponding to film thicknesses of 60 nm, 120 nm, 180 nm and 360 nm, respectively. The thinnest film grown for only 2 hours shows a prominent Raman peak at 217 cm⁻¹. The films corresponding to 4, 6 and 12 hours deposition durations shows a shift of the same peak to 217.4 cm⁻¹. This increase in Raman frequency of this peak indicates a change from tensile stress to compressive stress in the CVD Cu₂O film. The shift in frequency corresponds to the two different growth regimes, starting with discrete island growth observed after 2 hours of CVD process exhibiting compressive stress. As the course of CVD process continues, the coalescence of these islands occurs and are being subjected to compressive stress.

2.4.4.2 High Smoothness Regime.

Adjusting the growth temperature to between 125°C and 200°C enables the Cu₂O thin films to be deposited as a continuous and pinhole-free coating with relatively low surface roughness as shown in **Figure 2.5**. The Cu₂O thin films maintain a smooth, uniform morphology independent of the film thickness in contrast to the films deposited in the high growth rate regime at higher temperatures which promotes the agglomeration of copper especially in thinner coatings [16]. As a tradeoff for achieving the deposition of uniform continuous films, growth rates under these conditions are much slower.

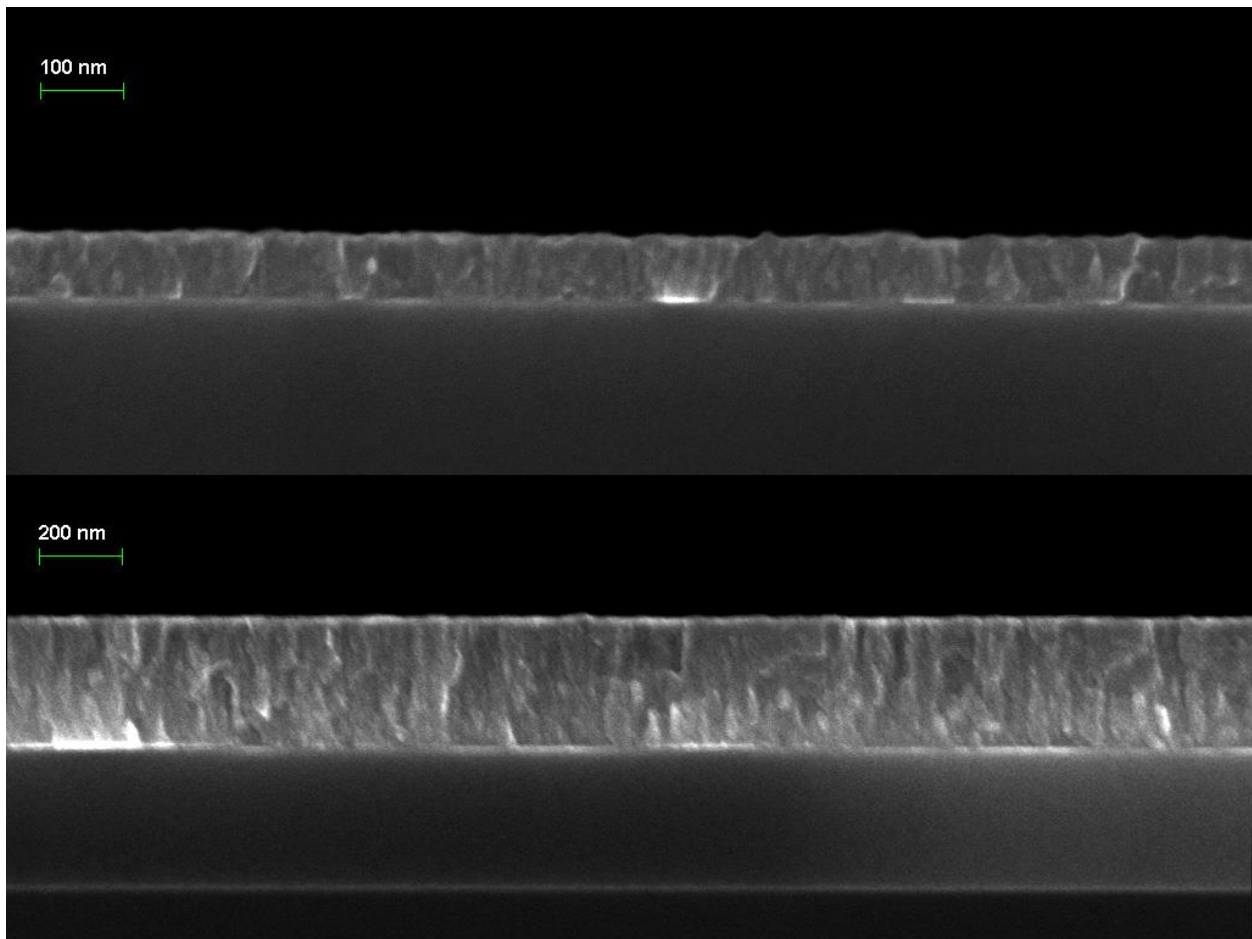


Figure 2.5. Cross-sectional SEM images showing Cu₂O thin films grown under CVD conditions that preserve a continuous film at various film thickness of (a) 80 nm, and (b) 320 nm.

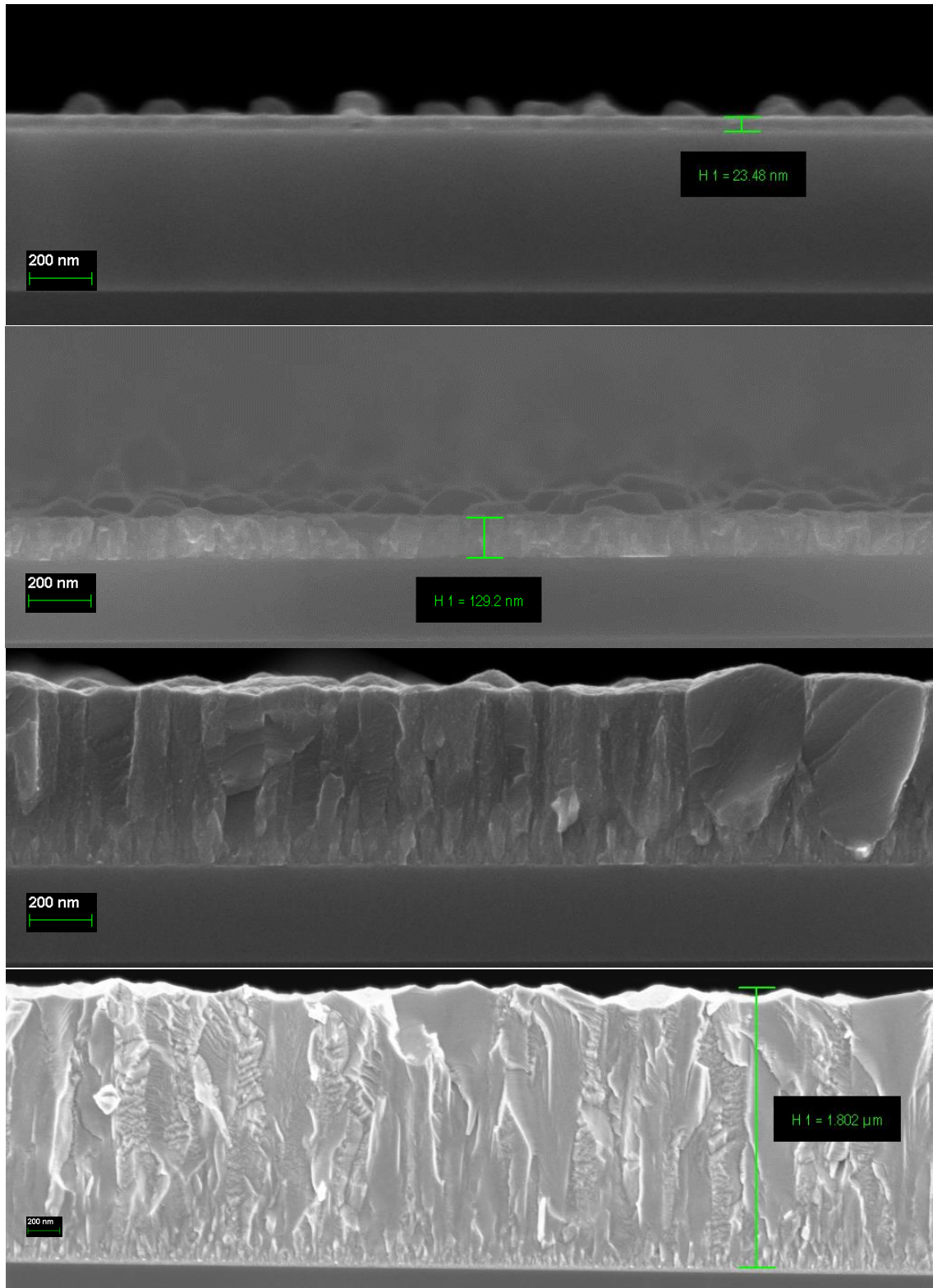


Figure 2.6. Evolution of CVD Cu₂O film shown in a series of SEM micrographs. At low film thickness, islands nucleate and grow on top of a continuous compact film. As the film thickens, the clusters coalesce to form a continuous firm with larger grain sizes.

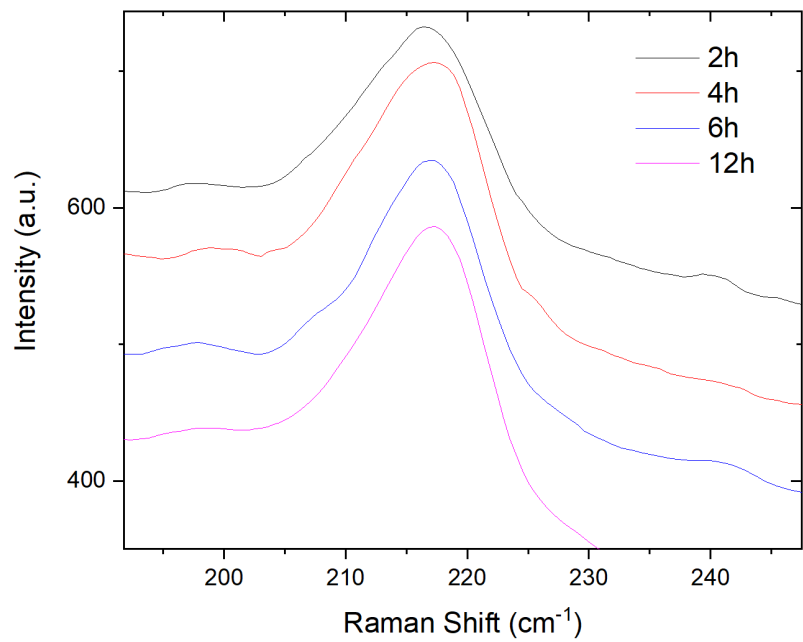
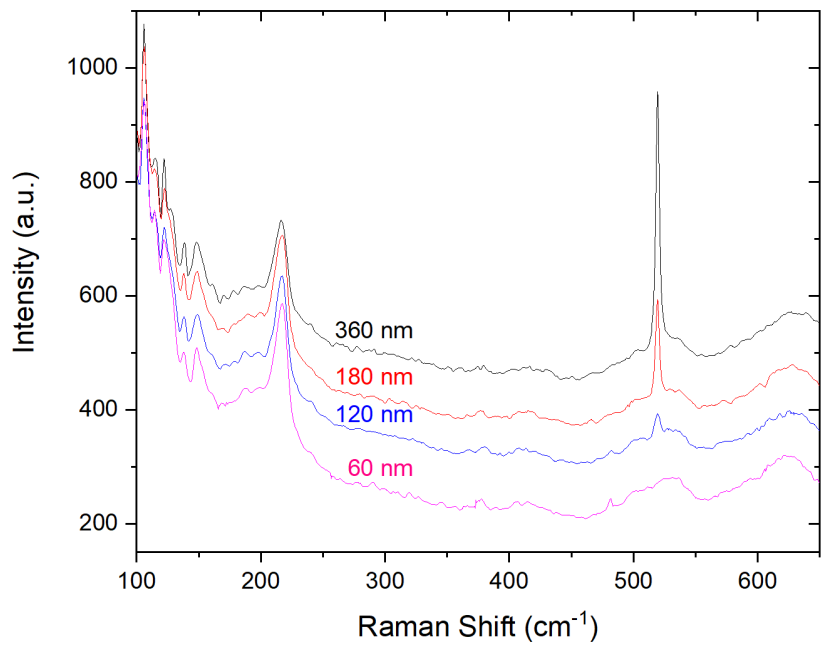


Figure 2.7. (a) Raman spectrum of CVD Cu_2O films of varying film thickness deposited at 200°C . The Raman peak at 519 cm^{-1} is observed to shrink as the film thickness increases. (b) A shift in the Raman peak at around 217 cm^{-1} due to the film experiencing tensile stress before the islands coalesce and compressive stress as the film grows thicker.

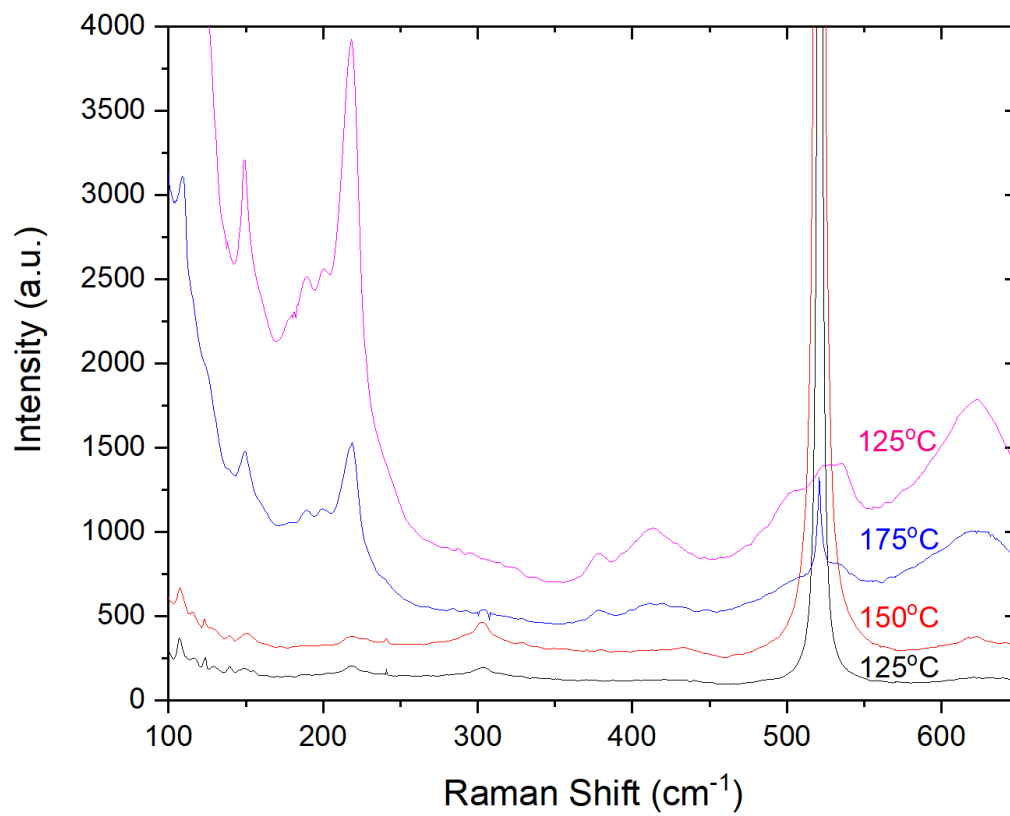


Figure 2.8. Raman spectra of CVD Cu₂O films deposited at various temperatures ranging from 125°C to 200°C.

2.4.5 Electrical Properties

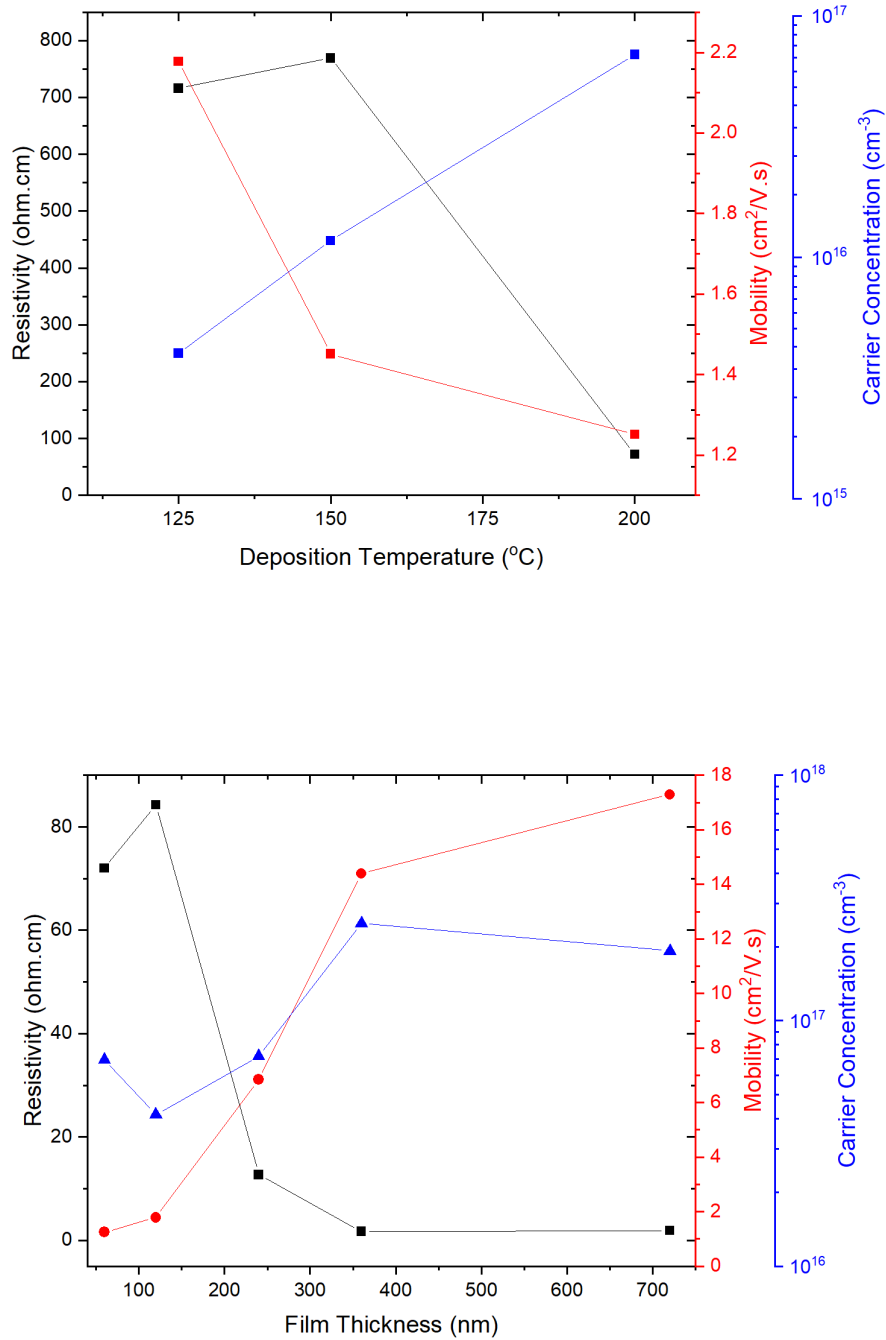


Figure 2.9. Resistivity, carrier concentration and Hall mobility of Cu₂O CVD thin films (a) of thickness of about 50-nm for various deposition temperatures, and (b) for various film thickness deposited at 200°C.

Figure 2.9a shows the hall mobility, hole carrier concentration and resistivity plotted as a function of deposition temperature during the CVD of Cu_2O . These films have a thickness of ≈ 50 nm which is characteristic of the typical range of film thicknesses in applications involving thin film coatings. The hall mobility of the films decreases at higher substrate temperatures, suggesting higher disorientation of the film morphology. Thin films of Cu_2O grown by CVD exhibit a strong preference towards non-continuous film surfaces at thicknesses of under 100 nm, which is evident from the aggregated material as observed in the cross-sectional SEM images in **Figure 2.6**. The corresponding increase in hole carrier concentrations with increasing deposition temperature is attributed to the increased introduction of oxygen vacancies during the CVD process, leading to more conductive Cu_2O films at higher process temperatures. **Figure 2.9b** shows the electrical properties of Cu_2O films grown to various thicknesses ranging from 60 nm to 750 nm at the same substrate temperature of 200°C under the high growth conditions that produces rough crystalline cuprous oxide films. The change in growth mode at the film thickness of approximately 100 nm is evident in the drastic change electrical characteristics. While the hole density remains constant with film thickness, the mobility experiences a remarkable increase from $1\text{-}2\text{ cm}^2\text{ V}^{-1}\text{ s}^{-1}$ for film thicknesses of 120 and 240 nm to over $14\text{ cm}^2\text{ V}^{-1}\text{ s}^{-1}$. The hall mobility remains fairly constant initially as the film was predominantly growing islands of Cu_2O which are connected to each other only through the compact layer of film they nucleated on. Subsequently as the deposition proceeds, the islands coalesce together to form a continuously layer comprised of larger grains, consequently enhancing carrier transport planar to the substrate, giving rise to the observed increase in hall mobilities. Consequently, the improvement in film

morphology results in a decrease in the resistivities of the material from around 80 ohm·cm down to single digit resistivity values.

2.4.6 Structural Properties

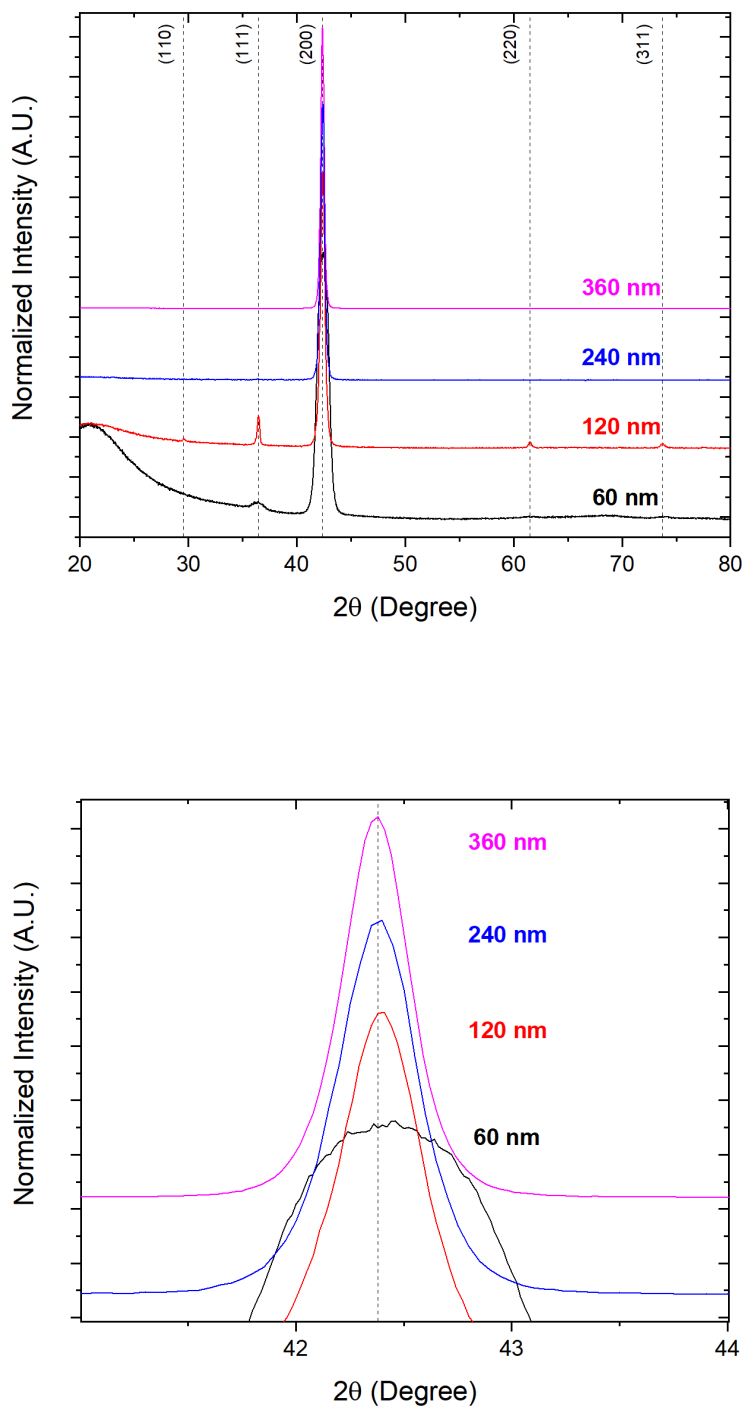


Figure 2.10. XRD spectra of Cu₂O thin films (a) for various film thickness deposited in the high-growth regime at 200°C, and (b) a close-up view showing the left shift in the (200) peak.

X-ray diffraction scans of films with different film thicknesses are shown in **Figure 2.10a** with diffraction intensities normalized to the (200) diffraction peak which corresponds to the cubic phase of Cu₂O according to JCPDS card No. 05-0667. All films demonstrate the (200) peak centered at 42.4° exhibiting the highest intensity and whose full-width at half-maximum (FWHM) decreases with increasing CVD deposition time, indicating an increase in crystallite size as the film grows thicker. At 60-nm thickness, the Cu₂O film shows broad, weak diffraction peaks of the (111) and (311) phases centered at 36.5° and 73.7°, respectively, as the dominance of the (200) phase becomes more prominent. Doubling the deposition time to obtain a 120-nm thick film results in increases of the amplitudes and the narrowing the widths of both peaks. In addition, two more peaks are observed at around 29.5° and 61.5° attributed to the (110) and (220) reflection planes, respectively. When the film thickness is increased to 240 nm and beyond, the diffraction peaks for (110), (111), (220) and (331) is observed to disappear, demonstrating a single preferred crystal orientation favoring the (200) crystal planes in thicker Cu₂O films. This behavior of the XRD spectra with varying film thickness is in excellent agreement with our SEM study of the film morphology that reveals a distinct change from preferential growth of Cu₂O islands at around film thickness of 200 nm to highly polycrystalline, columnar grain structure. The (200) diffraction peaks display a shift from 42.44° to 42.38° with increasing film thicknesses in **Figure 2.10b**, suggesting an increase in compressive stress which aligns with our investigations by Raman spectroscopy.

2.4.7 Optical Properties

In **Figure 2.11**, $(\alpha h\nu)^2$ was plotted against the photon energy in the determination of the optical band gap E_g of the Cu₂O thin films based on the Tauc relation [24]

$$(\alpha h\nu)^2 = A(h\nu - E_g)^n$$

where A is a constant, $h\nu$ is the photon energy, E_g is the allowed energy gap, and $n = 1/2$ for allowed direct transition in Cu₂O. The absorption coefficient α is calculated from the approximation

$$\alpha = -\frac{\ln(T)}{d}$$

where T is the transmittance of the film, and d is the film thickness. The values for the optical band gaps are obtained from the x-intercept of an extrapolation of the linear portion of the Tauc plots. The optical band gap values are found to vary in the range of 2.4 eV to 2.6 eV depending on film thicknesses, with thinner films exhibiting large band gap values. Our CVD grown films demonstrate optical band gap values that are consistent with both experimental [25] and theoretical studies [26]. This band gap widening effect with increasing film thickness is a well-established observation in similar thin film studies [27] explained by the larger grain sizes present in thicker films, in addition to the elimination of defects that widens the localized states in the band gap and consequently inhibiting optical absorption [28]. Precise control of the optical band gaps of Cu₂O is easily achieved by the accurate manipulation of film thickness using CVD, making it extremely useful for tuning the performances of the film when used as a hole transport layer in photovoltaic applications [29].

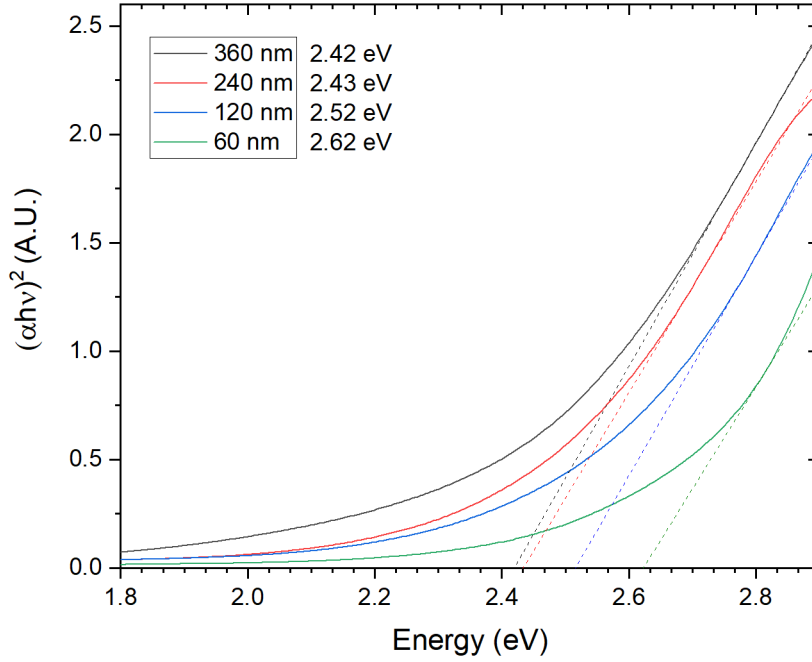


Figure 2.11. Tauc plot of $(\alpha h\nu)^2$ vs. photon energy for Cu_2O CVD films at film thicknesses of 60 nm, 120 nm, 240 nm and 360 nm.

2.4.8 Photoluminescence

The Cu_2O thin film demonstrates a strong, sharp band-to-band photoluminescence emission at room temperature centered at 588 nm, indicative of an electronic band gap of 2.1 eV. The presence of significant PL emission lines due to a radiative inter-band recombination process from room temperature excitation suggests low defect contents in the CVD grown Cu_2O film. It is found that the electronic band gap of Cu_2O thin films increases with decreasing temperature. The dependence of Cu_2O band gap is observed to closely follow the semi-empirical relation proposed by Vashni [30]

$$E_g(T) = E_0 - \alpha T^2 / (T + \beta)$$

where α and β are parameters characteristic of the semiconductor material and is the transition energy at 0K. Fitting the parameters E_0 , α and β yields the values 2.1093 eV, 1.0192×10^{-5} eV/K and 485.02 K², respectively, in close agreement with similar Cu₂O studies [31]. At above 150K, we observe the band gap to vary linearly with temperature. The photoluminescence intensity attributed to the band-to-band transition is observed to increase with decreasing temperature due to the suppression of non-radiative recombination channels.

To better understand the various defect-mediated PL emissions, the spectra through the temperature range were fitted with Gaussian curves. Using the least number of Gaussian bands to fit the PL spectrum, the best fitting result consists of six PL situated at 1.67 eV (744 nm), 1.60 eV (777 nm), 1.52 eV (817 nm), 1.43 eV (870 nm), 1.35 eV (917 nm), and 1.27 eV (973 nm), respectively as shown in **Figure 2.13a**. Well-known transitions include the 1.67 eV peak originates from the doubly charged oxygen vacancy (V_{O}^{2+}), the 1.52 eV peak corresponds to the singly charged oxygen vacancy (V_{O}^{+}), and the 1.35 eV is emitted from the transition involving the copper vacancy (V_{Cu}) [32-34]. Peaks at 1.60 eV, 1.43 eV and 1.27 eV remain unidentified and warrants further investigation. From the PL spectra taken at room temperature, it can be deduced that V_{Cu} is the dominant defect present in the film. Reducing the temperature exhibits remarkably large increase in PL intensity of the V_{O}^{2+} defect emission peak. As radiative processes begin to dominate at lower temperatures, all defect emissions are observed to exhibit stronger PL emissions, with the higher energy defect peaks attributed to oxygen vacancies experiencing larger increases in emission intensities compared to the PL emissions involving copper vacancies.

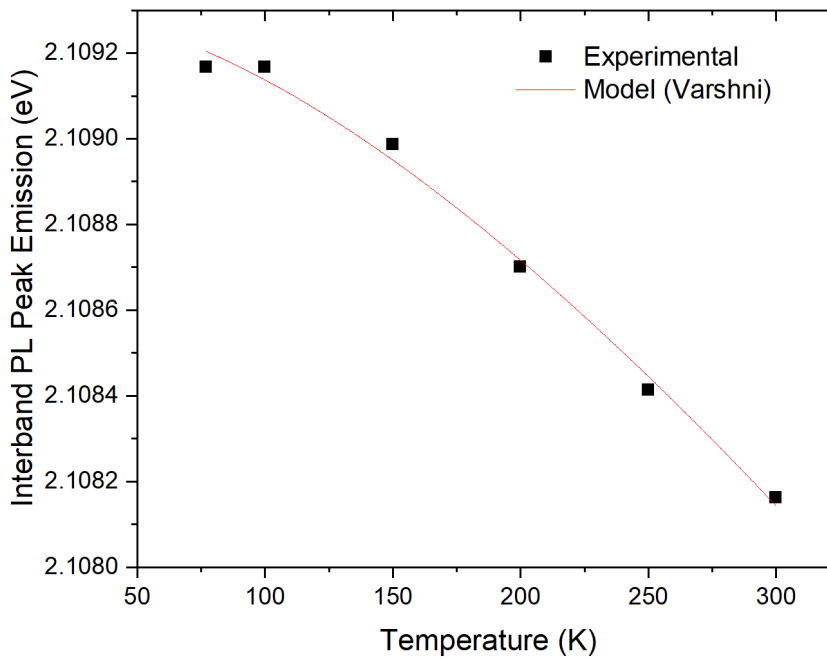
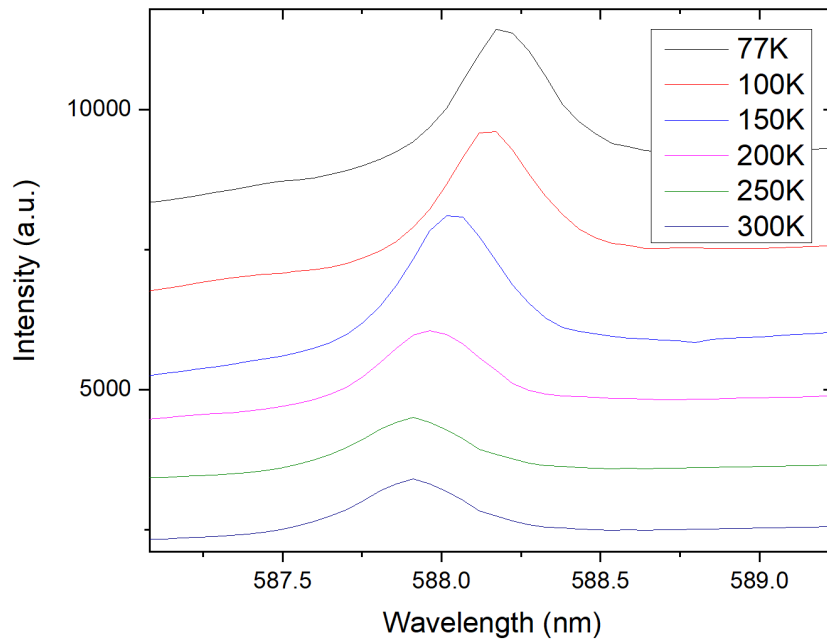


Figure 2.12. (a) Inter-band photoluminescence emission profile of Cu_2O thin film at various temperature, and (b) the variation in band gap values of Cu_2O at different temperatures compared to a fitted model based on the Varshni relation.

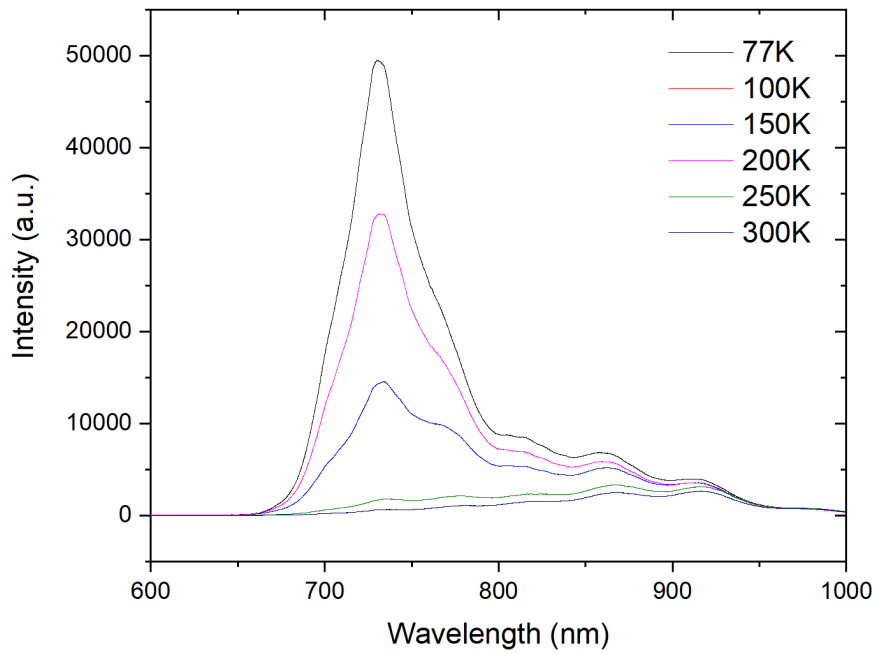
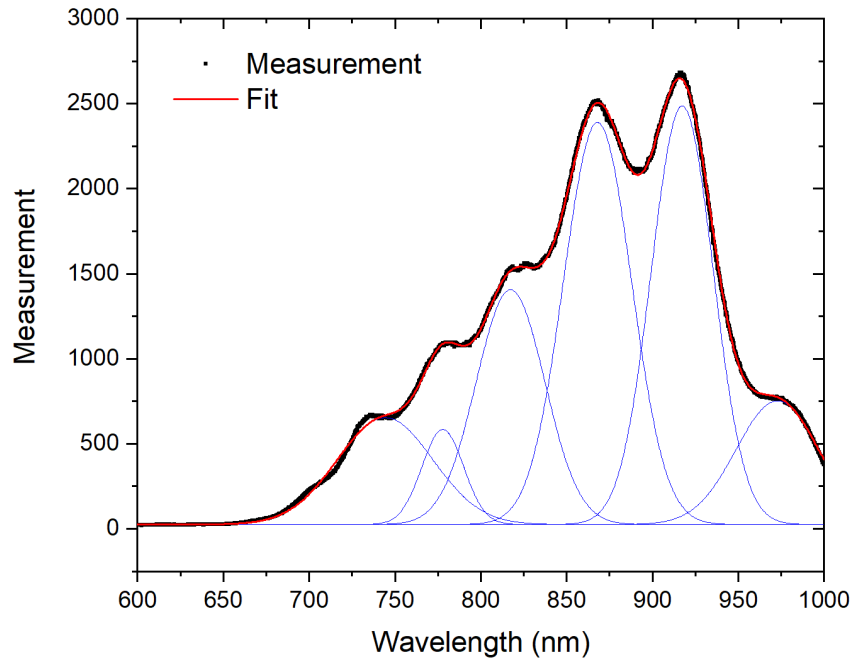


Figure 2.13. PL spectrum showing (a) the various PL components that make up the PL emission spectra obtained at room temperature, and (b) the temperature dependence of various defect-related PL bands.

2.5 Conclusion

In summary, we report on the chemical vapor deposition to produce high quality Cu₂O thin films of a single oxide phase. In this methodology, highly crystalline films can be deposited with high growth rates at temperatures of 200°C, while smooth, uniform films can be produced between 125°C and 200°C. The Cu₂O films form a cubic phase, with a wide optical bandgap of up to 2.6 eV, demonstrating hole mobilities as high as 14 cm² V⁻¹ s⁻¹ and carrier concentration in the order of 10¹⁷ cm⁻³. Low defect densities enabled photoluminescence from inter-band transitions to be observed at room temperature. XPS and Raman spectroscopy highlighted the high purity of the films produced with no detectable amounts of CuO present. Such properties make CVD Cu₂O highly attractive for applications in semiconductor devices and in photovoltaics.

2.6 References

1. Matsuzaki, K., et al., *Epitaxial growth of high mobility Cu₂O thin films and application to p-channel thin film transistor*. Applied Physics Letters, 2008. **93**(20): p. 202107.
2. Dolai, S., et al., *Cuprous oxide (Cu₂O) thin films prepared by reactive d.c. sputtering technique*. Vacuum, 2017. **141**: p. 296-306.
3. Moharam, M.M., et al., *Potentiostatic deposition of Cu₂O films as p-type transparent conductors at room temperature*. Thin Solid Films, 2016. **616**: p. 760-766.
4. Lee, Y.S., et al., *Atomic layer deposited gallium oxide buffer layer enables 1.2 V open-circuit voltage in cuprous oxide solar cells*. Adv Mater, 2014. **26**(27): p. 4704-10.
5. *Diversity of electronic transitions and photoluminescence properties of p-type cuprous oxide films: A temperature-dependent spectral transmittance study*. Journal of Applied Physics, 2015. **117**(4): p. 045701.
6. Polat, Ö., et al., *Nanostructured columnar heterostructures of TiO₂ and Cu₂O enabled by a thin-film self-assembly approach: Potential for photovoltaics*. Materials Research Bulletin, 2013. **48**(2): p. 352-356.
7. Darvish, D.S. and H.A. Atwater, *Epitaxial growth of Cu₂O and ZnO/Cu₂O thin films on MgO by plasma-assisted molecular beam epitaxy*. Journal of Crystal Growth, 2011. **319**(1): p. 39-43.
8. Iwanowski, R.J. and D. Trivih, *Cu/Cu₂O Schottky barrier solar cells prepared by multistep irradiation of a Cu₂O substrate by H⁺ ions*. Solar Cells, 1985. **13**(3): p. 253-264.
9. Fernando, C.A.N. and S.K. Wetthasinghe, *Investigation of photoelectrochemical characteristics of n-type Cu₂O films*. Solar Energy Materials and Solar Cells, 2000. **63**(3): p. 299-308.
10. Jiang, T., et al., *Photoinduced charge transfer process in p-Cu₂O/n-Cu₂O homojunction film and its photoelectric gas-sensing properties*. J Colloid Interface Sci, 2013. **405**: p. 242-8.
11. Tsai, T.-Y., et al., *p-Cu₂O-shell/n-TiO₂-nanowire-core heterostructure photodiodes*. Nanoscale Research Letters, 2011. **6**(1): p. 575.
12. Ottosson, M. and J.-O. Carlsson, *Chemical vapour deposition of Cu₂O and CuO from CuI and O₂ or N₂O*. Surface and Coatings Technology, 1996. **78**(1): p. 263-273.
13. Holzschuh, H. and H. Suhr, *Deposition of copper oxide (Cu₂O, CuO) thin films at high temperatures by plasma-enhanced CVD*. Applied Physics A, 1990. **51**(6): p. 486-490.
14. Pan, G.-F., et al., *CVD synthesis of Cu₂O films for catalytic application*. RSC Advances, 2015. **5**(53): p. 42477-42481.
15. Eisermann, S., et al., *Copper oxide thin films by chemical vapor deposition: Synthesis, characterization and electrical properties*. physica status solidi (a), 2012. **209**(3): p. 531-536.
16. Chen, C.-Y.Y.a.J.S., *Investigation of Copper Agglomeration at Elevated Temperatures*. Journal of the Electrochemical Society, (150): p. G826-G830.
17. W. Hartman, J., et al., *Agglomeration Of Cu Electroplating Seed Layers On Ultra-Thin Ta, Ta_{1-x}N_x, Ta_{1-x}O_x, Contaminated Ta, and Composite Ta/Ta_{1-x}N_x Diffusion Barriers*. Vol. 564. 2011.

18. Maruyama, T., *Copper Oxide Thin Films Prepared from Copper Dipivaloylmethanate and Oxygen by Chemical Vapor Deposition*. Japanese Journal of Applied Physics, 1998. **37**(Part 1, No. 7A): p. 4099-4102.
19. Li, Z., S.T. Barry, and R.G. Gordon, *Synthesis and Characterization of Copper(I) Amidinates as Precursors for Atomic Layer Deposition (ALD) of Copper Metal*. Inorganic Chemistry, 2005. **44**(6): p. 1728-1735.
20. Niaura, G., *Surface-enhanced Raman spectroscopic observation of two kinds of adsorbed OH⁻ ions at copper electrode*. Electrochimica Acta, 2000. **45**(21): p. 3507-3519.
21. Chan, H.Y.H., C.G. Takoudis, and M.J. Weaver, *Oxide Film Formation and Oxygen Adsorption on Copper in Aqueous Media As Probed by Surface-Enhanced Raman Spectroscopy*. The Journal of Physical Chemistry B, 1999. **103**(2): p. 357-365.
22. Singhal, A., et al., *Copper(I) Oxide Nanocrystals - One Step Synthesis, Characterization, Formation Mechanism, and Photocatalytic Properties*. European Journal of Inorganic Chemistry, 2013. **2013**(14): p. 2640-2651.
23. Deng, Y., et al., *In Situ Raman Spectroscopy of Copper and Copper Oxide Surfaces during Electrochemical Oxygen Evolution Reaction: Identification of Cu(III) Oxides as Catalytically Active Species*. ACS Catalysis, 2016. **6**(4): p. 2473-2481.
24. Tauc, J. and A. Menth, *States in the gap*. Journal of Non-Crystalline Solids, 1972. **8-10**: p. 569-585.
25. B. Balamurugan, B.R.M., *Optical and structural properties of nanocrystalline copper oxide thinfilms prepared by activated reactive evaporation*. Thin Solid Films, 2001. **396**: p. 90-96.
26. Malerba, C., et al., *Absorption coefficient of bulk and thin film Cu₂O*. Solar Energy Materials and Solar Cells, 2011. **95**(10): p. 2848-2854.
27. Sönmezoğlu, S., et al., *The effects of film thickness on the optical properties of TiO₂-SnO₂ compound thin films*. Physica Scripta, 2011. **84**(6): p. 065602.
28. Rabeh, M.B., et al., *The Effect of Thickness on Optical Band Gap and N-type Conductivity of CuInS₂ Thin Films Annealed in Air Atmosphere*. Energy Procedia, 2014. **44**: p. 52-60.
29. Chatterjee, S. and A.J. Pal, *Introducing Cu₂O Thin Films as a Hole-Transport Layer in Efficient Planar Perovskite Solar Cell Structures*. The Journal of Physical Chemistry C, 2016. **120**(3): p. 1428-1437.
30. Varshni, Y.P., *Temperature dependence of the energy gap in semiconductors*. Physica, 1967. **34**(1): p. 149-154.
31. Biccari, F., *Defects and Doping in Cu₂O*. 2012: Lulu.Com.
32. Gastev, S.V., A.A. Kaplyanskii, and N.s. Sokolov, *Relaxed excitons in Cu₂O*. Vol. 42. 1982. 389-391.
33. Ito, T. and T. Masumi, *Detailed Examination of Relaxation Processes of Excitons in Photoluminescence Spectra of Cu₂O*. 1997. **66**: p. 2185-2193.
34. K. Teh, C. and F. L. Weichman, *Photoluminescence and optical absorption studies of the effects of heat treatment on cuprous oxide*. Vol. 61. 2011. 1423-1427.

3 Improved Cu₂O-Based Solar Cells Using Atomic Layer Deposition to Control the Cu Oxidation State at the p-n Junction

3.1 Chapter Abstract

Solar cells are produced by atomic layer deposition (ALD) of *n*-type amorphous zinc-tin-oxide buffer layers on electrochemically-deposited *p*-type cuprous oxide, Cu₂O, absorber layers. The diethylzinc precursor in the ALD process reduces Cu²⁺-related defects at the heterojunction interface, improving the solar-cell open-circuit voltage. An NREL-certified power conversion efficiency of 2.85% is reported.

3.2 Introduction

Recombination at a defect-rich interface is one of the major efficiency-loss mechanisms in polycrystalline heterojunction thin-film solar cells.^[1, 2] Cuprous oxide (Cu_2O) is considered a promising Earth-abundant semiconductor for thin-film solar cells compatible with terawatt-level deployment.^[3-5] However, the power conversion efficiency (PCE) of Cu_2O -based solar cells has remained significantly lower than the theoretical single-junction maximum efficiency of $> 20\%$, often due to low open-circuit voltages (V_{OC}) resulting from rapid interfacial recombination.^[6-8] This interfacial recombination is believed to originate mostly from (i) non-ideal band-alignment with an adjacent n -type transparent conductive oxide (TCO) layer (*e.g.* Al-doped ZnO or indium-tin-oxide) and (ii) a high density of trap states in the region near the heterojunction interface. Various buffer layers including Ga_2O_3 , TiO_2 , and amorphous zinc-tin-oxide (a-ZTO) have been applied at the junction interface to provide more ideal band alignment.^[6, 9, 10]

To reduce the interfacial trap density and further enhance heterojunction quality, any defects at the heterojunction interface should be minimized.^[11] In particular, a cupric oxide (CuO) layer on the Cu_2O surface is highly undesirable since it has a smaller bandgap ($E_{\text{g}} = \sim 1.4 \text{ eV}$) than Cu_2O ($E_{\text{g}} = \sim 2 \text{ eV}$) and its conduction band energy near 4 eV from the vacuum level can create deep states at the interface, enhancing interfacial recombination.^[3, 12-14] A CuO layer is formed readily on a Cu_2O or Cu surface during quenching and/or exposure to an oxygen-rich ambient.^[7, 15] Similar surface chemistry changes are common for many thin-film solar cell materials including copper indium gallium selenide (CIGS).^[16] In the past, chemical treatments have been employed to modify the surface chemistry of air-exposed CIGS films.^[16, 17] For Cu_2O prepared by a thermal oxidation method, similar methods for Cu_2O surface modification, including wet etching, heat treatments, and a catalyst layer, have been introduced to remove the CuO surface layers,

resulting in enhancements of solar cell performance.^[5, 7, 18] However, even if the surface treatments remove the CuO layer completely, a nanometer-scale-thick CuO layer can re-grow when the surface is exposed to air thereafter.^[15] Thus, a surface modification process with high controllability should be performed *in situ* immediately prior to overlayer deposition during solar cell fabrication (*e.g.* buffer layer deposition) to achieve higher PCE. Recently, Wilson *et al.*, proposed a method to control interface stoichiometry of Cu₂O *in situ* by controlling the oxygen partial pressure during sputtering of a ZnO over-layer.^[14]

In this communication, we demonstrate a method to tune the chemical state of the interfacial layer of Cu₂O absorbers by chemical means, by engineering the atomic layer deposition (ALD) reaction conditions of an a-ZTO buffer layer in an all-oxide thin-film solar cell device architecture (ZnO:Al/a-ZTO/Cu₂O). During the past decade, ALD has demonstrated utility in a range of photovoltaic device-processing applications, including buffer-layer deposition and surface passivation.^[19, 20] The discrete nature of the ALD process enables a high degree of tunability of the layer properties as well as an excellent uniformity over large-scale substrates.^{[19-}

21]

3.3 Experiments

Atomic layer deposition of a-ZTO thin films: The a-ZTO thin-films were deposited using a custom-built cylindrical ALD reactor with a sample stage 30 cm long and 3 cm wide, and a chamber volume of 0.627 L. The aluminum substrate stage and the entire wall of ALD chamber were kept at the same ALD reaction temperature inside a Lindberg Blue M tube furnace (Thermo Scientific). Diethylzinc (Sigma Aldrich) and 1,3-bis(1,1-dimethylethyl)-4,5-dimethyl-(4R,5R)-1,3,2-diazastannolidin-2-ylidene were used as Zn and Sn precursors, respectively. The Zn and Sn

precursors were kept at constant temperature of 25 and 40 °C, respectively. A H₂O₂ solution (50 wt.% in H₂O, Sigma Aldrich) was used as a common oxidant for a-ZTO growth to enable the ALD reaction with the Sn(II) precursor at reaction temperature below 170 °C, which was not possible by using H₂O. Due to a high vapor pressure of H₂O₂, as-received H₂O₂ solution was placed in a glass container held at 25 °C and it was vaporized into a trap, which is made of stainless steel with a volume of 35 mL, prior to the release into the ALD reactor. One super-cycle of a-ZTO consisted of ZnO and SnO₂ sub-cycles with a ratio of 3:1. During each sub-cycle, the exposures of diethylzinc, tin precursor, and H₂O₂ were estimated to be approximately 0.32, 0.033, and 0.027 Torr-s, respectively.

Solar Cell Fabrication: A 200-nm-thick Au bottom-electrode with 5-nm-thick Ti adhesion layer was deposited on a 1 × 1 inch² SiO₂ by e-beam evaporation. To define a cell area of 3 × 5 mm², a 2.5-μm-thick SiO₂ layer was deposited by plasma-enhanced chemical vapor deposition and areas defined by photolithography were etched by a buffered-oxide-etchant (7:1, J. T. Baker). A 2.5-μm-thick Cu₂O film was deposited on the exposed Au area at 40 °C by the galvanostatic electrochemical method.^[34] A lactate-stabilized copper sulfate aqueous solution was prepared with 3 M lactic acid (Sigma Aldrich), 0.2 M cupric sulfate pentahydrate (CuO₄·5H₂O, Sigma Aldrich) and de-ionized water (18.3 MΩ·cm, Ricca Chemical), and then 2 M sodium hydroxide (NaOH, Sigma Aldrich) aqueous solution was added to adjust the pH of the solution to 12.5. All reagent-grade chemicals were used and the solution was filtered and stirred thoroughly. A constant current density of 0.23 mA·cm⁻² was applied for 2 hours using a Keithley 2400 sourcemeter with a Pt counter electrode to grow the Cu₂O films. The Cu₂O film surfaces were rinsed with de-ionized water. The a-ZTO and ZnO:Al thin-films were deposited by ALD as described in detail elsewhere.^[9] 1-μm-thick Al top-electrodes were deposited by e-beam evaporation with a grid

spacing of 0.5 mm defined by a lift-off process. A 95-nm-thick MgF_2 film as an anti-reflective layer was deposited by thermal evaporation.

Characterization: Surface morphologies of the devices were analyzed using an Ultra 55 FESEM (Zeiss). XPS measurements were performed using a K-alpha XPS (Thermo Scientific). Samples were etched *in situ* by an Ar ion beam for a depth profiling. The J - V and the C - f characteristics of the devices were measured by using Agilent 4156C and Keithley 2400 semiconductor characterization systems. The standard 1-sun illumination was generated by a Newport Oriel 91194 solar simulator with a 1600W ozone-free Xe-lamp with a AM1.5G filter and a Newport Oriel 6895 flux controller calibrated by an NREL-certified Si reference cell equipped with a BG-39 window.

3.4 Results and Discussion

3.4.1 Using ALD to Control of the Oxidation State of Copper at the Interface

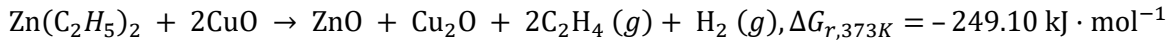
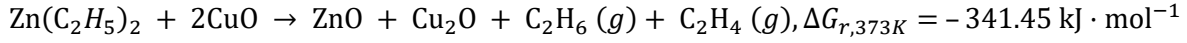
We exploit the fact that ALD can involve highly reactive metal-precursors and oxidizers, which can also affect surface chemistry of substrates. We utilize the thermodynamics of the half-cycle reaction in the ALD sequence of a-ZTO buffer layer deposition to control the surface chemistry of as-grown Cu_2O thin-film, and describe how this approach could be generalized to other buffer-layer materials. The CuO (Cu^{2+} state) interfacial layer at a-ZTO/ Cu_2O can be reduced to Cu_2O (Cu^{1+} state) by pulsing a Zn precursor, and additional oxidation of Cu_2O surface by an oxidant pulse can be suppressed by lowering the ALD reaction temperature. By engineering the surface chemistry associated with the ALD reaction temperature, the chemical state of Cu at the interface can be controlled and a high-quality heterojunction can be formed. We demonstrate the

enhanced performance of Cu₂O-based solar cells by controlling interface chemistry, resulting in an improved V_{OC} .

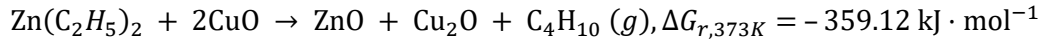
A nanometer-scale-thick surface layer of CuO phase is normally formed on Cu₂O films grown by electrochemical deposition. **Figure 3.1** shows XPS spectra of the Cu-2*p* core levels for an as-grown Cu₂O film surface and a Cu₂O surface sputtered by argon ions at 1 keV *in situ*. Peaks at 932.2 and 934.2 eV indicate Cu¹⁺ and Cu²⁺ states, respectively.^[22, 23] Broad satellite peaks near 940 – 945 eV originate from the CuO phase, which is a characteristic of materials having a d^9 configuration in the ground state.^[23] Thus, the existence of the satellite peaks is an evidence of formation of the CuO phase in addition to the peak assigned to the Cu²⁺ state at ~934 eV. After sputtering the sample surface for 1 min, the signals from the CuO phase disappear and only signals from the Cu₂O phase are observed. The XPS spectra with depth profiling suggest that the CuO forms only at the near-surface region of the Cu₂O. The CuO is likely due to exposure of the sample to ambient atmosphere, in which an abundance of oxygen can promote the complete oxidation of copper cations to Cu²⁺ (CuO).^[23, 24] Considering the electron escape depth of ~5 nm and the XPS signal intensity of CuO phase relative to Cu₂O phase, the surface CuO layer is expected to have an approximate thickness of only 1 nm, perhaps suggesting that the formation of a thicker surface layer is limited by oxygen diffusion through CuO.

To remove the surface CuO layer and create a high-quality a-ZTO/Cu₂O interface, the thermodynamics of the a-ZTO ALD reaction are investigated. The optimized a-ZTO ALD consists of ZnO and SnO₂ deposition reactions with a pulse ratio of 3:1.^[9, 25] The starting sequence is a pulse of diethylzinc (DEZ) as a Zn precursor, followed by a pulse of hydrogen peroxide (H₂O₂) as an oxidizer. It has been reported that the injection of ALD metal precursors can reduce an underlying layer if the reactions are energetically favorable.^[26, 27] The Gibbs free energy of reaction

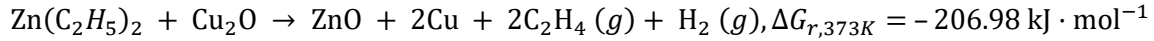
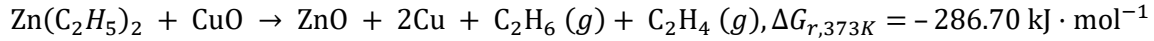
(ΔG_r) can predict whether the surface reactions in a-ZTO ALD are spontaneous. Plausible reactions of DEZ with CuO and their ΔG_r at 373 K are the following:^[28]



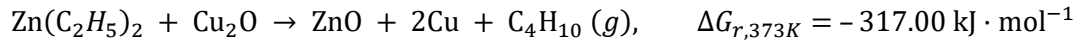
or



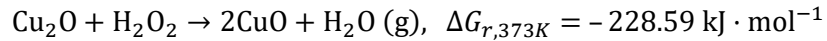
In addition, the reduction of Cu₂O to metallic Cu by DEZ is also possible by the following reactions:



Or



On the other hand, the H₂O₂ sequence after the DEZ pulse can oxidize Cu₂O to CuO by the following reaction:



All reactions have negative ΔG_r at 373 K, indicating that both reduction and oxidation reactions are thermodynamically favorable in the presence of reducing and oxidizing precursors, respectively.

As the thermodynamic analysis predicts, the Zn precursor in the a-ZTO ALD process is experimentally observed to reduce the CuO surface layer to Cu₂O. **Figure 3.3a** shows normalized

XPS spectra of Cu-2*p* at the Cu₂O surface after DEZ and an Sn(II) precursor (1,3-bis(1,1-dimethylethyl)-4,5-dimethyl-(4*R*,5*R*)-1,3,2-diazastannolidin-2-ylidene) were pulsed on Cu₂O films with CuO surface layers. Here, nine super-cycles (three DEZ pulses and one Sn(II) precursor pulse per one super-cycle) of metal precursor injections were used, skipping the injection of H₂O₂. Two reaction temperatures of 90 and 170 °C were investigated. At both temperatures, the intensities of the CuO peaks decreased after the injection of metal precursors, which indicates that the CuO layer was partially reduced to Cu₂O or Cu. The similar decrease in the intensity of the CuO peak for both temperatures suggests that the reduction rate is rapid at both temperatures. A control experiment was performed (the Cu₂O samples were kept in the chamber without doing any ALD treatment), which showed negligible change of XPS spectra as shown in **Figure 3.2**.

When only Sn(II) precursor pulses were introduced to the Cu₂O film while not injecting DEZ or H₂O₂ with the same conditions mentioned above, negligible reduction of the CuO layer was observed. In contrast, the injection of DEZ without any Sn(II) precursor or H₂O₂ significantly decreased the size of the CuO peak. Thus, the reduction of the CuO layer is mainly driven by DEZ, forming a stable ZnO without the aid of the oxidant (**Figure 3.3b**). The reduction of Cu₂O by the Sn(II) precursor is thermodynamically or kinetically unfavorable. Interestingly, the reduction of CuO is most effective when only DEZ was introduced without any Sn(II) precursor, which suggests the surface-adsorbed Sn(II) precursor inhibits further adsorption of DEZ. The reduction of CuO is possible by the reactions of DEZ to form ZnO as described in Reactions 1 – 6. Figure 2b shows the XPS spectra of Zn-2*p* core levels after only DEZ molecules were introduced to the Cu₂O film at 90 °C. The Zn peak at 1021.6 eV (Zn-2*p*_{3/2}) corresponds to the peak of a reference ALD ZnO film grown by DEZ and H₂O₂. The thickness of the ZnO layer formed after the DEZ pulse to the Cu₂O film is estimated to be about 1 nm thick. Based on these observations, we

conclude that starting the a-ZTO ALD process with the DEZ sequence is more effective to reduce the CuO surface layer than the process starting with the Sn(II) precursor sequence.

Although both reduction reactions to Cu₂O and metallic Cu are thermodynamically possible, metallic Cu is not detected after the metal precursor injections. It is difficult to distinguish Cu¹⁺ from metallic Cu by XPS, because the peak positions of Cu-2*p* from the both states are close.^[22] Instead, Cu₂O and Cu metal can be distinguished from the Cu-*LMM* Auger transition kinetic energy.^[24] The Cu-*LMM* kinetic energies from Cu₂O and metallic Cu have been reported to be 916.5 and 918.4 eV, respectively, with an Al-K α radiation when the peaks were referenced to the C-1*s* binding energy at 284.6 eV.^[24] As shown in **Figure 3.3c**, the kinetic energy of 916.9 eV is observed when the CuO phase was reduced by the DEZ during the a-ZTO ALD process. Both the peak position and shape are closer to the signal from Cu₂O than from metallic Cu. To compare with the signal from the metallic Cu phase, a 20-nm-thick metallic Cu film was deposited by e-beam evaporation at room temperature and an a-ZTO film was grown on the Cu film. Obviously, the metallic Cu is observed at 919 eV, as well as a peak from the Cu₂O phase (formed by air exposure of Cu film after the growth) at 917 eV. The metallic Cu phase was detected successfully by XPS in the a-ZTO/Cu sample, owing to the a-ZTO layer protecting the Cu surface from the further oxidation by air. However, no metallic Cu phase was observed in the a-ZTO/Cu₂O sample. This indicates the formation of Cu may be limited kinetically at the a-ZTO/Cu₂O sample, although the thermodynamic criteria for the formation of Cu are satisfied according to the Reactions 4 – 6. In addition, we investigated the potential for Cu diffusion through a-ZTO layers, since any trace of metallic Cu is known to pose significant diffusion issues as experienced in Cu-related processes of various semiconductor applications.^[29] 10-nm-thick a-ZTO films, thicker than an electron escape depth of ~5 nm in XPS, were deposited on Cu₂O at reaction temperatures

between 90 and 170 °C. No signal from Cu is detected by XPS for all temperatures shown in **Figure 3.3d**. The Auger signal and the Cu-diffusion investigation did not indicate any trace of metallic Cu, which suggests that the reactions by Reaction 4 – 6 are limited by a high activation-energy (slow kinetics).

On the other hand, H₂O₂ exposure after the DEZ sequence can re-oxidize the Cu₂O surface layer to the CuO phase. **Figure 3.4** shows the normalized XPS spectra of Cu-2*p* for three different Cu₂O samples: as-grown Cu₂O film and the H₂O₂-exposed Cu₂O films at reaction temperatures of 90 and 170 °C. Here, 36 H₂O₂ pulses were introduced to the Cu₂O samples, which is equal to the total H₂O₂ pulses of nine super-cycles. The increased satellite peak intensities at 940 – 945 eV for both temperatures indicate that the surface of the Cu₂O film is partly re-oxidized to CuO by H₂O₂. As the reaction temperature is raised from 90 to 170 °C, the relative intensity of the Cu²⁺ peak at 934 eV to the Cu¹⁺ peak at 932 eV is increased. This result suggests that more oxidation of Cu₂O to CuO occurs at higher ALD temperatures.

Since the reduction and oxidation reactions possess different temperature dependences, the surface chemistry of Cu₂O films can be controlled by changing the reaction temperature. To investigate the chemical state of Cu at the a-ZTO/Cu₂O interface by XPS, 3-nm-thick a-ZTO films were grown on Cu₂O films at different reaction temperatures in the range of 90 – 170 °C. **Figure 3.5a** shows the normalized XPS spectra of Cu-2*p* from the a-ZTO/Cu₂O samples. The Cu²⁺ peak at 934 eV is not detected in samples with ALD reaction temperatures below 120 °C. This result suggests that the a-ZTO ALD process itself can effectively reduce the detrimental CuO layer to Cu₂O. However, at the reaction temperature of 170 °C, a small peak shoulder near ~934 eV is observed. The peak shoulder is further investigated by deconvoluting the spectrum into multiple peaks as shown in **Figure 3.5b**. The peak shoulder is attributed to the Cu²⁺ state centering at ~933.7

eV. As discussed in the previous experiments, a higher reaction temperature could increase the oxidation rate by H_2O_2 significantly, while the reduction rate by DEZ was not affected in the temperature range between 90 and 170 °C.

Thus, it can be concluded that the oxidation reaction by H_2O_2 competes with the reduction reaction by DEZ in the a-ZTO ALD process. As the reaction temperature increases, the oxidation reaction becomes faster than the reduction reaction, possibly due to different activation energies. It should be noted that the CuO formation by H_2O_2 is likely diffusion-limited by the a-ZTO layer: the oxidation by H_2O_2 becomes weaker as the a-ZTO layer gets thicker; thus the a-ZTO layer appears to protect the Cu_2O layer from further oxidation by H_2O_2 . The Cu^{2+} peak intensities relative to Cu^{1+} shown in **Figure 3.5b** are much smaller than ones where only H_2O_2 was injected, as shown in **Figure 3.4**. The protection of the substrate surface from the oxygen precursor by growing layers has also been proposed in other ALD processes.^[27, 30] Our XPS results suggest that a lower reaction temperature for a-ZTO ALD is beneficial for reducing the CuO surface layer to Cu_2O and preventing further re-oxidation by H_2O_2 .

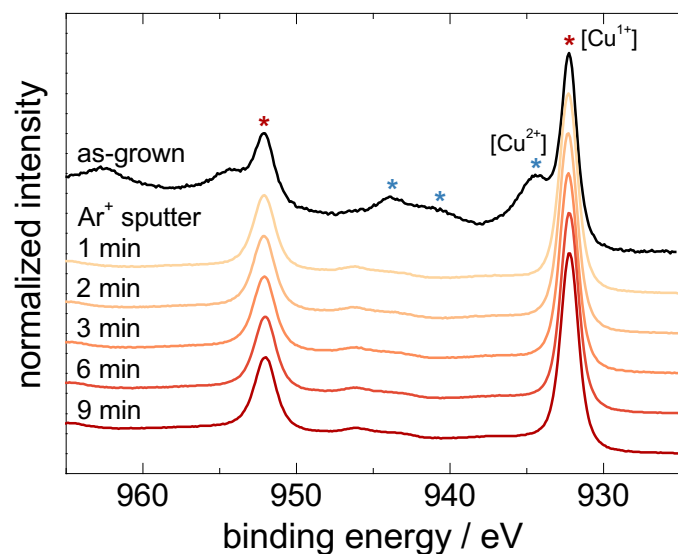


Figure 3.1. XPS spectra of Cu-2p core levels for an as-grown Cu_2O film surface and sputtered surfaces by Ar-ion at 1 keV in situ. The peaks from Cu^{1+} and Cu^{2+} states are shown in red and blue asterisks respectively. The native CuO surface layer, which is removed by sputtering, is estimated to be 1 nm thin.

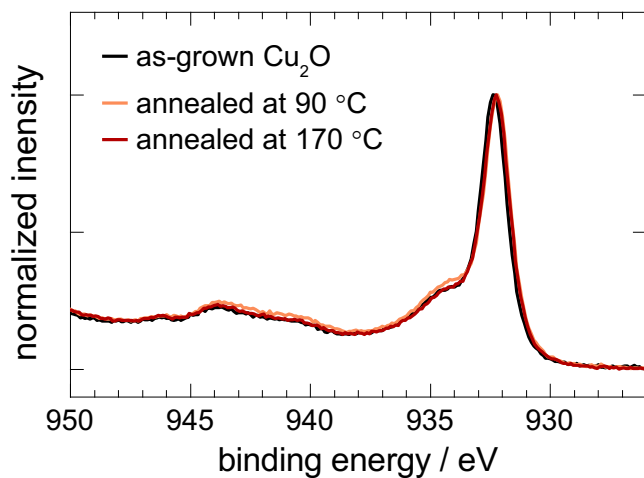


Figure 3.2. Normalized XPS spectra of Cu-2p of Cu_2O surfaces before and after heat treatments. As grown Cu_2O samples were kept in the ALD chamber under vacuum without ALD treatment. The same duration with the ALD treatment was used.

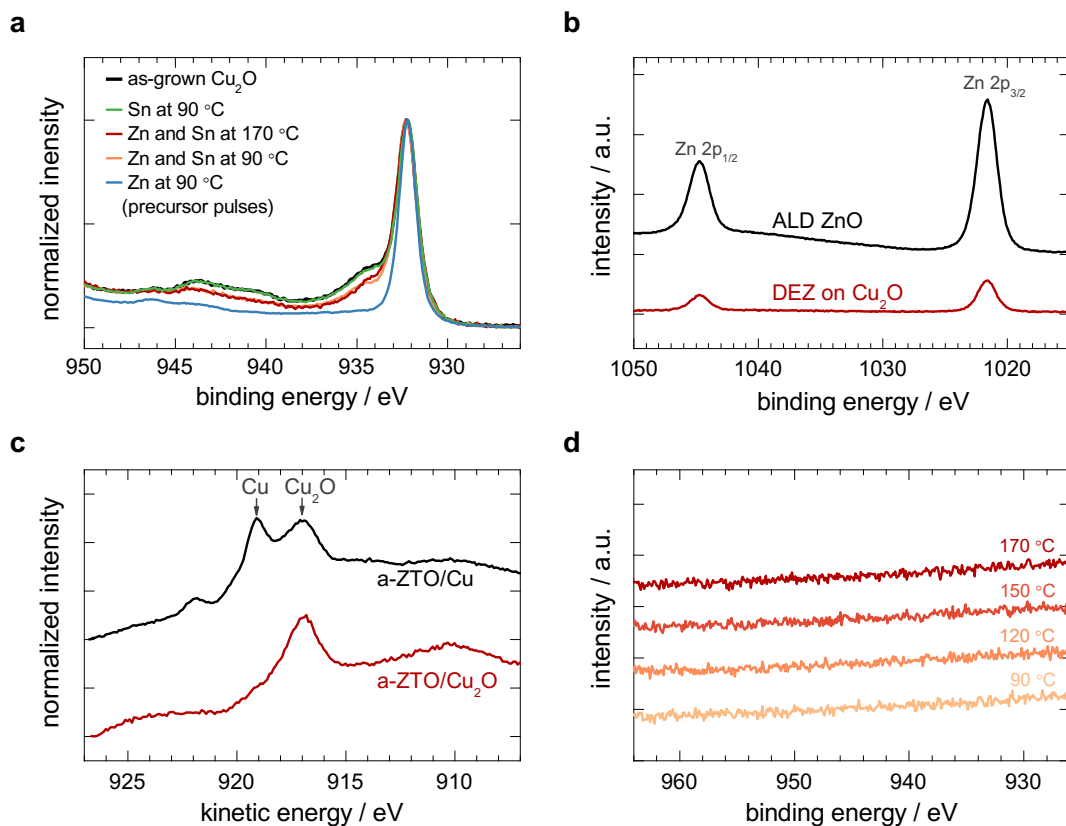


Figure 3.3. The Zn precursor in the a-ZTO ALD process is experimentally observed to reduce the oxidation state of the Cu₂O absorber's native CuO surface layer to Cu₂O. **(a)** Normalized XPS spectra of Cu-2p of Cu₂O surface after a pulse of DEZ and Sn(II) molecules on electrochemically-deposited Cu₂O films having nanometer-scale-thick CuO surface layers. **(b)** XPS spectra of Zn-2p core levels after a pulse of only DEZ molecules on the Cu₂O film at 90 °C, showing same Zn-2p core level with ZnO film grown by ALD using DEZ and H₂O₂. **(c)** The Cu-LMM kinetic energies from Cu₂O and metallic Cu after the growth of a-ZTO layer by ALD at 90 °C. (20-nm-thick Cu film was prepared by e-beam evaporation at room temperature for the comparison). **(d)** XPS spectra of Cu-2p core levels with 10-nm-thick a-ZTO films deposited on Cu₂O at reaction temperatures between 90 and 170 °C, showing no signal from elemental Cu for all temperatures, which indicates no Cu diffusion occurred.

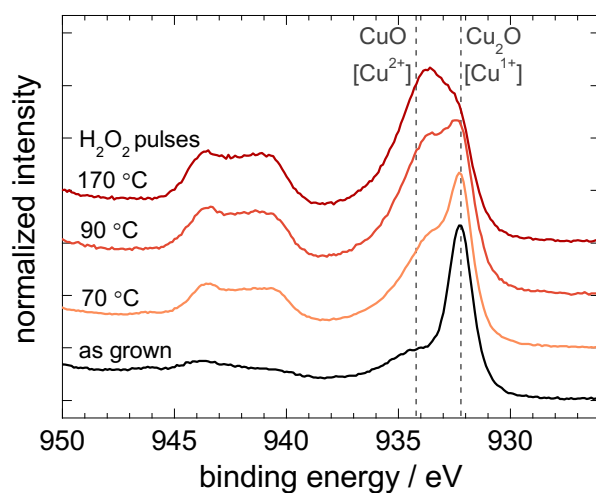


Figure 3.4. H₂O₂ exposure can re-oxidize the Cu₂O surface layer to CuO. Shown are normalized XPS spectra of Cu-2*p* for three different Cu₂O films. Only H₂O₂ pulses were injected on Cu₂O samples at reaction temperatures of 90 and 170 °C.

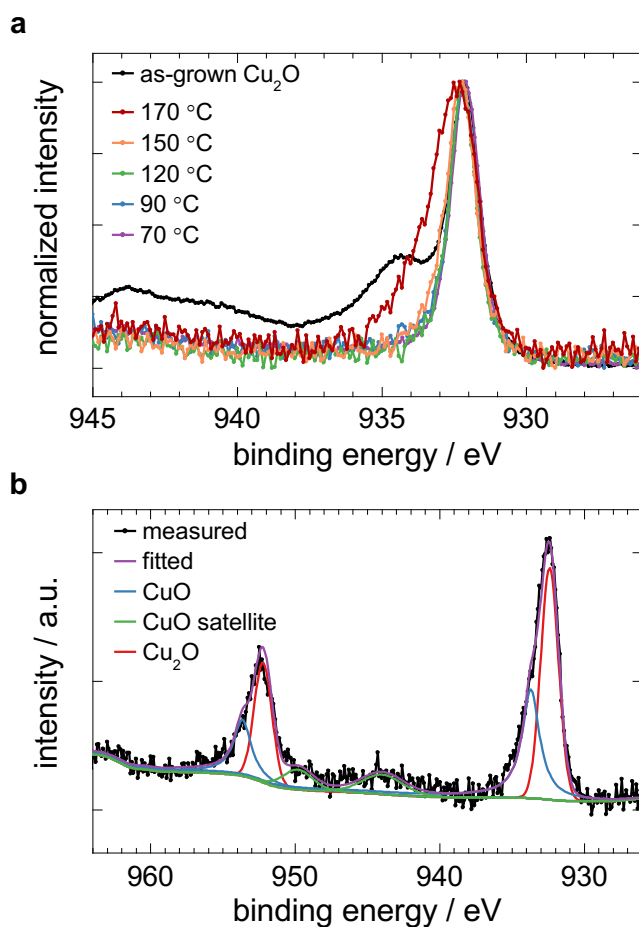


Figure 3.5. ALD reaction temperature can control the oxidation state of the Cu₂O surface layer. **(a)** Normalized XPS spectra of Cu-2*p* from the Cu₂O samples after the growth of a-ZTO films at reaction temperatures between 90 and 170 °C. **(b)** The deconvoluted XPS spectra of Cu-2*p* of Cu₂O surface with a-ZTO film grown at 170 °C, showing a peak shoulder at ~933.7 eV corresponding to the Cu²⁺ state.

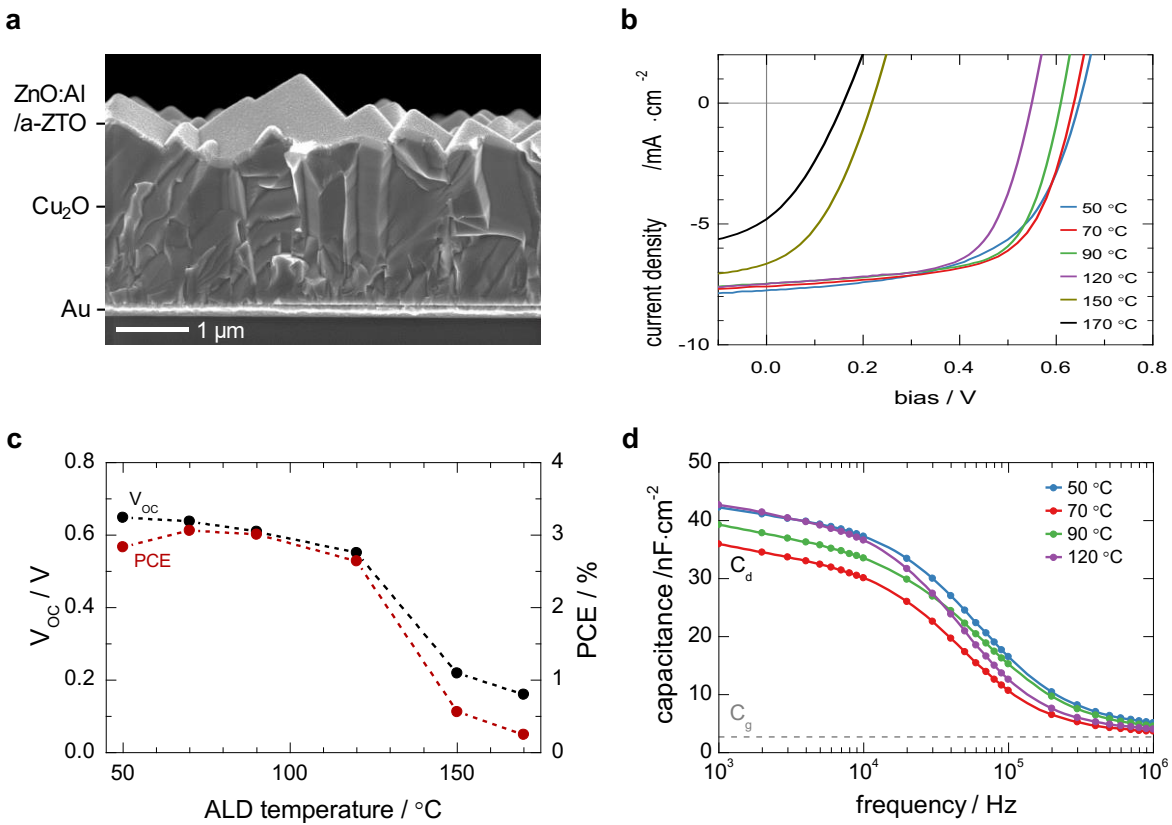


Figure 3.6. Characteristics of solar cell devices with varying Cu oxidation state at the Cu₂O/a-ZTO interface controlled by ALD temperature. (a) A cross-sectional SEM image of Cu₂O-based solar cells with the device structure (ZnO:Al / a-ZTO / Cu₂O / Au). (b) J-V characteristics of the devices under 1-sun (AM 1.5G) illuminated conditions. (c) A summary of V_{oc} and PCE of the devices as a function of the a-ZTO ALD temperature. (d) C-f characteristics of solar cell devices at room temperature with 0 mV and 10 mV for DC and AC bias, with a-ZTO films at reaction temperatures between 50 and 120 °C.

3.4.2 Impact of Cu Oxidation States on the Cu₂O-based Solar Cells

To demonstrate the effect of the interface chemistry control on solar cell performance, we fabricated Cu₂O-based solar cells with a-ZTO ALD reaction temperatures at 50 – 170 °C. **Figure 3.6a** shows a cross-sectional scanning electron microscopy (SEM) image of the device structure: ZnO:Al TCO (80 nm) / a-ZTO buffer (10 nm) / Cu₂O absorber (2.5 μm) / Au bottom electrode (200 nm). The ZnO:Al TCO layer was deposited *in situ* at 120 °C after the formation of the a-ZTO buffer layer on electrochemically-deposited Cu₂O. Here, the first ALD reaction started with the injection of DEZ as discussed. Except for the ALD temperature of the a-ZTO buffer layer growth, all processing parameters were identical for all devices. Devices with a-ZTO ALD temperatures of 150 and 170 °C showed slightly darker color than other devices, possibly due to a CuO layer formed at interface. The devices were completed by coating Al top-electrode (1 μm) and MgF₂ anti-reflective layer (95 nm).

As the analysis of ALD reactions predicted, decreasing the ALD temperature enhances the solar-cell device performance. Current-density vs. voltage (*J-V*) characteristics of the devices were measured under 1-sun (AM 1.5G, 100 mW·cm⁻²) illumination conditions as shown in **Figure 3.6b**. While the short-circuit current densities (*J_{sc}*) remain between 7 and 8 mA·cm⁻², the *V_{oc}* shows a strong dependence on the a-ZTO ALD temperature. The changes of *V_{oc}* and PCE of the devices are summarized as a function of the a-ZTO ALD temperature in **Figure 3.6c**. By decreasing the ALD temperature down to 50 °C, *V_{oc}* increases up to 0.65 V. However, the devices with ALD temperatures over 150 °C show a significant reduction of *V_{oc}* below 0.3 V. This drastic change can be explained by the increase of CuO content at higher ALD temperatures, increasing defect density at the a-ZTO/Cu₂O interface. The highest PCE of 3.06% is achieved with an a-ZTO ALD

temperature of 70 °C. The device with an ALD temperature of 50 °C shows the highest V_{OC} , but its reduced fill-factor results in a lower PCE.

The possibility of bulk Cu_2O thermal degradation was ruled out by an additional experiment. A heat treatment of a Cu_2O layer at 150 °C before a-ZTO deposition at 70 °C was performed. The heat-treated device showed performance comparable to the device made without the heat treatment (**Figure 3.8**), suggesting that the high temperature during a-ZTO deposition degrades only the heterojunction interface.

The heterojunction quality of the fabricated devices is further investigated by measuring capacitance vs. frequency ($C-f$) characteristics as shown in **Figure 3.6d**. A direct-current bias of 0 V and an alternating-current bias of 10 mV were applied at room temperature. At high frequencies near 1 MHz, all devices show capacitances converging to 3 – 5 $nF \cdot cm^{-2}$, which is close to a simple geometric capacitance ($C_g \sim 2.7 nF \cdot cm^{-2}$) due to dielectric freeze-out. At low frequencies, on the other hand, the capacitances plateau to a depletion capacitance (C_d), which is dominated by the energy levels and densities of interfacial and bulk defects in the depleted region.^[31] As the ALD temperature for a-ZTO decreases from 120 to 70 °C, the capacitance at 1 kHz decreases from 42.7 to 35.9 $nF \cdot cm^{-2}$, which suggests reduced Cu^{2+} -related defect densities at the a-ZTO/ Cu_2O interface. However, the ALD temperature of 50 °C shows a higher capacitance than that of 70 °C, possibly due to bulk defects in the a-ZTO layer. Too-low ALD reaction temperature often results in increased carbon and nitrogen-related impurities, which might be mitigated with plasma-assisted ALD.^[32, 33]

The device with the highest efficiency was characterized independently at the National Renewable Energy Laboratory (NREL). The $J-V$ characteristic of the device under the ASTM G173 global 1-sun illumination is shown in **Figure 3.7**. The device was measured on a

temperature-controlled stage, after a 10-minute light-soak at the maximum power condition (a forward bias of 0.49 V) and a 5-minute cool down. A spectral mismatch correction was applied using a normalized quantum efficiency (QE) spectrum (**Figure 3.9**) to measure accurate device performance. The device shows a PCE of 2.85%. The V_{OC} , J_{SC} , and fill-factor of the device are 622 mV, $7.25 \text{ mA}\cdot\text{cm}^{-2}$, and 63.1%, respectively. A small discrepancy from the result shown in **Figure 3.6** is observed, which could be from a spectral mismatch of the light source and a different device temperature during the measurements. The measurement at NREL is the first verified efficiency of Cu_2O -based thin-film solar cells measured independently to date.

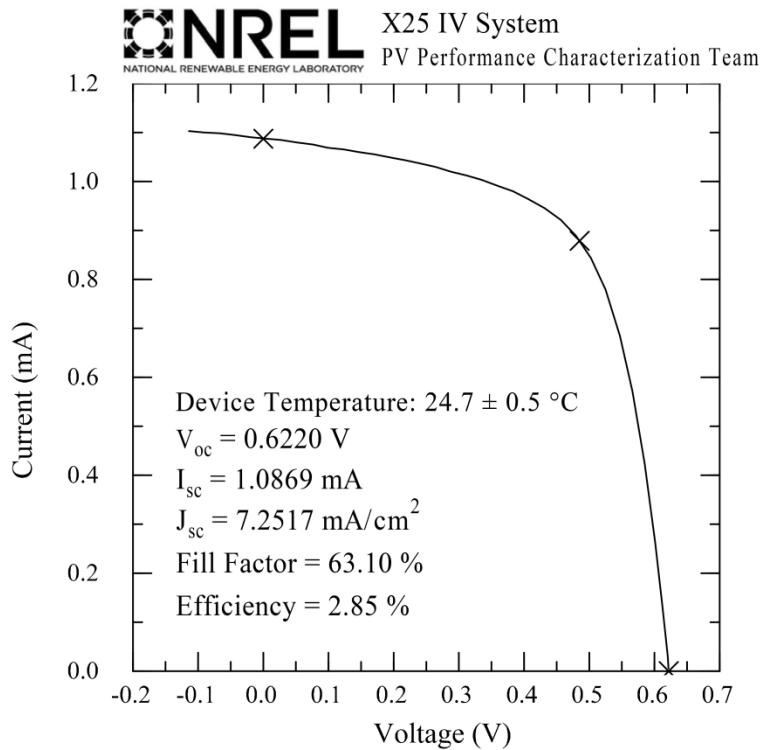


Figure 3.7. NREL certified J - V characteristics of the best device, with an a-ZTO buffer layer grown at $70 \text{ }^\circ\text{C}$, under 1-sun (ASTM G173 global) illumination.

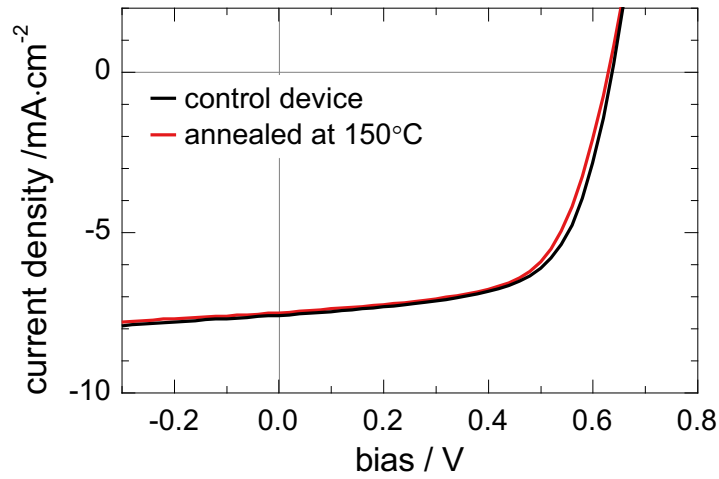


Figure 3.8. *J-V* characteristics of the devices under 1-sun (AM 1.5G) illuminated conditions with and without the additional heat treatment of Cu_2O film at 150°C for 2 hours under vacuum, before the deposition of a-ZTO buffer layer at 70°C and ZnO:Al layer at 120°C .

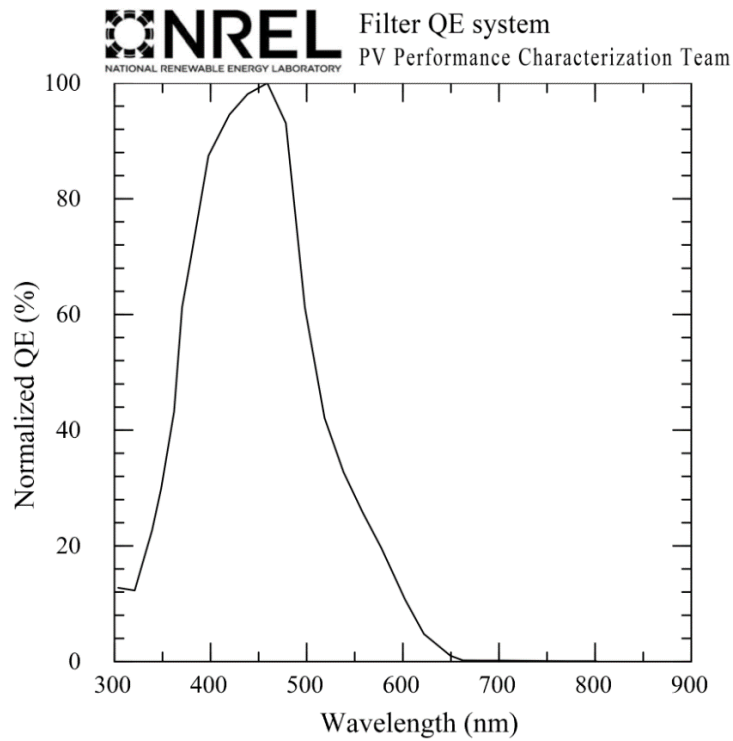


Figure 3.9. Normalized QE spectrum of the device with a-ZTO buffer layer grown at 70°C . A filtered QE system at NREL was used.

3.5 Conclusions

In summary, the presence of a deleterious CuO layer at the a-ZTO/Cu₂O interface can be minimized by optimizing the a-ZTO ALD process to reduce this layer to Cu₂O, enhancing the heterojunction open-circuit voltage. In our Cu₂O thin films grown by electrochemical deposition, a nanometer-scale thick CuO surface layer is formed by air exposure. Starting the first ALD sequence with the highly reactive DEZ pulse effectively reduces the CuO surface layer to Cu₂O by forming ZnO. As the ALD temperature is increased, re-oxidation of Cu₂O to CuO by H₂O₂ becomes a dominant reaction over the reduction of CuO by DEZ. By engineering the Cu₂O surface chemistry with the a-ZTO ALD temperature, the chemical state of Cu at the interface can be controlled and the formation of a high-quality heterojunction is demonstrated. The controlled interface chemistry increases the V_{OC} of a-ZTO/Cu₂O solar cells, resulting in an independently verified PCE of 2.85%. This approach may also be useful in other material systems that employ ALD overlayers (buffer layers and TCOs), to improve interface quality by engineering cation chemical states locally at the interface.

3.6 Reference

- [1] R. W. Birkmire, E. Eser, *Annu. Rev. Mater. Sci.* 1997, 27, 625.
- [2] W. Jaegermann, A. Klein, T. Mayer, *Adv. Mater.* 2009, 21, 4196.
- [3] B. K. Meyer, A. Polity, D. Reppin, M. Becker, P. Hering, P. J. Klar, T. Sander, C. Reindl, J. Benz, M. Eickhoff, C. Heiliger, M. Heinemann, J. Bläsing, A. Krost, S. Shokovets, C. Müller, C. Ronning, *Phys. Status Solidi B* 2012, 249, 1487.
- [4] K. P. Musselman, A. Wisnet, D. C. Iza, H. C. Hesse, C. Scheu, J. L. MacManus-Driscoll, L. Schmidt-Mende, *Adv. Mater.* 2010, 22, E254.
- [5] C. Xiang, G. M. Kimball, R. L. Grimm, B. S. Brunschwig, H. A. Atwater, N. S. Lewis, *Energy Environ. Sci.* 2011, 4, 1311.
- [6] S. Jeong, S. H. Song, K. Nagaich, S. A. Campbell, E. S. Aydil, *Thin Solid Films* 2011, 519, 6613.
- [7] A. Mittiga, E. Salza, F. Sarto, M. Tucci, R. Vasanthi, *Appl. Phys. Lett.* 2006, 88, 163502.
- [8] K. P. Musselman, A. Marin, A. Wisnet, C. Scheu, J. L. MacManus-Driscoll, L. Schmidt-Mende, *Adv. Funct. Mater.* 2011, 21, 573.
- [9] Y. S. Lee, J. Heo, S. C. Siah, J. P. Mailoa, R. E. Brandt, S. B. Kim, R. G. Gordon, T. Buonassisi, *Energy Environ. Sci.* 2013, 6, 2112.
- [10] T. Minami, Y. Nishi, T. Miyata, *Appl. Phys. Express* 2013, 6, 044101.
- [11] T. S. Gershon, A. K. Sigdel, A. T. Marin, M. F. A. M. van Hest, D. S. Ginley, R. H. Friend, J. L. MacManus-Driscoll, J. J. Berry, *Thin Solid Films* 2013, 536, 280.

- [12] M. T. Greiner, M. G. Helander, W. M. Tang, Z. B. Wang, J. Qiu, Z. H. Lu, *Nat. Mater.* 2012, *11*, 76.
- [13] F. P. Koffyberg, F. A. Benko, *J. Appl. Phys.* 1982, *53*, 1173.
- [14] S. Wilson, Y. Tolstova, H. A. Atwater, presented at the 39th IEEE Photovoltaic Specialists Conference, Tampa, June, 2013.
- [15] J.-W. Lim, J. Iijima, Y. Zhu, J. H. Yoo, G.-S. Choi, K. Mimura, M. Isshiki, *Thin Solid Films* 2008, *516*, 4040.
- [16] B. Canava, O. Roussel, J. F. Guillemoles, D. Lincot, A. Etcheberry, *Phys. Status Solidi C* 2006, *3*, 2551.
- [17] B. Canava, J. Vigneron, A. Etcheberry, J. F. Guillemoles, D. Lincot, *Appl. Surf. Sci.* 2002, *202*, 8.
- [18] Y. Nishi, T. Miyata, J.-I. Nomoto, T. Minami, *Thin Solid Films* 2012, *520*, 3819.
- [19] J. R. Bakke, K. L. Pickrahn, T. P. Brennan, S. F. Bent, *Nanoscale* 2011, *3*, 3482.
- [20] J. A. van Delft, D. Garcia-Alonso, W. M. M. Kessels, *Semicond. Sci. Technol.* 2012, *27*, 074002.
- [21] P. Poodt, A. Lankhorst, F. Roozeboom, K. Spee, D. Maas, A. Vermeer, *Adv. Mater.* 2010, *22*, 3564.
- [22] J. C. Klein, A. Proctor, D. M. Hercules, J. F. Black, *Anal. Chem.* 1983, *55*, 2055.
- [23] J. Ghijsen, L. H. Tjeng, J. van Elp, H. Eskes, J. Westerink, G. A. Sawatzky, M. T. Czyzyk, *Phys. Rev. B* 1988, *38*, 11322.

- [24] S. Poulston, P. M. Parlett, P. Stone, M. Bowker, *Surf. Interface Anal.* 1996, 24, 811.
- [25] J. Heo, S. B. Kim, R. G. Gordon, *Appl. Phys. Lett.* 2012, 101, 113507.
- [26] S. W. Lee, J. H. Han, S. K. Kim, S. Han, W. Lee, C. S. Hwang, *Chem. Mater.* 2011, 23, 976.
- [27] S. W. Lee, Y. Liu, J. Heo, R. G. Gordon, *Nano Lett.* 2012, 12, 4775.
- [28] The Gibbs free energies of reactions were calculated from the Gibbs free energy data of each chemical species from the library of HSC Chemistry software (5.11 edition, Outokumpu Research Oy: Pori, Finland, 2002).
- [29] Z. Li, R. G. Gordon, D. B. Farmer, Y. Lin, J. Vlassak, *Electrochem. Solid-State Lett.* 2005, 8, G182.
- [30] S. W. Lee, J. Heo, R. G. Gordon, *Nanoscale* 2013, 5, 8940.
- [31] T. Walter, R. Herberholz, C. Müller, H. W. Schock, *J. Appl. Phys.* 1996, 80, 4411.
- [32] J. Fan, H. Liu, Q. Kuang, B. Gao, F. Ma, Y. Hao, *Microelectron. Reliab.* 2012, 52, 1043.
- [33] S. T. Lehti, *Eur. Phys. J. D* 2013, 67, 1.
- [34] P. E. de Jongh, D. Vanmaekelbergh, J. J. Kelly, *Chem. Mater.* 1999, 11, 3512.

4 Gallium Oxide Buffer Layer for Cuprous Oxide Solar Cells

4.1 Chapter Abstract

The power conversion efficiency of solar cells based on copper (I) oxide (Cu_2O) is enhanced by atomic layer deposition of a thin gallium oxide (Ga_2O_3) layer. By improving band-alignment and passivating interface defects, the device exhibits an open-circuit voltage of 1.20 V and an efficiency of 3.97%, showing potential of over 7% efficiency.

4.2 Introduction

With the growing demand for low-cost solar cells that are truly scalable to the terawatts level, Earth-abundant and air-stable semiconductor materials are considered a promising candidate class of materials.^[1-3] Cuprous oxide (Cu_2O) is an Earth-abundant semiconductor with over 20 % single-junction theoretical maximum power conversion efficiency (PCE).^[4] In particular, its large bandgap (E_g) of ~ 2 eV is suitable for a top-cell in a tandem device with conventional silicon- or CIGS-based solar cells.^[5] Due to the intrinsic p -type conductivity of this material, creating a p - n homojunction of Cu_2O has been considered challenging.^[6, 7] Instead, the most effective approach to fabricate Cu_2O -based solar cells has been a heterojunction device architecture with an n -type transparent conducting oxide (TCO) including zinc oxide (ZnO) and indium tin oxide.^[8-11] However, the PCEs of Cu_2O -based heterojunction devices have remained low, largely due to staggered gap (type-II heterojunction) electronic band alignment with the TCO layers as well as a high density of defects at the heterojunction interface.^[8, 12] The type-II heterojunction creates an effective energy gap for interface recombination ($E_{g,\text{IF}}$) smaller than the E_g of Cu_2O , resulting in a higher interface recombination rate and a significantly reduced open-circuit voltage (V_{OC}).^[13]

To mitigate the non-ideal heterojunction, various buffer layers have been inserted between the Cu_2O and TCO layers.^[8, 9, 14] Properly controlled electronic band alignment of the buffer layer and defect density at the interface region has enhanced the device performance significantly. So far, a gallium oxide (Ga_2O_3) buffer layer grown by pulsed laser deposition technique has shown the highest PCE of 5.38 % among Cu_2O -based solar cells with a V_{OC} of 0.8 V.^[9] Ga_2O_3 is a wide-bandgap semiconductor ($E_g \approx 5$ eV) that has been studied for UV-transmitting optoelectronic applications, demonstrating surface-defect passivation properties.^[15, 16] While theoretical and experimental studies showed n -type conductivity of this material, undoped Ga_2O_3 thin-films often

behave like an insulator due to the large bandgap.^[17, 18] For solar cell applications, undoped Ga₂O₃ has been used as an insulating layer in conductor-insulator-semiconductor type solar cells and dye-sensitized solar cells.^[19-21] In those solar cell applications, the Ga₂O₃ layer was sufficiently thin (less than ~2 nm) to allow a tunneling current. In Cu₂O-based solar cells, on the other hand, a Ga₂O₃ layer up to 90 nm did not obstruct photo-current, which suggests that the electronic band of the Ga₂O₃ layer is favorably aligned with neighboring layers, Cu₂O and aluminum-doped zinc oxide (ZnO:Al).^[22]

In this communication, we demonstrate Cu₂O-based heterojunction thin-film solar cells with a higher V_{OC} by incorporating an atomic layer deposited Ga₂O₃ buffer layer. The atomic layer deposition (ALD) technique is increasingly applied for photovoltaic applications, in particular for depositing buffer layers and surface passivation layers.^[23, 24] On an electrochemically-deposited Cu₂O layer, we deposit a 10-nm-thick Ga₂O₃ buffer layer that reduces interfacial recombination by improving band-alignment across the heterojunction and reducing the interface defect density. The band-alignment of the Ga₂O₃ layer is characterized by X-ray photoelectron spectroscopy (XPS) and optical measurements. The Ga₂O₃ buffer layer shows an improved conduction-band offset relative to the Cu₂O layer, compared with that of other buffer layers reported previously. Also, the XPS measurements reveal that the ALD conditions for the buffer layer growth reduce the density of Cu²⁺-related defects at the Ga₂O₃ / Cu₂O interface. Using Ga₂O₃ buffer layers, we fabricate Cu₂O-based thin-film solar cells, demonstrating a National Renewable Energy Laboratory (NREL)-certified PCE and V_{OC} of 3.97 % and 1.20 V, respectively; a pseudo-efficiency of 7.2% was obtained by J_{SC} - V_{OC} measurements, which removes the effects of series resistance.^[25, 26] The device characteristics are further investigated by temperature-dependent current density vs.

voltage ($J-V$) and bias-dependent external quantum efficiency (EQE) measurements to elucidate the performance-loss mechanisms in these devices.

4.3 Experiments

Solar Cell Fabrication: A silicon wafer with a 0.3- μm -thick thermal oxide (SiO_2) surface layer was diced into $1 \times 1 \text{ inch}^2$ sized pieces to be used for substrates. A stack of Ti (5 nm) / Au (200 nm) / Ti (5 nm) layers was deposited by e-beam evaporation, followed by a deposition of a 2.5- μm -thick SiO_2 layer by plasma-enhanced chemical vapor deposition. To define a 3×6 cell array with a cell area of $3 \times 5 \text{ mm}^2$, the SiO_2 / Ti layers were etched selectively by photolithography and buffered-oxide-etchant (7:1, J. T. Baker), exposing the Au layer. A 2.5- μm -thick Cu_2O film was deposited on the exposed Au area by the galvanostatic electrochemical method at 40 °C, as described in detail elsewhere.^[8, 41] A 10-nm-thick Ga_2O_3 buffer layer and a 80-nm-thick ZnO:Al TCO layer were deposited by ALD on the entire area of the substrate. The ZnO:Al layer was deposited using trimethylaluminum, diethylzinc, and de-ionized water as Al, Zn, and O sources, respectively. A trimethylaluminum pulse was introduced after every set of 19 pulses of diethylzinc to reduce the sheet resistance of the ZnO:Al layer down to $\sim 1 \text{ k}\Omega\cdot\text{sq}^{-1}$. 1- μm -thick Al top-electrodes were deposited by e-beam evaporation with grid spacing of 0.5 mm defined by a lift-off process. To isolate cells, the Ga_2O_3 and ZnO:Al layers were wet-etched partially by a photolithography process. A 95-nm-thick MgF_2 film as an anti-reflective layer was deposited by thermal evaporation.

Characterization: Surface morphologies were probed by atomic force microscopy using MFP-3D SA (Asylum Research). The microstructures of the Ga_2O_3 films were characterized by XRD using a PANalytical X'Pert Pro diffractometer with Cu- $K\alpha$ radiation. Surface morphologies of the

devices were analyzed using an Ultra 55 FESEM (Zeiss). XPS measurements were performed by using a PHI VersaProbe II (Physical Electronics) and a K-alpha XPS (Thermo Scientific). The optical properties of the Ga_2O_3 films were measured by using a Lambda 950 UV-VIS-NIR spectrophotometer (PerkinElmer) equipped with an integrating sphere, and by a V-VASE32 spectroscopic ellipsometer (J. A. Woollam Co.). The J - V characteristics of the devices were measured by using a Keithley 2400 sourcemeter. The EQE of the device was measured by using a QEX7 (PV Measurements) calibrated with a NIST-certified Si photodiode.

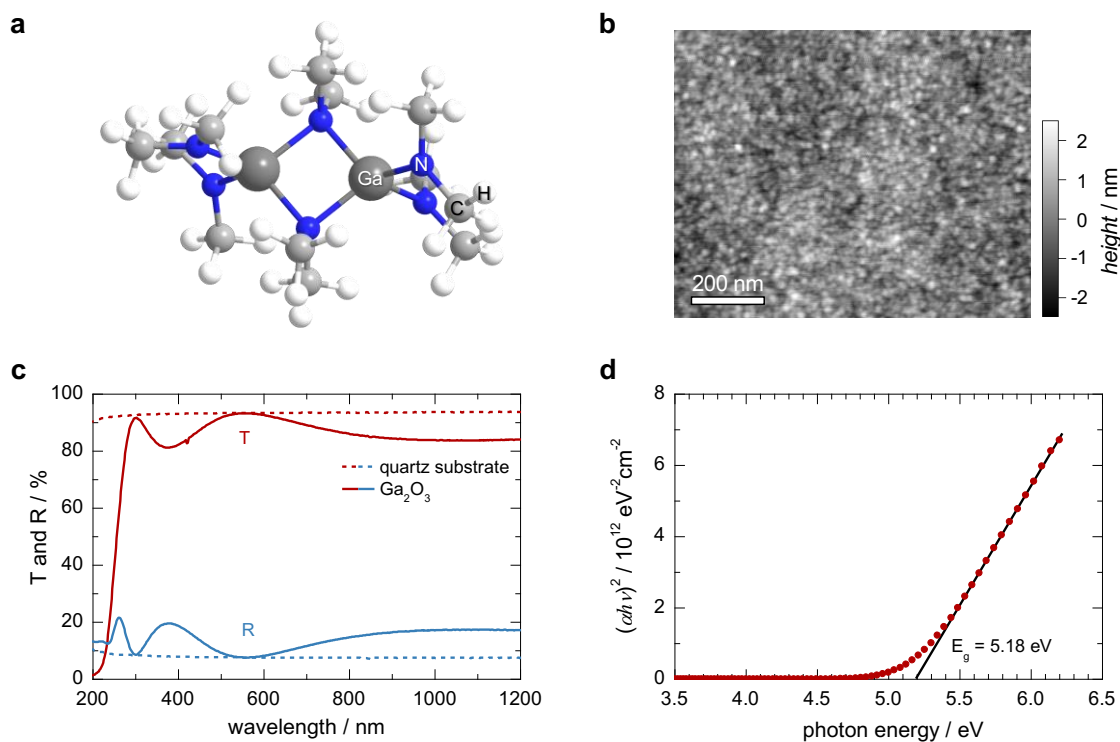


Figure 4.1. (a) The molecular structure of the ALD Ga precursor, bis(μ -dimethylamino)tetrakis(dimethylamino)digallium. (b) The surface morphology of a Ga_2O_3 film deposited on Si wafer measured by AFM. (c) The optical transmission (T) and reflection (R) spectra of a 0.2- μm -thick Ga_2O_3 film on a UV-grade quartz substrate. (d) Bandgap estimation of the ALD Ga_2O_3 film by a linear extrapolation.

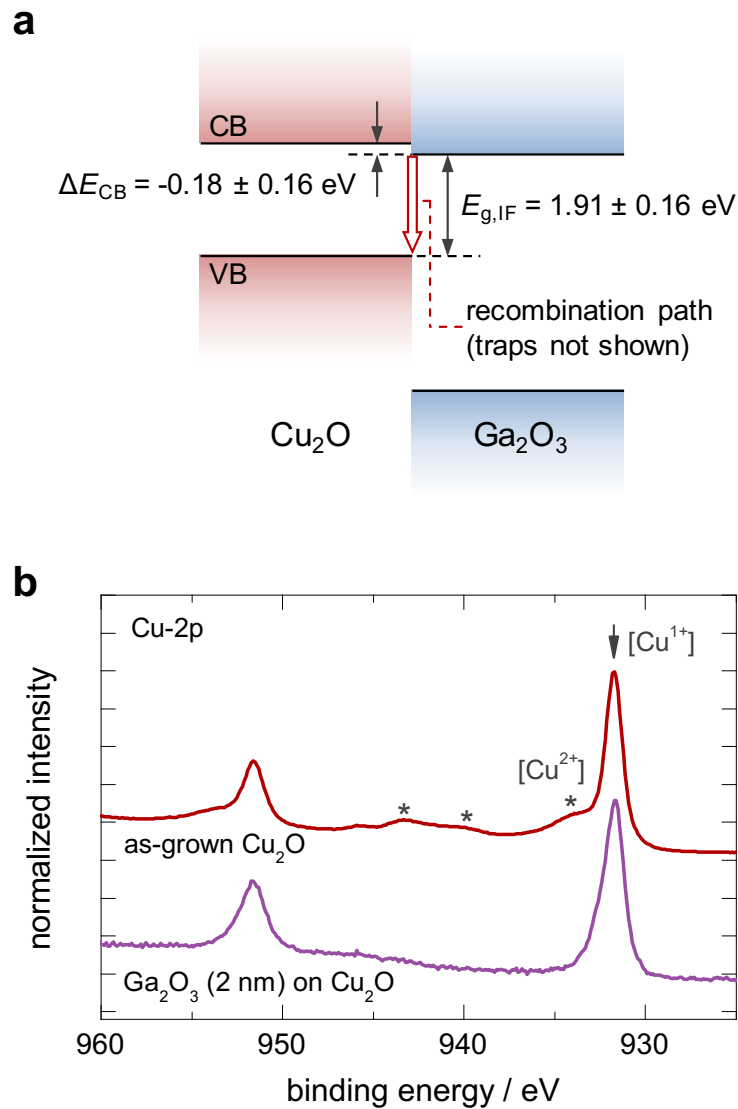


Figure 4.2. (a) The electronic band alignment of the $\text{Ga}_2\text{O}_3 / \text{Cu}_2\text{O}$ heterojunction derived from XPS and optical bandgap measurements, showing a type-II heterojunction with a ΔE_{CB} of $-0.18 \pm 0.2 \text{ eV}$. (b) The XPS spectra of the Cu-2p core level for an as-grown Cu_2O sample and a Ga_2O_3 (2 nm) / Cu_2O stack sample, which shows a reduction of the Cu^{2+} -related peaks (asterisks) by the Ga_2O_3 overlayer.

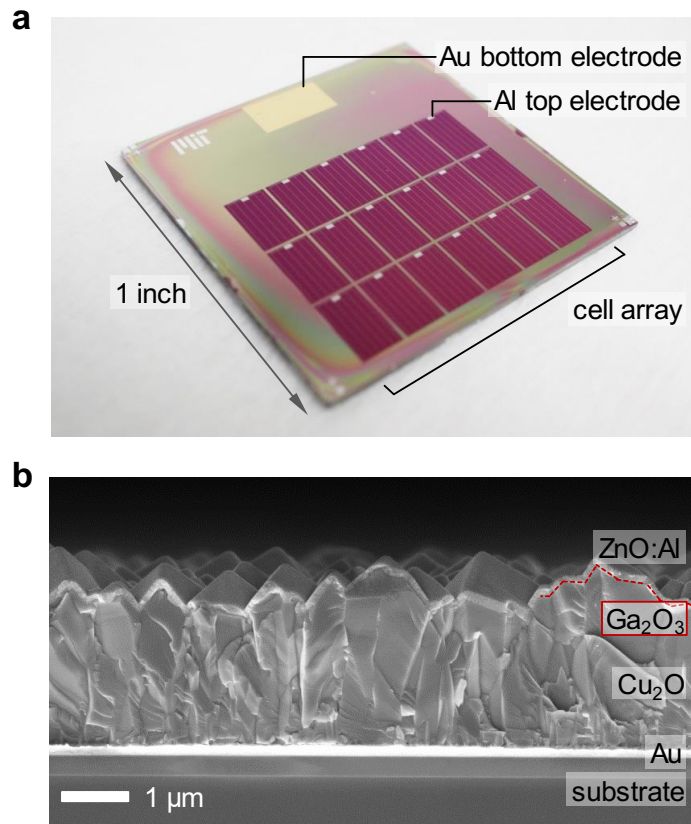


Figure 4.3. (a) A photograph of the fabricated Cu₂O-based thin-film solar cell device, showing a 3 × 6 array of fully-isolated 3 mm × 5 mm size cells. (b) A cross-sectional SEM image of the device, showing the device structure of ZnO:Al (80 nm) / Ga₂O₃ (10 nm) / Cu₂O (~2.5 μm) / Au (200 nm) on a SiO₂ (0.3 μm) / Si substrate. The red dashed line indicates the ALD Ga₂O₃ buffer layer.

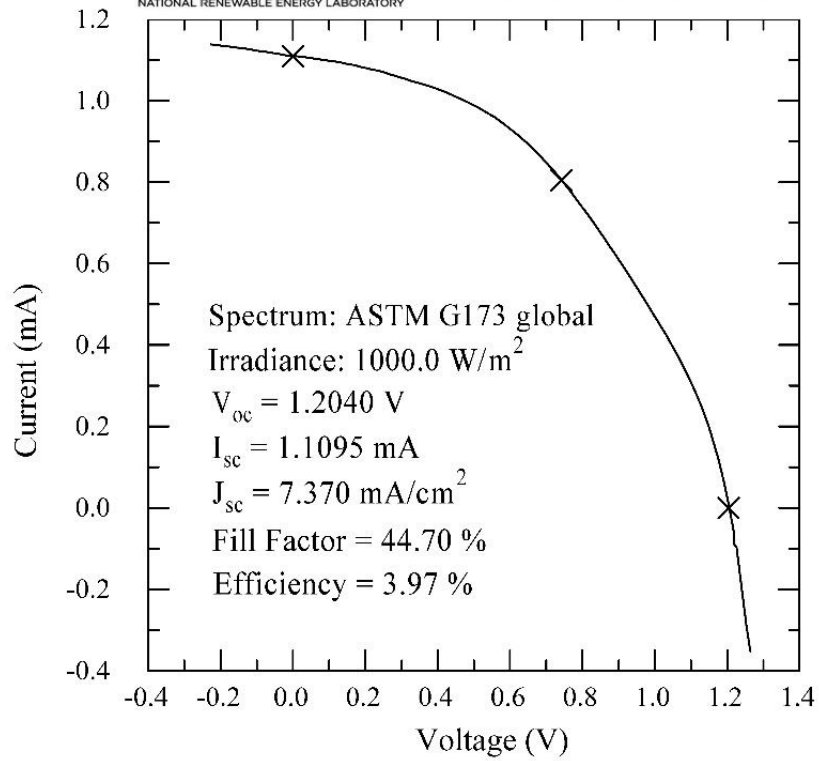


Figure 4.4. The J - V curve and photovoltaic characteristics under AM1.5 global normal spectral irradiance (ASTM G173, IEC 60904-3 edition 2 at 25 °C), measured at NREL.

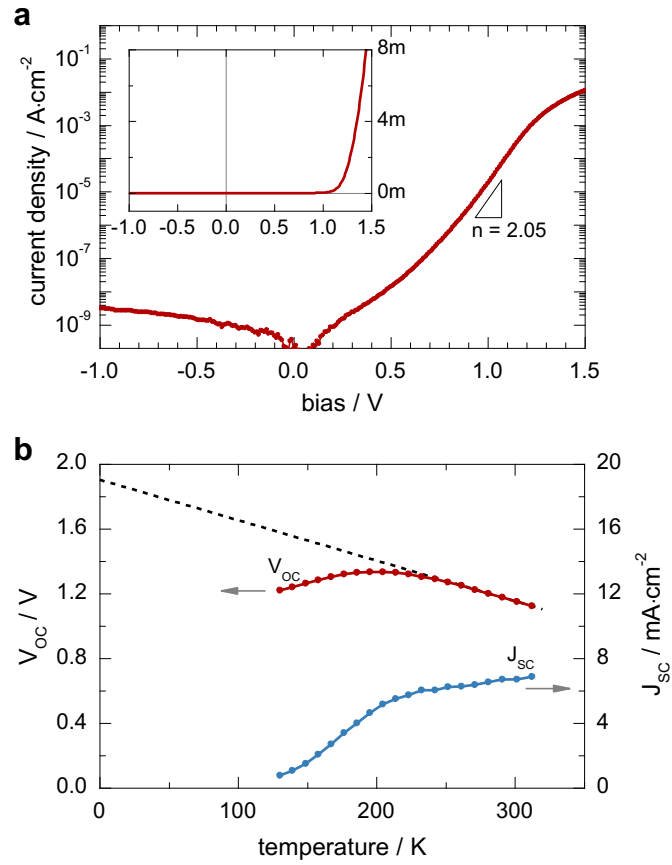


Figure 4.5. (a) J-V characteristics of the device under a dark condition in a semi-log scale and a linear scale (inset). The slope of the semi-log scale plot shows an ideality factor of ~ 2.05 near a bias condition of 1 V. (b) Temperature-dependence of the VOC and JSC of the device under a ~ 0.9 -sun illumination condition. The dotted line indicates a linear extrapolation of the VOC to a temperature of 0 K.

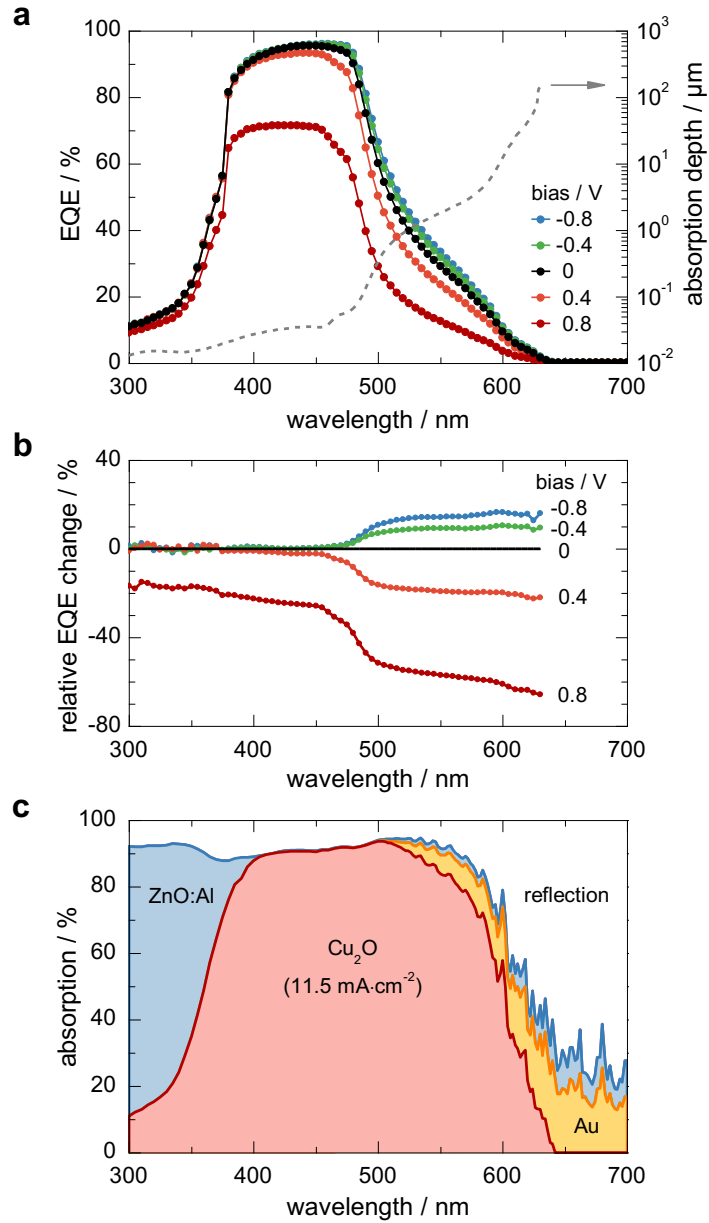


Figure 4.6. (a) The spectra of bias-dependent EQE of the device and calculated absorption depth (α^{-1}) of Cu_2O . (b) The change of EQE under various bias conditions relative to a zero bias condition. (c) Calculated optical absorption spectra of each layer in the device by the FDTD optical simulation, indicating a J_{SC} entitlement of $11.5 \text{ mA}\cdot\text{cm}^{-2}$. The simulation shows a negligible optical loss by the Ga_2O_3 layer. The achieved J_{SC} ($7.37 \text{ mA}\cdot\text{cm}^{-2}$) suggests this device is not optically limited, but instead limited by poor carrier collection.

4.4 Results and Discussion

Ga₂O₃ thin-films were deposited at 120 °C in a custom-built cylindrical ALD reactor with a sample stage 30 cm long and 3 cm wide, and a chamber volume of 0.627 L. Bis(μ-dimethylamino)tetrakis(dimethylamino)digallium (**Figure 4.1a**) and H₂O were used as a gallium precursor and an oxygen source respectively.^[27] During the ALD process of Ga₂O₃ films, the temperatures of the gallium precursor and oxygen source were maintained at 107 and 25 °C, respectively. High purity N₂ was used as a carrier gas. The exposures of the gallium precursor and H₂O were estimated to be approximately 3 and 5 Torr·s, respectively. The deposition rate was measured to be ~0.2 nm per cycle. The atomic ratio between Ga and O in the deposited film was measured by Rutherford backscattering spectrometry (RBS). **Figure 4.7** shows the RBS spectrum of a Ga₂O₃ film deposited on a glassy carbon substrate, which indicates a near stoichiometric ratio of Ga:O of 1:1.6. We investigate the microstructure of the Ga₂O₃ film using atomic force microscopy (AFM) and X-ray diffraction (XRD) measurements. The AFM image in **Figure 4.1b** shows a smooth surface morphology of a 50-nm-thick Ga₂O₃ film with a grain size range of 10 – 20 nm and a root mean square roughness value of ~0.3 nm. The XRD spectrum shown in **Figure 4.8** exhibits no specific peaks from the film, which suggests near amorphous or nano-crystalline structure of the film. The film is electrically insulating to measure the resistivity.

To estimate the optical bandgap of the Ga₂O₃ films, we measured the optical transmission and reflection spectra of Ga₂O₃ films by using a UV-VIS-IR spectrophotometer. As shown in **Figure 4.1c**, a 200-nm-thick Ga₂O₃ film deposited on a UV-grade quartz substrate showed excellent optical transmission over a wavelength range down to ~300 nm. The film's optical bandgap is estimated by a linear extrapolation using the relation of $(\alpha h \nu)^2 \propto (h \nu - E_g)$, where α , h , and ν are the optical absorption coefficient, Planck constant, and photon frequency, respectively.

The band gap of the Ga₂O₃ film was estimated to be 5.18 eV, which is slightly larger than the values (4.9 – 5.0 eV) reported previously.^[16, 28]

Using the optical bandgap, the electronic band alignment of the Ga₂O₃ relative to Cu₂O is investigated by X-ray photoelectron spectroscopy (XPS), following the procedure by Waldrop *et al.* (**Figure 4.9 and Figure 4.10**).^[29] The binding energies of Cu-2*p* and Ga-2*p* core levels ($E_{Cu-2p}^{Cu_2O}$ and $E_{Ga-2p}^{Ga_2O_3}$) with respect to valence band edge positions of Cu₂O and Ga₂O₃ bulk films ($E_{VBM}^{Cu_2O}$ and $E_{VBM}^{Ga_2O_3}$) are measured to be 932.47 ± 0.04 and 1114.46 ± 0.15 eV, respectively.^[8] We also prepared a stack sample which consists of a ~1-nm-thick Ga₂O₃ layer grown by ALD on an electrochemically deposited ~2.5- μ m-thick Cu₂O film grown following the procedure described in previous studies.^[8, 30] The Ga₂O₃ over-layer is sufficiently thin to measure the binding energies of Cu and Ga core levels simultaneously from the sample. The relative energy difference of 185.26 eV between the two core levels ($E_{Cu-2p}^{Ga_2O_3/Cu_2O} - E_{Ga-2p}^{Ga_2O_3/Cu_2O}$) were used to calculate the conduction band offset in the Ga₂O₃ / Cu₂O stack sample (ΔE_{CB}) by the relation

$$\Delta E_{CB} = \left(E_{Cu-2p}^{Ga_2O_3/Cu_2O} - E_{Ga-2p}^{Ga_2O_3/Cu_2O} \right) + \left(E_{Ga-2p}^{Ga_2O_3} - E_{VBM}^{Ga_2O_3} \right) - \left(E_{Cu-2p}^{Cu_2O} - E_{VBM}^{Cu_2O} \right) - \left(E_g^{Ga_2O_3} - E_g^{Cu_2O} \right), \quad (1)$$

where $E_g^{Ga_2O_3}$ and $E_g^{Cu_2O}$ are the bandgap of the bulk Ga₂O₃ (5.18 eV) and Cu₂O (2.09 eV), respectively.^[31] The ΔE_{CB} is determined to be -0.18 ± 0.16 eV (cliff) with a valence band offset of -3.27 ± 0.16 eV, indicating a type-II heterojunction where the interface recombination takes place between holes from Cu₂O and electrons from Ga₂O₃. As depicted in **Figure 4.2a**, the effective energy gap for interface recombination ($E_{g,IF}$) in the heterojunction is 1.91 ± 0.16 eV which is the energy level difference between the valence band edge of Cu₂O and the conduction band edge of Ga₂O₃.^[13]

In addition, the chemical state of Cu at the interface is identified by XPS to investigate the defect density at the Ga₂O₃ / Cu₂O interface. The Cu²⁺-related state at the interface has been considered to create deleterious traps that promote interface recombination.^[30, 32] **Figure 4.2b** shows the XPS spectra of the Cu-2*p* core levels of the Ga₂O₃ / Cu₂O stack sample and an as-grown Cu₂O bulk sample. The bulk Cu₂O sample shows two main peaks at 932.3 and 952 eV corresponding to the 2*p*_{1/2} and 2*p*_{3/2} levels of Cu¹⁺ state (Cu₂O). A shoulder peak at 934.0 eV and broad satellite peaks at the 940 – 945 eV region can be also observed, both of which were attributed to the presence of the Cu²⁺ state (CuO) on the surface.^[33] A ~1 nm CuO surface layer is normally formed by an air exposure after electrochemical deposition of Cu₂O. On the other hand, the Ga₂O₃ / Cu₂O stack sample does not show the shoulder peak and satellite peaks from CuO, but two peaks of Cu¹⁺ only. Similar reduction behavior of CuO to Cu₂O by diethylzinc as a Zn ALD precursor has been reported previously, which reduced the density of Cu²⁺-related defect at interface and improved the device performance.^[30] The change of Cu-2*p* spectra suggests that the gallium precursor passivates the Cu²⁺-related interface defect effectively during the Ga₂O₃ ALD process, by reducing the CuO surface layer to Cu₂O.

To demonstrate the effect of the Ga₂O₃ buffer layer on Cu₂O-based solar cell performance, we fabricated Cu₂O-based thin-film solar cells by incorporating a 10-nm-thick Ga₂O₃ layer.

Figure 4.3 shows a cross-sectional scanning electron microscopy (SEM) image and a schematic structure of the device: ZnO:Al *n*-type TCO (thickness: 80 nm) / Ga₂O₃ buffer (10 nm) / Cu₂O *p*-type absorber (2.5 μm) / Au bottom electrode (200 nm). Due to the (111)-preferred growth orientation of polycrystalline Cu₂O thin-films by the electrochemical deposition condition, the morphology of the Cu₂O layer shows a rough surface texture that reduces optical reflection. The ZnO:Al and Ga₂O₃ layers were deposited conformally on the rough surface of Cu₂O by ALD at 120 °C. The same ALD chamber was used, without breaking vacuum, to create a clean interface

between ZnO:Al and Ga₂O₃. The devices were completed by depositing an Al top-electrode grid (1 μm) and a MgF₂ anti-reflective layer (95 nm). The optimal thickness of the MgF₂ layer was determined by optical simulation using a finite-difference time-domain (FDTD) optical simulation using the FDTD Solutions software (Lumerical Solutions, Inc.) to enhance optical absorption of the device.

The photovoltaic performance of a device was characterized independently at the NREL. The J - V characteristic of the device under 1-Sun AM1.5 global normal spectral irradiance (ASTM G173, IEC 60904-3 edition 2 at 25 °C) is shown in **Figure 4.4**. The device was placed on a temperature-controlled stage to maintain the device temperature at 24.6 ± 0.5 °C. A spectral mismatch correction was also applied using an EQE spectrum with a light bias of 0.4 mA by a white light-emitting-diode to measure accurate device performance, as shown in **Figure 4.11**. The device exhibits a PCE of 3.97%. The V_{OC} , the short circuit current density (J_{SC}), and fill-factor (FF) of the device are 1.20 V, $7.37 \text{ mA} \cdot \text{cm}^{-2}$, and 44.7%, respectively. The low FF originates from the high series-resistance of the device and reduced photo-generated carrier collection efficiency at increased forward bias condition. Since the TCO and electrodes are designed to have a series resistance smaller than $0.7 \Omega \cdot \text{cm}^2$, the resistance from Cu₂O and Ga₂O₃ layers could be a major contribution to the series resistance of the device. An implied J - V curve is characterized by J_{SC} - V_{OC} measurements under a steady-state illumination, as shown in **Figure 4.12**. The implied J - V curve indicates that the FF can be improved up to 84% if the non-idealities are eliminated, which would yield a device with a pseudo-PCE of 7.2%.^[25, 26] The V_{OC} in this study represents a significant improvement over previously reported state-of-the-art Cu₂O-based devices, including the Cu₂O / GaN ($V_{OC} = 0.85$ V) and Cu₂O / CH₃CN liquid junction (0.82 V) devices as well as the device with a Ga₂O₃ buffer layer grown by pulsed laser deposition (0.8 V).^[4, 9, 34] This

breakthrough is made possible by improved band-alignment and reduced interface-defects by the ALD-Ga₂O₃ layer. However, the measured V_{OC} is still lower than the expected limit (~ 1.7 V) proposed by King *et al.*, which can be attained when only radiative recombination occurs in Cu₂O.^[35]

To investigate the dominant recombination process in the device, J - V characteristics of the device were also measured under a dark condition. **Figure 4.5a** shows a semi-log scale and linear scale plot of J - V of a 3×5 mm² size device at room temperature. The J - V plot shows a rectifying curve that can be modeled by using the Shockley's diode equation

$$J = J_0 \left(\exp\left(\frac{qV}{nkT}\right) - 1 \right), \quad (2)$$

where J_0 , q , n , k , and T are the saturation current density, electron charge, diode ideality factor, Boltzmann constant, and temperature of the device. Since the J - V characteristics near zero bias and high forward-bias regions are affected by a shunt resistance and a series resistance, respectively, we fit the measured J - V curve near 1.0 V bias to **Equation 2**. The fitted parameters of J_0 and n are estimated to be 1.8×10^{-13} A·cm⁻² and 2.05, respectively. The ideality factor near 2 indicates that Shockley-Read-Hall (SRH) recombination occurs primarily in the space charge region (SCR). In the case that J_0 is driven by SRH recombination in the SCR of the Cu₂O layer only, the associated ideal J_0 is expected to be on the order of $10^{-17} - 10^{-18}$ A·cm⁻² for Cu₂O by the relation $J_0 \approx \exp(-E_g/2kT)$.^[36] If the dominating SRH recombination is assumed to occur at the Cu₂O / Ga₂O₃ interface, the relation provides a range of J_0 in the order of $10^{-15} - 10^{-18}$ A·cm⁻² by using the $E_{g,IF}$ of 1.91 ± 0.16 eV. The fitted J_0 being higher than the ideal values suggests that an additional pre-factor (J_{00}) should be involved in the description of J_0 to explain the recombination

in the poly-crystalline and non-epitaxial heterojunction device, which typically contains a high density of interface defects.

The origin of recombination in the device is further analyzed by a temperature-dependent J - V measurement under an illuminated condition. The device was placed in the cryostat under vacuum, illuminated with a solar simulator and a set of neutral density filters to achieve ~ 0.9 -sun light intensity. To determine the activation energy (E_A) of J_0 , we plot V_{OC} and J_{SC} as a function of device temperature from 130 to 312 K, as shown in **Figure 4.5b**. The temperature-dependence of V_{OC} can be modeled as

$$V_{OC} = \frac{E_A}{q} - \frac{nkT}{q} \ln \left(\frac{J_{00}}{J_{SC}} \right), \quad (3)$$

where J_{00} is the temperature-independent pre-factor of J_0 in the relation of $J_0 = J_{00} \exp(-E_A/nkT)$.^[37] If the n , J_{SC} , and J_{00} are independent of T , an extrapolation of V_{OC} to $T = 0$ K indicates the E_A of the J_0 . Due to a high carrier-activation energy (0.16 – 0.42 eV) of Cu_2O , a significant carrier freeze-out occurs in the Cu_2O layer as temperature decreases, resulting in a higher resistance.^[38] In the low-temperature regime, the photovoltaic performance is reduced significantly, possibly because the device becomes highly resistive. The linear portion of V_{OC} at a temperature range between 270 and 312 K is used for the extrapolation. The extrapolated E_A is approximately 1.9 eV, which is consistent with the $E_{g,IF}$ measured by the XPS and optical bandgap. The estimated E_A suggests that the dominating recombination in the devices occurs at the $\text{Cu}_2\text{O} / \text{Ga}_2\text{O}_3$ interface. The fitted value of J_0 being higher than the ideal case can be attributed largely to the J_{00} , which can be a measure of the heterojunction interface quality.^[13] To further enhance the V_{OC} of the $\text{Cu}_2\text{O} / \text{Ga}_2\text{O}_3$ devices, a lower J_{00} and a higher J_{SC} are desired, which can be achieved

by reducing the density of interface recombination centers and enhancing the collection efficiency of photo-generated carriers, respectively.

The collection efficiency of photo-generated carriers by the device is investigated by bias-dependent EQE measurements. **Figure 4.6a** shows EQE spectra of the device in the wavelength range between 300 and 700 nm under various bias conditions (-0.8, -0.4, 0, 0.4, and 0.8 V) and the absorption depth (α^{-1}) calculated from the α of Cu_2O .^[31] At zero bias, the spectrum shows EQE higher than 90% over a wavelength range between 390 and 480 nm. On the other hand, the EQE drops significantly for the long wavelength range (> 480 nm) where the photons are absorbed far from the heterojunction interface. The low EQE in the long wavelength range originates from the limited drift- and diffusion-lengths of photo-generated carriers of electrochemically deposited Cu_2O thin films.^[8, 39, 40] **Figure 4.6b** shows the change of EQE under biased conditions relative to the zero-bias condition. The change of the EQE occurs predominantly in the long wavelength range, which indicates that the photo-generated carrier collection relies considerably on a drift in the depletion region. At a forward bias of 0.8 V which is near the maximum power condition, the decreased drift length as well as the series resistance reduce the EQE significantly. Compared to the short-circuit condition, forward bias reduces the electric field assisting carrier drift due to the flatter band bending near the junction. **Figure 4.6c** shows the simulated optical absorption spectra of each layer in the device, calculated by the FDTD optical simulation. The simulated absorption spectrum of the Cu_2O layer shows a J_{SC} entitlement of $11.5 \text{ mA}\cdot\text{cm}^{-2}$ with the current device geometry, compared to a theoretical entitlement of $\sim 15 \text{ mA}\cdot\text{cm}^{-2}$.^[11] The bias-dependent EQE and the simulated optical absorption spectrum of Cu_2O suggest that the FF and J_{SC} of the device can be further enhanced by improving the minority carrier diffusion length in Cu_2O .

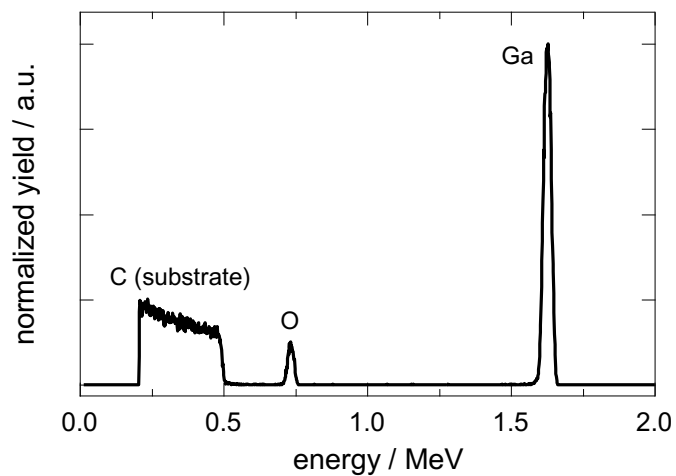


Figure 4.7. The RBS spectrum of a 200-nm-thick Ga_2O_3 film deposited on a glassy carbon substrate. The atomic ratio of Ga:O is measured to be 1:1.6.

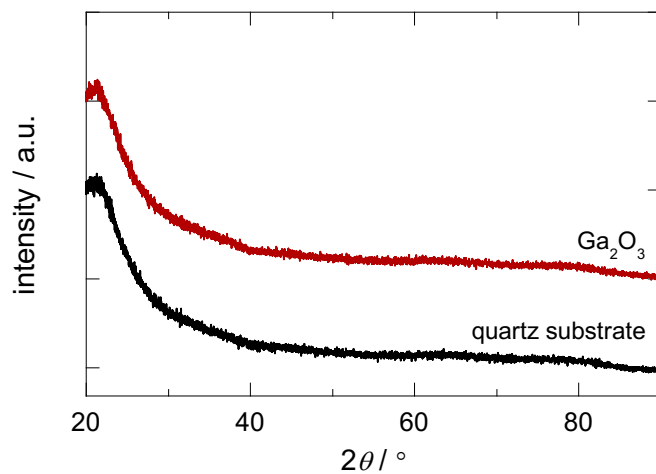


Figure 4.8. XRD spectra ($\theta - 2\theta$ scan) of a blank quartz substrate and 200-nm-thick Ga_2O_3 film deposited on a quartz substrate.

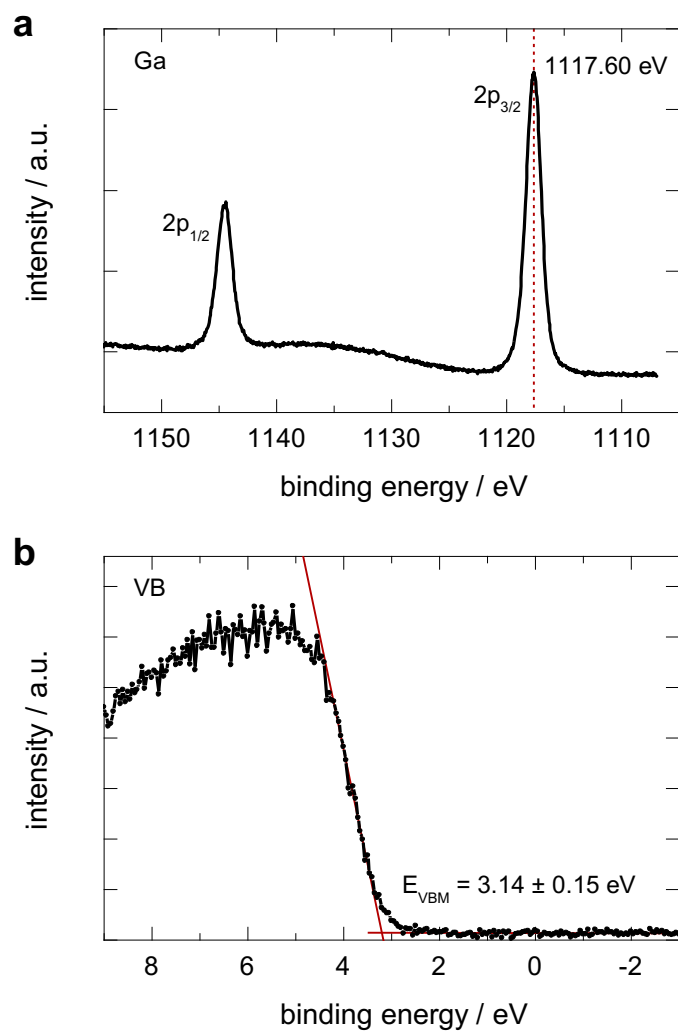


Figure 4.9. XPS spectra of Ga₂O₃ thin-film for (a) Ga-2p core level (b) valence band. The positions of the Ga-2p_{3/2} peak and the valence band edge are measured to be 1117.60 eV and 3.14 ± 0.15 eV, respectively.

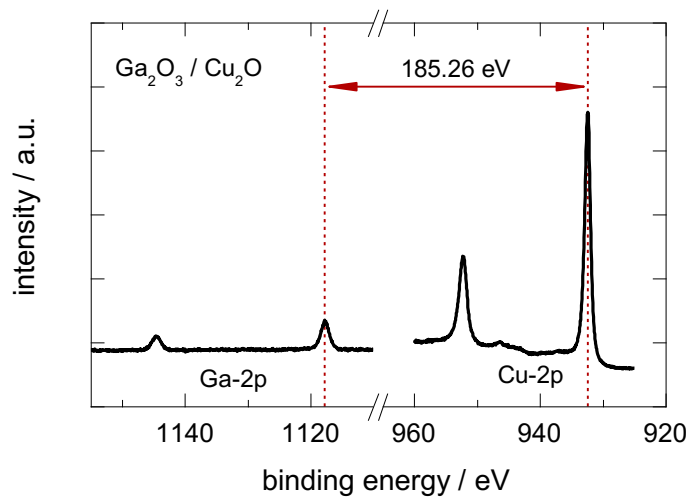


Figure 4.10. XPS spectra of Ga-2*p* and Cu-2*p* core levels of the Ga₂O₃ (1 nm) / Cu₂O stack sample. The energy level difference between the peaks of Ga-2*p*_{3/2} and Cu-2*p*_{3/2} is measured to be 185.26 eV.

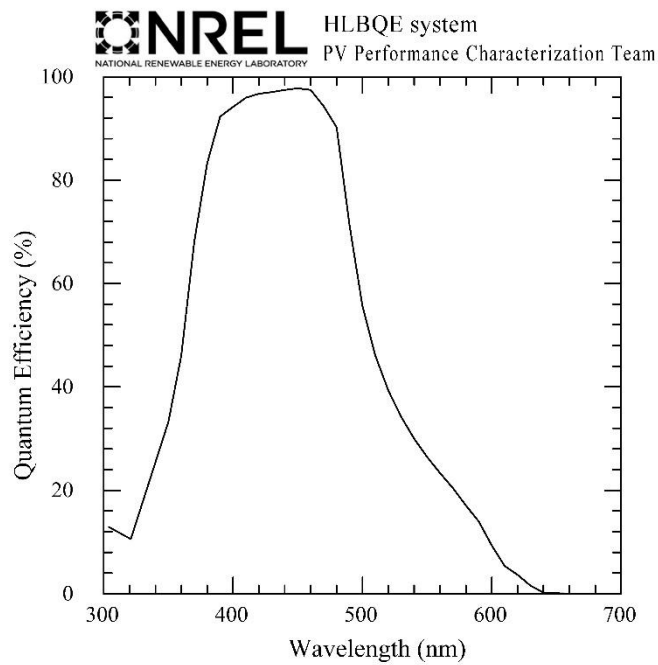


Figure 4.11. An EQE spectrum of the device, under a zero voltage bias and a light bias of 0.4 mA into the 0.15-cm²-size cell area. A white light-emitting-diode is used to enhance bias light intensity and a bias current.

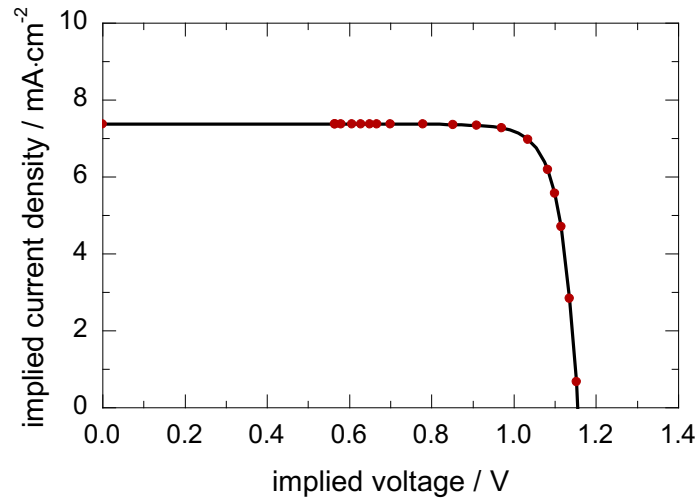


Figure 4.12. An implied photovoltaic $J_{\text{imp}}-V_{\text{imp}}$ curve determined from $J_{\text{SC}}-V_{\text{OC}}$ measurements using a steady-state illumination, exhibiting a pseudo-PCE of 7.2% and a pseudo-FF of 84%. A solar simulator with a set of neutral density filters were used to produce various illumination intensities (n -sun). The V_{OC} at n -sun and J_{SC} at n -sun under the various illumination conditions were measured. The J_{imp} and V_{imp} were obtained by the relations of $J_{\text{imp}} = J_{\text{SC at 1-sun}} - J_{\text{SC at } n\text{-sun}}$ and $V_{\text{imp}} = V_{\text{OC at } n\text{-sun}}$.

4.5 Conclusions

In conclusion, we have successfully demonstrated that atomic layer deposited Ga₂O₃ is a highly suitable buffer layer for enhancing the PCE and V_{OC} of Cu₂O-based solar cells. Pairing Cu₂O with a 10-nm-thick Ga₂O₃ layer provides a near ideal conduction band offset, reducing interface recombination. The gallium ALD precursor provides an effective reduction of Cu²⁺-related defects at heterojunction interface as well as a highly conformal deposition of the buffer layer on the rough Cu₂O surface. NREL certified the PCE of a device with a Ga₂O₃ buffer layer to be 3.97% with a V_{OC} of 1.20 V at a temperature of 24.6 ± 0.5 °C. The temperature-dependent J - V characteristics of the device indicate that the dominant recombination process occurs near the Ga₂O₃ / Cu₂O interface. The EQE spectra also show that the device performance is still limited significantly by inefficient photo-generated carrier collection in addition to the high series resistance; enhancement of carrier collection length and complete removal of series resistance are estimated to enable device efficiencies approaching 11.5% ($V_{OC} = 1.20$ V, $J_{SC} = 11.5$ mA·cm⁻², and FF = 84%).

4.6 Reference

- [1] A. Shah, P. Torres, R. Tscharnner, N. Wyrsh, H. Keppner, *Science* **1999**, *285*, 692.
- [2] C. Wadia, A. P. Alivisatos, D. M. Kammen, *Environ. Sci. Technol.* **2009**, *43*, 2072.
- [3] S. Rühle, A. Y. Anderson, H.-N. Barad, B. Kupfer, Y. Bouhadana, E. Rosh-Hodesh, A. Zaban, *J. Phys. Chem. Lett.* **2012**, *3*, 3755.
- [4] B. K. Meyer, A. Polity, D. Reppin, M. Becker, P. Hering, P. J. Klar, T. Sander, C. Reindl, J. Benz, M. Eickhoff, C. Heiliger, M. Heinemann, J. Bläsing, A. Krost, S. Shokovets, C. Müller, C. Ronning, *Phys. Status Solidi B* **2012**, *249*, 1487.
- [5] Z. M. Beiley, M. D. McGehee, *Energy Environ. Sci.* **2012**, *5*, 9173.
- [6] J. Robertson, S. J. Clark, *Phys. Rev. B* **2011**, *83*, 075205.
- [7] D. O. Scanlon, G. W. Watson, *J. Phys. Chem. Lett.* **2010**, *1*, 2582.
- [8] Y. S. Lee, J. Heo, S. C. Siah, J. P. Mailoa, R. E. Brandt, S. B. Kim, R. G. Gordon, T. Buonassisi, *Energy Environ. Sci.* **2013**, *6*, 2112.
- [9] T. Minami, Y. Nishi, T. Miyata, *Appl. Phys. Express* **2013**, *6*, 044101.
- [10] A. Mittiga, E. Salza, F. Sarto, M. Tucci, R. Vasanthi, *Appl. Phys. Lett.* **2006**, *88*, 163502.
- [11] K. P. Musselman, A. Wisnet, D. C. Iza, H. C. Hesse, C. Scheu, J. L. MacManus-Driscoll, L. Schmidt-Mende, *Adv. Mater.* **2010**, *22*, E254.
- [12] K. P. Musselman, A. Marin, A. Wisnet, C. Scheu, J. L. MacManus-Driscoll, L. Schmidt-Mende, *Adv. Funct. Mater.* **2011**, *21*, 573.

- [13] R. Scheer, *J. Appl. Phys.* **2009**, *105*, 104505.
- [14] Z. Duan, A. Du Pasquier, Y. Lu, Y. Xu, E. Garfunkel, *Sol. Energy Mater. Sol. Cells* **2012**, *96*, 292.
- [15] C. A. Lin, H. C. Chiu, T. H. Chiang, T. D. Lin, Y. H. Chang, W. H. Chang, Y. C. Chang, W.-E. Wang, J. Dekoster, T. Y. Hoffmann, M. Hong, J. Kwo, *Appl. Phys. Lett.* **2011**, *98*, 062108.
- [16] M. Orita, H. Ohta, M. Hirano, H. Hosono, *Appl. Phys. Lett.* **2000**, *77*, 4166.
- [17] N. Ueda, H. Hosono, R. Waseda, H. Kawazoe, *Appl. Phys. Lett.* **1997**, *70*, 3561.
- [18] J. B. Varley, J. R. Weber, A. Janotti, C. G. Van de Walle, *Appl. Phys. Lett.* **2010**, *97*, 142106.
- [19] A. K. Chandiran, M. K. Nazeeruddin, M. Grätzel, *Adv. Funct. Mater.*, DOI:10.1002/adfm.201302352.
- [20] A. K. Chandiran, N. Tetreault, R. Humphry-Baker, F. Kessler, E. Baranoff, C. Yi, M. K. Nazeeruddin, M. Grätzel, *Nano Lett.* **2012**, *12*, 3941.
- [21] R. Singh, M. A. Green, K. Rajkanan, *Sol. Cells* **1981**, *3*, 95.
- [22] T. Minami, Y. Nishi, T. Miyata, *Thin Solid Films* **2013**, *549*, 65.
- [23] J. R. Bakke, K. L. Pickrahn, T. P. Brennan, S. F. Bent, *Nanoscale* **2011**, *3*, 3482.
- [24] R. Yang, T. Buonassisi, K. K. Gleason, *Adv. Mater.* **2013**, *25*, 2078.
- [25] M. J. Kerr, A. Cuevas, R. A. Sinton, *J. Appl. Phys.* **2002**, *91*, 399.
- [26] M. Wolf, H. Rauschenbach, *Adv. Energy Convers.* **1963**, *3*, 455.

- [27] C. L. Dezelah IV, J. Niinistö, K. Arstila, L. Niinistö, C. H. Winter, *Chem. Mater.* **2006**, *18*, 471.
- [28] D. J. Comstock, J. W. Elam, *Chem. Mater.* **2012**, *24*, 4011.
- [29] J. R. Waldrop, R. W. Grant, *Appl. Phys. Lett.* **1996**, *68*, 2879.
- [30] S. W. Lee, Y. S. Lee, J. Heo, S. C. Siah, D. Chua, R. E. Brandt, S. B. Kim, J. P. Mailoa, T. Buonassisi, R. G. Gordon, *Adv. Energy Mater.*, DOI: 10.1002/aenm. 201301916.
- [31] C. Malerba, F. Biccari, C. Leonor Azanza Ricardo, M. D’Incau, P. Scardi, A. Mittiga, *Sol. Energy Mater. Sol. Cells* **2011**, *95*, 2848.
- [32] S. S. Wilson, Y. Tolstova, H. A. Atwater, *IEEE Photovoltaic Spec. Conf.*, 39th, DOI: 10.1109/PVSC.2013.6744960.
- [33] J. Ghijsen, L. H. Tjeng, J. Vanelp, H. Eskes, J. Westerink, G. A. Sawatzky, M. T. Czyzyk, *Phys. Rev. B* **1988**, *38*, 11322.
- [34] C. Xiang, G. M. Kimball, R. L. Grimm, B. S. Brunschwig, H. A. Atwater, N. S. Lewis, *Energy Environ. Sci.* **2011**, *4*, 1311.
- [35] R. R. King, D. Bhusari, A. Boca, D. Larrabee, X. Q. Liu, W. Hong, C. M. Fetzer, D. C. Law, N. H. Karam, *Prog. Photovoltaics* **2011**, *19*, 797.
- [36] L. C. Olsen, F. W. Addis, W. Miller, *Sol. Cells* **1982**, *7*, 247.
- [37] M. Turcu, O. Pakma, U. Rau, *Appl. Phys. Lett.* **2002**, *80*, 2598.
- [38] Y. S. Lee, M. T. Winkler, S. C. Siah, R. Brandt, T. Buonassisi, *Appl. Phys. Lett.* **2011**, *98*, 192115.

- [39] Y. Liu, H. K. Turley, J. R. Tumbleston, E. T. Samulski, R. Lopez, *Appl. Phys. Lett.* **2011**, *98*, 162105.
- [40] K. P. Musselman, Y. Ievskaya, J. L. MacManus-Driscoll, *Appl. Phys. Lett.* **2012**, *101*, 253503.
- [41] Y. S. Lee, J. Heo, M. T. Winkler, S. C. Siah, S. B. Kim, R. G. Gordon, T. Buonassisi, *J. Mater. Chem. A* **2013**, *1*, 15416.

5 Enhancement of the Open Circuit Voltages in $\text{Cu}_2\text{O}/\text{Ga}_2\text{O}_3$ Heterojunction Solar Cells through the Mitigation of Interfacial Recombination

5.1 Chapter Abstract

Thin film solar cells are fabricated using chemical vapor deposition of cuprous oxide (Cu_2O) absorber layer and atomic layer deposition of gallium oxide (Ga_2O_3) buffer layers with in-situ heterojunction formation completely mitigates the creation of the detrimental cupric oxide (CuO) layer, resulting in a pristine photovoltaic junction that delivers an open-circuit voltage of 1.78 V. Numerical device simulations of a two-layer absorber architecture demonstrates the potential of combining in-situ junction formation with non-vacuum fabrication techniques.

5.2 Introduction

Cuprous oxide (Cu_2O) is an earth abundant semiconductor suitable for cost-effective deployments at terra-watt scales [1, 2] that are capable of delivering power conversion efficiencies (PCE) exceeding 20% in single junction solar cells and with open circuit voltages (V_{OC}) that are much typically higher than other absorber layers due to its wide band gap in excess of 2 eV [3-5]. Interfacial recombination is a major loss mechanism in current Cu_2O -based thin film solar cells that is hindering the path towards attaining its theoretical maximum efficiency [6] and is the primary reason for low V_{OC} in present day devices [7]. Recombination at the heterojunction interface is commonly attributed to a high surface recombination velocity originating predominantly from high densities of defect trap states and to non-ideal band alignments at the interface. Moreover, monolayers of cupric oxide (CuO) are readily formed at the surface of Cu_2O during the formation of the heterojunction when the surface of the active layer is exposed to an oxygen-rich ambient [8], as seen in cases where the device fabrication process involves unavoidable air exposure of the Cu_2O surface during material transfers between different deposition environments [9-11]. The resulting CuO layer that forms through surface oxidation has been identified to contribute to deep-level defect states at the heterojunction interface leading to enhanced recombination and appreciable performance degradation [12, 13]. By applying a suitable n-type buffer layer to construct a heterojunction with an almost flat alignment of the conduction bands, the junction quality can be further enhanced [14, 15]. Ga_2O_3 buffer layers have proven themselves to be one of the most suitable n-type partners to Cu_2O , leveraging the near-ideal band alignments to achieve V_{OC} values of up to 1.2 V [10]. In previous studies, the Cu_2O layer has always been exposed to air before the deposition of the Ga_2O_3 buffer layer owing to the limitation of utilizing separate deposition systems to be prepare the two

different layers (eg., electrochemical deposition with atomic layer deposition (ALD) [10], thermal oxidation with pulse laser deposition (PLD) [11]), thereby allowing the undesirable CuO layer to be form at the crucial junction. Numerous thin film photovoltaic materials including copper indium gallium selenide (CIGS) encounter similar challenges in surface chemistry transformations [16] and methods have been devised to reduce but not completely eliminate these oxidized layers [17]. When zinc-containing compounds (such as zinc-tin-oxide) acting as buffer layers are deposited on Cu₂O using ALD techniques, the reactive metal precursor vapors of diethylzinc can be injected before the start of the buffer layer deposition to reduce the surface CuO back to Cu₂O [18]. Although Ga₂O₃ provides a favorable band alignment with Cu₂O, the metal ALD precursor for gallium does not completely reduce the CuO layer, making it vital to explore new vacuum-compatible fabrication strategies that are capable of mitigating interfacial defects introduced by the surface oxidation of Cu₂O in order to maximize the exploitation of Ga₂O₃ as the n-type buffer layer of choice in Cu₂O-based solar cells.

In this work, we present an approach that successfully averts the formation of CuO at the heterojunction interface via an in-situ junction creation that embraces two compatible vapor deposition processes carried out in the same reaction zone. The pristine p-n junctions facilitated the suppression of deep-level defect formation originating from interfacial CuO and as a result enhances the V_{OC} performances of Cu₂O-based devices. In addition, a numerical simulation model was developed for optimizing a novel two-layer absorber layer device architecture that incorporates the aforementioned in-situ heterojunction formation strategy for coupling the high V_{OC} advantages to the high J_{SC} delivered by Cu₂O films synthesized using non-vacuum techniques, essentially capitalizing on the best of both approaches.

5.3 Methods

To fabricate the solar cell device, a Si wafer with 300 nm thick thermal oxide (SiO_2) cleaved into 1×1 inch² substrates and coated with a stack of Ti (5 nm)/Au (200 nm) layer by e-beam evaporation to form the back contacts. A 1.5- μm -thick Cu_2O absorber layer, a 20-nm-thick Ga_2O_3 buffer layer and a 120-nm-thick ZnO:Al window layer were deposited successively in the same growth chamber with and without intended air exposure between deposition runs. (N,N-di-sec-butylacetamidinato)dicopper(I) dimer $[\text{Cu}(\text{sBu}_2\text{AMD})]_2$ (Strem Chemical Company) and deionized water were chosen to prepare cuprous oxide by thermal CVD. The copper(I) precursor was sublimed from a bubbler maintained at a temperature of 98°C into a 100 sccm flow of purified nitrogen gas. Deionized water is evaporated from a bubbler maintained at a temperature of 25°C into a 5 sccm flow of purified nitrogen gas. Both reactants are mixed together with a 40 sccm flow of purified nitrogen before injection into the process chamber of a custom built hot-walled tubular reactor with a 316L sample stage 30 cm long and 3 cm wide. The process chamber is maintained at a temperature of 200°C using a Linberg Blue Minimite furnace and the process pressure is held at 10 Torr using a MKS exhaust throttle valve (253B) coupled to the MKS Baratron absolute capacitance manometer (626C12TBE) and regulated using an MKS 600 series pressure controller. Following the growth of the Cu_2O absorber, the Ga_2O_3 overlayer was deposited in the same chamber after cooling the substrates to a stable temperature of 120 °C using 100 ALD cycles at a deposition rate measured to be ~ 0.2 nm using spectroscopy ellipsometry. Bis(μ -dimethylamino)tetrakis(dimethylamino)digallium (Strem Chemical Company) and deionized H_2O were used as a gallium precursor and an oxygen source, respectively. During the ALD process of Ga_2O_3 films, the temperatures of the gallium source was maintained at 107 °C. High-purity N_2 was used as a carrier gas. The exposures of the

gallium precursor and H₂O were estimated to be approximately 3 and 5 Torr·s, respectively. ZnO:Al was deposited by ALD using trimethylaluminum, diethylzinc and deionized water as the Al, Zn, and O sources, respectively. The trimethylaluminum pulse is introduced after every set of 19 pulses of diethylzinc. The 500-nm-thick Ag top electrodes were deposited by e-beam evaporation. Surface morphologies and film thicknesses of the devices were analyzed using an Ultra 55 FESEM (Zeiss). The J-V characteristics of the devices with a cell area of 0.22 cm² were measured by using a Keithley 2400 source meter under the standard 1-sun illumination generated by a Newport Oriel 91194 solar simulator with a 1600 W ozone-free Xe-lamp with a AM1.5G filter and a Newport Oriel 6895 flux controller calibrated by a NREL-certified Si reference cell equipped with a BG-39 window. The K-alpha XPS (Thermo Scientific) was used to perform XPS measurements and to obtain conduction band offsets between the absorber and the buffer layer. Hall mobility, carrier concentration and resistivity are measured using a hall effect measurement system with thin films of the material deposited on 1 x 1 cm² Si substrates with 300-nm-thick SiO₂. The solar cell capacitance simulator SCAPS-1D was employed to perform simulations of the Cu₂O-based devices [19]. A numerical model was built to fit the J-V characteristics of the target solar cell using experimentally measurable parameters while others are estimated and fitted and fine-tuned to an excellent agreement with the observed J-V measurements as shown in **Figure 5.6b**.

5.4 Results and Discussion

5.4.1 Interfacial Cu Oxidation States at the $\text{Cu}_2\text{O}/\text{Ga}_2\text{O}_3$ Bilyaers

The surfaces of Cu_2O films are expected to be readily oxidized in ambient air to form a nanometer thick layer of CuO . During investigations of the material composition by XPS as shown in **Figure 5.2a**, distinct peaks are observed at 932.2 eV and 934 eV, which are attributed to the presence of Cu^{1+} (Cu_2O) and Cu^{2+} (CuO), respectively [20]. Broad peaks in the 940-945 eV region are typically identified as satellite peaks characteristic of the +2 oxidation state of Cu. To probe deeper than the ≈ 5 -nm photoelectron escape depth, in-situ Ar^+ ion sputtering was utilized to remove layers of material. Depth profiling using XPS as shown in **Figure 5.1** show that the extent of oxidation is limited to several monolayers on the film surface.

Figure 5.2b shows the XPS spectra of the Cu-2p core levels for three samples of Cu_2O films, each with a 3-nm-thick Ga_2O_3 overlayer and various interface treatments applied to the surface of Cu_2O to study the oxidation states of copper at the absorber-buffer interface. Thin films for the bilayer samples were fabricated by first depositing a 1.5 μm thick film of Cu_2O by chemical vapor deposition whereas the 5 nm thick overlayer of Ga_2O_3 was coated on the Cu_2O film by atomic layer deposition. The first $\text{Cu}_2\text{O}/\text{Ga}_2\text{O}_3$ bilayer sample was deposited in the same chamber without breaking vacuum. The absence of CuO in the sample can be established from the high resolution XPS measurements showing no detectable peaks corresponding to Cu^{2+} states in the Cu-2p scans. The surface of Cu_2O is exposed only to purified nitrogen carrier gases, to the gallium ALD precursor which is reducing in nature which assists in the preservation of a single oxide phase, and to water vapor that has been to processed to contain minimal oxygen content. Under these conditions, no CuO is expected to form at the $\text{Cu}_2\text{O}/\text{Ga}_2\text{O}_3$ interface. In contrast, the second sample was deposited in the same chamber but with both depositions separated by an

additional step for cooling the sample stage down to room temperature, followed by exposure of the Cu_2O film surface to oxygen present in the air, then evacuating the chamber before finally reheating the specimen in purified nitrogen to the deposition temperature of the Ga_2O_3 ALD process in preparation for the overlayer deposition. A CuO layer of approximately 1 nm thickness is estimated to have formed on the surface of Cu_2O when exposed to ambient air at room temperatures. The deleterious cupric oxide layer is exacerbated in the third $\text{Cu}_2\text{O}/\text{Ga}_2\text{O}_3$ sample by exposing the Cu_2O surface to ambient air at an elevated temperature of 200 °C for 1 minute to create a CuO layer estimated to be 3 nm thick before proceeding with the Ga_2O_3 deposition at 120 °C. All three samples show peaks corresponding to Cu^{1+} (Cu_2O) at 932.2 eV. The sample with an intentional heating of the surface in air displayed the strongest Cu^{2+} (CuO) peaks at ≈ 934 eV with increased prominence of the 940-945 eV satellite peaks which are also characteristic of the +2 oxidation state of Cu. The second sample that was exposed to air at room temperature had smaller peaks attributed to the presence of CuO . Although exposure to ALD metal precursor vapors have been reported to reduce the exposed surface if the reactions are energetically favorable[18], the presence of trace amounts of CuO is indicative of bis(μ -dimethylamino)tetrakis(dimethylamino)digallium being less effective relative to diethylzinc at reducing the charge state of Cu from +2 to +1.

5.4.2 $\text{Cu}_2\text{O}/\text{Ga}_2\text{O}_3$ Heterojunction Solar Cell Devices

To investigate the effect of surface oxidation of the absorber material on the performance of the solar cell, photovoltaic devices with three different surface treatments similar to the bilayer samples in our XPS studies were fabricated. The device stack of the solar cells comprises of Au back contact (500 nm)/ Cu_2O absorber (1.5 μm)/ Ga_2O_3 buffer (20 nm)/ $\text{ZnO}:\text{Al}$ TCO (80

nm)/Ag top electrode (500 nm) as shown in the cross-sectional scanning electron microscopy (SEM) image in **Figure 5.3b**. Current density vs. voltage (J-V) characteristics of the devices were measured under 1-sun (AM 1.5G, 100 mw cm⁻²) illumination conditions as shown in **Figure 5.3a**. A strong dependence of device efficiency and open-circuit voltage is observed when varying the integrity of the heterojunction interface. Forming the Cu₂O/Ga₂O₃ interface in the same chamber without a vacuum break between both depositions yielded the best performing device exhibiting a PCE of 2.36% and a V_{OC} of 1.78 V. When the Cu₂O surface is exposed to air during the vacuum break, a thin layer of CuO was formed through oxidation of the surface by oxygen present in the air. XPS analysis detected the presence of Cu²⁺ on the Cu₂O surfaces that were intentionally oxidized but could not be detected on the sample where the air exposure was avoided during in-situ junction formation. Heat treatment during air exposure of the Cu₂O surface is successful at increasing the amount of surface oxidation, which therefore continued to reduce the V_{OC} even further and significantly degraded the fill-factor until an almost linear J-V characteristic was observed. The J_{SC} remained constant for all fabricated devices as the introduction of interfacial defects through air exposure and heat treatment had negligible impact on the photogeneration capabilities of the device stack.

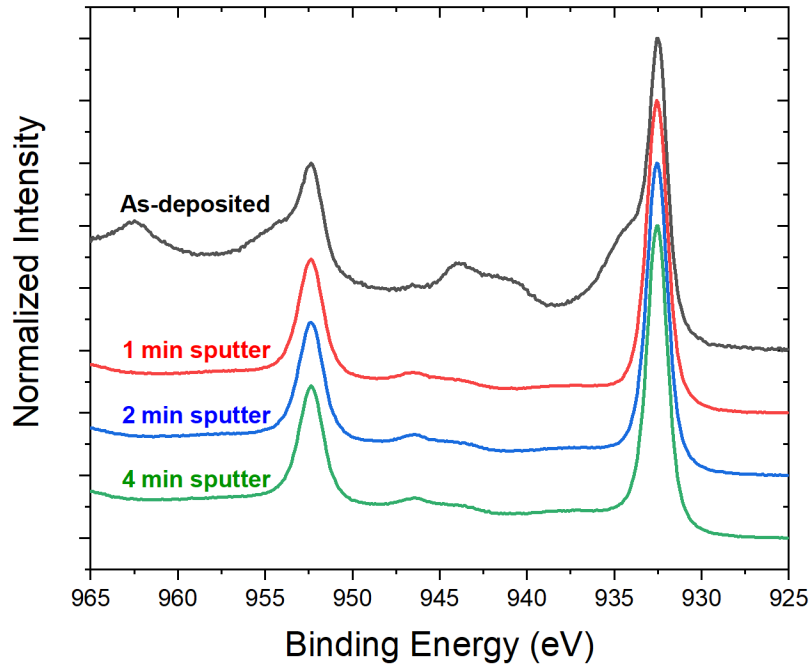


Figure 5.1. XPS depth profile measurement of the Cu-2p core levels sputtered in-situ by Ar⁺ ions showing the presence of CuO is limited to only the surface of the CVD grown film.

Table 3. Comparison of solar cell parameters of devices with different oxidative exposures to the Cu₂O/Ga₂O₃ heterojunction interface

Oxidative Treatments at the Cu₂O/Ga₂O₃ Interface	J_{sc} (mA/cm²)	V_{oc} (V)	FF (%)	η (%)
With air exposure	1.97	1.79	67	2.4
Without air exposure	1.94	1.35	62	1.6
With heated air exposure	1.93	1.12	59	1.3

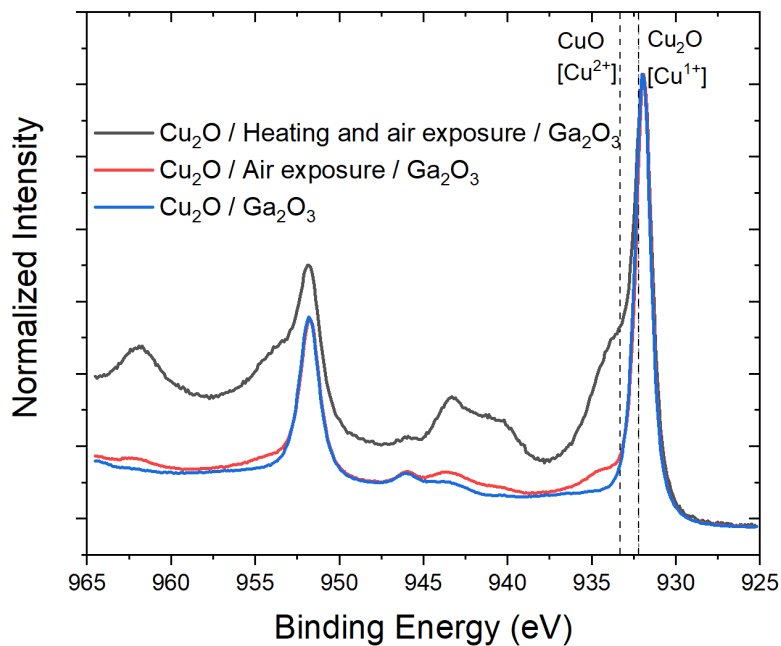
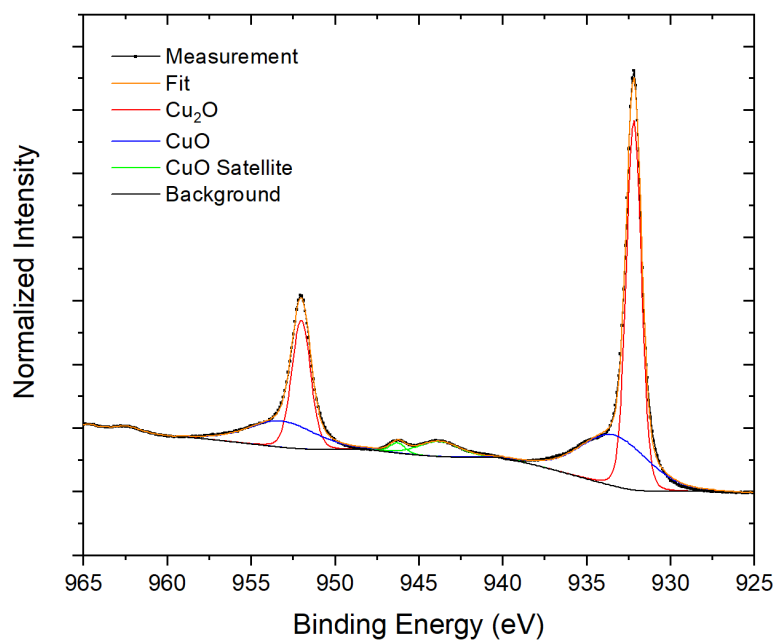


Figure 5.2. (a) Normalized XPS spectra of Cu-2p of a Cu₂O/Ga₂O₃ heterojunction exposed to room temperature air, showing a peak shoulder at ≈ 933.3 eV attributed to the Cu²⁺ phase. (b) Comparison of normalized XPS spectra of Cu-2p from the Cu₂O samples with various amounts of CuO at the Cu₂O/Ga₂O₃ heterojunction after exposure to varying amounts of air to the Cu₂O surface before the deposition of the Ga₂O₃ overlayers.

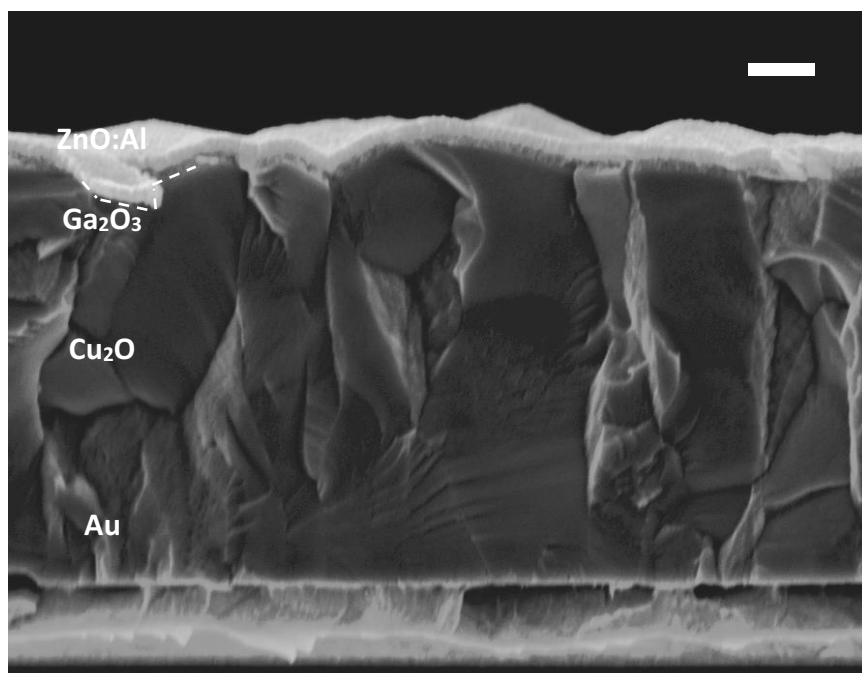
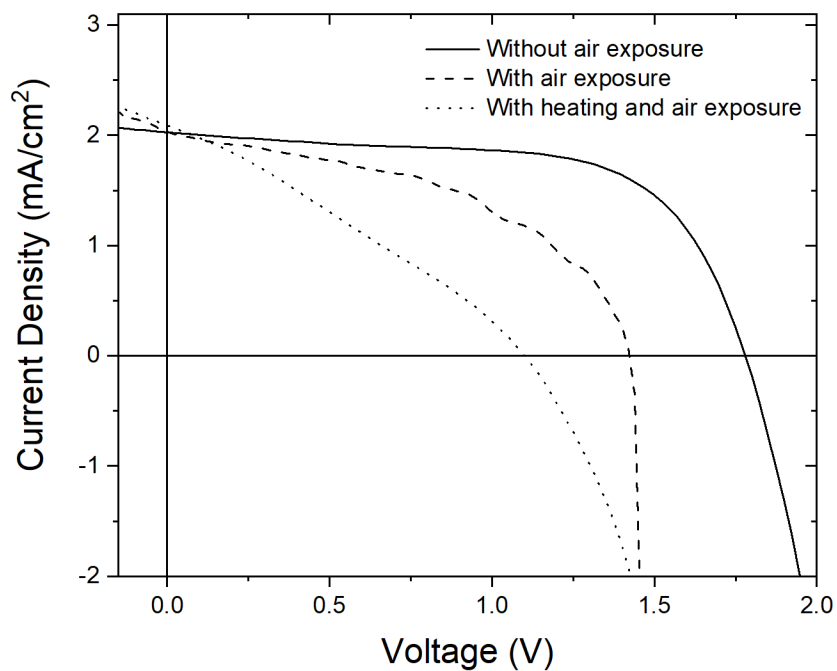


Figure 5.3. (a) J-V characteristics of the devices with varying oxidative air exposure treatments at the $\text{Cu}_2\text{O}/\text{Ga}_2\text{O}_3$ interface under 1-sun (AM 1.5G) illumination conditions. (b) A cross-sectional SEM image of Cu_2O -based solar cells with the device structure ($\text{Au}/\text{Cu}_2\text{O}/\text{Ga}_2\text{O}_3/\text{ZnO:Al}$). Scale bar represents 200 nm.

5.4.3 Numerical Simulations of Solar Cell Devices using SCAPS-1D

5.4.3.1 Interfacial and Bulk Defect Density

Defect densities at both the heterojunction interfaces and in the bulk of the photovoltaic materials are prime factors that determine device performances. To more comprehensively visualize the effects of air exposure at the interfaces of our devices and gain quantitative insights into the degree to which the resultant interfacial recombination affects cell parameters, we perform simulations of current-voltage curves while varying the amounts of interfacial defects as shown in **Figure 5.4a**. As observed, the open circuit voltage of the cells shows a dramatic increase with a corresponding decrease in the interfacial defect density. For simulated devices with interfacial defect densities lower than $1 \times 10^{12} \text{ cm}^{-3}$, the current density and fill factor remaining at an almost constant value. By further increasing the concentration of defects at the interface, the diode characteristic is observed to start significantly deviating away from the J-V characteristics of an ideal diode, resulting in the noticeable degradation of both the fill factor and J_{SC} . This J-V behavior demonstrates the importance of interfacial passivation to enable the suppression of interfacial defects which is shown to be the primary factor affecting the open circuit voltage of our devices. The effects of absorber layer quality on the solar cell parameters are captured in the device simulations by comparing devices with bulk defect densities of $1 \times 10^{14} \text{ cm}^{-3}$, $1 \times 10^{15} \text{ cm}^{-3}$ and $1 \times 10^{16} \text{ cm}^{-3}$. The simulated devices show increasing J_{SC} with decreasing bulk defect densities. Our calculations suggest that there is tremendous headroom for improvement in J_{SC} by replacing the CVD grown Cu_2O layer with Cu_2O synthesized using galvanostatic electrochemical deposition [10, 21, 22] or thermal oxidation of copper sheets[23, 24] with our simulation models predicting the potential of doubling our current cell efficiencies

with just this single change to our device stack. Based on our device modelling, the performance of $\text{Cu}_2\text{O}/\text{Ga}_2\text{O}_3$ devices with no air exposure at the heterojunction interface is bulk recombination dominated with an extracted surface recombination velocity in the range of 10 cm/s and the bulk defect density in the CVD- Cu_2O absorber layer is fitted to $1 \times 10^{14} \text{ cm}^{-3}$.

5.4.3.2 Carrier Concentrations and Band Offsets

Simulations of device performance characteristics were carried out to obtain the optimal conduction band offset between the absorber and buffer layer. **Figure 5.5a** shows the device stack favoring lower carrier concentration for the absorber layer and a higher carrier concentration for the buffer layer for maximizing the photovoltaic efficiencies. To motivate further studies on overcoming the challenges of increasing the electron density of ALD- Ga_2O_3 [25], the results are exhibited as a function of both the conduction band offset and the carrier concentration of the buffer layer while keeping the carrier concentration of the absorber layer constant at the optimal $1 \times 10^{16} \text{ cm}^{-3}$. The conduction band offsets at the junction can possibly be tuned by doping Ga_2O_3 prepared in an ALD process with a suitable dopant, such as aluminum or indium to raise to lower and to raise the conduction band of the undoped buffer material, respectively. The simulated behaviors can be classified into two clusters with the first populated by devices whose Ga_2O_3 buffer layers have majority carrier concentrations that lie below $1 \times 10^{18} \text{ cm}^{-3}$. In this scenario the optimal conduction band offset was found to be at +0.1 eV. This positive offset forms a type-I conduction band spike at the $\text{Cu}_2\text{O}/\text{Ga}_2\text{O}_3$ interface which is small enough to allow unimpeded current flow into the Ga_2O_3 layer via thermionic emission. As we increase the conduction band offset, the spike becomes sufficiently large enough to suppress the collection of light-generated carriers. When a negative conduction band offset is introduced at

the junction, the type-II cliff structure increases the interfacial recombination velocity which. In these cases where the offset deviates away from +0.1 eV, the device efficiencies are reduced as shown in our numerical calculations. Interestingly the second group distinguished by higher buffer layer carrier concentrations has an optimal conduction band offsets in the range of +0.2 to +0.4 eV which are much larger than devices with buffer layers of lower electron concentrations. The best performing Cu₂O devices with a 1.78 V V_{OC} that we characterized was measured to have a carrier concentration of $1 \times 10^{16} \text{ cm}^{-3}$ for the undoped Ga₂O₃ buffer layer and a negative conduction band offset of -0.2 eV that forms a type-II cliff structure. Such devices have larger sensitivity to conduction band offsets relative to the carrier densities of the Ga₂O₃ buffer layer which are also more challenging to achieve experimentally. Based on our modelling studies, we can most readily achieve the greatest efficiency improvements of our present-day devices by increasing the conduction band offset to be slightly positive with the introduction of aluminum into the Ga₂O₃ buffer layer. Increasing the buffer layer carrier densities to exceed 10^{18} cm^{-3} not only widens the depletion region in the absorber to reduce recombination at the interface but also narrows the conduction band spike at the Cu₂O/Ga₂O₃ interface, enabling the tunneling of photogenerated carriers through the barrier, which in turn enables the use of larger conduction band offsets to further mitigate interface recombination.

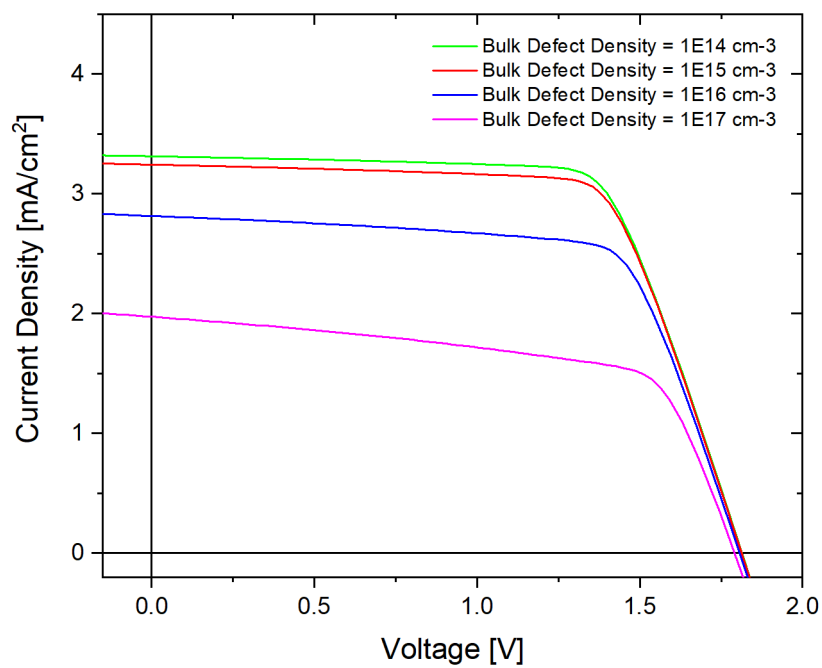
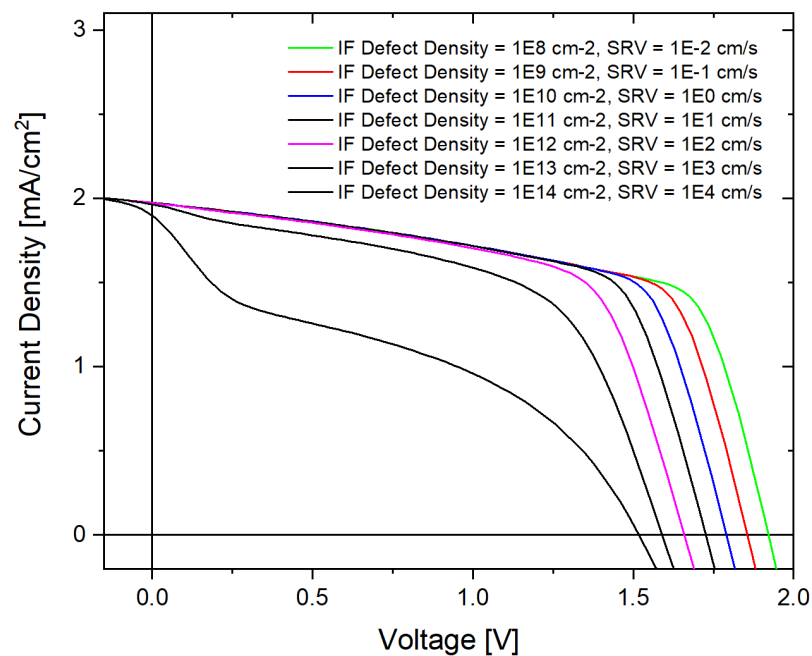


Figure 5.4. Comparison of current-voltage characteristics of $\text{Cu}_2\text{O}/\text{Ga}_2\text{O}_3$ devices (a) with different degrees of air exposure at the interface, proxied using varying amounts of interfacial defect densities, and (b) with varying amounts of bulk defect density in the Cu_2O absorber layer.

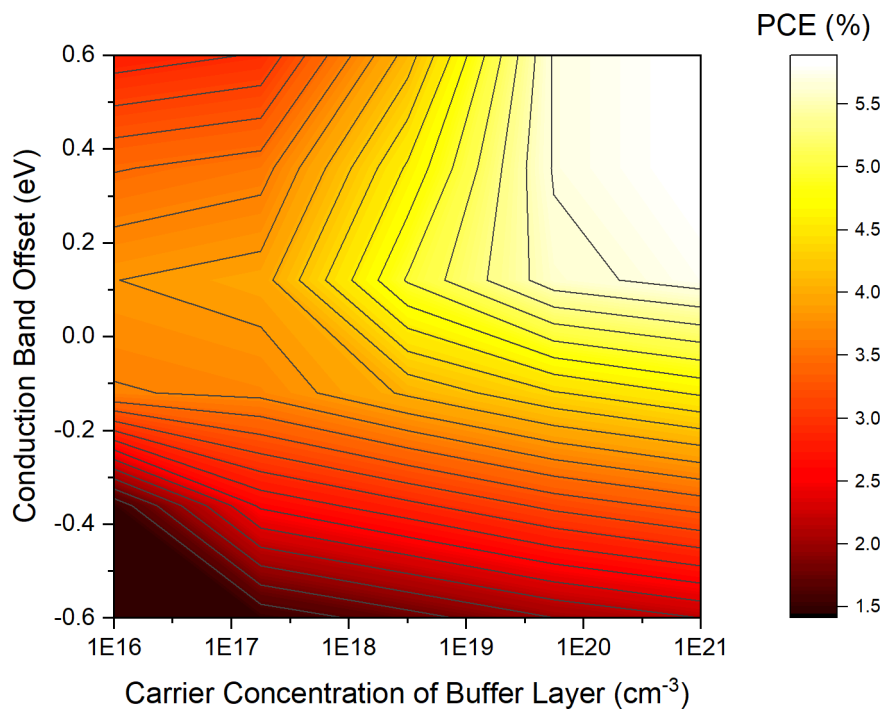
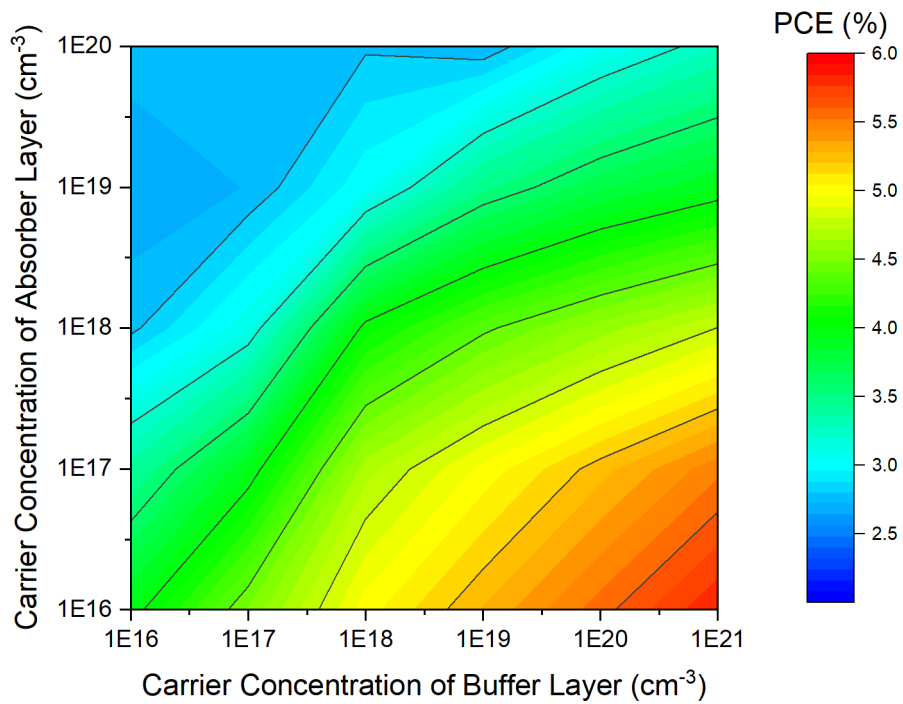


Figure 5.5. Simulated cell efficiencies for $\text{Cu}_2\text{O}/\text{Ga}_2\text{O}_3$ devices (a) with varying carrier concentrations of both the Cu_2O absorber layer and the undoped Ga_2O_3 hole transport buffer layer, and (b) with varying carrier concentration of the Cu_2O absorber layer and varying conduction band offset of Cu_2O absorber with Ga_2O_3 buffer layer.

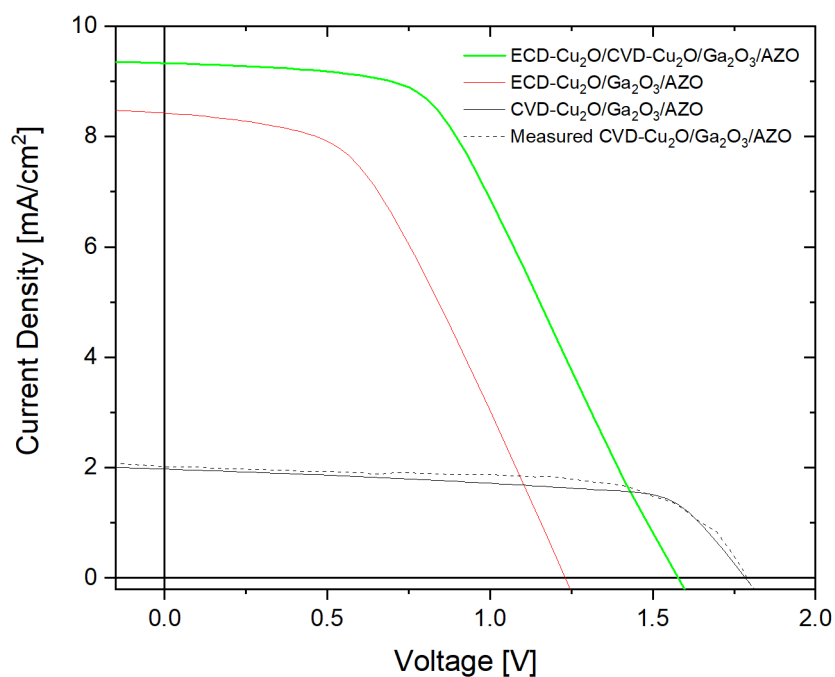
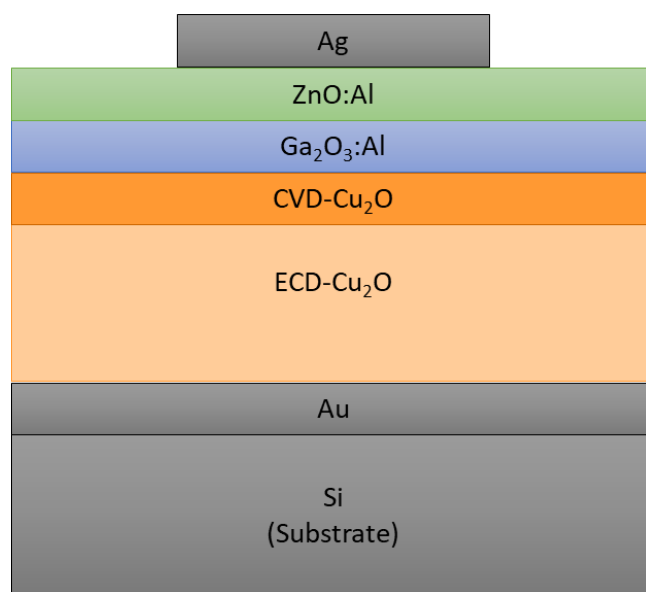


Figure 5.6. (a) Device stack comprising of a 2-layer absorber consisting of a thick layer electrochemically deposited with an ultra-thin layer deposited using chemical vapor deposition, including silver front metallization, aluminum-doped zinc oxide window layer, gallium oxide buffer layer, gold back contact coated on thermally oxidized silicon substrates. (b) Comparison of current-voltage measurement (dashed line) simulations (solid line) using different absorber layers in the $\text{Cu}_2\text{O}/\text{Ga}_2\text{O}_3$ device stack.

5.4.3.3 Device Architecture with Two-Layer Absorber

Additional simulations were performed to provide guidance and to evaluate the potential of fabricating the bulk of the Cu_2O absorber using the electrochemical deposition (ECD) technique which produces higher quality materials known to deliver devices exhibiting much higher photocurrents compared to the CVD grown material. An ultra-thin CVD layer of Cu_2O is used to form the p-n junction with the Ga_2O_3 window layer which leverages the ability to deposit both layers in the same deposition system without any exposure to oxygen so as to maintain the integrity of the junction for achieving the low interfacial recombination velocities. The predicted J-V characteristics are depicted in **Figure 5.6b**, clearly highlighting the strengths of the two Cu_2O fabrication techniques individually and when combined. Simulated devices using an ECD- Cu_2O absorber were able to achieve a J_{SC} of 8.4 mA/cm^2 but suffered from a lower V_{OC} of 1.2 V. In comparison, the CVD- Cu_2O devices displayed better V_{OC} of almost 1.8 V at the expense of a lower J_{SC} of 2.0 mA/cm^2 . Numerical models of the 2-layer absorber system illustrated in **Figure 5.6a** enjoyed significant enhancements in device performance, obtaining a cell efficiency of 7.2%. A small drop of 170 mV in V_{OC} is observed when progressing from the CVD- Cu_2O absorber to the 2-layer absorber stack which can be explained by the dominance of the smaller optical band gap of the electrochemically deposited material. The upside is an increase in the wavelengths that can be absorbed from the incident irradiation, improved photocurrent collection efficiencies from lower bulk defect densities and the opportunity to form the critical junction with Ga_2O_3 window layer without interfacial defects generated from surface oxidation. Consequently, the use of two different absorber components led to appreciably improved overall device performances. When presented with the compromise of lower voltages in exchange for larger photogeneration, an optimization was done by varying the thickness of the CVD grown

layer as shown in **Figure 5.7**. By increasing the film thickness of CVD-Cu₂O, the V_{OC} experienced a negligible change while the J_{SC} and FF and hence device efficiency increases initially to achieve an efficiency value of 13.2% before decreases much more dramatically as a result of the lower hole mobility of the thicker CVD deposited film relative to the more crystalline Cu₂O grown by ECD. The highest PCE was obtained from a film thickness of 20 nm for the CVD-grown Cu₂O layer.

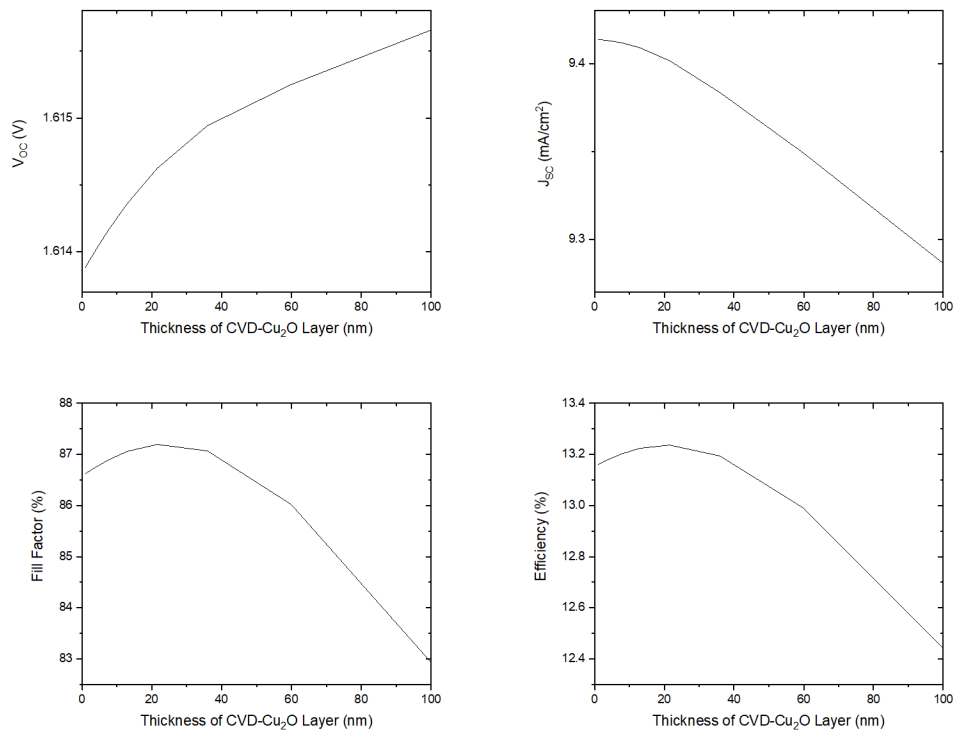


Figure 5.7. Simulated J-V characteristics of an optimized Cu₂O-based device using the 2-layer absorber approach.

5.5 Conclusion

In summary, the defective CuO layer can be eliminated at the Cu₂O/Ga₂O₃ interface by creating the heterojunction in-situ using compatible deposition processes that circumvents vacuum breaks in the cell fabrication process. This approach of developing compatible

deposition processes to form the heterojunction in the same system without air exposure can be applied to other material systems to improve the quality of the interfaces and therefore mitigate interfacial recombination to achieve enhanced solar cell performances. Improved device efficiencies of over 13% can potentially be achieved using the proposed 2-absorber approach with an optimized thickness of 20 nm for the CVD-Cu₂O layer to extract a high V_{OC} by maintaining the pristine heterojunction formed between CVD-Cu₂O and ALD-Ga₂O₃ while simultaneously leveraging the low bulk defect densities of the primary Cu₂O absorber layer grown by a different method for enhancements of both J_{SC} and fill factors.

5.6 References

1. Meyer, B.K., et al., *Binary copper oxide semiconductors: From materials towards devices*. *physica status solidi (b)*, 2012. **249**(8): p. 1487-1509.
2. Olsen, L.C., F.W. Addis, and W. Miller, *Experimental and theoretical studies of Cu₂O solar cells*. *Solar Cells*, 1982. **7**(3): p. 247-279.
3. Niaura, G., *Surface-enhanced Raman spectroscopic observation of two kinds of adsorbed OH⁻ ions at copper electrode*. *Electrochimica Acta*, 2000. **45**(21): p. 3507-3519.
4. Chan, H.Y.H., C.G. Takoudis, and M.J. Weaver, *Oxide Film Formation and Oxygen Adsorption on Copper in Aqueous Media As Probed by Surface-Enhanced Raman Spectroscopy*. *The Journal of Physical Chemistry B*, 1999. **103**(2): p. 357-365.
5. Singhal, A., et al., *Copper(I) Oxide Nanocrystals - One Step Synthesis, Characterization, Formation Mechanism, and Photocatalytic Properties*. *European Journal of Inorganic Chemistry*, 2013. **2013**(14): p. 2640-2651.
6. Jiang, T., et al., *Photoinduced charge transfer process in p-Cu₂O/n-Cu₂O homojunction film and its photoelectric gas-sensing properties*. *J Colloid Interface Sci*, 2013. **405**: p. 242-8.
7. Jeong, S., et al., *An analysis of temperature dependent current-voltage characteristics of Cu₂O-ZnO heterojunction solar cells*. *Thin Solid Films*, 2011. **519**(19): p. 6613-6619.
8. Lim, J.-W., et al., *Nanoscale investigation of long-term native oxidation of Cu films*. *Thin Solid Films*, 2008. **516**(12): p. 4040-4046.
9. Mittiga, A., et al., *Heterojunction solar cell with 2% efficiency based on a Cu₂O substrate*. *Applied Physics Letters*, 2006. **88**(16): p. 163502.
10. Lee, Y.S., et al., *Atomic layer deposited gallium oxide buffer layer enables 1.2 V open-circuit voltage in cuprous oxide solar cells*. *Adv Mater*, 2014. **26**(27): p. 4704-10.
11. Minami, T., Y. Nishi, and T. Miyata, *Heterojunction solar cell with 6% efficiency based on an n-type aluminum-gallium-oxide thin film and p-type sodium-doped Cu₂O sheet*. *Applied Physics Express*, 2015. **8**(2): p. 022301.
12. Hoye, R.L.Z., et al., *Perspective: Maintaining surface-phase purity is key to efficient open air fabricated cuprous oxide solar cells*. *APL Materials*, 2015. **3**(2): p. 020901.
13. Wilson, S.S., et al., *Interface stoichiometry control to improve device voltage and modify band alignment in ZnO/Cu₂O heterojunction solar cells*. *Energy Environ. Sci.*, 2014. **7**(11): p. 3606-3610.
14. Niemegeers, A., M. Burgelman, and A. De Vos, *On the CdS/CuInSe₂ conduction band discontinuity*. *Applied Physics Letters*, 1995. **67**(6): p. 843-845.
15. Duan, Z., et al., *Effects of Mg composition on open circuit voltage of Cu₂O-MgxZn_{1-x}O heterojunction solar cells*. *Solar Energy Materials and Solar Cells*, 2012. **96**: p. 292-297.
16. Canava, B., et al., *Increasing solar cell efficiencies based on Cu(In,Ga)Se₂ after a specific chemical and oxidant treatment*. *physica status solidi (c)*, 2006. **3**(8): p. 2551-2554.
17. Xiang, C., et al., *820 mV open-circuit voltages from Cu₂O/CH₃CN junctions*. *Energy & Environmental Science*, 2011. **4**(4): p. 1311.
18. Lee, S.W., et al., *Improved Cu₂O-Based Solar Cells Using Atomic Layer Deposition to Control the Cu Oxidation State at the p-n Junction*. *Advanced Energy Materials*, 2014. **4**(11): p. 1301916.

19. Burgelman, M., et al., *Modeling thin-film PV devices*. Progress in Photovoltaics: Research and Applications, 2004. **12**(2-3): p. 143-153.
20. Poulston, S., et al., *Surface oxidation and reduction of CuO and Cu₂O studied using XPS and XAES*. Vol. 24. 1996. 811-820.
21. Lee, Y.S., et al., *Ultrathin amorphous zinc-tin-oxide buffer layer for enhancing heterojunction interface quality in metal-oxide solar cells*. Energy & Environmental Science, 2013. **6**(7): p. 2112-2118.
22. Izaki, M., et al., *Electrochemically constructed p-Cu₂O/n-ZnO heterojunction diode for photovoltaic device*. Journal of Physics D: Applied Physics, 2007. **40**(11): p. 3326-3329.
23. Minami, T., et al., *High-Efficiency Oxide Solar Cells with ZnO/Cu₂O Heterojunction Fabricated on Thermally Oxidized Cu₂O Sheets*. Applied Physics Express, 2011. **4**(6): p. 062301-6.
24. Li, J., et al., *Oxidation and reduction of copper oxide thin films*. Journal of Applied Physics, 1991. **69**(2): p. 1020-1029.
25. Siah, S.C., et al., *Dopant activation in Sn-doped Ga₂O₃ investigated by X-ray absorption spectroscopy*. Applied Physics Letters, 2015. **107**(25): p. 252103.

6 Probing Defect Mitigating Enhancements of High Temperature Annealing Treatments on Tin Sulfide Thin Films Solar Cells

6.1 Chapter Abstract

Thin film solar cells fabricated using non-toxic and earth-abundant tin sulfide (SnS) absorber layers have performance limited by mid-gap defects that should be mitigated by effective strategies. Effects of high temperature annealing treatments on performance enhancements were studied using photoluminescence techniques for the SnS absorber layers annealed under different ambience such as H₂S and N₂ and for un-annealed one. Decoupling of charge recombination on the surface from the bulk and in grain interior from grain boundaries were used to elucidate the impact of annealing conditions on photovoltaic device performances, leading to an enhanced open-circuit voltage of 0.38 V and an optimized photo-conversion efficiency of 4.99%.

6.2 Introduction

Tin (II) sulfide (SnS) attracted immense interests as a promising absorber material for thin film solar cells, demonstrating a suitable band gap (1.1 eV direct, 1.3 eV indirect) [1-3] and high absorption coefficient in the visible spectrum ($>10^4 \text{ cm}^{-1}$) [3, 4] while boosting non-toxicity and elemental abundance of Sn and S. A wide range of approaches have been successfully employed in the fabrication of SnS, including atomic layer deposition [2], pulsed chemical vapor deposition [5], and thermal evaporation [6-8]. The best performing SnS solar cells leveraged post-deposition anneal treatments of the SnS absorber layer, capturing significant improvements in device performance [9], whereas devices with unannealed SnS absorbers have been limited to low open-circuit voltages (V_{OC}) not exceeding 0.3 V. Grain boundaries and bulk defects are widely regarded to have detrimental effects on V_{OC} , minority carrier lifetimes, and therefore on the overall device performances [10].

High temperature anneal treatment provide a defect mitigation strategy that enables bulk defect reduction in SnS for fabricating higher performing devices, particularly when using a H_2S -rich anneal ambient [9]. While a large body of literature exists on the use of SnS as a promising absorber layer for thin film solar cells, there has been little studies on the impact of various anneal treatments on SnS devices, particularly with the integration of recent advancements into the rest of the device stack. By leveraging a tunable Zn(O,S) buffer layer with an optimized conduction band offset to generate the desired spike structure at the SnS/ Zn(O,S) heterojunction to reduce interfacial recombination [5, 11, 12] and an ultra-thin layer of native SnO_2 at on the surface of SnS as a passivating layer [9, 13], the resulting device performances represent the state-of-the-art in SnS-based systems. Consequently, the suppression of recombination at the heterojunction interface allows bulk recombination to dominate the trap-assisted recombination

in this system and hence better isolate performance improvements to bulk defect mitigation due to the annealing processes. Photoluminescence (PL) is a valuable characterization technique for studying a wide range of properties of semiconductor materials. Being a quick, non-destructive and contactless technique, PL is an attractive method for studying the opto-electronic properties of photovoltaic materials that influence the performance of solar cells. Spectrally-resolved photoluminescence (SRPL) allows the defect concentration of the absorber material to be evaluated by monitoring the intensity of the PL emissions from inter-band recombination. Minority carrier lifetimes of SnS absorber films, which can be directly monitored using the time-resolved photoluminescence (TRPL) technique, are directly impacted by the energy level and density of the defect trap states. Sulfur vacancies are known to introduce mid-gap states in the bulk of the material [14], inducing recombination centers that suppress minority carrier lifetimes and degrade device performances. Depth profiling using PL enables the decoupled probing of defect mitigation at the surface and in the bulk of the SnS grains. Through exposing SnS to a range of anneal conditions, we are able to understand the influences of different post-deposition treatments on these defects and their impact on the carrier lifetimes, with the goal of engineering SnS absorber layers to demonstrate lifetimes exceeding 1 ns, which is essential for obtaining SnS device efficiencies of over 10 % [15].

In this work, we present the insights obtained from spectrally-resolved and time-resolved photoluminescence techniques to provide guidance in developing high temperature post-deposition treatments for optimizing the SnS absorber, leading to significant performance enhancement of SnS photovoltaic devices with minority carrier lifetimes of 1.3 ns and photo-conversion efficiencies (PCE) of up to 4.99 %.

6.3 Experimental

SnS thin film absorber layers were deposited on Mo-coated (500 nm) thermally oxidized silicon substrates using an ALD process from the reaction of bis(*N,N'*-diisopropylformamidinato)Sn(II) (Sn(famd)₂, Strem Chemicals) and hydrogen sulfide (H₂S, 4 % in N₂). The Mo-coated substrates were maintained at 120 °C and the Sn source was kept at 60 °C. Each ALD cycle of SnS consists of one dose of Sn precursor vapor assisted with N₂ gas, followed by one dose of H₂S, alternating continuously in a closed valve condition until the desired thickness has been achieved. The SnS films were then annealed in the ALD process chamber under several different conditions. The first condition involved annealing under a constant flow of 60 sccm of H₂S, maintained at a substrate temperature of 400 °C and under a process pressure of 10 Torr for an hour. The second condition involved annealing under a constant flow of 60 sccm of N₂, maintained at a substrate temperature of 400 °C and under a process pressure of 10 Torr for an hour. The third condition involved annealing at a substrate temperature of 400 °C and under a process pressure of 100 mTorr for an hour. The process chamber was maintained at the desired temperatures using a Linberg Blue Minimite furnace for both the ALD and annealing processes. The substrates were treated by a UV/ozone cleaner (Samco model UV-1, wavelengths = 185 nm and 254 nm) for 5 minutes at room temperature before being introduced into the process chamber. These substrates were supported by a 316L stainless steel substrate holder with an embedded K-type thermocouple probe for temperature monitoring. Pressure in the deposition chamber was monitored using a convection enhanced pirani gauge (275 Series Gauge Tube, Kurt J. Lesker) and controlled using a MKS exhaust throttle valve (253B) coupled to a MKS Baratron absolute capacitance manometer (626C12TBE) and regulated using an MKS 600 series pressure controller. Purified nitrogen gas

and H₂S gas used during the annealing process were metered using digital mass flow controllers (MKS ALTA 1480A).

A photovoltaic device structure of Si/SiO₂/Mo/SnS/SnO₂/Zn(O,S):N/ITO/Ag was used in this study. A Mo bilayer [16] was first sputtered on silicon (100) substrates with 300 nm thick layer of thermally oxidized silicon dioxide on the surface. The first layer of Mo was deposited at 10 mTorr for 30 minutes using RF magnetron sputtering, followed by a second layer at 2 mTorr for 30 minutes. ZnO thin film was deposited at 120 °C by ALD using alternating doses of diethylzinc (Zn(C₂H₅)₂, DEZ, >52 wt.% Zn basis, Sigma Aldrich). 300 nm of tin-doped indium oxide (ITO) was deposited at room temperature via RF magnetron sputtering. A shadow mask was used during the ITO deposition process to define an active device area of 0.24 cm². The photovoltaic device was completed by the e-beam evaporation of a 500 nm thick layer of Ag as the top electrode patterned with metal grid lines evaporated through a second shadow mask at room temperature.

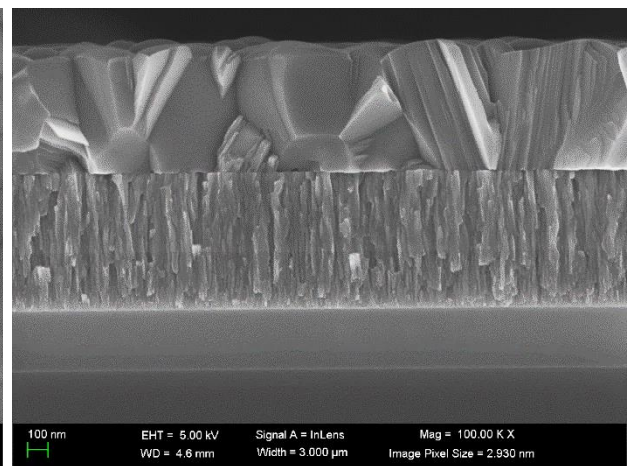
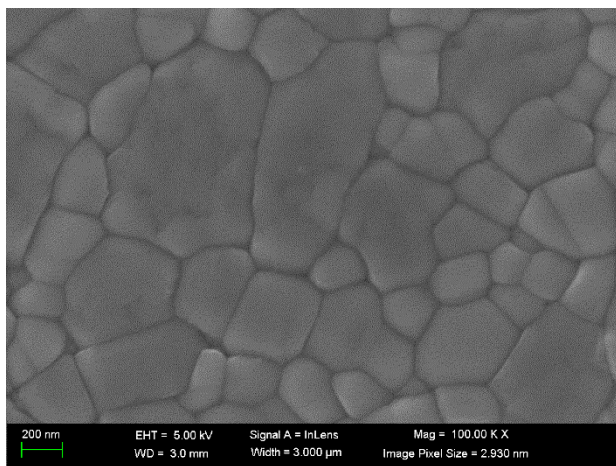
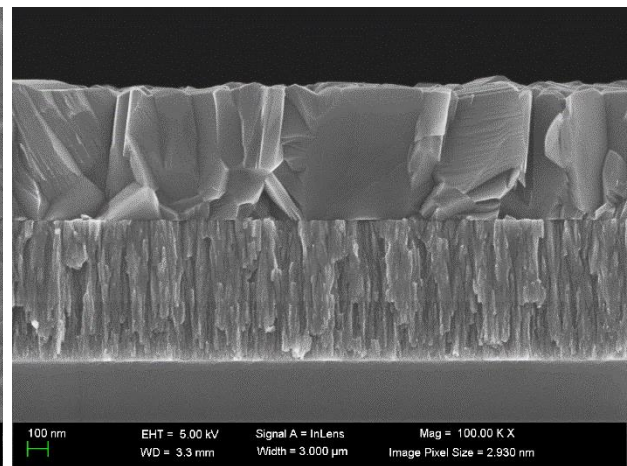
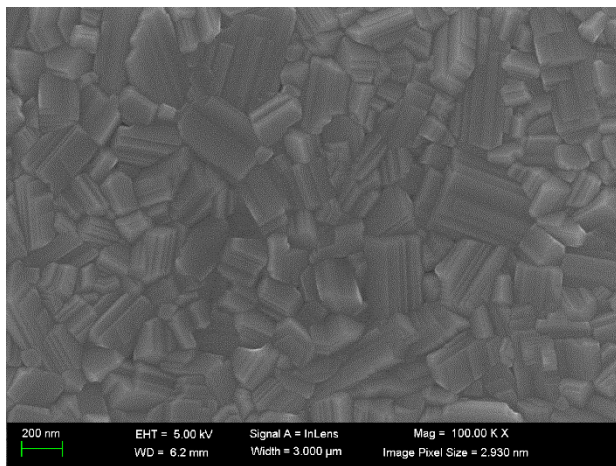
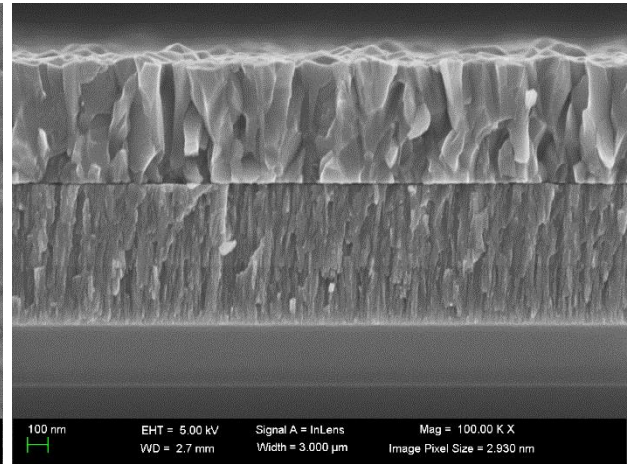
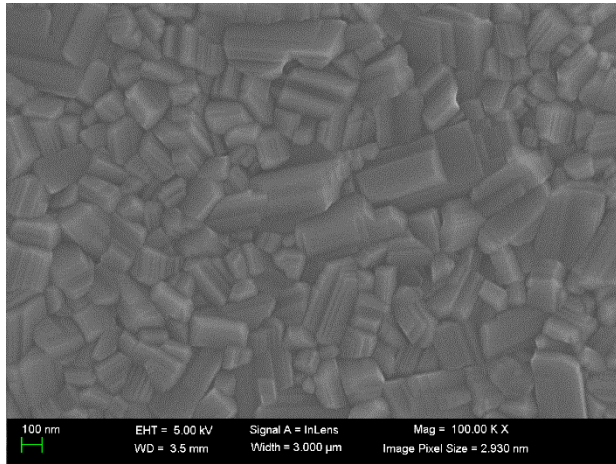
Steady-state spectrally-resolved photoluminescence (SRPL) measurements were performed using a 532 nm laser operating at 2 mW through a 50X confocal microscope objective with an 1800 blaze grating and a Synapse CCD detector (LabRam Evolution Multiline Raman/PL spectrophotometer, Horiba). Time-resolved photoluminescence (TRPL) measurements were performed using a Spectra Physics DeepSee Insight laser, tunable from 680 to 1300 nm with 120 fs pulses at 80 MHz was coupled into a Leica SP5 laser scanning confocal microscope. A Leica 40X air objective was used for imaging the samples in reflection. An IDQ ID-100 single photon avalanche photodiode (SPAD) detector was mounted on the non-descanned detector (NDD) port of the microscope. Different bandpass filters were placed in front of the detector to select out different emission spectral regions. The signal was processed with a Becker and Hickl SPC-150 time-correlated single photon counting (TCSPC) board. Depth-profile PL measurements were obtained by

collecting a Z-stack using the SP5 confocal microscope's internal photomultiplier tube detectors with tunable filters and the confocal aperture at one Airy unit. Three-dimensional SSPL maps were produced in single-photon excitation mode with an excitation wavelength of 775 nm and the PL signal was detected from 780 to 800 nm.

X-ray diffraction (XRD) measurements were performed using the Bruker D8 system with Cu K α radiation using a θ -2 θ scan. Field-emission scanning electron microscopy (FESEM) micrographs were obtained using the Zeiss Ultra-55 FESEM.

6.4 Results and Discussion

6.4.1 Film Morphology and Structure



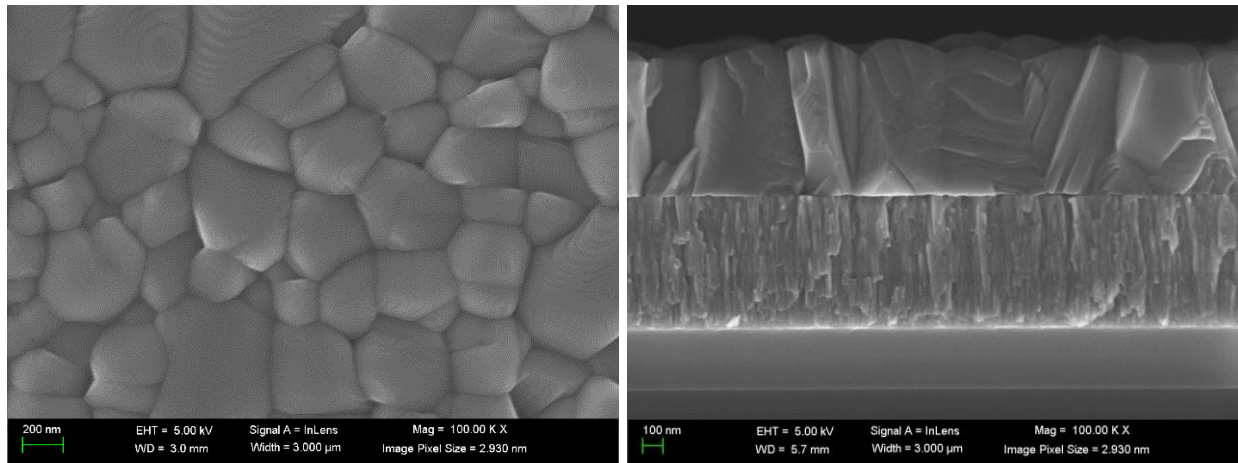


Figure 6.1. Plane-view and cross-section view SEM images of SnS ALD thin films for (a) unannealed and annealed in (b) H₂S atmosphere (10 Torr, 400°C, 1 hour), (c) N₂ atmosphere (10 Torr, 400°C, 1 hour), and (d) high vacuum (0.1 Torr, 400°C, 1 hour)

Film morphology and crystallinity were strongly influenced by the various anneal conditions. All SnS films preserved their crystallinity and experienced enhanced grain growth after being subjected to the high temperature annealing processes at 400 °C. From the cross-sectional SEM images in **Figure 6.1**, the H₂S anneal process promoted columnar grains with preferred grain orientations normal to the substrate plane. In addition, H₂S annealed SnS ALD films also maintained the rough surfaces of the as-deposited films. The highly columnar microstructure provides enhanced charge transport of the photo-generated carriers and the textured surface scatter the incident light, increasing the pathlength of light for increased light absorption. Both aforementioned properties of the films annealed in a H₂S atmosphere are highly desirable for photovoltaic applications. SnS films annealed in S-deficient conditions under 10 Torr and 100 mTorr of nitrogen displays markedly morphology as evident in **Figure 6.1c-d**. In contrast to annealing in a S-rich atmosphere, we observe that S-poor annealing conditions suppress the columnar microstructure and promoting growth of grains to be more lateral when compared to the unannealed SnS thin films. The surfaces of these films were much smoother than both the

unannealed films and the films annealed in a H₂S ambient. The average grain sizes when annealed in 10 Torr and 100 mTorr of nitrogen appear to be consistent with those annealed under the H₂S atmosphere, which means that the rate of grain growth is predominantly influenced by the anneal temperature independent of the anneal ambient as well as the process pressure.

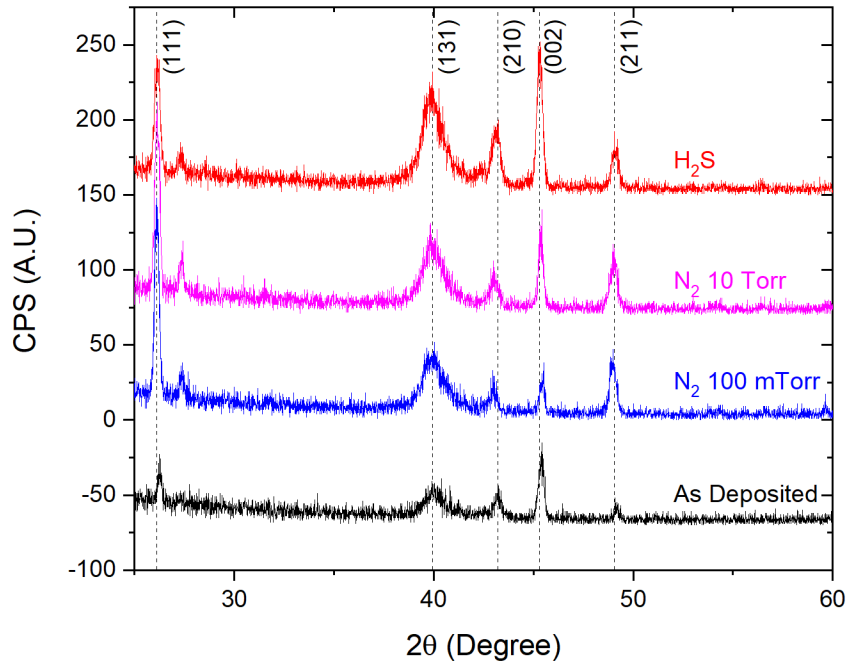


Figure 6.2. XRD spectrum of as-deposited SnS ALD thin films and of SnS ALD thin films annealed under 3 different ambient.

XRD measurements performed on the same set of SnS films confirm the change in crystallographic orientations of the films. Grains with the minimum free surface energies will experience higher growth rates than other crystal surfaces. Although all heat treatments were carried out on SnS ALD films synthesized using the same process parameters, different anneal conditions can result in the minimization of free surface energies of different SnS surfaces, therefore influencing the orientation and the growth rates of the various SnS grain surfaces.

Films annealed in the S-rich ambient experienced the greatest intensity increase of the (002) peak, while films annealed in the S-poor conditions displayed the greatest intensity increase of the (111) peak, explaining the vertically oriented grain growth when annealed under the H₂S ambient and the preference for a more lateral growth diagonal to the substrate when annealed under the N₂ ambient.

6.4.2 Electrical Characterization

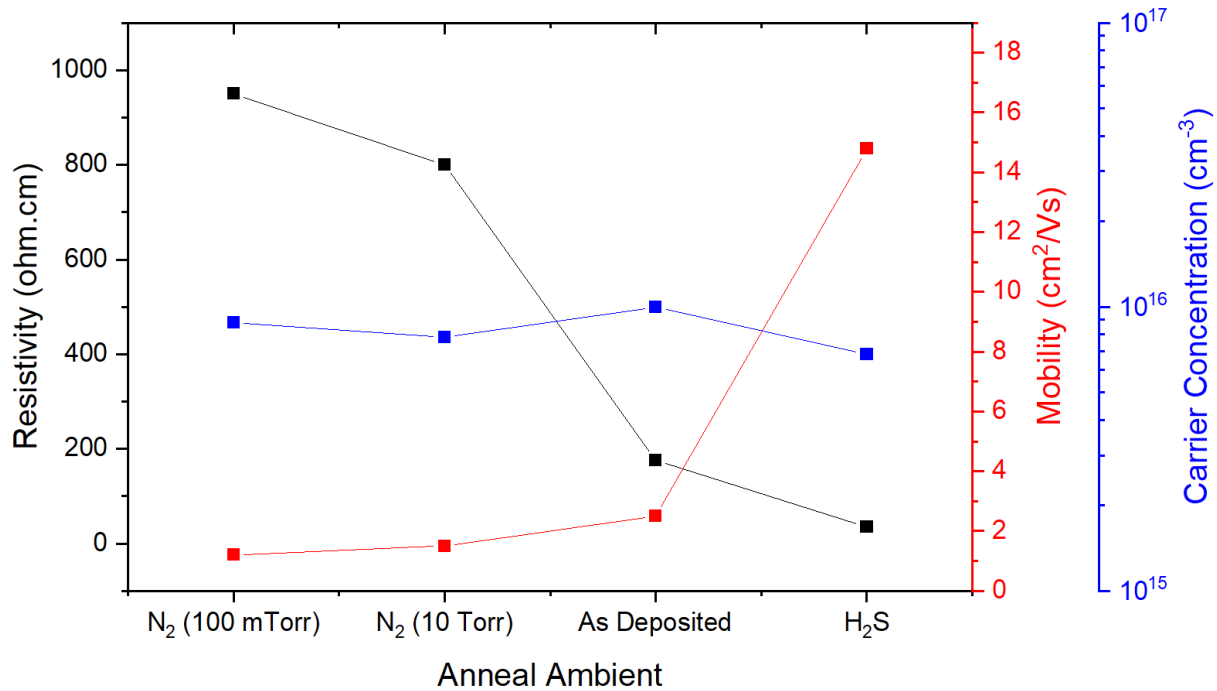
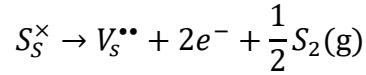
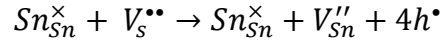


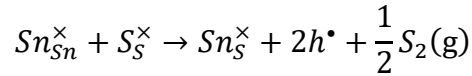
Figure 6.3. Hall measurement results of (black) resistivity, (red) mobility and (blue) hole density of SnS ALD thin films subjected to various anneal ambients during the post-deposition anneal treatment.

After the post-deposition anneal treatment at 400 °C for a duration of 1 hour, the electrical properties of the SnS ALD thin films were measured using the Hall effect measurement system and presented in **Figure 6.3**. The hole density of the annealed films remains relatively constant

within the range of $10^{15} - 10^{16} \text{ cm}^{-3}$. Annealing in a sulfur rich ambient yielded a considerable increase in the Hall mobility of up to $15 \text{ cm}^2/\text{Vs}$, giving rise to a drop in the resistivity of the film to $35 \text{ } \Omega \text{ cm}$. In contrast, high temperature treatments under a sulfur poor ambient led to a decrease in mobility to approximately $1 \text{ cm}^2/\text{Vs}$ with decreasing sulfur content in the anneal environment, corresponding to an increase in resistivity up to $950 \text{ } \Omega \text{ cm}$. Desulfurization of SnS is expected when annealed in a sulfur-deficient ambient such as in nitrogen gas, where it may have induced the formation of tin vacancies mediated through generating an antisite of Sn-on-S (S_S^\times), given by the equations



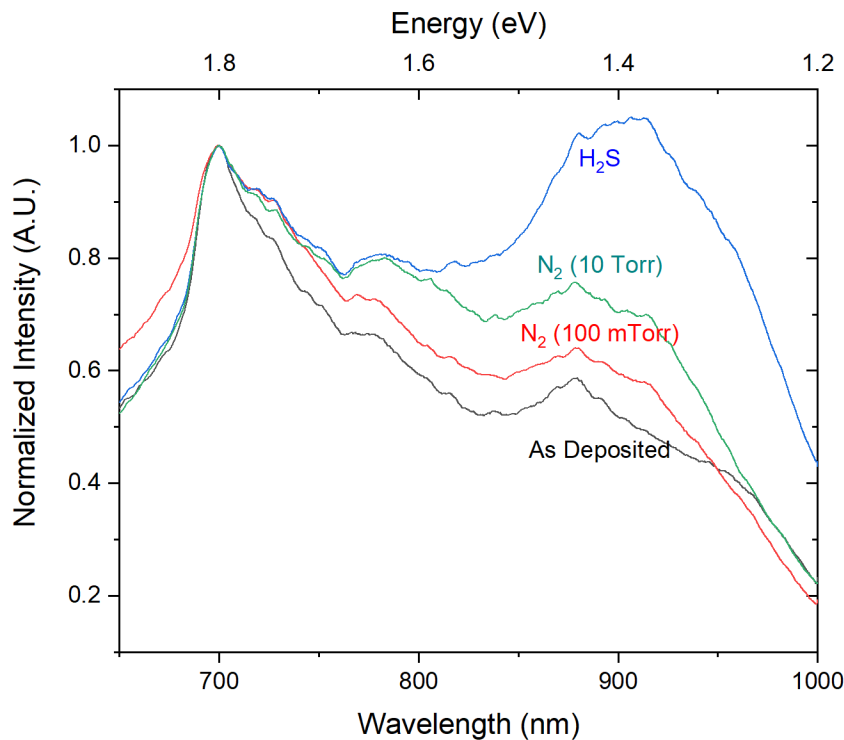
which is simplified to



This loss of sulfur increases the number of defects acting as point defect traps for holes in the material, causing the mobility of SnS annealed in sulfur-poor ambient to have a lower mobility than the as-deposited SnS despite having significantly larger grain sizes after the high temperature anneal processes. When SnS is annealed in nitrogen atmosphere under a lower pressure of 100 m Torr, we observe further reduction in Hall mobility compared to the film that was annealed under 10 Torr of N_2 . The lower mobility values can be attributed to more extensive desulfurization when exposed to lower pressures of N_2 at high temperatures, increasing to the amount of defect scattering of the charge carriers. Although sulfur vacancies have a lower formation enthalpy than tin vacancies in the Sn-rich limits, the tin vacancies act as a shallow

donor in SnS and are the dominant contributor to the p-type conductivity of SnS. As such, we do not expect significant changes in hole density in response to the passivation of sulfur vacancies from annealing in a sulfur-rich ambient. The preservation of a lower carrier density is an attractive characteristic of the post-deposition treatment for photovoltaic applications as an increase in the majority carrier concentration of SnS can lead to an undesired increase in the recombination of photo-generated minority carriers of opposite charge when trapped in a sub-gap state.

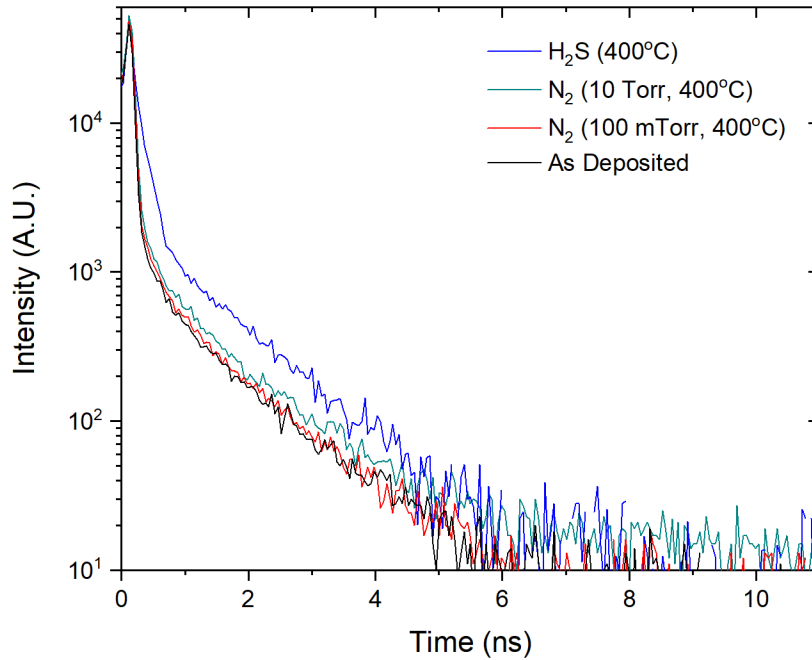
6.4.3 Spectral Resolved Photoluminescence Measurements



Two strong independent emission bands are discerned at around 700 nm and 900 nm. The PL peak at 1.4 eV is usually assigned to the band-to-band recombination of the forbidden direct

bandgap of SnS and the sharper emissions at 1.7eV is typically attributed to defect states [17, 18]. By comparing the normalized intensity ratios of the two emissions, it is found that the amount of sulfurization of the SnS strongly influences the band edge PL emission, with films annealed in a H₂S ambient demonstrating a much stronger band edge emission corresponding to a more defect-free material. Interestingly, the as-deposited SnS film showed a weaker PL signal at 1.3 eV compared to even the films that have been the most extensively desulfurized under 0.1 Torr of nitrogen during the anneal treatment. We can speculate that this indicates the dominance of recombination at grain boundaries of the as-deposited SnS film as opposed to recombination in the SnS bulk due to the sulfur vacancies. This discovery certainly highlights the importance of leveraging a high temperature post-deposition process for mitigating point defects in SnS-based devices. The PL spectrum also allowed us to decide on using an excitation wavelength of 800 nm and a 1000nm short-pass filter to evaluate the decay characteristics of the band-to-band emission when performing the subsequent time-resolved PL measurements.

6.4.4 Time Resolved Photoluminescence Measurements



A PL transient decay is observed when the SnS thin film is excited by a 800 nm laser, which can be modeled by a biexponential fit to obtain a fast and a slow lifetime component τ_1 and τ_2 commonly attributed to the carrier lifetimes near the surface and in the bulk of the film, respectively [19]. The unannealed SnS ALD film displayed a very low τ_1 of 0.02 ns and a slower τ_2 of 0.99 ns. When the film is annealed in the H₂S ambient, the fast lifetime component increased to 0.2 ns while the slow component lengthened remarkably to 1.3 ns. The increase in τ_2 after annealing in H₂S ambient is strongly correlated to its stronger inter-band recombination emission line observed in the spectrally resolved PL measurements. This is indicative of a reduction in bulk defect density arising from sulfur vacancies in SnS which have the detrimental effect of acting as recombination centers for the photo-excited carriers. On the other hand, SnS films that were exposed to sulfur-poor anneal conditions all displayed fast component τ_1 in sub-

200 ps region similar to the as-deposited SnS films and with a slower lifetime component τ_2 in the range of 0.88 ns to 0.99 ns. This is once again in agreement with the photoluminescence spectrum showing an increased deep level emission due to a higher concentration of sulfur vacancies in the film which behaves as recombination trap sites in the SnS bulk for the photo-generated electrons. The drastic change in τ_1 after annealing in H₂S but not in sulfur-poor ambient may suggest that the grain boundaries in as-deposited SnS were much more sulfur-deficient compared to the grain interior, and were thus highly defective due to the higher density of sulfur vacancies. Auger recombination was found to have a negligible contribution to the carrier lifetimes of all SnS samples as there was no observable changes in the PL transients with variations in excitation intensity.

Changes in PL intensity in the grain interiors and at the grain boundaries of SnS were monitored after being subjected to annealing treatments in H₂S and in N₂. **Figure 6.4a** shows the PL emission map of SnS film surfaces where the grain interiors display a remarkable increase in PL intensity from lower concentrations of sulfur vacancies when annealed in H₂S in contrast to films annealed in N₂ (**Figure 6.4b**) showing weaker emissions from within the grains as a result of sulfur loss during the anneal. The same conclusion can be drawn from depth-profile measurements in **Figure 6.4c,d-f** which also shows no significant variation in the PL intensity between the top and bottom regions of the grain, suggesting that the anneals in 10 Torr of H₂S is capable of suppressing sulfur vacancies throughout the height of the grain. Negligible changes were observed at the grain boundaries suggesting that radiative defects at grain boundaries are not dominated by mid-gap defects originating from sulfur vacancies.

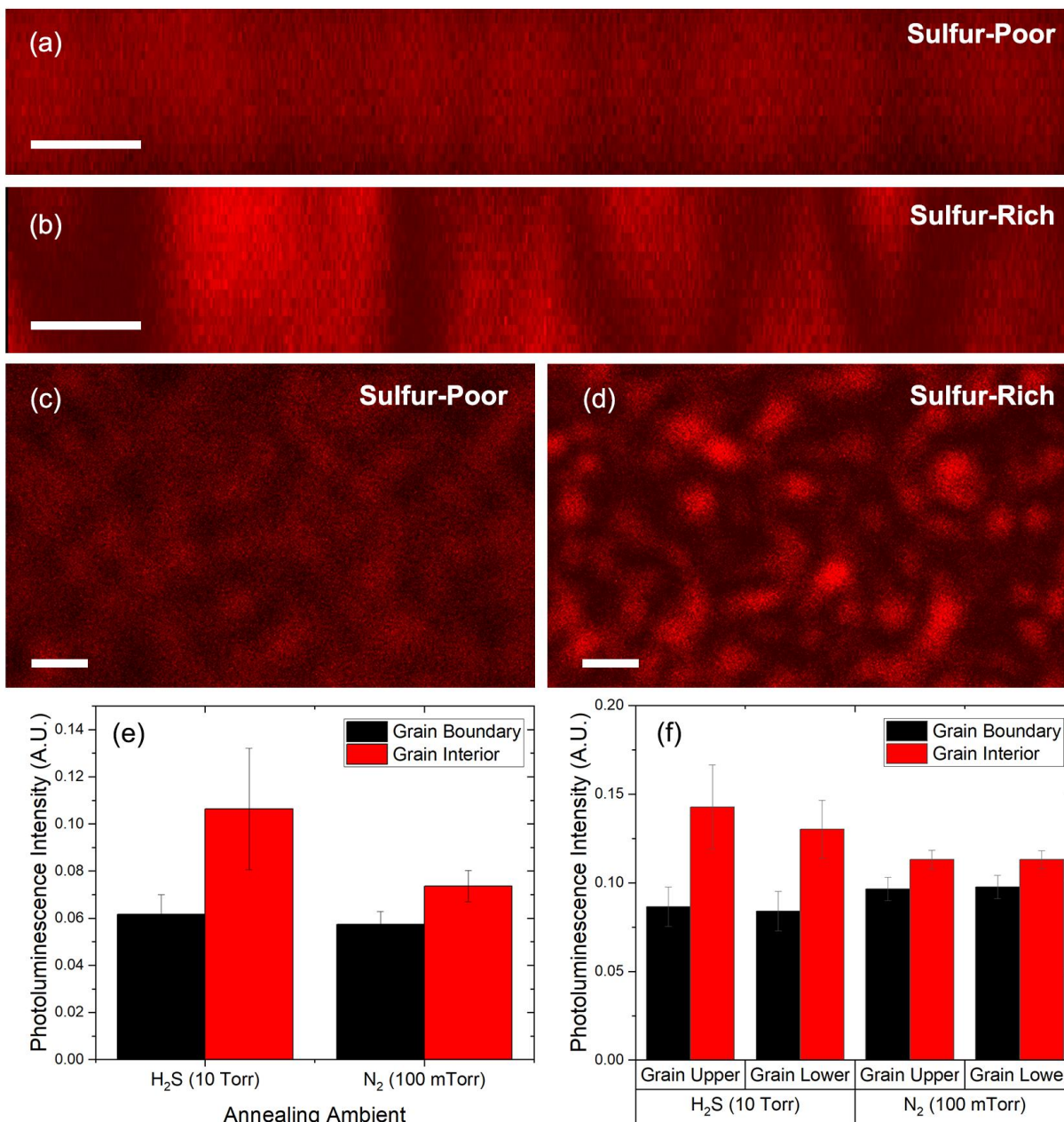


Figure 6.4. Cross-sectional PL intensity depth profile maps comparing the intensity enhancements in the grain interiors and grain boundaries of SnS films annealed in (a) 0.1 Torr of N₂ ambient and (b) 10 Torr of H₂S ambient, and topological intensity maps when annealed in (c) 0.1 Torr of N₂ ambient and (d) 10 Torr of H₂S ambient. All scale bars represent 1 μ m. Bar plots comparing the differences in photoluminescence intensities after annealing in a sulfur-rich and a sulfur-poor ambient (e) between the grain boundaries and grain interiors at the surface of the film, and (f) between the grain boundaries and grain interiors at the top and at the bottom of the grain from PL depth-profile measurements.

6.4.5 Photovoltaic Device Characterization

SnS/SnO₂/Zn(O,S) heterojunction solar cells were fabricated using an SnS absorber layers that were as-deposited, annealed in nitrogen at 10 Torr and at 100 mTorr, and annealed in H₂S at 10 Torr in order to understand the influence that different anneal conditions have on device performances. All devices have an ultra-thin layer of oxidized SnO₂ passivating interface between the SnS and the Zn(O,S) layers. The Zn(O,S) buffer layers were custom tailored for optimal band alignments and carrier densities for the different SnS absorbers. The device with as-deposited and nitrogen annealed SnS were partnered with Zn(O,S) with a 6:1 ZnO:ZnS ALD cycle ratio while the device with the H₂S annealed SnS utilized a Zn(O,S) layer with a ZnO:ZnS cycle ratio of 14:1 that was also doped with nitrogen by pulsing ammonia gas after the H₂S dose in the ZnS ALD subcycle to bring down the electron density.

Figure 6.5 compares photovoltaic devices made with SnS films that were as-deposited and annealed at 300 °C under ambient of varying S richness (N₂ at 10 Torr, N₂ at 10 mTorr, and in 4% H₂S at 10 Torr). The device with no post-deposition annealing of the SnS absorber showed the lowest performance ($V_{OC} = 0.23$ V, $J_{SC} = 2.5$ mA/cm², FF = 48 %, PCE = 0.27 %) due to the having the weakest absorber layer quality with its smaller average grain sizes of ≈ 80 nm. All annealed SnS films were carried out at the same temperature and displayed similar average grain sizes in the range of 400 nm to 600 nm, resulting in remarkable enhancement of device efficiencies compared to the device with no annealing of the SnS absorber from a considerable reduction SnS grain boundaries that can contribute to charge recombination. The device with SnS annealed in the most S-deficient ambient in 0.1 Torr of N₂ showed an improved cell performance ($V_{OC} = 0.249$ V, $J_{SC} = 17.8$ mA/cm², FF = 46.5 %, PCE = 2.1 %). Annealing SnS under a less S-deficient ambient in 10 Torr of N₂ showed overall improvements to the device

parameters ($V_{OC} = 0.253$ V, $J_{SC} = 19.7$ mA/cm², FF = 47.4 %, PCE = 2.4 %) as a result of reduced sulfur loss from SnS during the anneal which led to lower sulfur vacancies contributing to deep level traps. Annealing SnS under a S-rich ambient of 10 Torr of 4% H₂S provided the most favorable environment for not only reducing grain boundaries that can contribute to recombination but also suppressed sulfur vacancies which resulted in the longer minority carrier lifetimes observed in the TRPL measurements and demonstrating the best performing devices in this study ($V_{OC} = 0.376$ V, $J_{SC} = 24.1$ mA/cm², FF = 55.0 %, PCE = 4.99 %). The enhanced device efficiency comparing the as-deposited SnS absorber to the absorber annealed in 0.1 Torr of N₂ was predominately due to the improvements in J_{SC} as the larger grain sizes enabled better carrier collection. The reduction in grain boundary recombination outweighs the increase in recombination in the grain interior, displaying an overall increase in device efficiency. Progressing from the most S-poor to the S-rich annealing ambient, the post-anneal SnS absorber experiences a decrease in sulfur vacancies and an increase in minority carrier lifetime, resulting in a significant increase in device efficiency dominated by the large V_{OC} improvements.

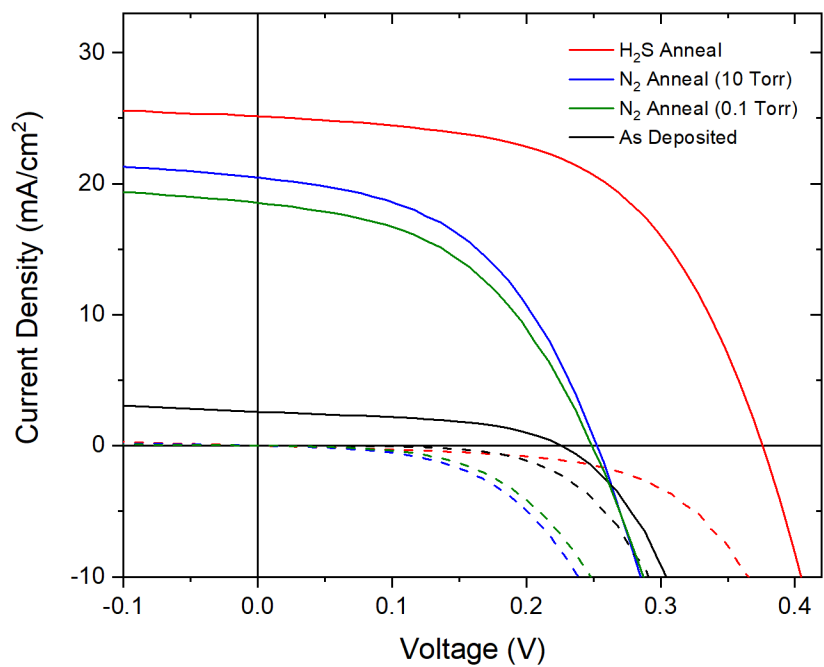


Figure 6.5. JV characteristics of Mo/SnS/SnO₂/Zn(O,S)/ZnO/ITO/Ag devices with various post-deposition anneal treatments applied to the SnS absorber, measured under AM 1.5 under dark (dashed) and AM 1.5 illumination (solid).

6.5 Conclusions

In summary, we demonstrated the effectiveness of high temperature post-deposition anneals in a sulfur rich atmosphere at increasing the minority carrier lifetimes of SnS ALD films through the mitigation of deep trap states by suppressing sulfur vacancies at grain interiors and throughout the entire height of the grain. High temperature treatments at 400 °C also promoted grain growth to sizes of 800 nm, leading to reduced concentration of grain boundaries available for recombination to occur. Despite inducing sulfur loss in an S-poor anneal ambient, devices experienced moderate V_{OC} and large J_{SC} enhancements attributed predominantly to the larger SnS grain sizes. Further improvements in device parameters were displayed by switching the ambient gas from N_2 to H_2S , mitigating mid-gap defects induced by sulfur vacancies in SnS grain interiors and throughout the entire grain height, achieving a champion solar cell with a V_{OC} of 0.376 V and a PCE of 4.99%.

6.6 Reference

1. Ramakrishna Reddy, K.T., N. Koteswara Reddy, and R.W. Miles, *Photovoltaic properties of SnS based solar cells*. Solar Energy Materials and Solar Cells, 2006. **90**(18-19): p. 3041-3046.
2. Sinsersuksakul, P., et al., *Atomic Layer Deposition of Tin Monosulfide Thin Films*. Advanced Energy Materials, 2011. **1**(6): p. 1116-1125.
3. Ichimura, M., et al., *Electrochemical deposition of SnS thin films*. Thin Solid Films, 2000. **361-362**: p. 98-101.
4. Koteswara Reddy, N., et al., *Temperature-dependent structural and optical properties of SnS films*. Journal of Applied Physics, 2007. **101**(9): p. 093522.
5. Sinsersuksakul, P., et al., *Enhancing the efficiency of SnS solar cells via band-offset engineering with a zinc oxysulfide buffer layer*. Applied Physics Letters, 2013. **102**(5): p. 053901.
6. Devika, M., et al., *Ohmic contacts to SnS films: Selection and estimation of thermal stability*. Journal of Applied Physics, 2008. **104**(12).
7. Miles, R.W., et al., *Thermally evaporated thin films of SnS for application in solar cell devices*. Thin Solid Films, 2009. **517**(17): p. 4702-4705.
8. Noguchi, H., et al., *Characterization of vacuum-evaporated tin sulfide film for solar cell materials*. Solar Energy Materials and Solar Cells, 1994. **35**: p. 325-331.
9. Sinsersuksakul, P., et al., *Overcoming Efficiency Limitations of SnS-Based Solar Cells*. Advanced Energy Materials, 2014. **4**(15): p. 1400496.
10. Sherkar, T.S., et al., *Recombination in Perovskite Solar Cells: Significance of Grain Boundaries, Interface Traps, and Defect Ions*. ACS Energy Lett, 2017. **2**(5): p. 1214-1222.
11. Park, H.H., et al., *Co-optimization of SnS absorber and Zn(O,S) buffer materials for improved solar cells*. Progress in Photovoltaics: Research and Applications, 2015. **23**(7): p. 901-908.
12. Sun, L., et al., *Band alignment of SnS/Zn(O,S) heterojunctions in SnS thin film solar cells*. Applied Physics Letters, 2013. **103**(18): p. 181904.
13. Tritsaris, G.A., B.D. Malone, and E. Kaxiras, *Structural stability and electronic properties of low-index surfaces of SnS*. Journal of Applied Physics, 2014. **115**(17): p. 173702.
14. Vidal, J., et al., *Band-structure, optical properties, and defect physics of the photovoltaic semiconductor SnS*. Applied Physics Letters, 2012. **100**(3).
15. Mangan, N.M.B., R. E.; Steinmann, V.; Jaramillo, R.; Li, J. V.; Poindexter, J. R.; Hartman, K.; Sun, L.; Gordon, R. G.; Buonassisi, T., *A Path to 10% Efficiency for Tin Sulfide Devices*. Photovoltaic Specialist Conference (PVSC), 2014 IEEE 40th, 2014: p. 2373-2378.
16. Scofield, J.H., et al., *Sputtered molybdenum bilayer back contact for copper indium diselenide-based polycrystalline thin-film solar cells*. Thin Solid Films, 1995. **260**(1): p. 26-31.
17. Devika, M., et al., *The physical properties of SnS films grown on lattice-matched and amorphous substrates*. physica status solidi (a), 2010. **207**(8): p. 1864-1869.
18. Sorgenfrei, T., et al., *Synthesis and single crystal growth of SnS by the Bridgman-Stockbarger technique*. Crystal Research and Technology, 2013. **48**(4): p. 193-199.

19. Barnard, E.S., et al., *Probing carrier lifetimes in photovoltaic materials using subsurface two-photon microscopy*. *Sci Rep*, 2013. **3**: p. 2098.

7 Atomic Layer Deposition of Tin

Germanium Oxide as a Tunable Electron

Transport Layer Optimized for SnS-based

Solar Cells

7.1 Chapter Abstract

Tin germanium oxide, $(\text{Sn,Ge})\text{O}_2$, films were prepared using atomic layer deposition and tailored to SnS absorber layer by incorporating tin oxide with various amounts of germanium to engineer the optimal energy band alignments at the interfaces of the photovoltaic devices. Electron densities were suppressed with germanium incorporation by up to one order of magnitude from 10^{20} to 10^{19} cm^{-3} , with nitrogen doping of $(\text{Sn,Ge})\text{O}_2$ further reducing carrier concentrations by another order of magnitude. Excellent tunabilities of both band energy levels and carrier concentrations enable $(\text{Sn,Ge})\text{O}_2$ to be optimized for SnS-based solar cells, demonstrating a high open-circuit voltage of 400 mV through effective mitigation of interfacial recombination at the absorber-buffer heterojunction.

7.2 Introduction

Tin monosulfide (SnS) is a promising earth abundant and non-toxic p-type semiconductor material for photovoltaic applications. SnS thin films have displayed many desirable properties including a suitable bandgap of 1.1 eV, high absorption coefficients exceeding 10^{14} cm^{-1} and relatively high mobilities ($\mu \sim 10 \text{ cm}^2\text{V}^{-1}\text{s}^{-1}$), making it an attractive alternative to leading thin film absorber materials [1-5]. The better performing SnS-based devices utilize a tunable n-type buffer layer to optimize the conduction band offset (CBO) at the p-n junction interface. Having a range of tunability in the n-type buffer is critical. A “spike” structure is formed when the conduction band edge of the p-type absorber layer is higher than in the n-type buffer layer ($E_{c,\text{absorber}} < E_{c,\text{buffer}}$) forming a barrier that impedes the collection of photogenerated currents, with the optimal offset to reside in the range of 0 eV and +0.4 eV. On the other hand, a “cliff” structure ($E_{c,\text{absorber}} > E_{c,\text{buffer}}$) results in an increase in unfavorable interface recombination[6, 7].

The best performing devices have previously been achieved with a p-SnS/n-SnO₂/n-Zn(O,S):N junction where Zn(O,S):N serves as the tunable n-type partner optimized to have a small “spike” structure at the interface for suppressing interfacial recombination[8, 9]. The addition of an ultra-thin SnO₂ ALD layer between the SnS and Zn(O,S):N layers was later discovered to significantly increase the open-circuit voltage[10]. It is believed that the SnO₂ acts as a diffusion layer that limits the zinc diffusion into SnS during the Zn(O,S):N ALD deposition process and causing increased recombination at the p-n interface and hence the degradation of the junction’s rectification properties. While a few monolayers of SnO₂ improved the device performance, the enhancement was diminished when the oxide layer thickness increases until it is thick enough to form a conduction band. This decrease in performance can be explained by the

unfavorable cliff structure of the SnS/SnO₂ junction disrupting the optimized spike structure formed at the SnS/Zn(O,S):N interface. Consequently, a small spike structure at the crucial interface optimizes for a reduction in the interface recombination while being small enough to avoid impeding the efficient collection of the photo-generated electrons.

Germanium-doped tin oxide is the next logical advancement towards the design of an improved n-type buffer layer for SnS-based solar cell devices. By replacing the Zn-based buffer layer Zn(O,S):N with a tin oxide based partner material, we completely eliminate the problem of introducing detrimental deep-level defects in SnS due to zinc diffusing from the buffer layer into the SnS absorber layer. Theoretical calculations also show the passivating effects that an oxide layer has on the surfaces of SnS where dangling bonds exist[11]. The optimal conduction band energy levels provided by an optimized Zn(O,S) layer is similarly achievable through fine-tuning the conduction band edges of SnO₂ by doping germanium into tin oxide, transforming the original cliff structure of undoped SnO₂ to a desired spike structure predominantly by raising the conduction band energy level of SnO₂. Using ALD as the fabrication technique of choice for (Sn,Ge)O₂ provides incredibly precise control over the doping levels of Ge and N simply by adjusting the precursor pulse ratios. By mirroring the tunability of Zn(O,S):N without the risk of having Zn diffusing across the heterojunction interface, (Sn,Ge)O₂ is seen as a promising n-type buffer layer suitable for not only SnS, but also highly applicable to various p-type absorber materials, such as Cu(In,Ga)(S,Se)₂ (CIGS)[12, 13] and Cu₂ZnSn(Se,S)₄ (CZTS)[14-16]. This work presents SnS-based photovoltaic devices using (Sn,Ge)O₂ as an n-type buffer layer with tunable band alignments and adjustable carrier densities, and proceeds to evaluate the effect of germanium and nitrogen doping on the CBO, material conductivity and the resulting performances of the SnS-based solar cell devices.

7.3 Experimental

An ALD process was used to deposit SnO₂ using tetrakis(dimethylamido)tin(IV) ([[(CH₃)₂N]₄Sn, TDMASn, 99.9% trace metals basis, Sigma Aldrich) and hydrogen peroxide (H₂O₂, 30% w/w in H₂O, Sigma Aldrich). Tin precursor vapor assisted by N₂ and hydrogen peroxide vapor were injected sequentially into the deposition chamber to allow the chemical reactions to occur successively on the substrate surfaces. To prepare (Sn,Ge)O₂, germanium was doped into SnO₂ by injecting the germanium precursor vapor of germanium(IV) methoxide (Ge(OCH₃)₄, Sigma Aldrich) alternated with doses of hydrogen peroxide vapor. The tin precursor source was kept at 60 °C, germanium precursor source at 30 °C and hydrogen peroxide at 30 °C. The ALD sequence for (Sn,Ge)O₂ was $[[(\text{TDMASn}/\text{N}_2/\text{H}_2\text{O}_2/\text{N}_2)] \times m + [(\text{Ge}(\text{OCH}_3)_4/\text{N}_2/\text{H}_2\text{O}_2/\text{N}_2) \times n]] \times o$, where m and n indicate the number of sub-cycles of SnO₂ and GeO₂ respectively and o indicates the number of super-cycles. The doping level of germanium can be tuned by adjusting the SnO₂/GeO₂ sub-cycle ratio m/n . The process chamber is maintained at temperatures varying from 200°C to 275°C using a Linberg Blue Minimite furnace. Thermally oxidized silicon wafers, glassy carbon planchets, and quartz were utilized as substrates for the deposition of (Sn,Ge)O₂ thin films. The substrates were treated by UV/ozone cleaner (Samco model UV-1, wavelengths = 185 nm and 254 nm) for 5 minutes at room temperature before being introduced into the process chamber. These substrates are supported by a 316L stainless steel substrate holder with an embedded K-type thermocouple probe for temperature monitoring. Pressure in the deposition chamber was monitored using a convection enhanced pirani gauge (275 Series Gauge Tube, Kurt J. Lesker).

The band alignments at the SnS/SnGeO₂ interface is determined by photoelectron spectroscopy [17]. An X-ray (Al K α) source is used to measure the binding energies of Sn and Ge core levels with respect to the valence band maximum energy of bulk SnS and (Sn,Ge)O₂ films using bilayered films of SnS with (Sn,Ge)O₂ overlayers. The transmittance and reflectance spectra of SnS and (Sn,Ge)O₂ were measured at normal incidence with an ultraviolet-visible-near-infrared (UV-vis-NIR) spectrophotometry (Hitachi U-4100 UV-vis-NIR spectrophotometer) in the wavelength range of 200 to 800 nm. 500 nm of ALD SnS and 100 nm of ALD (Sn,Ge)O₂ were deposited on quartz substrates for the optical characterization. Film thicknesses were measured using x-ray reflectivity measurements (PANalytical X-Pert Pro) and using cross-section scanning electron microscopy (Carl Zeiss Ultra 55 FESEM).

A photovoltaic device structure of Si/SiO₂/Mo/SnS/(Sn,Ge)O₂/ZnO/ITO/Ag was used in this study. A Mo bilayer was first sputtered on silicon (100) substrates with 300 nm thick layer of thermally oxidized silicon dioxide on the surface. The first layer of Mo was deposited at 10 mTorr for 30 minutes using RF magnetron sputtering, followed by a second layer at 2 mTorr for 30 minutes. The SnS thin film absorber layers were deposited on Mo-coated (500 nm) thermally oxidized silicon substrates using an ALD process from the reaction of bis(N,N'-diisopropylformamidinato)Sn(II) (Sn(famd)₂, Strem Chemicals) and hydrogen sulfide (H₂S, 4% in N₂). The Mo-coated substrates were maintained at 120 °C and the Sn source was kept at 60 °C. Each ALD cycle of SnS consists of one dose of Sn precursor vapor assisted with N₂ gas, followed by one dose of H₂S, alternating continuously in a closed valve condition until the desired thickness has been achieved. The SnS films were then annealed under a constant flow of 60 sccm of H₂S, maintained at a substrate temperature of 400 °C and under a process pressure of 10 Torr for an hour. ZnO thin film was deposited at 120 °C by ALD using alternating doses of diethylzinc

($\text{Zn}(\text{C}_2\text{H}_5)_2$, DEZ, >52 wt.% Zn basis, Sigma Aldrich) and deionized water vapor. 300 nm of tin-doped indium oxide (ITO) was deposited at room temperature via RF magnetron sputtering. A shadow mask was used during the ITO deposition process to define an active device area of 0.24 cm^2 . The photovoltaic device was completed by the e-beam evaporation of a 500 nm thick layer of Ag as the top electrode patterned with metal grid lines evaporated through a second shadow mask at room temperature.

7.4 Results and Discussion

7.4.1 Growth

(Sn,Ge)O₂ thin films were prepared at a deposition temperature of 200°C which is within the common temperature windows for the ALD processes of SnO₂ and GeO₂. Tin oxide films have been successfully deposited by ALD in the process temperatures of 50-300°C using TDMA(Sn) as the tin source[18]. Ge(OCH₃)₄ was discovered to not deposit a germanium oxide film on non-hydroxylated surfaces such as SiO₂ wafers at substrate temperatures of 200-300°C. Instead, the precursor required the OH-terminated surfaces of ALD-SnO₂ and temperatures of at least 200°C for the reaction with water vapor to occur and promoting the incorporation of germanium into SnO₂. The lower end of the overlapping ALD temperature window of 200°C was selected to exploit the reduced doping efficiency of germanium for establishing finer control over film compositions and access more uniform distribution of dopants throughout the film.

7.4.2 Elemental Composition

Table 4. Elemental composition of ALD (Sn,Ge)O₂ films measured by high resolution XPS. $x = [Ge]/([Sn]+[Ge])$

Elemental Composition				
SnO₂/GeO₂ ALD sub-cycle ratio	[Sn] (at. %)	[Ge] (at. %)	[O] (at. %)	<i>x</i>
1:0	33.5	0	66.5	0
59:1	34.8	0.1	65.1	0.003
29:1	37.0	0.3	62.7	0.009

19:1	38.2	0.5	61.3	0.013
9:1	34.4	1.3	64.4	0.05
3:1	34.4	6.2	59.5	0.15
1:1	22.5	14.7	62.5	0.40

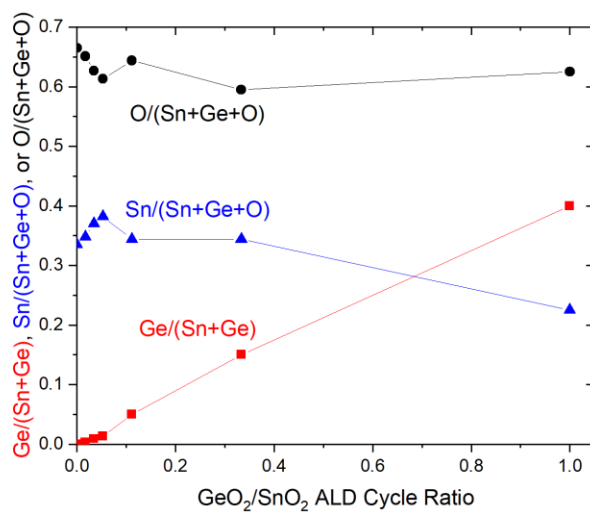
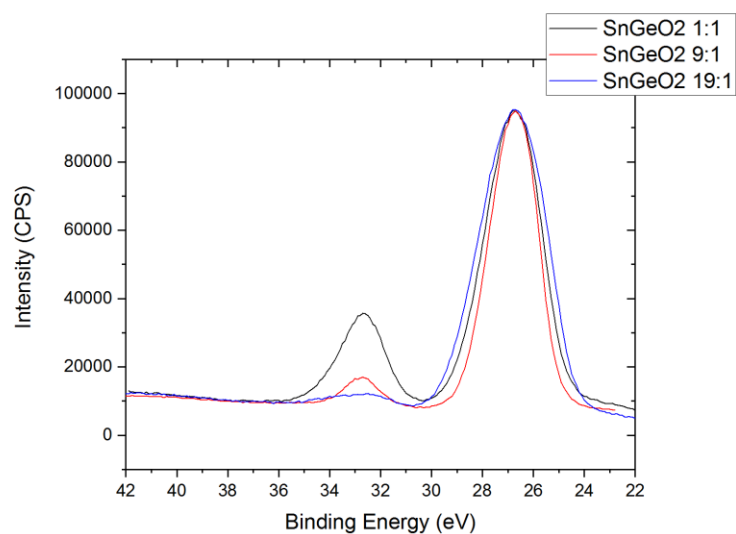


Figure 7.1. (a) The high resolution XPS spectra of the Ge-3d core level of SnO₂ ALD films and the increase in the XPS peak intensity with increasing amount of Ge incorporation in the film, and (b) plot displaying the variations in elemental compositions O/(Sn+Ge+O), Sn/(Sn+Ge+O), and Ge/(Sn+Ge) vs. the GeO₂/SnO₂ ALD cycle ratio.

Table 4 and **Figure 7.1b** shows the germanium content in the (Sn,Ge)O₂ film is approximately equal the precursor pulse ratio, indicating excellent doping efficiency of Ge in the presence of OH-terminated surfaces during the Ge precursor pulse, and slightly more so in films with greater amount of Ge incorporated. For example, GeO₂/SnO₂ ratios of 1:29 (0.03) and 1:1 (1) delivered film with [Ge]/([Sn]+[Ge]) values of 0.01 and 0.4, respectively. In **Figure 7.2c-d**, carbon and nitrogen peaks were observed only on the surface of the films due to exposure to ambient contaminants. Both elements are no longer detectable after *in-situ* sputtering of the film surface with Ar⁺ ions for 30 seconds in the XPS analysis chamber. The absence of C and N contaminants are indicative of the high purity of the (Sn,Ge)O₂ films as a result of the clean and complete reaction between both tin and germanium precursors with hydrogen peroxide when operating within the common ALD windows of both the SnO₂ and GeO₂ ALD processes.

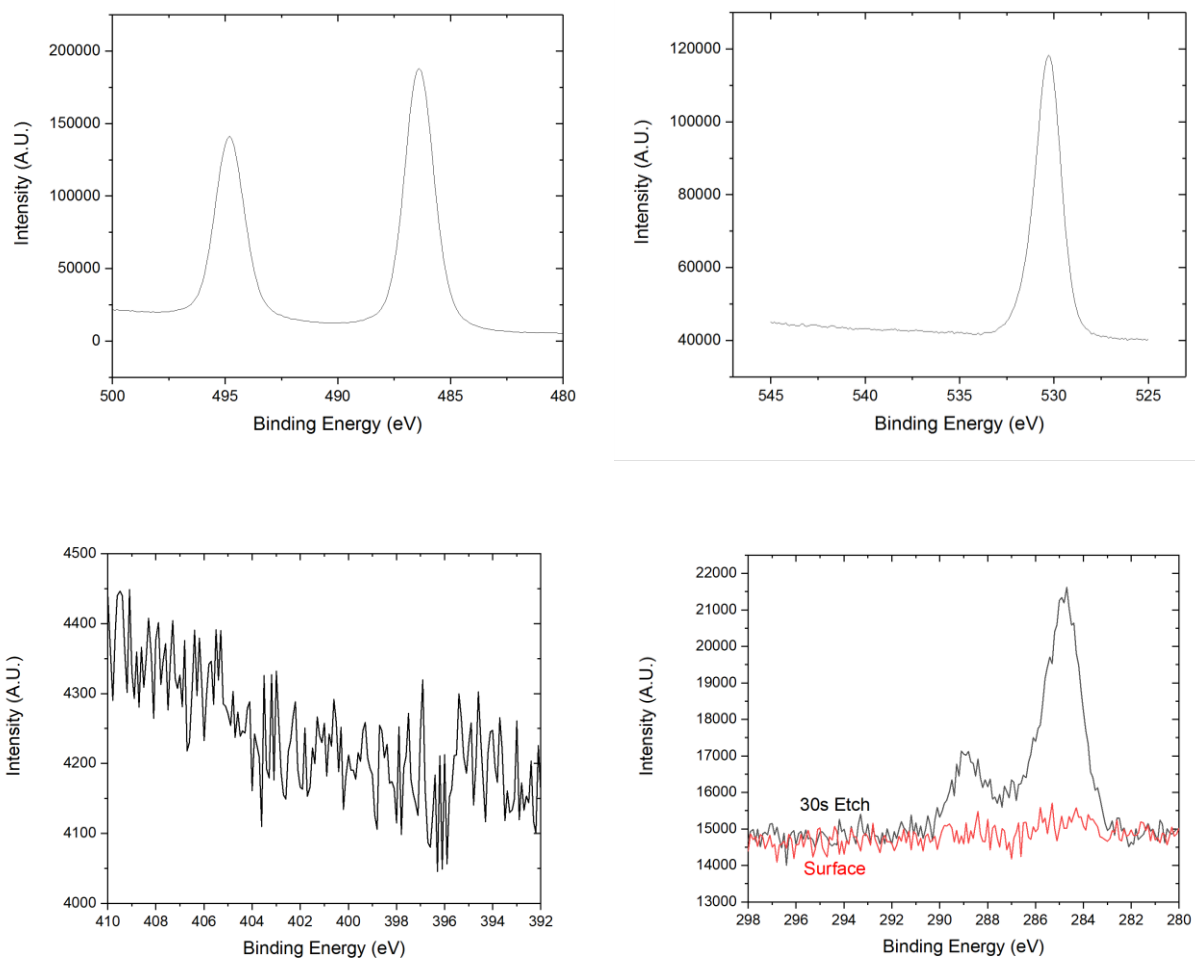
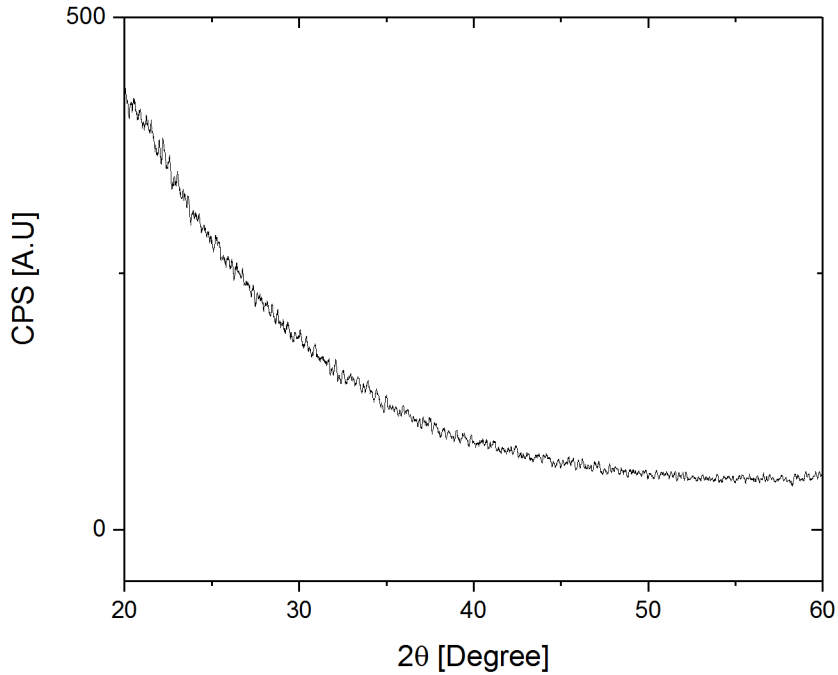


Figure 7.2. XPS measurements after 30 seconds of in-situ Ar⁺ sputtering of the film surface of the (a) Sn-3d core level, (b) O-1s core level, (c) C-1s core level, and (d) N-2p core level of a typical ALD (Sn,Ge)O₂ film.

7.4.3 Structural Properties



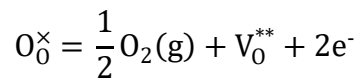
The X-ray diffraction pattern of (Sn,Ge)O₂ films deposited on 1 inch × 1 inch quartz substrates exhibits no specific peaks from the film, which suggests near amorphous or nano-crystalline structure of the film. Increasing the amount of germanium in the film does not induce any detectable change to the film crystallinity.

7.4.4 Electron Carrier Suppression from Germanium Incorporation

The carrier mobility, electron carrier density and resistivity are plotted as a function of the Ge/(Ge+Sn) ratio as shown in **Figure 7.3**. Hall measurements demonstrate that the (Sn,Ge)O₂ films have n-type conductivities with electron concentrations tunable between 10¹⁸ cm⁻³ and 10²⁰ cm⁻³. The electron hall mobility experienced little variations with varying amount of germanium

incorporation in the film which is expected as the material remains of an amorphous nature independent of germanium doping levels. The germanium doped tin oxide films show lower carrier concentration compared to the undoped tin oxide films. Since both tin and germanium carry are in the same +4 oxidation state, we do not expect any increase in the electron concentration from germanium acting as an electron donor. Instead, the conductivity of SnO₂ films are attributed to the presence of oxygen vacancies in the material[19].

Deconvolution of the O-1s XPS spectra of (Sn,Ge)O₂ ALD films as presented in **Figure 7.4** reveal two components with peak centers at 531.2 eV and 532.7 eV, respectively. Neither of these photoemission lines can be assigned to O-Ge bonds as both lines exist in the O-1s region of undoped SnO₂, with the higher energy emission reducing in intensity as more Ge is doped into the material, in contrast to the expected behavior of the O-Ge line. Instead, the lower energy peak O_L is assigned to the oxygen ions bonded to Sn ions, while the higher energy peak O_{OV} can be attributed to the presence of oxygen vacancies in the SnO₂ sublattice. It is observed that as the Ge content of the film is increased from 0 to 14 at.%, the O_{OV} peak assigned to oxygen vacancies reduced from 59% in the undoped SnO₂ film down to 2% in the highly doped material with 14 at.% of germanium, corresponding to a significant reduction in the concentration of oxygen vacancies. This is explained by the bond strength of Ge-O (657.5 kJ mol⁻¹) which are greater compared to that of Sn-O (528 kJ mol⁻¹), making it more effective at capturing oxygen and hence resulting in the suppression of the formation of oxygen vacancies. The electrical conductivity of SnO₂ is typically attributed to the formation of oxygen vacancies, as shown by the equation



where two electron carriers and a doubly charged oxygen vacancy are the result of the loss of an oxygen molecule for each SnO₂ molecule in the material. Thus, when the amount of germanium doping content is increased, the resulting reduction in oxygen vacancies corresponds to a decrease in the electron carrier concentration of the film, giving rise to an increased electrical resistivity.

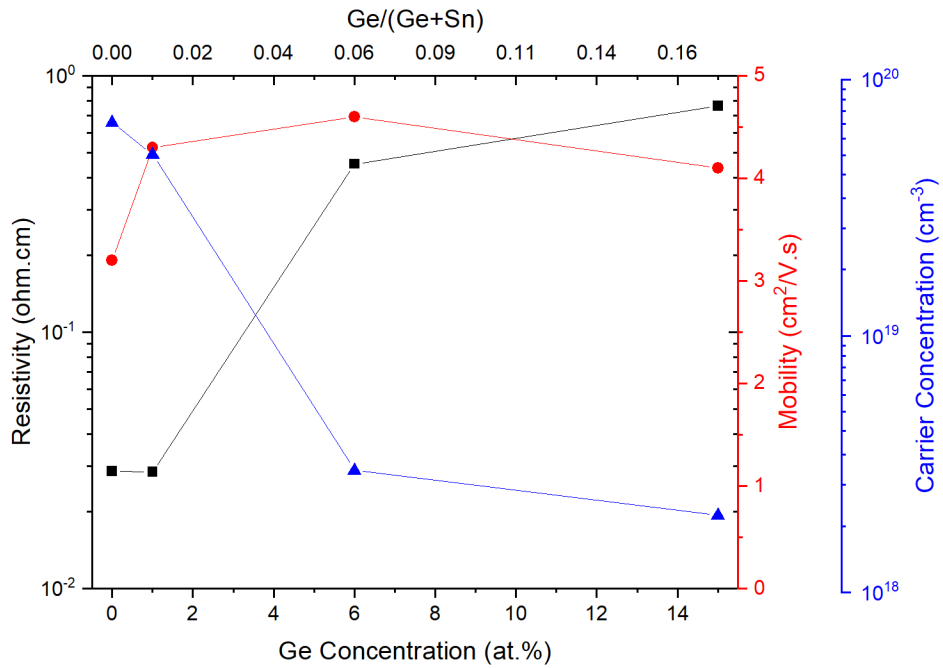


Figure 7.3. Plot of resistivities (black), electron carrier concentration (blue), and hall carrier mobility (red) with varying Ge content incorporated into SnO₂ films.

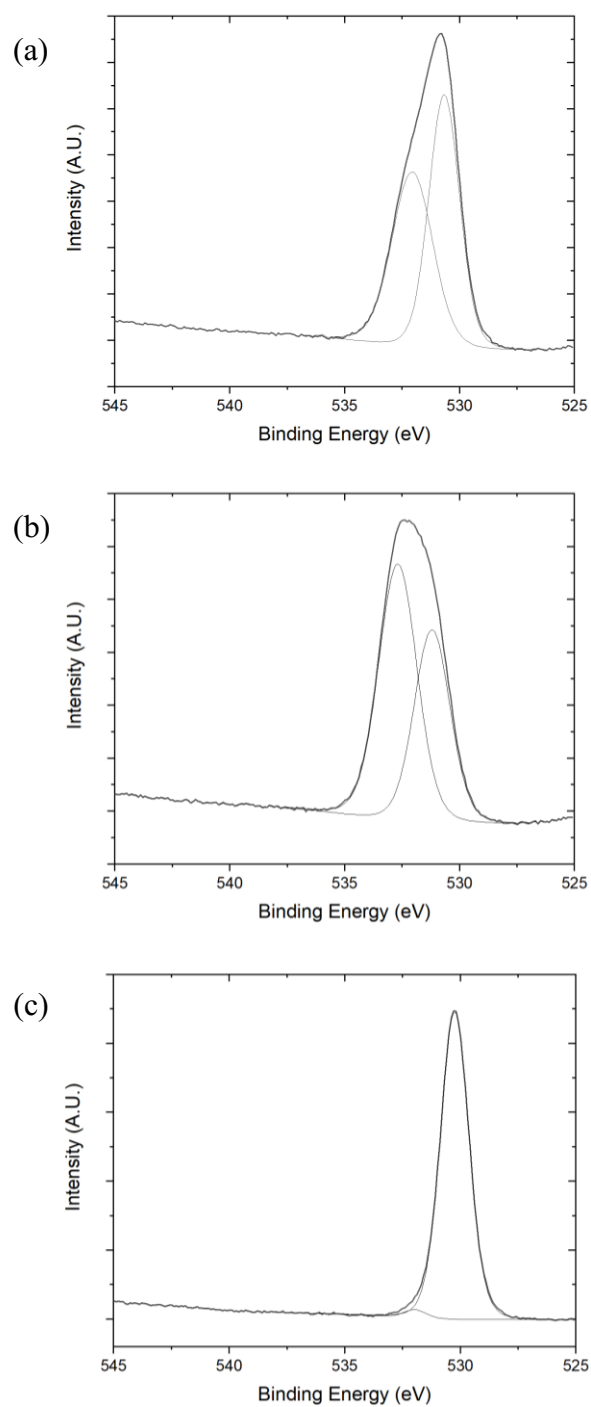


Figure 7.4. The O 1s region of XPS spectra of SnO₂ thin films with Ge contents of (a) 0 at.%, (b) 1 at.%, and (c) 14 at.% from films ALD deposited with SnO₂/GeO₂ ALD cycle ratios of 1:0, 9:1, and 1:1 respectively.

7.4.5 Band Gap and Band Alignment

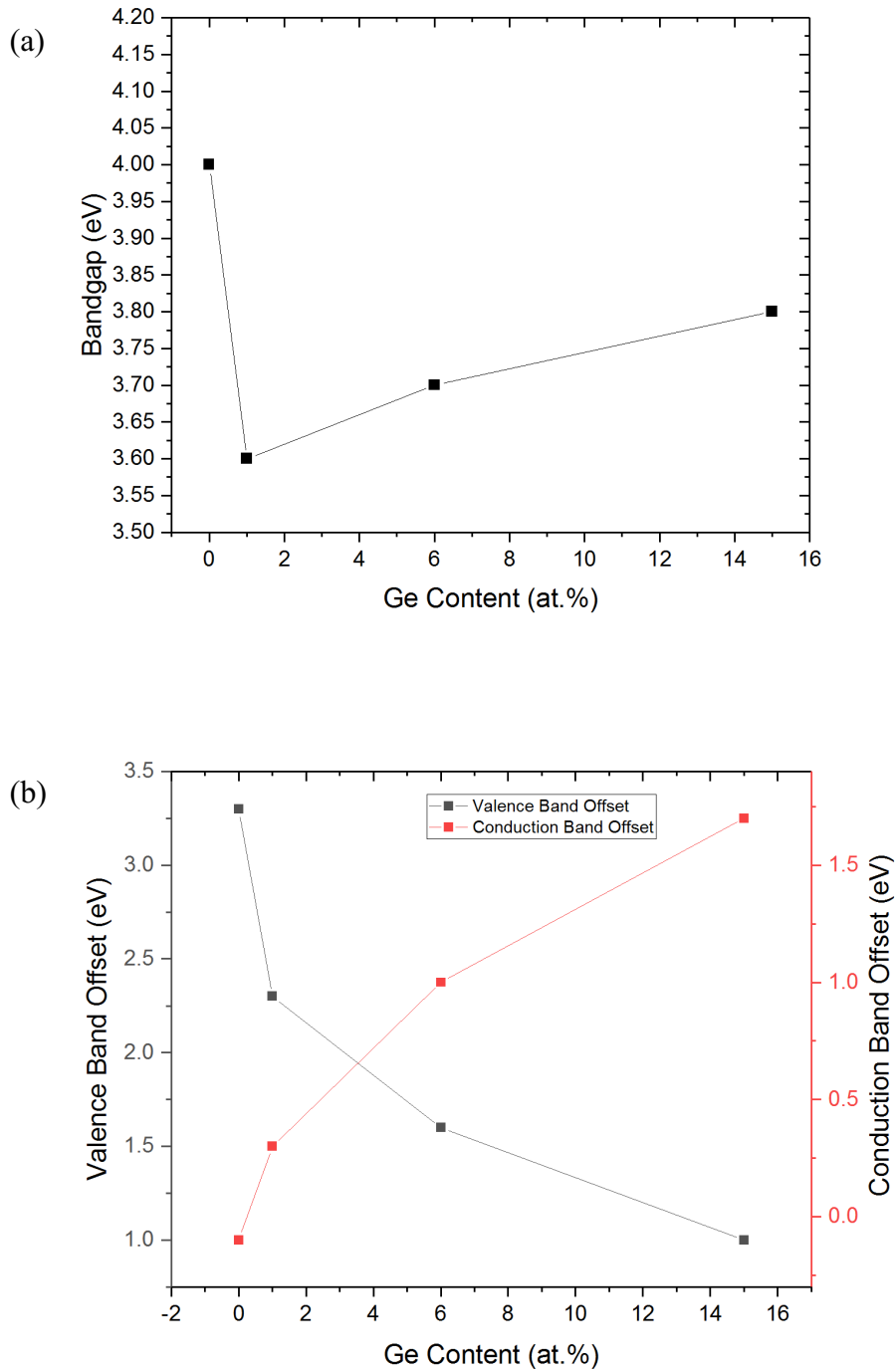


Figure 7.5. Effect of various amounts of germanium incorporation in SnO₂ films on (a) optical bandgaps as determined from absorption data, and (b) offsets of both the valence bands and conduction bands at the heterojunction formed with SnS.

The absorption coefficient α is obtained from the optical transmission and reflectance measurements and calculated using

$$\alpha = \frac{1}{d} \ln\left(\frac{1-R}{T}\right)$$

where d is the film thickness, R and T are the reflectance and transmittance of the film, respectively.

The optical bandgap energy value is obtained from plots of α^2 vs. photon energy for the various ALD films deposited on quartz substrates, using the Tauc relation for direct transitions[20]

$$\alpha(h\nu) \propto (h\nu - E_g)^{\frac{1}{2}}$$

where $\alpha(h\nu)$ is the absorption coefficient, $h\nu$ is the photon energy, and E_g is the optical bandgap.

The bandgap is then obtained by extrapolating to $\alpha \cdot h\nu = 0$. Both the electron and hole effective masses are assumed to be constant. Bilayer samples of 500-nm-thick SnS and 5-nm-thick SnO₂ with various concentrations of germanium dopants were fabricated to investigate the electronic band alignment of (Sn,Ge)O₂ relative to SnS. The valance band offset (ΔE_{VB}) and conduction band offset (ΔE_{CB}) in the SnS/(Sn,Ge)O₂ stack are respectively calculated using the relation

$$\Delta E_{VB} = (E_{Sn-3d}^{SnS/(Sn,Ge)O_2} - E_{Ge-3d}^{SnS/(Sn,Ge)O_2}) + (E_{Ge-3d}^{(Sn,Ge)O_2} - E_{VBM}^{(Sn,Ge)O_2}) - (E_{Sn-3d}^{SnS} - E_{VBM}^{SnS})$$

$$\Delta E_{CB} = (E_{Sn-3d}^{SnS/(Sn,Ge)O_2} - E_{Ge-3d}^{SnS/(Sn,Ge)O_2}) + (E_{Ge-3d}^{(Sn,Ge)O_2} - E_{VBM}^{(Sn,Ge)O_2}) - (E_{Sn-3d}^{SnS} - E_{VBM}^{SnS}) \\ + (E_g^{(Sn,Ge)O_2} - E_g^{SnS})$$

where $E_g^{(Sn,Ge)O_2}$ and E_g^{SnS} are the optical band gaps of bulk (Sn,Ge)O₂ and SnS, respectively[21].

Bandgap bowing is demonstrated in (Sn,Ge)O₂ in **Figure 7.5a** where the bandgap of SnO₂ narrows initially when fractions of germanium is added to SnO₂. At higher amounts of germanium incorporation, the bandgap begins to widen towards that of GeO₂ to complete the bowing of the bandgap. When increasing the doping levels of germanium reduce the electron concentrations to under 10¹⁹ cm⁻³, the decreased influence of the Burstein-Moss effect is believed to be competing with the bandgap widening towards GeO₂ values (5.8 eV[22]), contributing to the bowing effect of the bandgap. For all values of germanium content that was studied, the bandgap of (Sn,Ge)O₂ remains above 3.5 eV, enabling SnO₂ in the entire doping range highly suitable to serve as a window layer of solar cells by possessing excellent transparency in the AM 1.5 spectrum. **Figure 7.5b** shows (Sn,Ge)O₂ films exhibiting a monotonic decrease in the valence band offsets relative to SnS, resulting in an overall monotonic increase in conduction band offsets with increasing Ge content of the SnO₂ film. An almost-linear relationship is observed between the conduction band offsets and the amount of germanium doping despite experiencing bowing of its optical bandgap. This makes it trivial to tune the CBO simply by controlling the SnO₂/GeO₂ ALD cycle ratio.

7.5 SnS/(Sn,Ge)O₂ Heterojunction Solar Cell Devices

The optimal composition of the (Sn,Ge)O₂ buffer layer for partnering with SnS was determined by tuning the energy band alignments at the SnS/(Sn,Ge)O₂ heterojunction. Devices with an active area of 0.24 cm² were fabricated using 500 nm thick ALD SnS as the absorber and with different elemental compositions of (Sn,Ge)O₂ buffer layers, achieved by varying the ALD cycle ratios of SnO₂ to GeO₂ during the deposition process. SnO₂:GeO₂ ALD sub-cycle ratios of 59:1, 39:1, 19:1, 9:1, 3:1, and 1:1 were used to fabricate the devices, and a germanium-free SnO₂ buffer layer served as the buffer layer for the baseline device. The amount of germanium in these films for the various SnO₂:GeO₂ ALD sub-cycle ratios can be found in **Table 4**. The undoped SnO₂ layer formed a type-II “cliff” structure with SnS due to having a slightly negative conduction band offset which caused the device to suffer from increased interfacial recombination near the p-n junction. While SnO₂ provides beneficial passivating effects at the interface between SnS and Zn(O,S), it lacked the appropriate band alignment with SnS and resulted in non-rectifying devices when the SnO₂ layer exceeded several nanometers in film thickness. Since germanium has demonstrated the ability to raise the conduction band energy level of SnO₂, doping germanium into the film shifts the heterojunction into a type-I scenario with a positive conduction band offset, improving the rectification and hence the performance of the device. However, as we decrease the SnO₂/GeO₂ ALD sub-cycle ratio and consequently incorporate too much germanium into the material, the CBO with SnS increases considerably to the point where photo-generated electrons are being impeded. Although having a (Sn,Ge)O₂ buffer layer with an ALD cycle ratio of 19:1 demonstrated modest J-V characteristics under illumination relative to the undoped SnO₂ layer, the device had a low fill factor of 25% and displayed a lackluster PCE of 0.4%. Decreasing the amount of germanium content by switching

to a SnO₂/GeO₂ ALD cycle ratio of 29:1 is expected to provide improved performances with the presence of a sufficiently small conduction band spike at the heterojunction, but the actual device exhibited a poor ohmic J-V response. For this composition with a SnO₂/GeO₂ cycle ratio of 29:1, the electron density of (Sn,Ge)O₂ is higher than the film with a 19:1 cycle ratio. Doping (Sn,Ge)O₂ with nitrogen provided a significant recovery of the diode quality by decreasing the conductivity of the buffer layer. Nitrogen is introduced into the lattice of (Sn,Ge)O₂ by injecting an additional dose of purified NH₃ gas immediately following the water vapor dose at the end of each GeO₂ ALD subcycle. Nitrogen incorporation in the film successfully serves to reduce the larger electron density from $5 \times 10^{19} \text{ cm}^{-3}$ down an order of magnitude to $6 \times 10^{18} \text{ cm}^{-3}$ to compensate for the higher carrier density due to the reduction in germanium doping. Charge compensation occurs when acceptor levels that are created in the SnO₂ band gap neutralizes the electron density due to oxygen vacancies, leading to the reduced carrier density in the material[23].

The device utilizing the nitrogen doped (Sn,Ge)O₂ buffer layer with an ALD sub-cycle ratio of 29:1 demonstrates the best photovoltaic performance with $J_{sc} = 12.2 \text{ mA/cm}^2$, $V_{oc} = 0.40 \text{ V}$, $FF = 46\%$, and $PCE = 2.21\%$. This device has the highest reported V_{oc} to date for a SnS-based solar cell.

7.6 Conclusions

In conclusion, we have successfully demonstrated the atomic layer deposition of (Sn,Ge)O₂ as an extremely desirable buffer layer for SnS-based solar cells. Significant improvements in the open-circuit voltages can be captured through optimization of the conduction band alignments and carrier concentration of the buffer layer. Germanium doping raises the conduction band level of

SnO₂ while reducing the electron concentration by reducing the oxygen vacancies in the film. By incorporating nitrogen into the film using ammonia gas, the carrier concentration of (Sn,Ge)O₂ can be reduced to optimize for the absorber layer. Our results highlight the importance and advantages of exploiting an electrically and energetically tunable buffer material such as (Sn,Ge)O₂ with an adjustable conduction band energy level, enabling the CBO to be adapted to a wide range of absorber materials and surfaces, while at the same time being able to change the carrier concentration to match that of the absorber material. Furthermore, avoiding the use of zinc in the n-type partner layer enables mid-gap defects associated with these elements from the commonly used Zn(O,S) buffer layers across the p-n junction can be mitigated. By simultaneously serving as a passivating layer, a diffusion barrier, with tunable band alignments and tailored carrier concentrations to adapt to variations in the absorber layer, (Sn,Ge)O₂ has tremendous potential for developing into the ideal partner material for SnS absorber layers in solar cells.

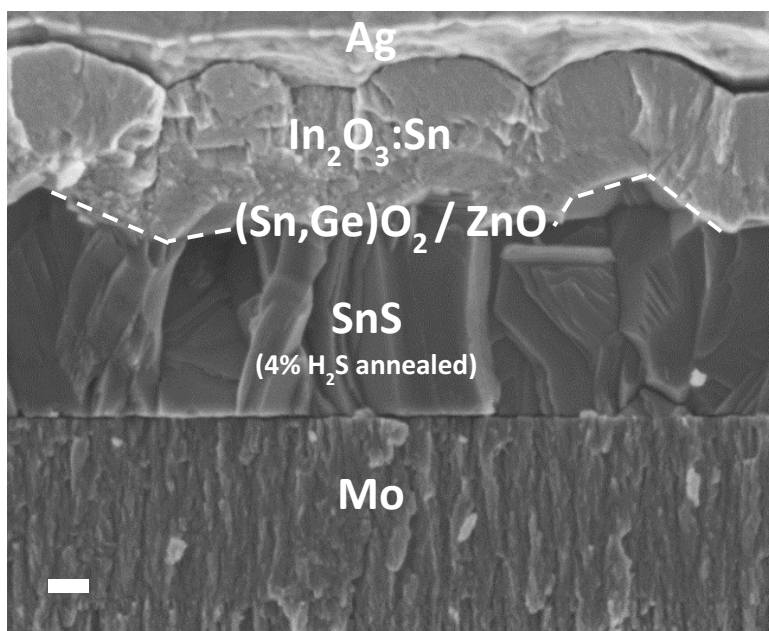
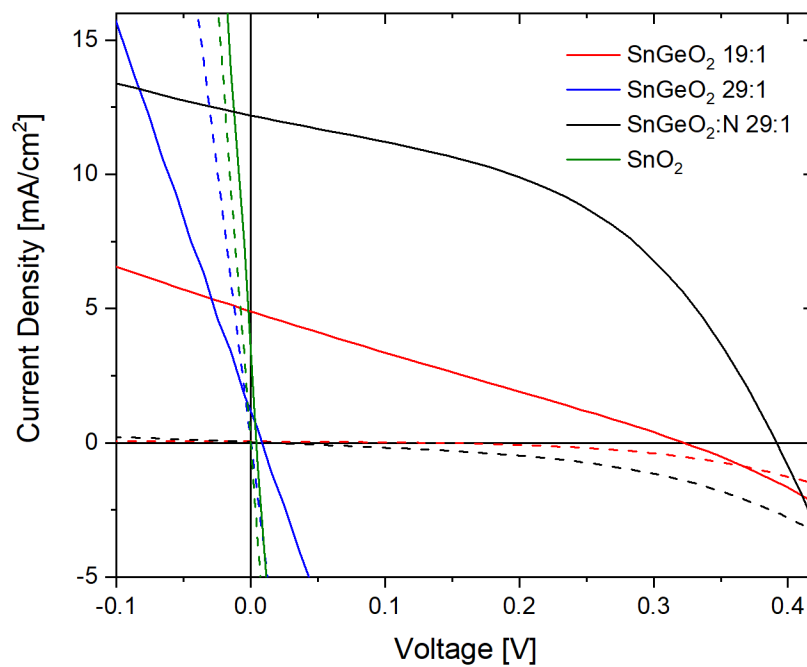


Figure 7.6. (a) Current density-voltage characteristics of Mo/SnS/(Sn,Ge)O₂/ZnO/ITO devices at various (Sn,Ge)O₂ compositions under dark (dotted line) and AM 1.5 illumination (solid line), and (b) a cross-sectional SEM image of the solar cell device with structure Mo back contact/SnS annealed in 4% H₂S absorber/(Sn,Ge)O₂ buffer/ZnO/In₂O₃:Sn window/Ag front contact. Scale bar represents 100 nm.

7.7 References

1. Sinsersuksakul, P., et al., *Atomic Layer Deposition of Tin Monosulfide Thin Films*. *Advanced Energy Materials*, 2011. **1**(6): p. 1116-1125.
2. Ramakrishna Reddy, K.T., N. Koteswara Reddy, and R.W. Miles, *Photovoltaic properties of SnS based solar cells*. *Solar Energy Materials and Solar Cells*, 2006. **90**(18-19): p. 3041-3046.
3. Ichimura, M., et al., *Electrochemical deposition of SnS thin films*. *Thin Solid Films*, 2000. **361-362**: p. 98-101.
4. Ortiz, A., et al., *Tin sulphide films deposited by plasma-enhanced chemical vapour deposition*. *Semiconductor Science and Technology*, 1996. **11**(2): p. 243-247.
5. Koteswara Reddy, N., et al., *Temperature-dependent structural and optical properties of SnS films*. *Journal of Applied Physics*, 2007. **101**(9): p. 093522.
6. Sun, L., et al., *Band alignment of SnS/Zn(O,S) heterojunctions in SnS thin film solar cells*. *Applied Physics Letters*, 2013. **103**(18): p. 181904.
7. Niemegeers, A., M. Burgelman, and A. De Vos, *On the CdS/CuInSe₂ conduction band discontinuity*. *Applied Physics Letters*, 1995. **67**(6): p. 843-845.
8. Sinsersuksakul, P., et al., *Enhancing the efficiency of SnS solar cells via band-offset engineering with a zinc oxysulfide buffer layer*. *Applied Physics Letters*, 2013. **102**(5): p. 053901.
9. Park, H.H., et al., *Co-optimization of SnS absorber and Zn(O,S) buffer materials for improved solar cells*. *Progress in Photovoltaics: Research and Applications*, 2015. **23**(7): p. 901-908.
10. Sinsersuksakul, P., et al., *Overcoming Efficiency Limitations of SnS-Based Solar Cells*. *Advanced Energy Materials*, 2014. **4**(15): p. 1400496.
11. Tritsarlis, G.A., B.D. Malone, and E. Kaxiras, *Structural stability and electronic properties of low-index surfaces of SnS*. *Journal of Applied Physics*, 2014. **115**(17): p. 173702.
12. Hultqvist, A., et al., *Experimental investigation of Cu(In_{1-x}Ga_x)Se₂/Zn(O_{1-z}S_z) solar cell performance*. *Solar Energy Materials and Solar Cells*, 2011. **95**(2): p. 497-503.
13. Repins, I., et al., *19.9%-efficient ZnO/CdS/CuInGaSe₂ solar cell with 81.2% fill factor*. *Progress in Photovoltaics: Research and Applications*, 2008. **16**(3): p. 235-239.
14. Shin, B., et al., *Thin film solar cell with 8.4% power conversion efficiency using an earth-abundant Cu₂ZnSnS₄ absorber*. *Progress in Photovoltaics: Research and Applications*, 2013. **21**(1): p. 72-76.
15. Wang, W., et al., *Device Characteristics of CZTSSe Thin-Film Solar Cells with 12.6% Efficiency*. *Advanced Energy Materials*, 2014. **4**(7): p. 1301465.
16. Barkhouse, D.A.R., et al., *Cd-free buffer layer materials on Cu₂ZnSn(S_xSe_{1-x})₄: Band alignments with ZnO, ZnS, and In₂S₃*. *Applied Physics Letters*, 2012. **100**(19): p. 193904.
17. Waldrop, J.R., et al., *Measurement of semiconductor heterojunction band discontinuities by x-ray photoemission spectroscopy*. *Journal of Vacuum Science & Technology A: Vacuum, Surfaces, and Films*, 1985. **3**(3): p. 835-841.
18. Elam, J.W., et al., *Atomic layer deposition of tin oxide films using tetrakis(dimethylamino) tin*. *Journal of Vacuum Science & Technology A*, 2008. **26**(2): p. 244-252.

19. Singh, A.K., et al., *Sources of electrical conductivity in SnO₂*. Phys Rev Lett, 2008. **101**(5): p. 055502.
20. Tauc, J. and A. Menth, *States in the gap*. Journal of Non-Crystalline Solids, 1972. **8-10**: p. 569-585.
21. Lee, Y.S., et al., *Atomic layer deposited gallium oxide buffer layer enables 1.2 V open-circuit voltage in cuprous oxide solar cells*. Adv Mater, 2014. **26**(27): p. 4704-10.
22. Lange, T., et al., *Physical properties of thin GeO₂ films produced by reactive DC magnetron sputtering*. Thin Solid Films, 2000. **365**(1): p. 82-89.
23. Suapadkorn, P., et al., *Nitrogen – Doped SnO₂ Thin Films Prepared by Direct Current Magnetron Sputtering*. Advanced Materials Research, 2013. **770**: p. 169-172.

8 Oxygen Doped Tin Sulfide Buffer Layer for SnS-Based Heterojunction Solar Cells

8.1 Chapter Abstract

Tin oxysulfide, Sn(S,O) films were prepared using atomic layer deposition and tailored to SnS absorber layer by incorporating tin sulfide with various amounts of oxygen to engineer the optimal energy band alignments at the interfaces of the photovoltaic devices. Hall mobility of Sn(S,O) thin films were enhanced up to $5.2 \text{ cm}^2/\text{Vs}$ and carrier densities were increased up to 10^{16} cm^{-3} from the incorporation of oxygen with a corresponding improvement in film conductivity. Excellent tunabilities of band energy levels enable Sn(S,O) to be optimized for SnS-based solar cells with conduction band offsets of between 0 to 0.34 eV, demonstrating the potential as an alternative buffer layer for SnS-based solar cells.

8.2 Introduction

Tin monosulfide (SnS) is a promising earth abundant p-type semiconductor material for photovoltaic applications. SnS thin films have displayed many desirable properties including a suitable bandgap of 1.1 eV [1] and relatively high mobilities ($\mu \sim 10 \text{ cm}^2\text{V}^{-1}\text{s}^{-1}$) making it an attractive alternative to thin film absorber materials. The better performing SnS-based devices utilize a tunable n-type buffer layer to optimize the conduction band offset (CBO) at the p-n junction interface. Having a range of tunability in the n-type buffer is critical. A “spike” structure is formed when the conduction band edge of the p-type absorber layer is higher than in the n-type buffer layer ($E_{c,\text{absorber}} < E_{c,\text{buffer}}$) forming a barrier that impedes the collection of photogenerated currents. On the other hand, a “cliff” structure ($E_{c,\text{absorber}} > E_{c,\text{buffer}}$) results in an increase in unfavorable interface recombination.

The focus of most studies on SnS solar cells have been on improving the bulk quality of the SnS absorber layer. The device stacks typically include CdS as the n-type buffer layer [2, 3], taking cues from CIGS solar cells [4] which also feature widespread adoption of CdS in forming the p-n junction. Theoretical studies have discovered the importance of designing heterojunctions with suitable conduction band alignments to minimize charge recombination at the junction interface, predicting an optimal conduction band offset (CBO) of 0 eV to + 0.4 eV[5]. Zn(O,S):N is an improved n-type buffer layer for SnS absorber that has the ability to tune its conduction band energy level as well as its carrier density to engineer the optimal conduction band offset at the SnS/Zn(O,S):N heterojunction and with the ideal carrier density relative to the SnS absorber[6]. When several monolayers of SnO₂ were inserted between the SnS absorber and the Zn(O,S):N buffer layer, remarkable improvements in device performance was observed[7]. It

was believed that oxygen from SnO₂ passivated dangling bonds at the SnS surfaces, reducing interface recombination, Furthermore, SnO₂ may have performed the role of a diffusion barrier against zinc from moving from the Zn(O,S):N material into SnS to form a deep level trap, combating bulk recombination within the SnS grains. However, increasing the thickness of SnS beyond a few monolayers degraded the device performance due to the suboptimal conduction band energy level of SnO₂.

By replacing the undoped SnO₂ layer with a p-type buffer layer with improved energy band alignments we are able to mitigate the problem of zinc diffusing from the partner layer into the SnS absorber layer while maintaining a favorable CBO. The optimal conduction band energy levels provided by an optimized Zn(O,S) layer is regained by tuning the conduction band edges by doping oxygen into SnS forming a small spike structure, predominantly by raising the conduction band energy level of SnS. This chapter presents Sn(S,O) as an alternative p-type buffer layer and demonstrates the excellent electrical characteristics and tunability of band energy levels in Sn(S,O).

8.3 Experimental

An ALD process was used to deposit SnS from the reaction of bis(N,N'-diisopropylacetamidinato)tin(II) Sn(MeC(N-iPr)₂)₂ (Sn(amd)₂, Strem Chemicals) and hydrogen sulfide (H₂S, 4% in N₂). Tin precursor vapor assisted by N₂ and hydrogen sulfide gas were injected sequentially into the deposition chamber to allow the chemical reactions to occur successively on the substrate surfaces. To prepare Sn(S,O), water was used as the co-reactant during the SnO cycle by injecting the tin(II) precursor vapor alternating with doses of water. The tin precursor source was kept at 60 °C, and water at 30 °C. The ALD sequence for Sn(S,O) was

$[[(\text{Sn}(\text{Actamd})/\text{N}_2/\text{H}_2\text{S}/\text{N}_2)] \times m + [(\text{Sn}(\text{Actamd})/\text{N}_2/\text{H}_2\text{O}/\text{N}_2) \times n]] \times o$, where m and n indicate the number of sub-cycles of SnS and SnO respectively and o indicates the number of super-cycles. The doping level of oxygen can be tuned by adjusting the SnS/SnO sub-cycle ratio m/n . The process chamber is maintained at temperatures varying from 80°C to 175°C using a Linberg Blue Minimite furnace. Thermally oxidized silicon wafers, glassy carbon planchets, and quartz were utilized as substrates for the deposition of Sn(S,O) thin films. The substrates were treated by UV/ozone cleaner (Samco model UV-1, wavelengths = 185 nm and 254 nm) for 5 minutes at room temperature before being introduced into the process chamber. These substrates are supported by a 316L stainless steel substrate holder with an embedded K-type thermocouple probe for temperature monitoring. Pressure in the deposition chamber was monitored using a convection enhanced pirani gauge (275 Series Gauge Tube, Kurt J. Lesker).

The band alignments at the SnS/Sn(S,O) interface was determined by photoelectron spectroscopy [8]. An X-ray (Al $K\alpha$) source was used to measure the binding energies of Sn and Ge core levels with respect to the valence band maximum energy of bulk SnS and Sn(S,O) films and the valence band energy alignments using a films of SnS with Sn(S,O) overlayers. The transmittance (T) and reflectance (R) spectra of SnS and Sn(S,O) were first measured at normal incidence with an ultraviolet-visible-near-infra-red (UV-vis-NIR) spectrophotometry (Hitachi U-4100 UV-vis-NIR spectrophotometer) in the wavelength range of 200 to 800 nm. 500 nm of ALD SnS and 100 nm of ALD Sn(S,O) were deposited on quartz substrates for the optical characterization. Film thicknesses were measured using x-ray reflectivity measurements (PANalytical X-Pert Pro) and using cross-section scanning electron microscopy (Carl Zeiss Ultra 55 FESEM).

8.4 Results and Discussion

8.4.1 ALD Growth Behavior

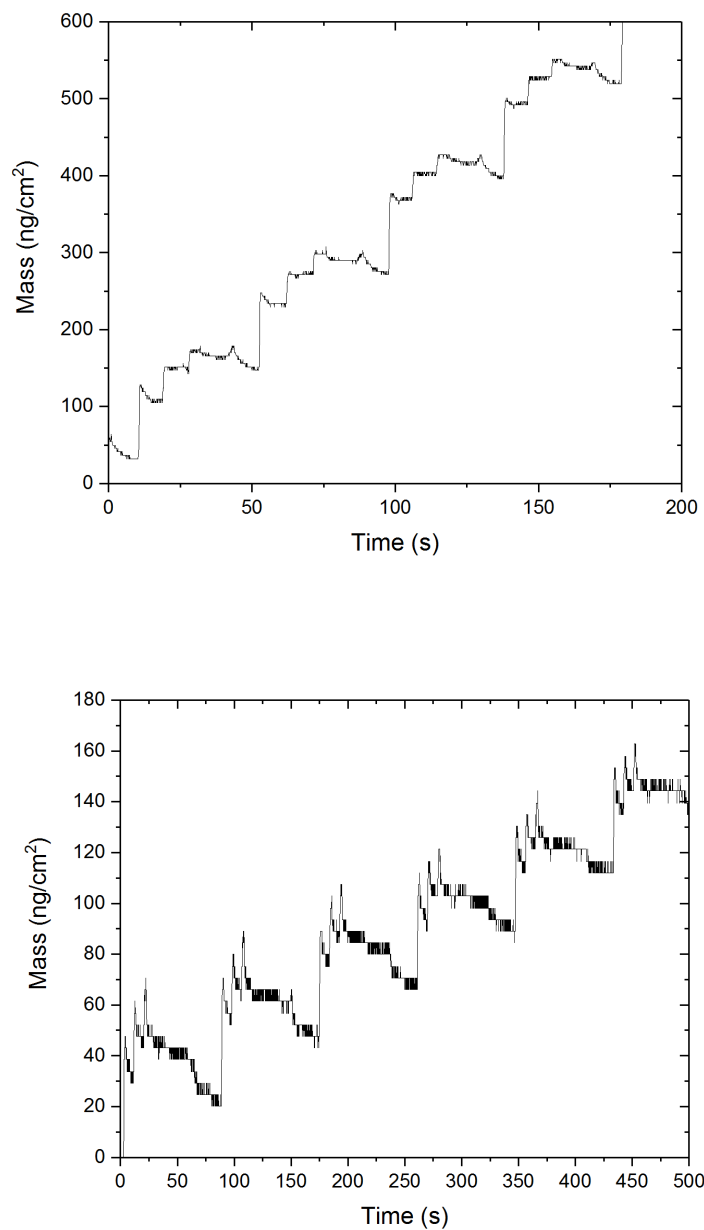


Figure 8.1. Mass change monitored using QCM during (a) 2 ALD super-cycles each containing a sub-cycle of SnS followed by a sub-cycle of SnO at 120 °C, and (b) 1 ALD cycle of SnO and 2 ALD cycles of SnS at 120 °C.

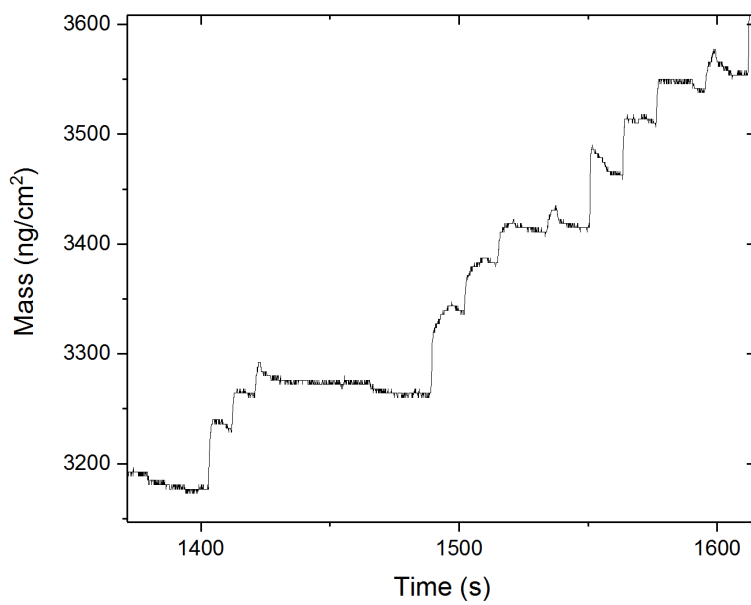
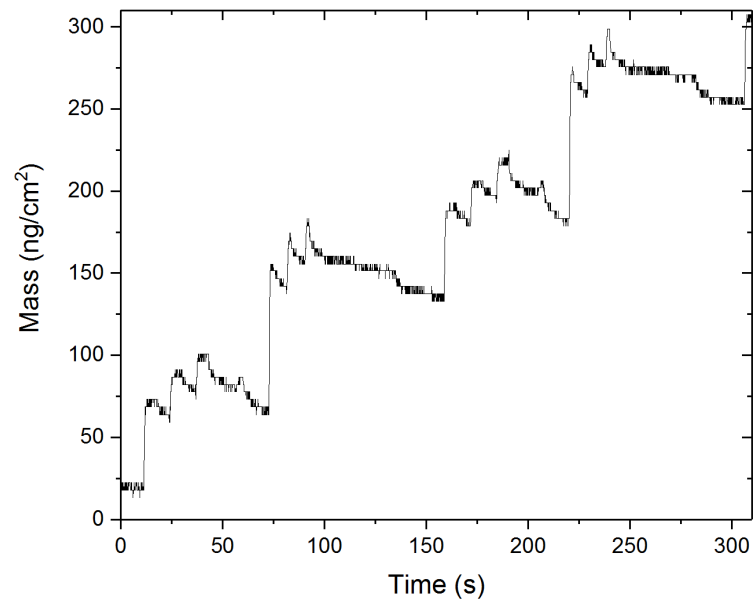


Figure 8.2. Mass change monitored using QCM during (a) 4 cycles of ALD SnS at 120 °C using Sn(Actamd) and H₂S, and (b) 6 cycles of SnO ALD at 120 °C using Sn(Actamd) and water.

Figure 8.2 a and b show close-ups of the mass change with time for SnS ALD and SnO ALD, respectively. The mass change increases linearly with time as the processes were carried out under surface saturation conditions, with the SnS ALD showing a larger mass change per ALD cycle compared to the SnO ALD as a result of incorporating heavier sulfur atoms instead of the lighter oxygen atoms. The overall growth per cycle (in Å per cycle) of SnS is also considerably higher than for SnO as the tin(ii) precursor has a higher reactivity with H₂S than with H₂O.

The elemental compositions of the Sn(S,O) films in Chapter 8.4.2 shows an oxygen doping efficiency that is lower than expected from their SnS/SnO₂ ALD sub-cycle ratios. To investigate this, QCM measurements are performed on two different ALD sequences, as shown in **Figure 8.2**. The first consists of alternative sub-cycles of SnS and SnO. A mass loss of 14 ng/cm² is observed, which is between that of a pure SnS ALD sequence and a pure SnO ALD sequence of 15 and 19 ng/cm² respectively. The second consists of 30 SnO sub-cycle followed by 2 SnS sub-cycles. We observe a mass gain instead of a mass loss during the H₂S exposure of the first SnS sub-cycle, reflecting the substitution of oxygen in the film with the heavier sulfur from the H₂S co-reactant. The mass change from the second SnS sub-cycle of 133 ng/cm² is lesser than in the first of 155 ng/cm², but still larger than the mass change in a pure SnS ALD sequence of 119 ng/cm², indicating a lesser but not insignificant extent of oxygen removal from the film. In the first ALD sequence, oxygen is being substituted with sulfur during the H₂S exposure of every other ALD sub-cycle, limiting the amount of oxygen that can be removed during H₂S exposure, which is consistent with the measured mass change value observed to be between that of the first SnS sub-cycle after multiple SnO sub-cycles, and that of the SnO sub-cycle in a pure SnO ALD process. The efficient removal of oxygen during exposures of H₂S is confirmed by the low oxygen concentrations in the ALD films quantified using high resolution XPS measurements.

Table 5. Average mass gain (Δm_1) and mass loss (Δm_2) for (a) the SnS ALD cycle, (b) the SnO ALD cycle, (c) the SnS cycle after the initial SnO cycle, and (d) the first and second SnS cycle after the initial SnO cycle.

ALD Sequence	Mass gain Δm_1 (ng/cm ²)	Mass Loss Δm_2 (ng/cm ²)	Mass Change Δm (ng/cm ²)
Figure 8.2a	134 ± 2	15 ± 2	119 ± 2
Figure 8.2b	37 ± 2	19 ± 2	18 ± 2
Figure 8.2c	65 ± 2	14 ± 2	51 ± 2
Figure 8.2d, first SnS cycle	151 ± 2	-4 ± 2	155 ± 2
Figure 8.2d, second SnS cycle	118 ± 2	-15 ± 2	133 ± 2

8.4.2 Film Composition

Table 6. Elemental composition of ALD Sn_n(S,O) films measured by high resolution XPS. $x = [O]/([O]+[S])$

SnS/SnO ALD sub-cycle ratio	Elemental Composition			
	[Sn] (at. %)	[S] (at. %)	[O] (at. %)	x
1:0	52	48	0	0
19:1	50	46	4	0.09
9:1	50	45	5	0.11
3:1	47	46	7	0.15
1:1	45	47	8	0.17

The compositions of the SnS films are calculated from the deconvolution of the relevant high-resolution XPS spectra as shown in **Table 6**. XPS spectra of oxygen doped SnS are characterized by a peak at 530.2 eV caused by the presence of oxygen. With increasing SnS/SnO₂ ALD sub-cycle ratio, the percentage of the component associated with Sn-O bonds is found to increase. The elemental quantifications by XPS reveal the low doping level of oxygen in the SnS films that is expected due to the removal of oxygen from the film upon exposure to H₂S gas in the ALD process, as discussed in Chapter 8.4.1.

Figure 8.4b presents the XPS Sn 3d³ and 3d⁵ core level spectra of a typical Sn(S,O) ALD film with both distinct peaks having close to an intensity ratio of 1.5 as a feature of the spin-orbit split. Both distinct peaks for Sn 3d³ and Sn 3d⁵ can be deconvoluted into a high energy component and a low energy component. The high energy can be attributed to the binding energies of Sn-O bonds and the lower energy component to Sn-O bonds. These peak assignments are consistent with further investigations on pure SnS and pure SnO ALD films as shown in the **Figure 8.4a**. The lower energy component of the Sn 3d³ and 3d⁵ core level are observed to shift to lower energies with an increase in oxygen concentration in the SnS ALD film. The undoped SnS ALD film has a single component for each of the two symmetrical peaks. Increasing the oxygen concentration leads to an increase in asymmetry due to the increasing intensity of a higher energy component contributed by the presence of Sn-O bonds. In addition, it is evident that increasing the level of oxygen doping leads to a shift of the low energy components (attributed to Sn-S bonds) towards lower binding energies and the higher energy components (attributed to Sn-O bonds) to shift towards higher binding energies. The maximum extend of this shift is determined to be -0.3 eV for the lower energy component and 0.8 eV for the higher energy component.

The high purity of the Sn(S₂O) films are displayed in the high resolution XPS measurements in the C 1s and N 2p regions, as a result of the complete reaction between both tin(IV) precursor with both hydrogen Sulfide and water vapor. Carbon and nitrogen peaks were observed only on the surface of the films due to exposure to ambient contaminants but are not found in the bulk of the film that is exposed by sputtering the surface using Ar⁺ ions as evident in the XPS depth profiling measurements in **Figure 8.3**.

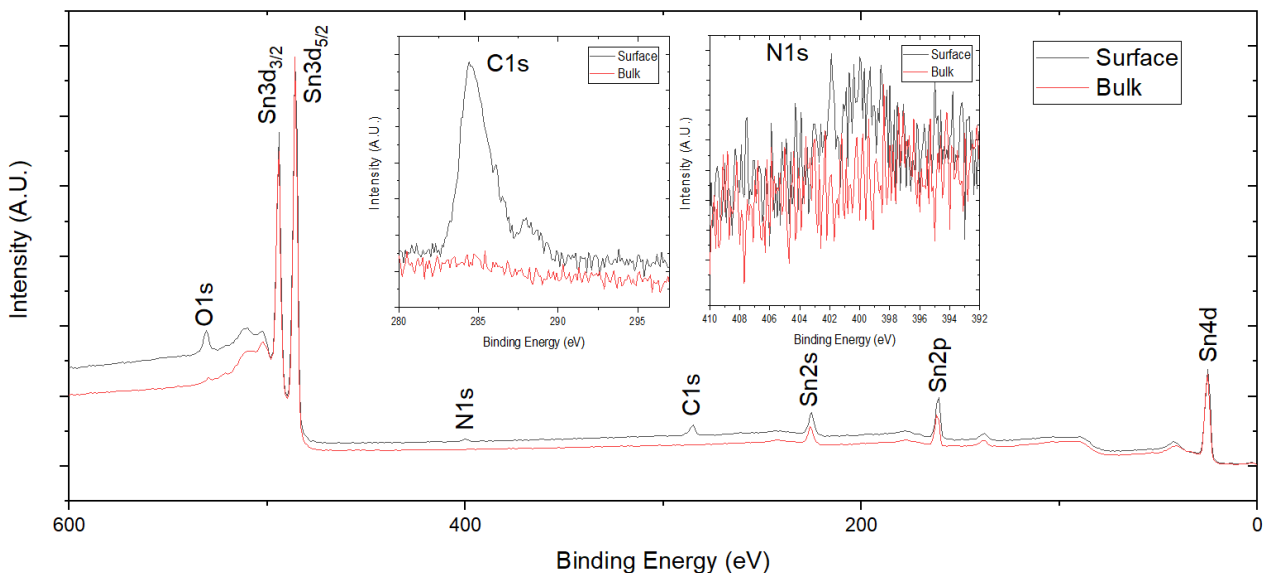


Figure 8.3. Depth profile measurements of Sn(S₂O) 19:1 ALD film, showing the survey spectra. Inset: (a) High resolution spectra of the C 1s core level, and (b) high resolution spectra of the N 1s core level.

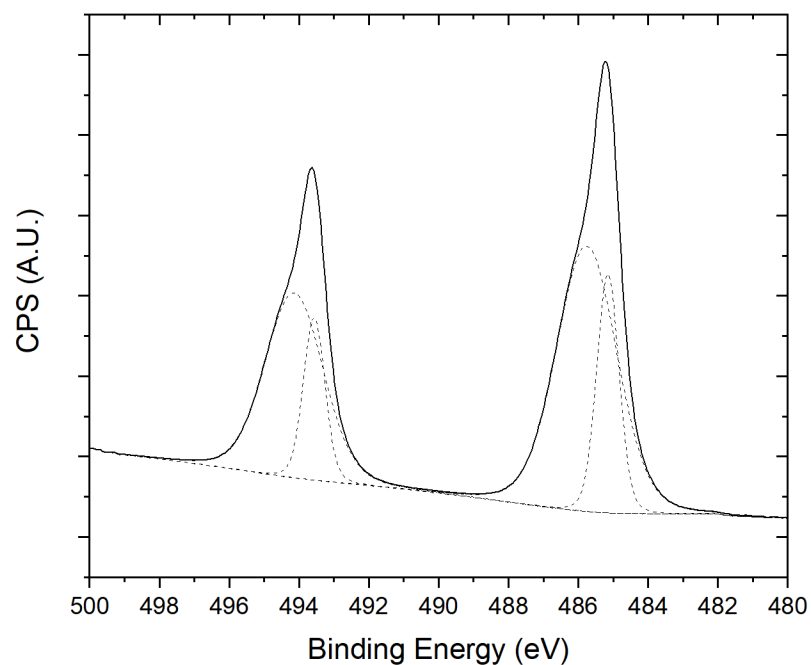
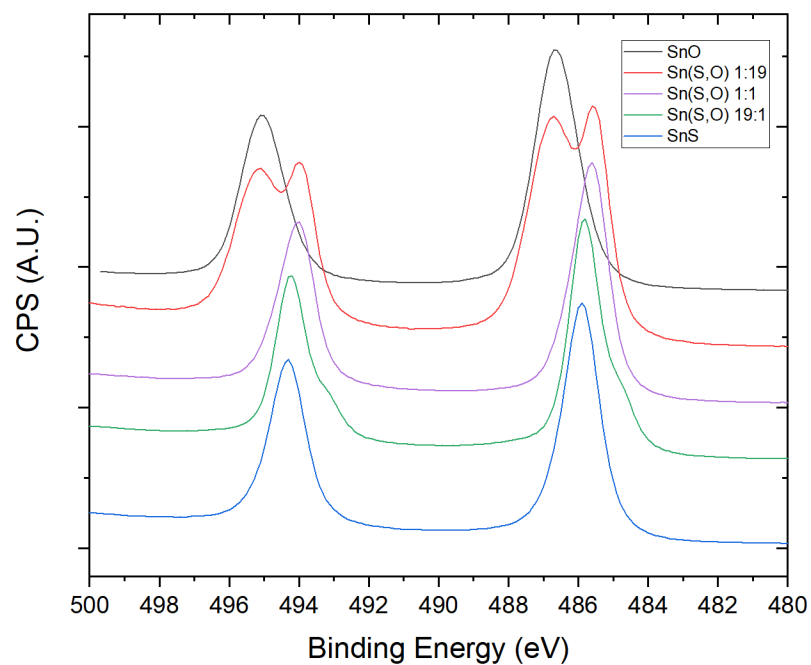


Figure 8.4. High resolution XPS spectra showing (a) the Sn 3d core levels of SnS ALD films with various O concentrations, and (b) the deconvolution of the Sn 3d core levels of Sn(S,O) 19:1 ALD film. The dotted lines are the split-orbital components of the deconvoluted spectra, the solid lines are the experimental data.

8.4.3 Film Morphology and Structure

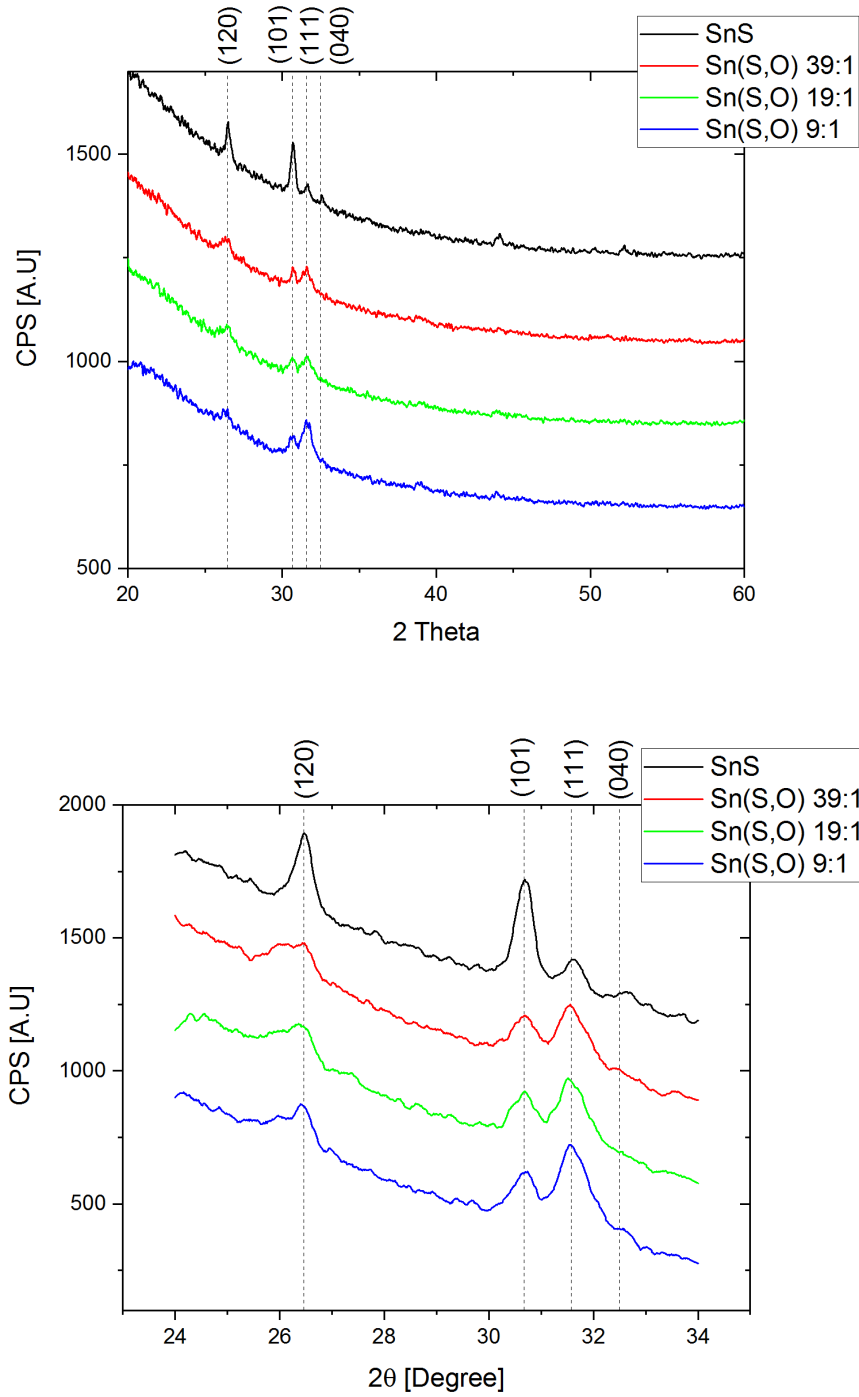


Figure 8.5. XRD spectrum of undoped and oxygen doped SnS films with ALD subcycle ratios 39:1, 19:1, 9:1. (b) is the expansion of (a) to clearly show the (111) and (040) peaks.

The XRD spectra show a shift in preferred crystal orientation from the (040) and (101) planes to the (111) planes as the oxygen content in the SnS film increases. This indicates a preference towards growth in the plane of the substrate to growth in the direction perpendicular to the substrate.

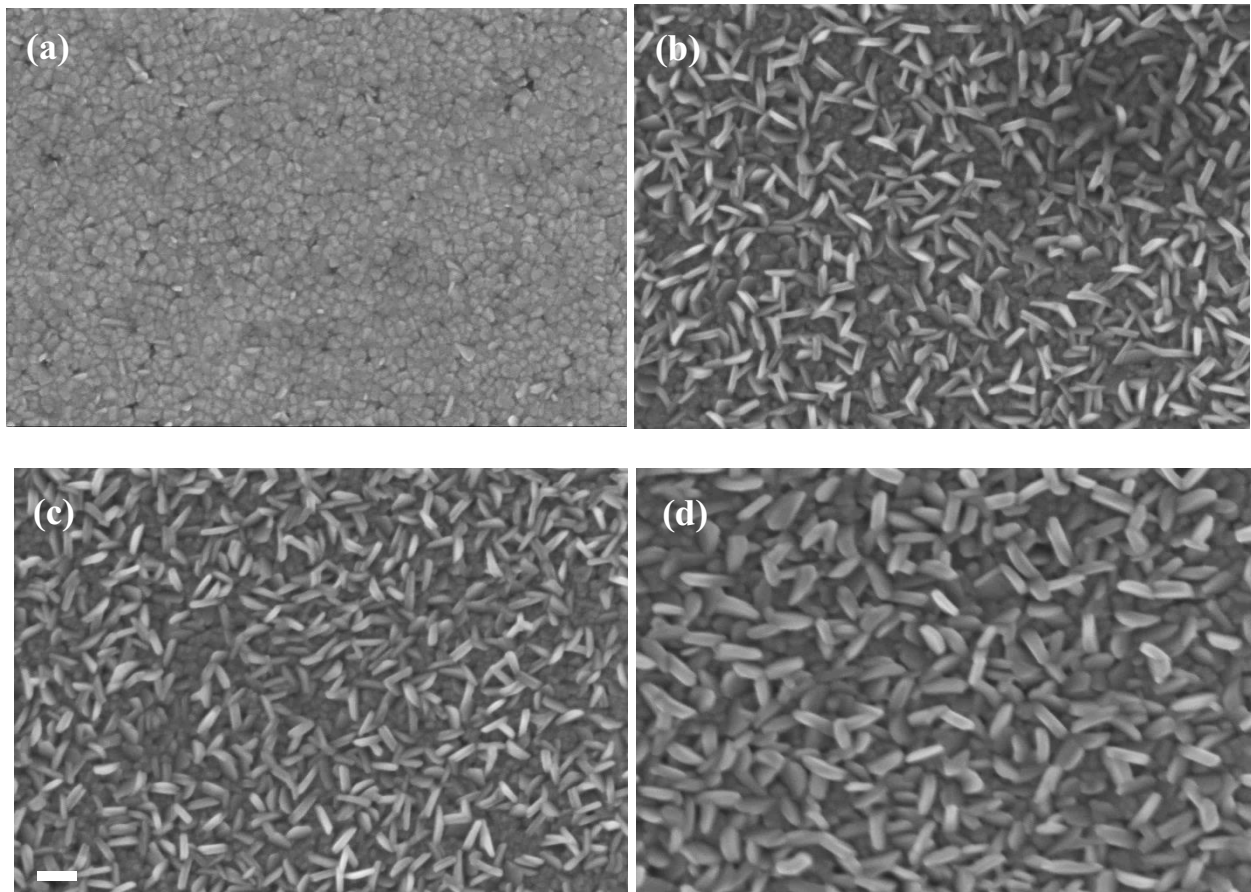


Figure 8.6. Plane-view SEM micrographs of (a) SnS films, and Sn(S₂O) films with SnS/SnO ALD sub-cycle ratios of (b) 39:1, (c) 19:1, and (d) 1:1. All ALD films were deposited on thermal oxide for 800 ALD cycles at 120°C. The scale bar is 100 nm.

The effects of oxygen doping in SnS thin films have a significant role in determining the surface morphologies, as reflected by the SEM images in **Figure 8.6**. Undoped SnS displays a characteristic grain pattern consisting of rectangular plates coalescing together and oriented in a direction normal to the plane of the substrate. An increase in oxygen concentration in the SnS film demonstrates an increase preference for the growth of larger grains, and hence increased crystallinity of the films, as evident in the larger plate-like grains shown in the plane-view SEM images. The cross-section view of the films reflects a similar effect in grain growth, revealing more distinct columnar grain structures with grain boundaries oriented perpendicular to the substrate surface with increasing oxygen incorporation. Oxygen doping is thus shown to be a viable low temperature approach for tuning the grain sizes of SnS ALD films.

8.4.4 Electrical Properties

The carrier mobility, electron carrier density and resistivity are plotted in **Figure 8.7** as a function of the O/(O+S) ratio. Oxygen doping was observed to increase the Hall mobility of SnS from 2.7 cm²/Vs. This increase can be explained by oxygen passivating dangling bonds that exist along the grain boundaries of SnS, leading to suppressed carrier recombination in the SnS film[9]. Increasing the oxygen content of SnS films resulted in an increase in hole concentration by 1-2 orders of magnitude from 1 × 10¹⁴ cm⁻³, with the oxygen doped films having hole concentrations that remain within an order of magnitude (between 3 × 10¹⁵ cm⁻³ and 1 × 10¹⁶ cm⁻³). Since the conductivity of SnS originates from the combined behavior of p-type doping from Sn vacancies and the n-type doping from S vacancies, this increase in hole concentration can be explained by the incorporation of oxygen dopant in the sulfur vacancy site. Oxygen doping was demonstrated to result in an overall decrease in resistivity of the Sn(S,O) film.

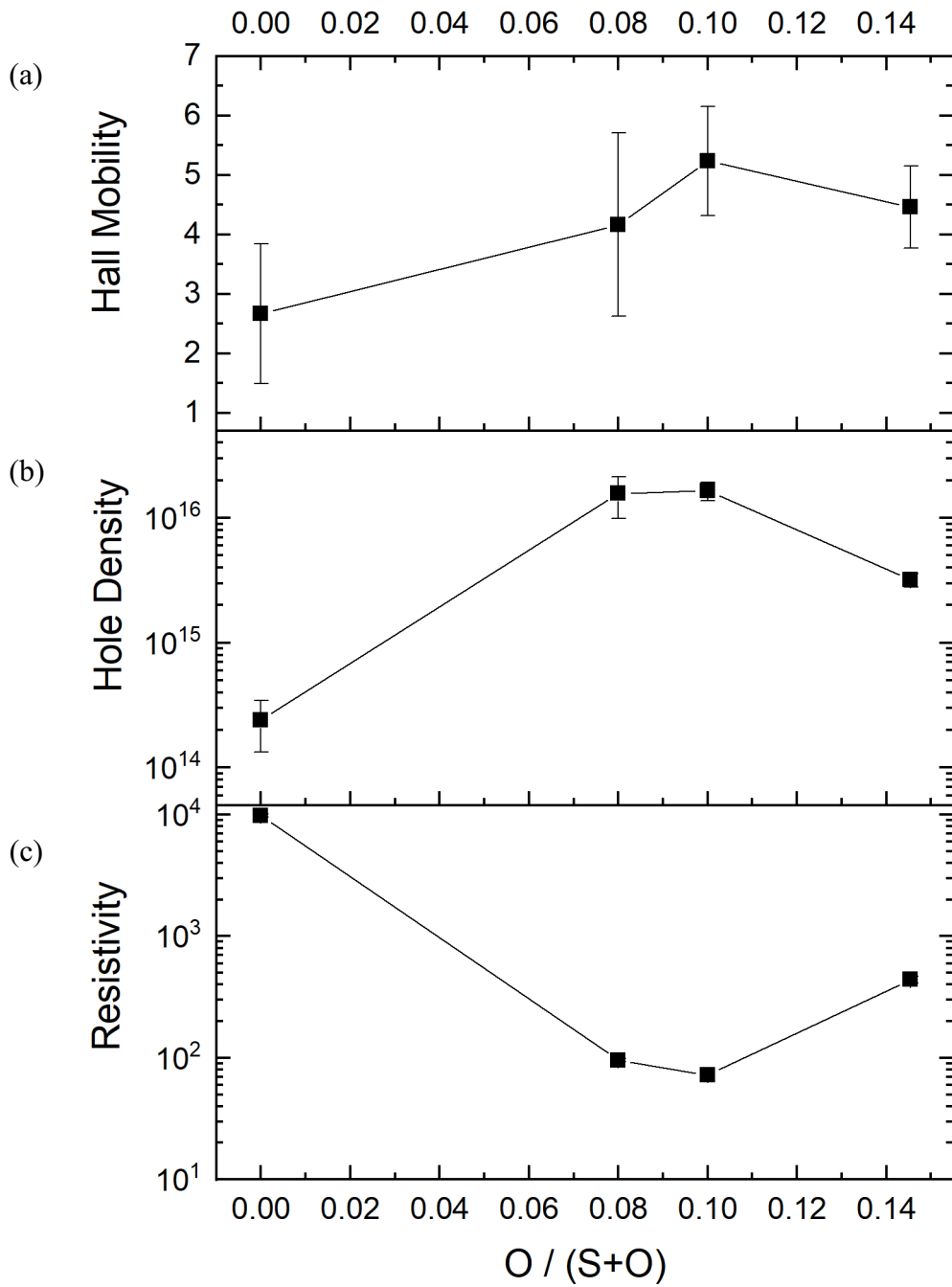


Figure 8.7. Plot of (a) Hall mobility, (b) hole carrier concentration, and (c) resistivity of Sn(S,O) thin films with various O/(O+S) ratios.

8.4.5 Optical Properties

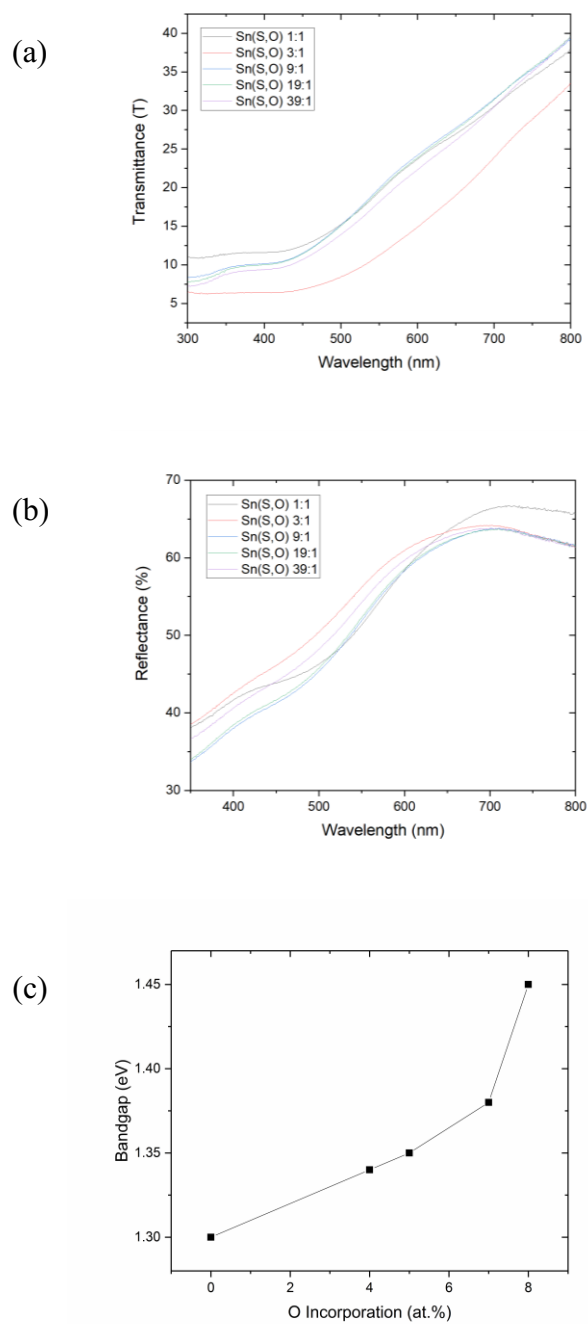


Figure 8.8. UV-VIS-NIR measurements of Sn(S,O) thin films with different Sn/SnO ALD subcycle ratios, displaying the (a) transmittance, and (b) reflectance traces. (c) The extracted optical band gap values from the Tauc plot.

The absorption coefficient α is obtained from the optical transmission and reflectance measurements (**Figure 8.8a, b**) and calculated using

$$\alpha = \frac{1}{d} \ln\left(\frac{1-R}{T}\right)$$

where d is the film thickness. The optical bandgap energy value is then obtained from plots of α^2 vs. photon energy for the various ALD films deposited on quartz substrates, using the Tauc relation for direct transitions [10]

$$\alpha(h\nu) \propto (h\nu - E_g)^{\frac{1}{2}}$$

where $\alpha(h\nu)$ is the absorption coefficient, $h\nu$ is the photon energy, and E_g is the optical bandgap. The bandgap is then obtained by extrapolating to $\alpha \cdot h\nu = 0$. Both the electron and hole effective masses are assumed to be constant.

The optical band gap of SnS is observed to increase monotonically from 1.3 eV with no oxygen doping to 1.45 eV with 8 at.% of O incorporated, shown in **Figure 8.8c**. This trend makes it trivial to tune the band gap of SnS, with the flexibility to also create a graded band structure. In comparison, the Cu(In,Ga)(S,Se)₂ (CIGS) absorber layer can tune its band gap between 1.01 eV to 1.67 eV by varying to amount of Ga in the material[11].

8.4.6 Band Alignment

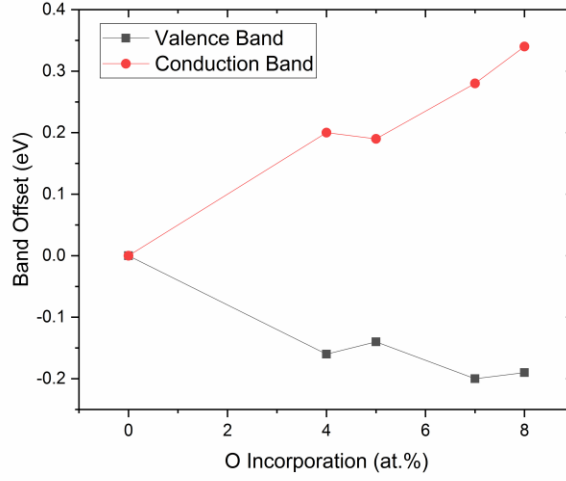


Figure 8.9. Energy level offsets at the SnS/Sn(S,O) heterojunction interface for valence bands (red) and conduction bands (black).

Bilayer samples of 500-nm-thick SnS and 5-nm-thick Sn(S,O) with various concentrations of oxygen dopants were fabricated by ALD to investigate the electronic band alignment of Sn(S,O) relative to SnS. The valence band offset (ΔE_{VB}) and conduction band offset (ΔE_{CB}) in the SnS/Sn(S,O) stack are respectively calculated using the relation

$$\Delta E_{VB} = (E_{Sn-3d}^{SnS/Sn(S,O)} - E_{O-1s}^{SnS/Sn(S,O)}) + (E_{O-1s}^{Sn(S,O)} - E_{VBM}^{Sn(S,O)}) - (E_{Sn-3d}^{SnS} - E_{VBM}^{SnS})$$

$$\Delta E_{CB} = (E_{Sn-3d}^{SnS/Sn(S,O)} - E_{O-1s}^{SnS/Sn(S,O)}) + (E_{O-1s}^{Sn(S,O)} - E_{VBM}^{Sn(S,O)}) - (E_{Sn-3d}^{SnS} - E_{VBM}^{SnS}) \\ + (E_g^{Sn(S,O)} - E_g^{SnS})$$

where $E_g^{Sn(S,O)}$ and E_g^{SnS} are the optical band gaps of bulk Sn(S,O) and SnS, respectively.

The valence band offsets decreases monotonically while the conduction band offsets increases monotonically with increasing amounts of oxygen in the Sn(S,O) film. The conduction band offset has demonstrated tunability from 0 eV to +0.4 eV, which is within the optimal offset values predicted by simulation studies[5], theoretically making Sn(S,O) a suitable buffer layer to SnS for reducing charge recombination at the critical heterojunction interface.

8.5 Conclusions

In summary, it was demonstrated that SnS can be doped with oxygen to change the conduction band level. Oxygen doping has shown to promote grain growth during the ALD of SnS, leading to increase in Hall mobility from 2.7 cm²/Vs to 5.2 cm²/Vs, and the hole density to increase from 10¹⁴ cm⁻³ to 10¹⁶ cm⁻³. The optical band gap of Sn(S,O) widens from 1.3 eV to 1.45 eV, and contributes to the conduction band offset of the SnS/Sn(S,O) heterojunction to be adjusted from 0 eV to 0.34 eV. By simultaneously acting as a diffusion barrier to zinc while having an optimal conduction band alignment with the SnS absorber, Sn(S,O) can potentially be a promising alternative to Zn(O,S) buffer layers in SnS solar cells.

8.6 Reference

1. Ramakrishna Reddy, K.T., N. Koteswara Reddy, and R.W. Miles, *Photovoltaic properties of SnS based solar cells*. Solar Energy Materials and Solar Cells, 2006. **90**(18-19): p. 3041-3046.
2. Ghosh, B., et al., *Fabrication of vacuum-evaporated SnS/CdS heterojunction for PV applications*. Solar Energy Materials and Solar Cells, 2008. **92**(9): p. 1099-1104.
3. Malaquias, J., et al., *Assessment of the potential of tin sulphide thin films prepared by sulphurization of metallic precursors as cell absorbers*. Thin Solid Films, 2011. **519**(21): p. 7416-7420.
4. Scheer, R., et al., *CuInS₂ based thin film solar cell with 10.2% efficiency*. Applied Physics Letters, 1993. **63**(24): p. 3294-3296.
5. Niemegeers, A., M. Burgelman, and A. De Vos, *On the CdS/CuInSe₂ conduction band discontinuity*. Applied Physics Letters, 1995. **67**(6): p. 843-845.
6. Park, H.H., et al., *Co-optimization of SnS absorber and Zn(O,S) buffer materials for improved solar cells*. Progress in Photovoltaics: Research and Applications, 2015. **23**(7): p. 901-908.
7. Sinsermsuksakul, P., et al., *Overcoming Efficiency Limitations of SnS-Based Solar Cells*. Advanced Energy Materials, 2014. **4**(15): p. 1400496.
8. Waldrop, J.R., et al., *Measurement of semiconductor heterojunction band discontinuities by x-ray photoemission spectroscopy*. Journal of Vacuum Science & Technology A: Vacuum, Surfaces, and Films, 1985. **3**(3): p. 835-841.
9. Tritsarlis, G.A., B.D. Malone, and E. Kaxiras, *Structural stability and electronic properties of low-index surfaces of SnS*. Journal of Applied Physics, 2014. **115**(17): p. 173702.
10. Tauc, J. and A. Menth, *States in the gap*. Journal of Non-Crystalline Solids, 1972. **8-10**: p. 569-585.
11. Gloeckler, M. and J.R. Sites, *Band-gap grading in Cu(In,Ga)Se₂ solar cells*. Journal of Physics and Chemistry of Solids, 2005. **66**(11): p. 1891-1894.

Appendix A. Deposition Systems

A1. Hybrid ALD-CVD Reactor: Cu_2O , Ga_2O_3 , ZnO:Al

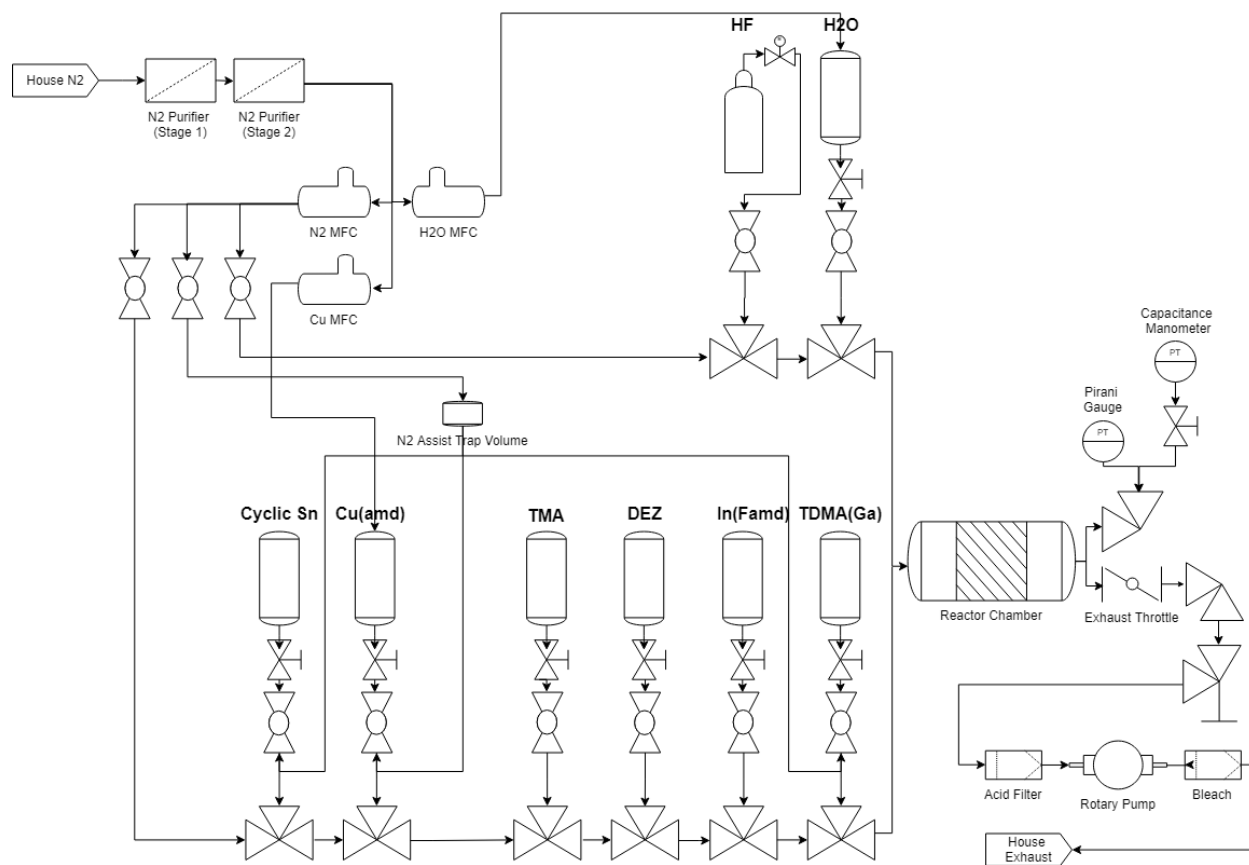


Figure 8.10. Schematic of the deposition system for CVD Cu_2O , ALD Ga_2O_3 , ALD ZnO:Al .

A2. ALD Reactor: SnS, ZnOS:N

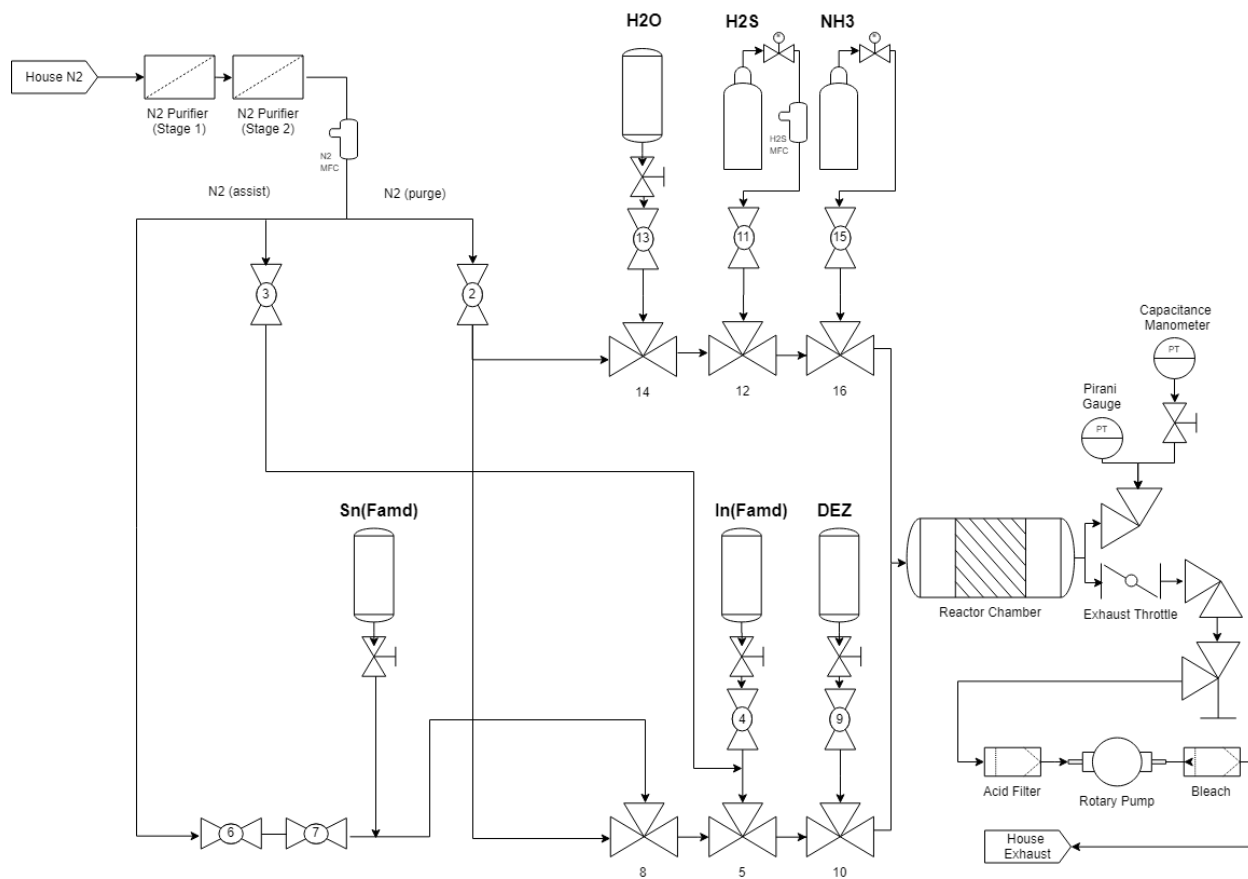


Figure 8.11. Schematics of the ALD deposition system for SnS and ZnOS:N, and the H₂S annealing of SnS.

A3. ALD Reactor: SnS, In₂O₃

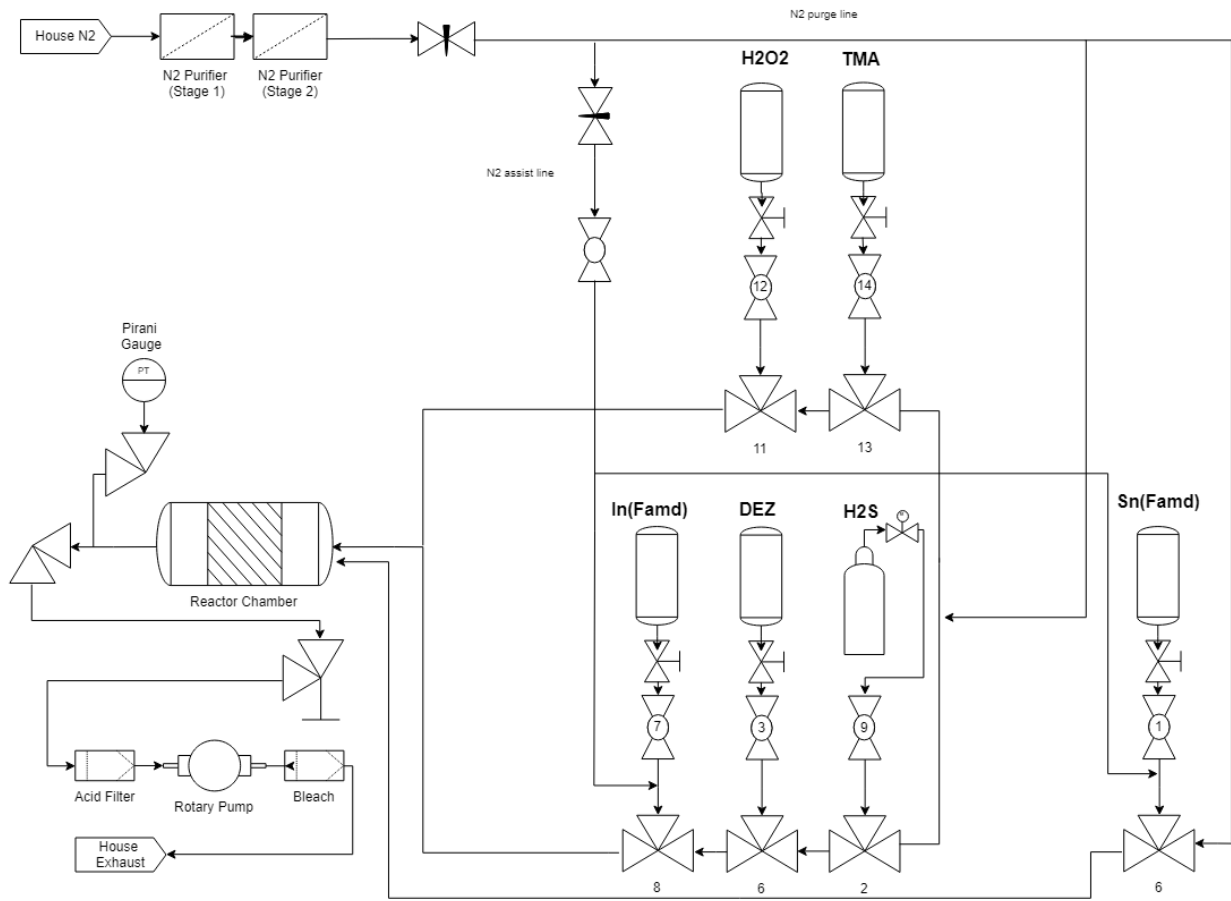


Figure 8.12. Schematics of the ALD deposition system for SnS and In₂O₃.

A4. ALD Reactor: (Sn, Ge)O₂

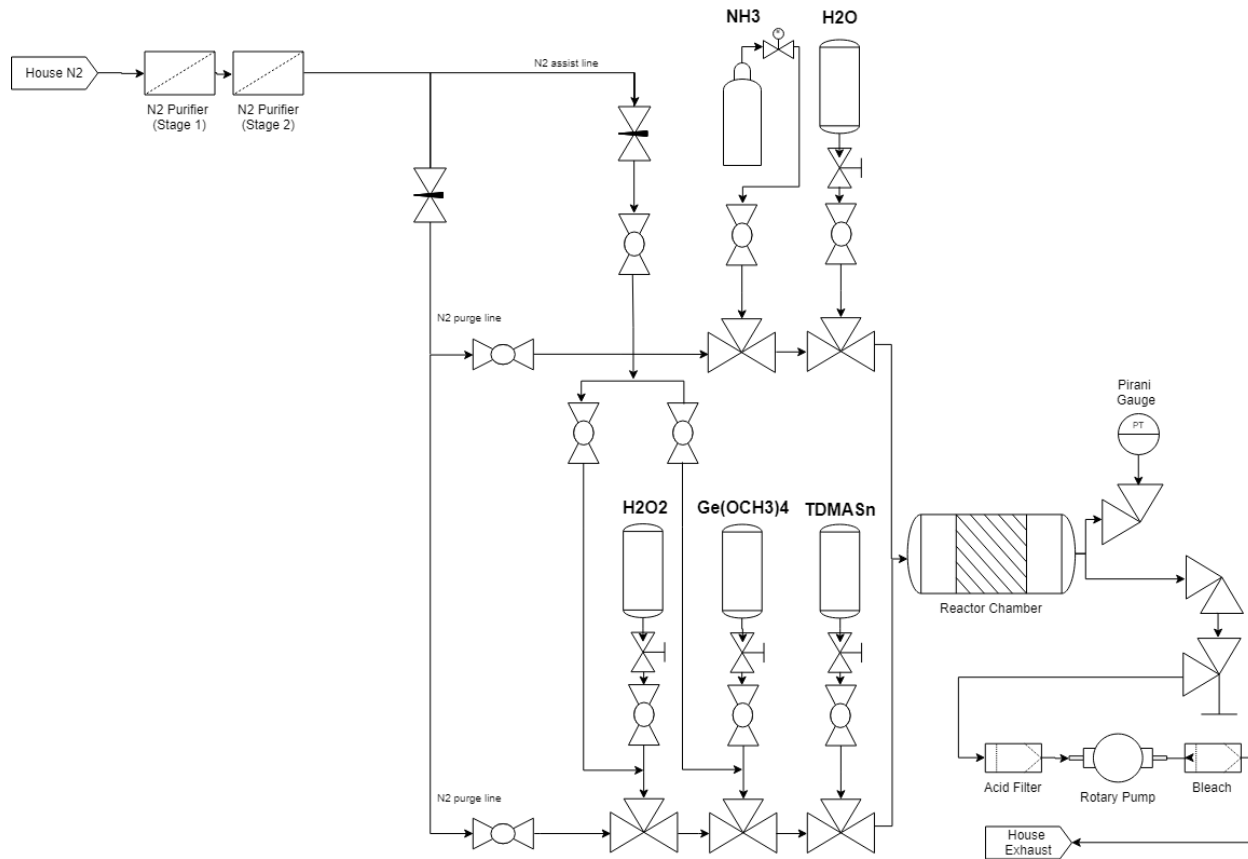


Figure 8.13. Schematics of the ALD deposition system for (Sn,Ge)O₂.

A5. Thermal Oxidation System: Cu_2O

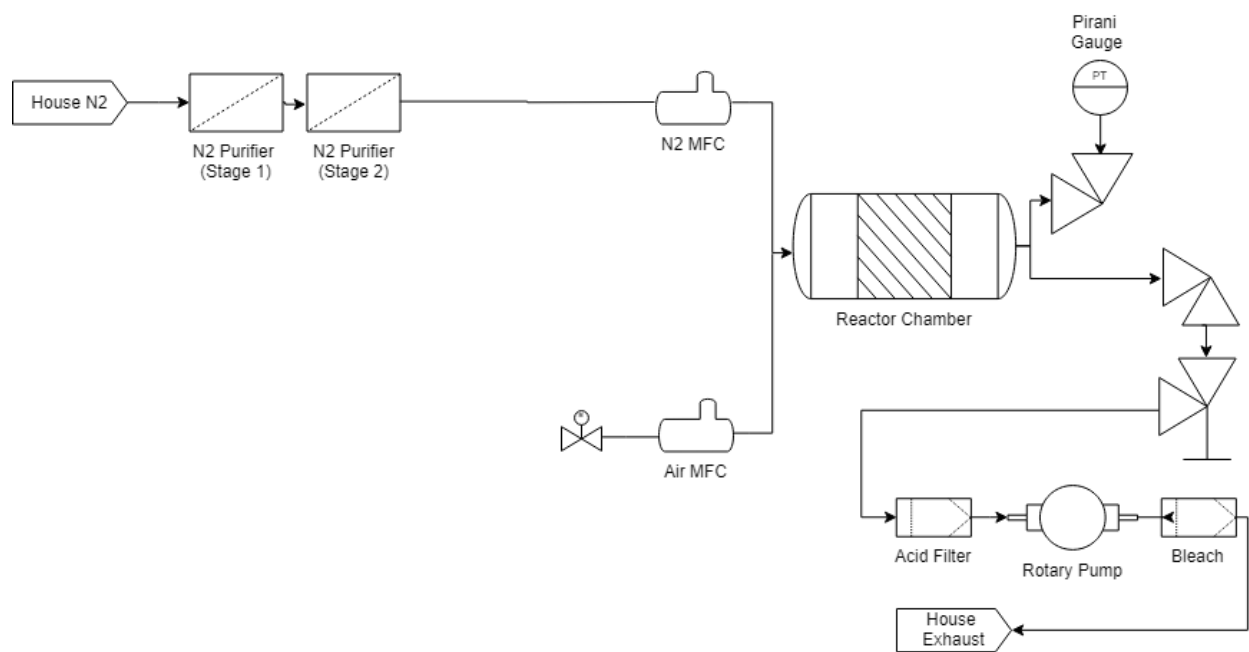


Figure 8.14. Schematics of the thermal oxidation system for oxidizing Cu sheets to Cu_2O

Appendix B. Thermal Oxidation of Cu

Sheets to Cu₂O

Experimental

Copper sheets (99.9999% purity metal basis, 100 μm thick) were cut into 1 cm × 1 cm pieces and two 1 mm holes were punched into two corners on one side of the sheet. The Cu sheets were suspended on a quartz boat by threading platinum wires through the 2 punched holes and introduced into the middle of the quartz tube of the annealing furnace, shown in **Figure 8.15a**. Each quartz rack can fit a maximum of three Cu sheets with ample spacing between them to avoid samples from touching each other during the annealing process which may cause them to be stuck together.

Oxidizing Cu sheets to Cu₂O is done using a 3-stage oxidation process, illustrated in **Figure 8.15b**. First, the samples were brought to a temperature of 1050 °C in a nitrogen ambient created by flowing 100 sccm of purified N₂ into the reaction zone. After 2 hours of annealing in N₂, the flow of N₂ is stopped and 100 sccm of ambient air is metered into the reaction chamber and maintained for 2 hours. Finally, the annealing atmosphere is purged and replaced with purified N₂ by flowing 100 sccm of purified N₂ for 2 hours, then cooling the sample to 100 °C before removal.

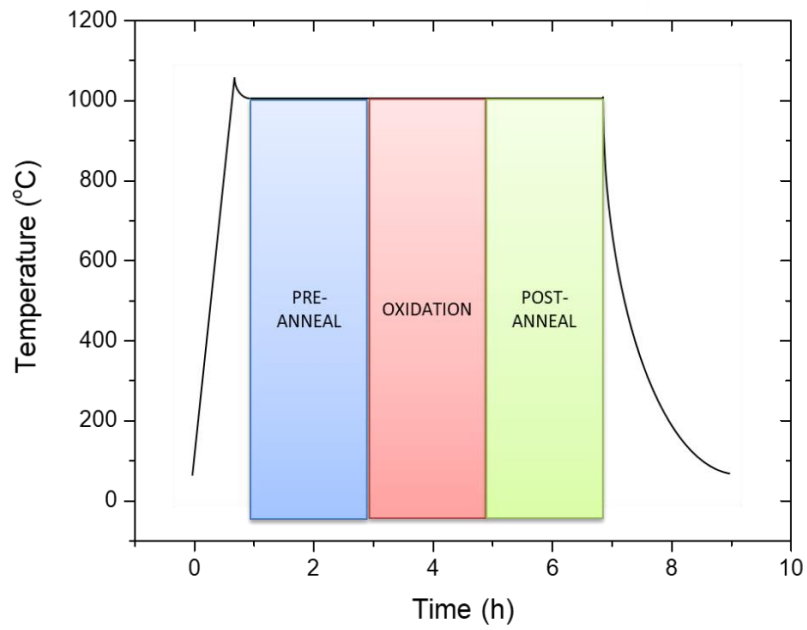


Figure 8.15. (a) Copper sheets suspended on a quartz rack using platinum wires and positioned in the middle of the annealing furnace. (b) Temperature profile of the 3-stage oxidation process for oxidizing Cu sheets to Cu_2O .

Results and Discussion

Grains of 1 mm in diameter can be achieved using the high temperature oxidative process to oxidize Cu sheets into Cu_2O , as shown in **Figure 8.16**. **Figure 8.17a** shows the spectrally-resolved steady-state photoluminescence map focused on a millimeter size Cu_2O grain whose optical image is shown in **Figure 8.17b**. The different colors indicate PL emissions of different wavelength. Grain boundaries of Cu_2O produce intense defect emissions compared to the grain interior which produces lower intensity PL emissions of a shorter wavelength. This is suggestive of grain boundaries being high in defect densities and capable of contributing significantly to undesired charge recombination at these interfaces. Thermal oxidation produces significantly larger grain sizes than other preparation methods such as chemical vapor deposition and electrochemical deposition, which we predict will deliver higher photocurrents. Hence, thermally oxidized Cu_2O will be an excellent candidate for the 2-absorber device architecture discussed in Chapter 5 due to the high J_{SC} it can deliver.

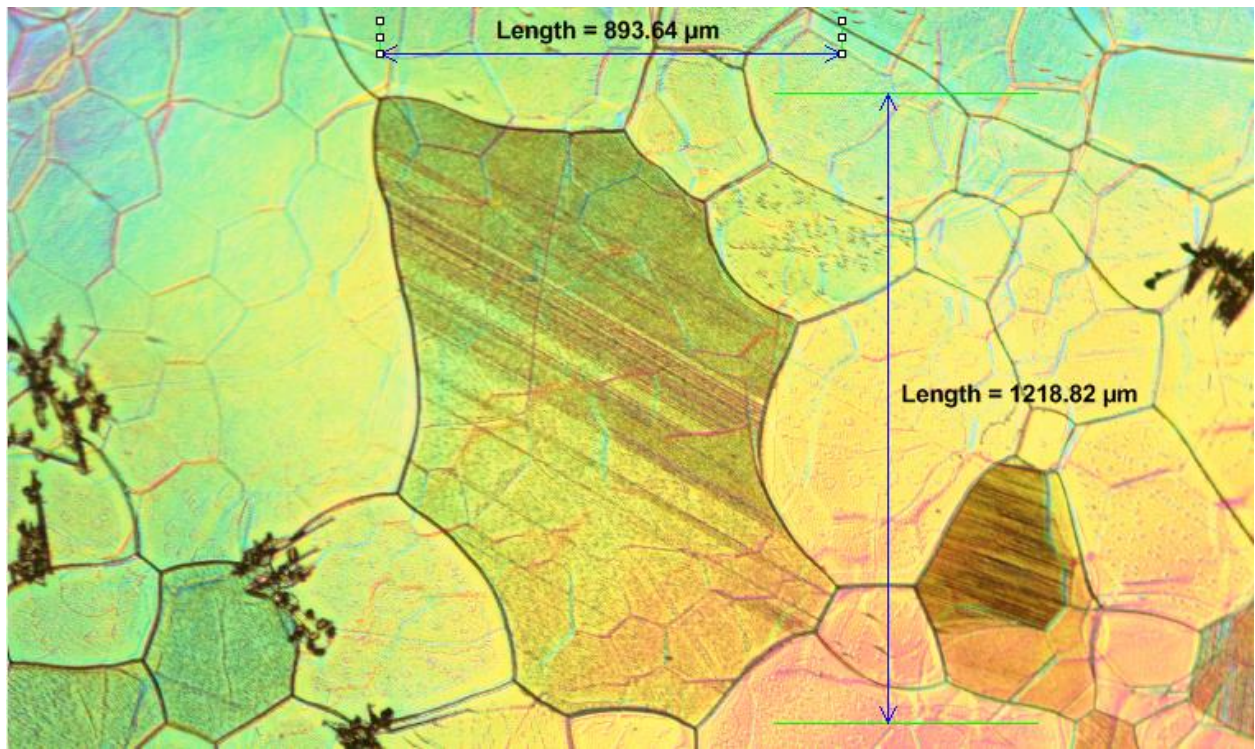


Figure 8.16. (a) Optical micrograph of the thermally oxidized Cu₂O surface showing the merging of small grains into larger grains of up to 1.2 mm in dimension. (b) 35mm camera image of the thermally oxidized Cu₂O sheet.

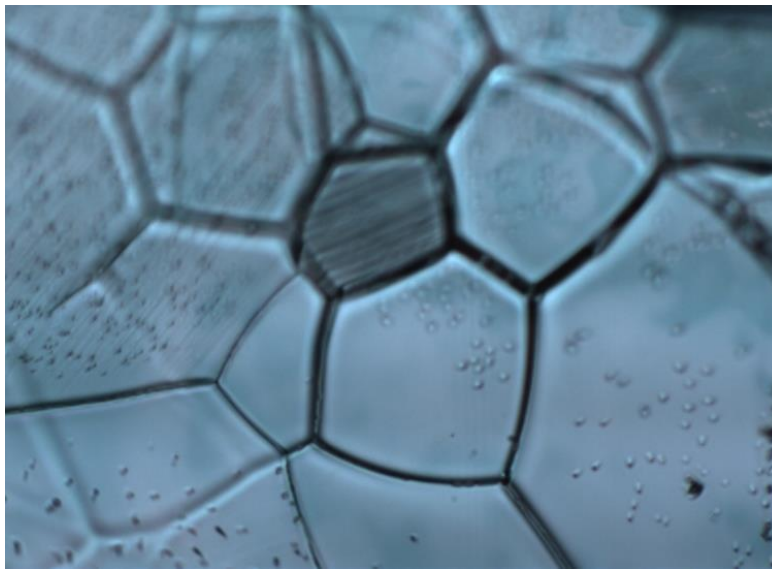
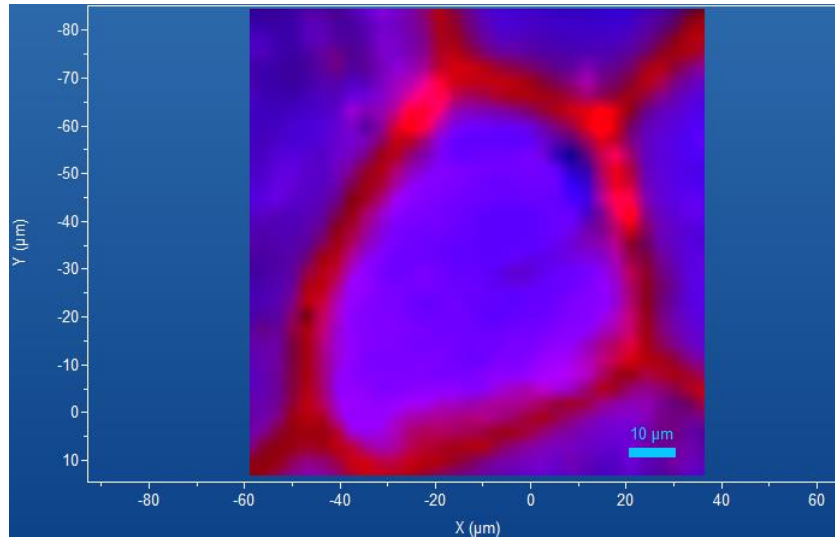


Figure 8.17. (a) Spectrally-resolved photoluminescence image focused on a Cu_2O grain. (b) Confocal microscope image of the same Cu_2O grain.

Appendix C. High Temperature Annealing

Treatments of Doped Ga₂O₃ Thin Films

Table 7. Summary of post-anneal sheet resistances of Ga₂O₃, Sn-doped Ga₂O₃ and Ge-doped Ga₂O₃ under various annealing conditions.

Bulk ALD Film	Dopant	Sheet Resistances after Post Deposition Anneal (ohm/sq)				
		Atmosphere	Anneal Temperature			
			400°C	600°C	800°C	1000°C
Ga ₂ O ₃	Undoped	N ₂	10 ⁹	10 ⁹	10 ⁹	10 ⁹
		H ₂	10 ⁹	10 ⁹	Film removed	Film removed
	Sn (1:9, 1:19)	N ₂	10 ⁹	10 ⁹	10 ⁹	10 ⁹
		H ₂	10 ⁹	10 ⁹	Film removed	Film removed
	Ge (1:1)	N ₂	10 ⁹	10 ⁹	10 ⁹	10 ⁸
		H ₂	10 ⁹	10 ⁹	Film removed	Film removed

Experimental

200 nm thick Ga₂O₃ thin films were grown by ALD using TDMA(Ga) and water vapor at a substrate temperature of 120 °C using 1000 ALD cycles on 1" × 1" Si/SiO₂ substrates. Sn-doped Ga₂O₃ was deposited using the same conditions but with the insertion of a SnO₂ ALD sub-cycle using TDMA(Sn) as the Sn source and with Ga₂O₃/SnO₂ subcycle ratios of 9:1 and 19:1. Ge-doped Ga₂O₃ was deposited with the insertion of a GeO₂ ALD sub-cycle using Ge(OCH₃)₄ as the Ge source and with an Ga₂O₃/GeO₂ subcycle ratio of 1:1. The as-deposited ALD films of undoped Ga₂O₃, Sn-doped Ga₂O₃ and Ge-doped Ga₂O₃ were annealed in the ALD deposition chamber at temperatures of 400, 600, 800, and 1000 °C for a duration of 2 hours before cooling back down to room temperature. The anneal ambient was constructed by flowing either purified N₂ or purified H₂ at a flow rate of 100 sccm while maintaining the process pressure at 10 Torr. The electrical resistivity of the annealed Ga₂O₃ films were subsequently measured using a Hall effect 4-point probe measurement system.

Results and Discussion

Ge-doped Ga₂O₃ films experienced a reduction in film resistivity when annealed at 1000 °C in a N₂ atmosphere. All Ga₂O₃ films were completely removed from the substrate after annealing in a H₂ ambient at temperatures of 800 °C and higher. It is plausible that Ga₂O₃ have been reduced to a volatile sub-oxide under these conditions.

Appendix D. Photovoltaic Device

Simulations

Experimental

The 1-D simulation software SCAPS [1] was utilized in all the device simulation studies carried out involving thin film solar cells with SnS and with Cu₂O absorbers. Each SCAPS instance runs using only a single core on both Windows and Linux operating systems despite being executed on multi-core systems. As a result, simulation studies were significantly accelerated by running SCAPS simulations in parallel and a job queue.

Parallel computation of SCAPS simulations enabled all the system cores to be fully utilized. Reserving a single CPU thread for the OS was found to provide the best performance. Since the simulation processes are only computationally heavy and are not memory-intensive loads, an optimal system will involve a large number of CPU cores and minimal memory. 8 GB of memory was sufficient to support Windows 10 and 31 SCAPS instances running on a 16-core CPU. A simulation platform based on Python was used to provide the multi-core processing capabilities of SCAPS by managing the underlying execution of the SCAPS software. It has also been designed to be agnostic to the simulation package for futureproofing the platform when given the correct preprocessing of input parameters and postprocessing of simulation results. A redis server [2] was set up locally to provide the (non-persistent) in-memory data store which backs a job queue system *rq* [3]. When sweeping a simulation parameter space, the monolithic job can be batched into several smaller subspaces, which are queued in *rq* for consumption by workers spawned by the simulation platform. This architecture of a multi-processing simulations

platform consuming from a queue enables the system to be highly resilient to crashes of the simulation engine, especially from corner cases in simulation parameters that fail to converge to solutions.

Future Directions

The current architecture paves the way for horizontal scaling to multiple processing nodes to form a computing cluster capable of handling highly parallelized distributed computing. The *rq* service and redis server can be hosted either on a dedicated node, or on one of the systems consuming simulation jobs from *rq*. Leveraging the recent advances in CPU architectures (AMD Ryzen 3000 series) and process nodes (TSMC 7nm+ EUV process node), cost effective computing nodes can each be built with workstation-grade 16-core CPUs (AMD Ryzen 3800X) and 8 GB DDR non-ECC memory without moving to costly datacenter-grade platforms with similar core counts typically clocked at half the clock frequencies (approximately half the processing power) of their workstation counterparts.

Since the architecture is built on cross-platform code with Python, it will be trivial to migrate from Windows to Linux to access the more efficient simultaneous multithreading (SMT) and stability of computing environment. However, SCAPS is a Windows based software and does not run in a Linux environment. Docker, a containerization technology can be used to generate a container with the Windows environment in which SCAPS can execute in. The simulation platform will require a modification to manage docker containers in addition to the SCAPS software running inside them. A more dated alternative to docker is Wine (recursive backronym

for Wine is Not an Emulator) [4], a Linux software that allows a Windows application like SCAPS to run on a Linux system.

The aforementioned improvements will enable the generation of large datasets of model-performance input-output pairs where the SCAPS models generated from the parameter space sweeps will result in device simulation results such as the J-V (under dark and illuminated conditions) and quantum efficiency characteristics. These data can potentially be used to train a deep neural network for automated high throughput analysis of solar cell devices using their experimentally measured J-V and EQE curves, bypassing the labor intensive and computationally expensive traditional workflow of model design and curve fitting. Similar deep learning approaches can be further extended to include other characterization techniques including spectroscopy (PL, Raman, FTIR, XRD, XPS) and imaging (SEM, 2D/3D PL, lock-in-thermography).

References

1. Burgelman, M., et al., *Modeling thin-film PV devices*. Progress in Photovoltaics: Research and Applications, 2004. **12**(2-3): p. 143-153.
2. Sanfilippo, S. *Redis*. Available from: <https://redis.io/>.
3. Driessen, V. *RQ: Simple job queues for Python*. Available from: <https://python-rq.org/>.
4. Amstadt, B. *WineHQ - Run Windows applications on Linux, BSD, Solaris and macOS*. Available from: <https://www.winehq.org/>.